SPACE SCIENCE ACTIVITIES IN CHINA

National Report 2022—2024

Chief Editor: GUO Huadong

Deputy Chief Editor: WANG Chi, LI Lei

Editorial Staffs: SUN Weiying, SONG Yana

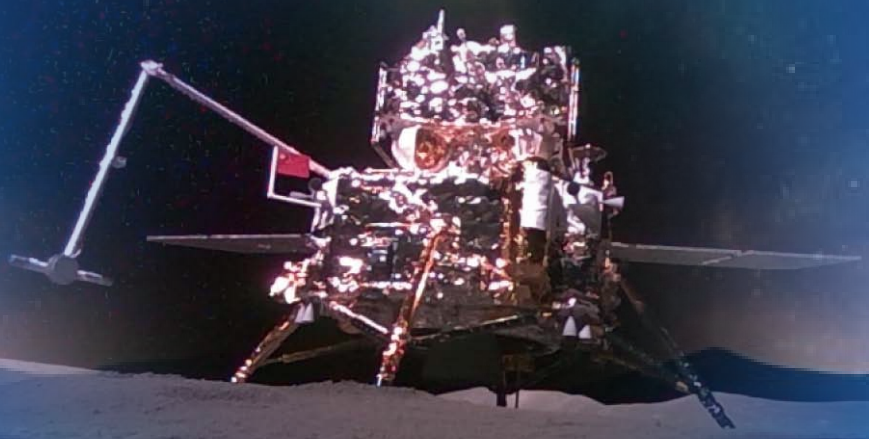

CNCOSPAR

JULY 2024

Preface

The space science program, the deep space exploration program, and the manned spaceflight program in China experienced rapid progress during the 2022–2024 period.

The two phases of Strategic Priority Program on Space Science initiated by the Chinese Academy of Sciences in 2011 have produced substantial scientific output, with the Phase I including the Dark Matter Particle Explorer (DAMPE), ShiJian-10 (SJ-10), Quantum Experiments at Space Scale (QUESS) and Hard X-ray Modulation Telescope (HXMT), and Phase II including Taiji-1 (the first technology demonstration mission of Taiji Program), the Gravitational wave high-energy Electromagnetic Counterpart All-sky Monitor (GECAM), the Advanced space-based Solar Observatory (ASO-S), the Einstein Probe (EP), and the Solar wind Magnetosphere Ionosphere Link Explorer (SMILE).

The Advanced space-based Solar Observatory (ASO-S), China's first comprehensive solar mission in space, and the Einstein Probe (EP), a mission dedicated to time-domain astronomy to monitor the sky in the soft X-ray band, were launched on Oct. 9, 2022 and Jan. 9, 2024 respectively. The Solar wind Magnetosphere Ionosphere Link Explorer (SMILE), an ESA-China joint mission, is scheduled to be launched by the end of 2025.

SDGSAT-1, the world's first science satellite dedicated to assisting the United Nations 2030 Sustainable Development Agenda, has been operational for over two and a half years, providing valuable data to facilitate the implementation of the Sustainable Development Goals internationally. The Space-based multiband Variable Object Monitor (SVOM), a China-France joint mission mainly designed to study Gamma-Ray Bursts, was launched into an orbit of about 635 km on June 22, 2024.

In the future, new scientific missions will be planned to answer questions in five scientific themes namely, the Extreme Universe, Space-Time Ripples, the Panoramic View of the Sun and Earth, the Habitable Planets, and Biological & Physical Science in Space.

For lunar and deep space exploration, the Chang'E-6 lunar exploration mission reentered the atmosphere and successfully landed on Earth on June 25, 2024, completing its historic mission to collect the first ever samples from the far side of the moon.

In the field of manned spaceflight, the Chinese Space Station (CSS) has been fully deployed by the end of 2022, and the facility has entered into the application and development phase. It has conducted scientific research projects in various fields, such as space life science and biotechnology, space mate-

rials science, microgravity fundamental physics, fluid physics, combustion science, space new technologies, and applications.

For the ground observation, the second phase of the Chinese Meridian Project (CMP) has passed the technique acceptance, and is expected to operate as a whole in 2025 after national acceptance of the second phase. From 2022 to 2023, utilizing the monitoring data collected by the CMP, scientists have made major breakthroughs in fields of ionosphere, middle and upper atmosphere, and coupling between layers.

Human beings have been relentlessly leveraging the development of space science to explore the frontiers of the vast universe and push the boundaries of human knowledge to its limits. International cooperation is an integral part of Chinese space science endeavors. There are international collaboration elements in all individual space science missions in China. As illustrated in the EP and SMILE mission, international partners are welcome to take part in Chinese scientific programs.

In this report, the PIs of scientific missions and the leading experts in various fields of space science in China will present the major programs, the highlights of mission achievements, the status of the missions to be launched, and the future mission planning.

I wish you can get a general picture of the recent progress in space research in China and also invite you to use the published data of the Chinese space science missions.

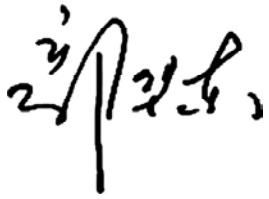

President
Chinese National Committee for COSPAR

Article Index

1 Manned Spacefight Program

GU Yidong, GAO Ming, ZHAO Guangheng, WANG Qiang, LYU Congmin, ZHONG Hongen, LIU Guoning. Recent Progress in Space Science and Applications on Chinese Space Station in 2022–2024. *Chinese Journal of Space Science*, 2024, **44**(4)

Recent Progress in Space Science and Applications on Chinese Space Station in 2022–2024

GU Yidong, GAO Ming, ZHAO Guangheng, WANG Qiang, LYU Congmin, ZHONG Hongen, LIU Guoning

Key Laboratory of Space Utilization, Technology and Engineering Center for Space Utilization, Chinese Academy of Sciences, Beijing 100094

Abstract

Chinese Space Station (CSS) has been fully deployed by the end of 2022, and the facility has entered into the application and development phase. It has conducted scientific research projects in various fields, such as space life science and biotechnology, space materials science, microgravity fundamental physics, fluid physics, combustion science, space new technologies, and applications. In this review, we introduce the progress of CSS development and provide an overview of the research conducted in Chinese Space Station and the recent scientific findings in several typical research fields. Such compelling findings mainly concern the rapid solidification of ultra-high temperature alloy melts, dynamics of fluid transport in space, gravity scaling law of boiling heat transfer, vibration fluidization phenomenon of particulate matter, cold atom interferometer technology under high microgravity and related equivalence principle testing, the full life cycle of rice under microgravity and so forth. Furthermore, the planned scientific research and corresponding prospects of Chinese space station in the next few years are presented.

Key words

Chinese Space Station (CSS), Space material science, Micro-gravity fluid physics, Fundamental physics, Space life sciences and biotechnology

1 Construction and Operation of CSS during 2022–2024

With the successful launches of the Wen Tian experiment module in July 2022 and the Meng Tian experiment module in October 2022, the three modules configuration of the Chinese Space Station has been completed in orbit and entered a stage of application and development lasting more than ten years. In the past two years, four Tianzhou cargo spaceships (TZ-4, 5, 6, 7) have been launched and 5 Shenzhou manned spaceships (SZ-14, 15, 16, 17, 18), fifteen astronauts have entered the space station, completing four short-term missions with six people on board, and conducted Tian gong Classes.[1].

Chinese Space Station (CSS), known as the National Space Laboratory, with the most comprehensive support capabilities, and unique advantages such as human participation and spaceship transportation. It has the capability to conduct large-scale space science research based on a variety of advanced scientific research and

Received May 25, 2020

technology experimental facilities[2]. In order to explore the frontier of space science, promote space applications, and develop space technology, CMS has carried out in-depth discussions and demonstrations, with over 1000 scientists from various fields and more than 200 research institutes participating, and has formulated forward-looking scientific and application mission plans for the next ten years[3]. In 2023, CMS released project guidelines to the whole society, openly call for science and application proposals[4], which received positive responses from all sectors of China and provided strong support for future achievements.

So far, the scientific experiment racks and payloads are operating well. More than 100 scientific and applied projects have been carried out, achieving outstanding progress and results in space life science and biotechnology, microgravity fluid and thermophysics, combustion science, space materials, microgravity fundamental physics, and new space application technologies. Overall, the Chinese Space Station has achieved normalized project collections, experimental materials delivery, in-orbit scientific experiments, ground analysis, and preliminary application benefits.

2 Recent Scientific Research in Space

2.1 Space Materials Science

Material scientific researches on Chinese space station are mainly carried out in containerless material experimental rack and high-temperature material experimental rack. Some typical progresses have been made, for instance, the rapid solidification of ultra-high temperature alloy melts has been investigated, getting precise measurements of supercooled liquid alloys so as to promote the understanding of large undercooling behavior, solidification process along with crystal growth in space; effective control of the solidification process and structure of monotectic alloy was realized, samples with the multi-layer structure were obtained; the preparation method of space InAsSb ternary semiconductor crystals has been studied, presenting the growth of high-quality InAsSb crystals in space for the first time, which is difficult to prepare on the ground. The performance of the transistor made of the crystal material is greatly improved, improving the development of ultra-fast electronic and optoelectronic devices. Some noteworthy results are presented in detail as follows.

2.2.1 Accurate Measurement of Liquid Properties of Refractory Alloys

The thermophysical properties of supercooled liquid alloys are crucial to condensed matter physics and solidification theory. Related research in outer space in a containerless environment has unique advantages because Electrostatically Levitated (ESL) droplets on the ground are bound to be affected by gravity, resulting in a change in droplet shape and buoyancy-driven convection. Fortunately, this disadvantage can be solved well in a microgravity environment. As one of the most significant materials for aerospace, Nb-Si refractory alloy has an excellent strength-to-density ratio and high-temperature performance but still lacks the understanding of the alloy in liquid. Nb-Si has been chosen as the near-eutectic alloy for the space-based ESL experiments. The schematic of the ESL furnace on CSS is shown in Figure 1, which mainly consists of three pairs of high-

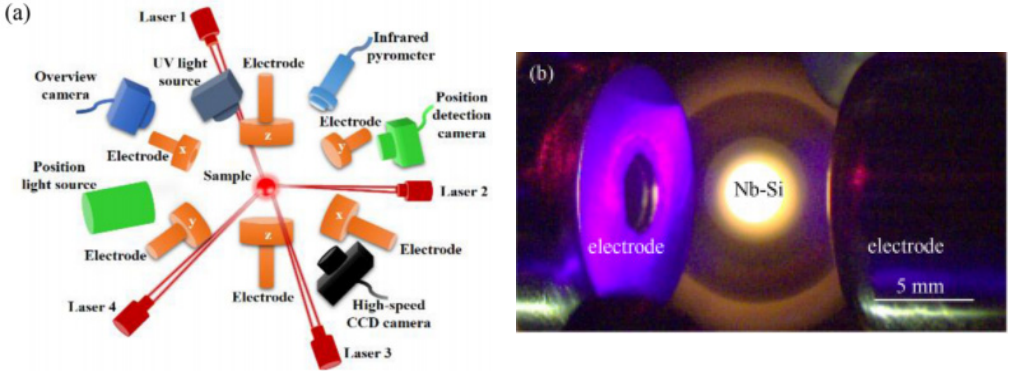

Fig.1 Electrostatic levitation facility and experimental conditions on board the Chinese Space Station. (a) The schematic of the ESL system. (b) Image of a levitated NbSi alloy droplet[5]

v oltage electrodes with a feedback loop, four semiconductor lasers with the tetrahedral configuration, a position detection camera, and so forth.

Aiming to determine the thermophysical properties of liquid Nb-Si refractory alloys over a broad temperature range along with the atomic structures of high- temperature liquids, the scientists from Northwestern Polytechnical University in China attempted to develop a path to get large undercooling of liquid refractory alloys with high activity, to achieve the fine sphericity of liquid alloys and to find the reliable thermophysical properties and the characteristics of atomic cluster in the undercooled Nb-Si alloy melts[9]. The team successfully experimented with a series of operations under microgravity *via* heating, melting, cooling, undercooling, solidification, and the thermal physical properties measuring for the refractory alloys. The experimental samples were returned to the ground aboard the Shenzhou manned spacecraft, as shown in Figure 2.

The team found that under this microgravity condition, the levitated alloy melt will appear perfectly spherical under the action of surface tension, deviating from the ideal sphericity by only about 0.5%, showing extremely high sphericity, see Figure 3(a)

2.1.2 Alloy Surface Nucleation and Structure Control

The researchers successfully achieved ultra-high temperatures of 2338 K and extreme metastable states of 1752 K by heating and melting the refractory alloy in a containerless rack onboard. They obtained an extreme metastable alloy melt with an undercooling degree of 437 K, reaching the theoretical limit of 0.2 Te for uniform nucleation, see Figure 3(b). The evolution of the Nb-Si alloy liquid structure was determined with the Voronoi Polyhedron (VP) method, see Figure 4.

The surface microstructure consists of the primary solid solution (Nb) and the surrounding (Nb) /Nb_3Si eutectic phase, as shown in Figure 5.

This discovery is confirmed to realize the dual regulation of “macro form and micro-texture”. Under the microgravity condition, the natural convection disappears, and the weak Marangoni convection effect appears, which can cause peculiar changes in the flow field distribution of alloy melt. These abundant microscopic flows contribute to the formation of specific structures and structures during the process of eutectic solidification，which becomes a new way to regulate the surface microstructure[8].

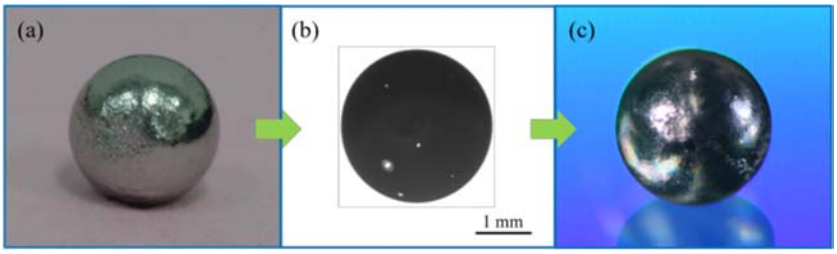

Fig.2 Refractory alloy space station experiment samples. (a) The refractory alloy on the ground was carried into the core module of the Chinese Space Station by Tianzhou-3 cargo spacecraft. (b) Projection of the 2200K ultra-high temperature alloy melt in the space station experiment. (c) The alloy pellets prepared by solidification on the space station were returned to the ground laboratory on board the Shenzhou 14 manned spacecraft[5]

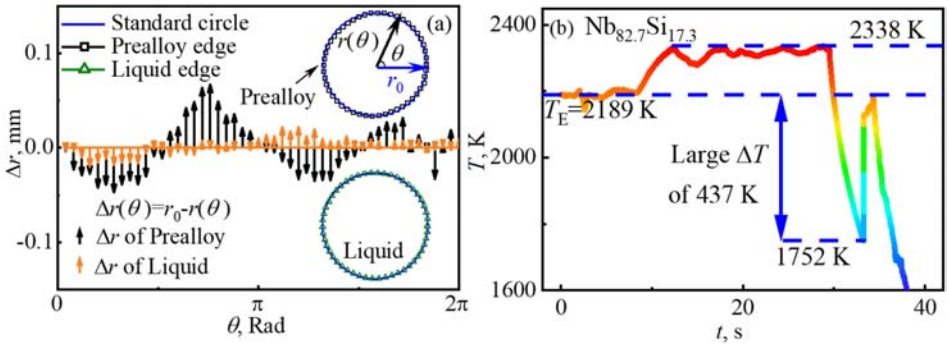

Fig.3 (a) The circular deviation of floating prealloy surface is notably pronounced, but after undergoing heating and melting, the circular deviation of the floating droplet surface becomes comparatively minimal. (b) The Nb-Si alloy reaches an ultrahigh temperature of 2338K and experiences deep undercooling of 437 K[6]

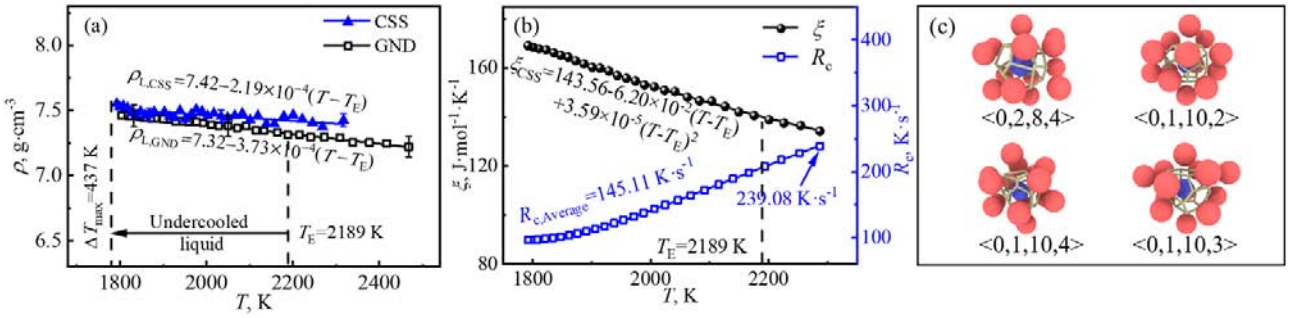

Fig.4 Properties and structure of liquid Nb-Si alloy obtained by space station experiment: (a) liquid density, (b) liquid heat radiance ratio,(c) the predominant Voronoi polyhedral structure in liquid alloys[9]

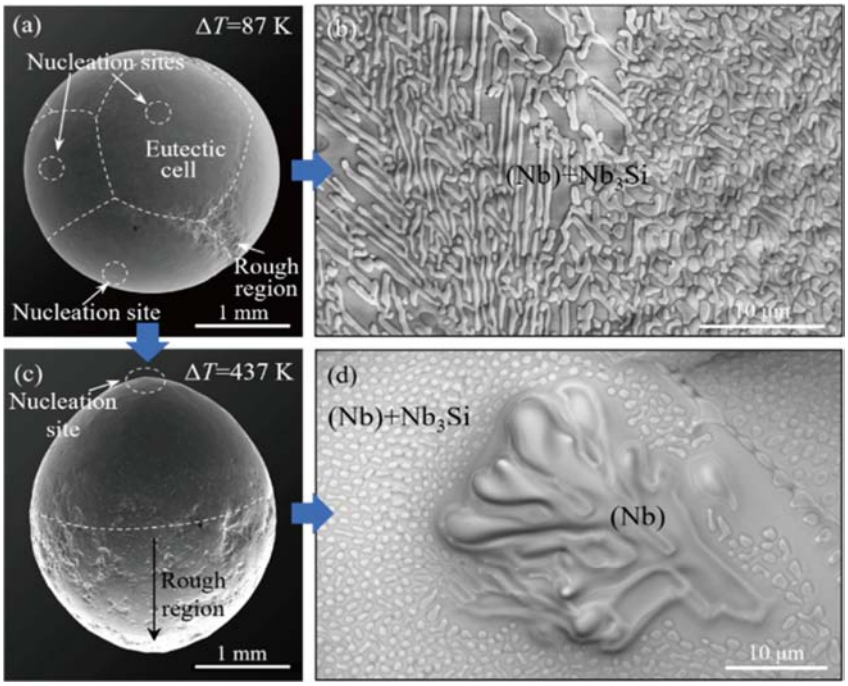

Fig.5 The spherical and olive alloy samples prepared in the space station experiment were: (a) photos of small subcooled spherical samples; (b) typical growth microstructure of small undercooling spherical samples; (c)photos of large undercooling olive samples; (d) large undercooling olive-shaped samples (Nb) lead eutectic growth in microstructure[6]

The weak Marangoni convection effect appears, which can cause new changes in the flow field of alloy melt. Such microscopic flows play a critical role in the formation of distinct structures during eutectic solidification. For example, the application of an electrostatic field can induce perturbations in the alloy melt, resulting in the emergence of surface periodic ripple structures and vortex, presenting a novel method for controlling surface microstructure[6], see Figure 6.

2.1.3 "Decoupled" Growth of Eutectic Alloys

A decoupling effect was found induced by the microgravity and containerless states aboard the space station, which led to the independent dendrite growth of two eutectic phases within an extremely undercooled liquid Nb-Si refractory alloy. The confronting fluid flow pattern driven by polar heterogeneous nucleation was found to stimulate the elongated surface deformation of alloy droplets at a high dendrite growth velocity. The direct observation of the solidification process provides comprehensive insights into dendritic growth velocity, formation of shrinkage cavity, and other phenomena under microgravity. In experiments, the alloy spheres were melted at eutectic temperature and reached a maximum temperature, multiple smooth eutectic cells can be distinguished on the surface, indicating the presence of multiple nucleation sites during solidification[10], see Figure 7.

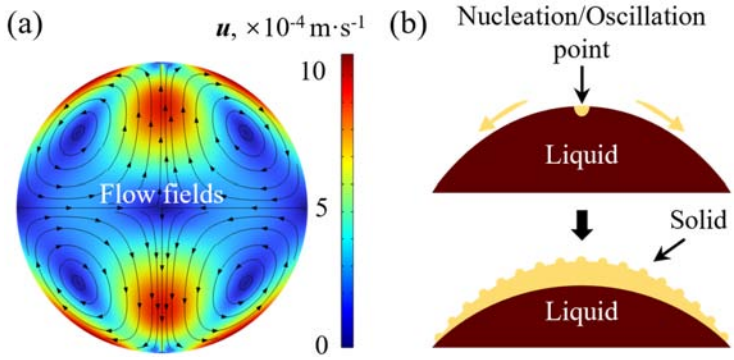

Fig.6 Flow behavior and surface wave formation of space station alloy melt: (a) flow field distribution in alloy melt under microgravity; (b) schematic diagram of alloy surface wave structure formation[6]

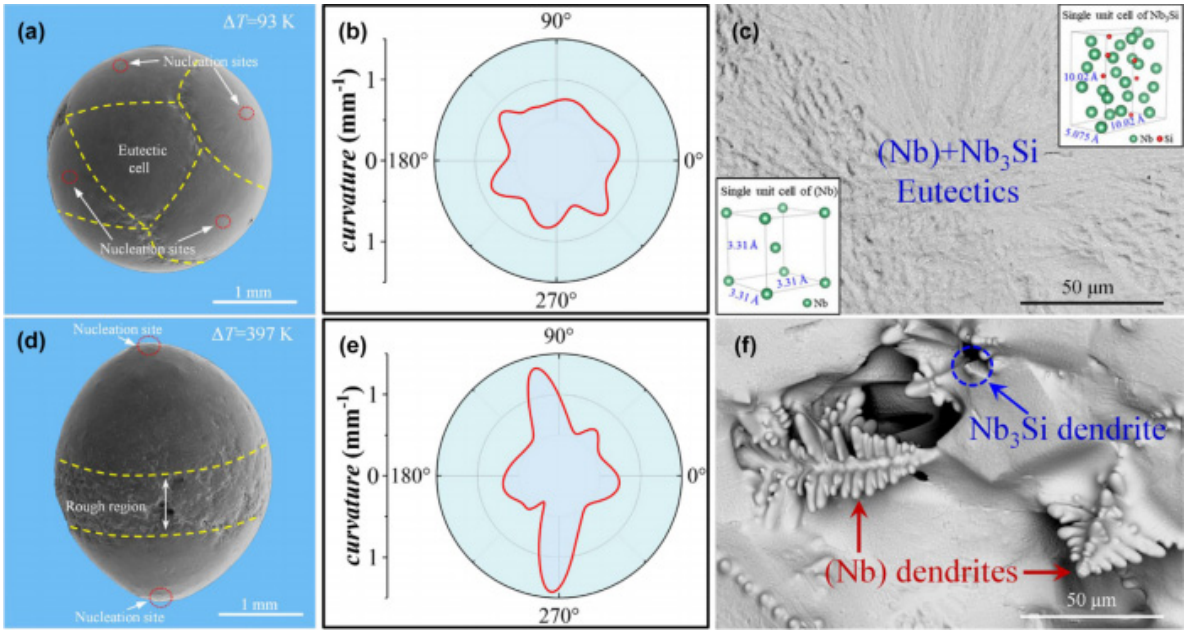

Fig.7 Macroscopic shapes of eutectic Nb-Si alloy droplets solidified with different undercoolings aboard CSS[10].

Rapid solidification kinetics within undercooled Nb-Si alloy leads to the macroscopic surface deformation of the solidified droplets and decoupled growth of eutectic phases under microgravity and containerless states. It is regarded to be related to the reduction in convection and the decoupling effect caused by rapid solidification kinetics.

These researches advanced our understanding of large undercooling behavior, solidification process as well as crystal growth in space. Knowledge serves to generate new regulatory methods for material preparation.

2.1.4 Immiscible Alloy Solidified in Space

The solidification process of the alloy with a miscible gap in the liquid-liquid phase diagram is known as liquid-liquid decomposition, which holds significant potential for the development of high-performance in-situ particle composites and core/shell structure composites. Due to the phase segregation effect during ground solidification, it is important to conduct solidification experiments under microgravity conditions. The microstructure of most composite materials fails to get the expected effect due to the influence of the cooling rate and surface contamination of the crucible. To address this issue, a research team from the Institute of Metal Research of the Chinese Academy of Sciences conducted containerless solidification experiments on Chinese space station to achieve fast cooling rates and avoid contamination[11]. The Ti-Go-Gd immiscible ball experienced a cooling, as shown in Figure 8.

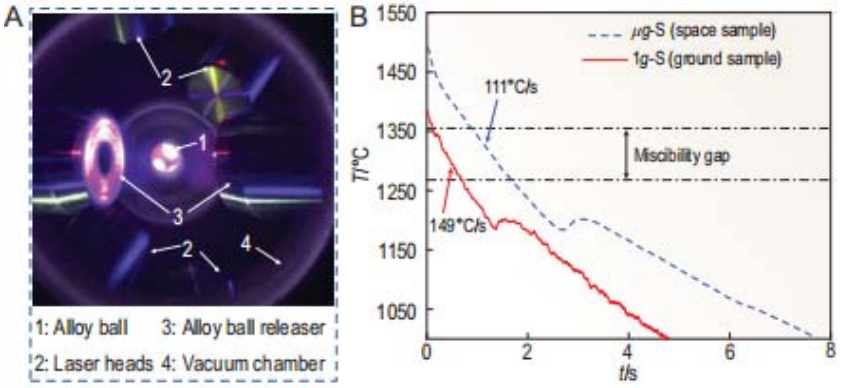

Fig.8 Solidification microstructure formation of Ti-Co-Gd alloy. (a) Electrostatic levitation device. (b) Cooling curves of samples[11]

The differences between the microstructures of the two samples which studied respectively on the ground and space are caused by the gravity-related convective flow of the melt and the Stokes motion of the Gd-rich droplets. When solidifying the alloy on the ground, the Gd-rich droplets sink in the matrix melt and the natural convection occurs in the matrix melt. It is the Stokes motion of the Gd-rich droplets together with the natural convection that promotes the collisions and coagulations between the Gd-rich droplets and leads to a rapid coarsening of the droplets, causing the formation of a phase-segregated microstructure, as shown in Figure 9.

In space, the Marangoni migration of droplets together with the diffusional transfer of solute Gd causes the formation of the Gd-poor region next to the Gd-rich phase shell. Enhancing the cooling rate promotes the formation of a well-dispersed microstructure.

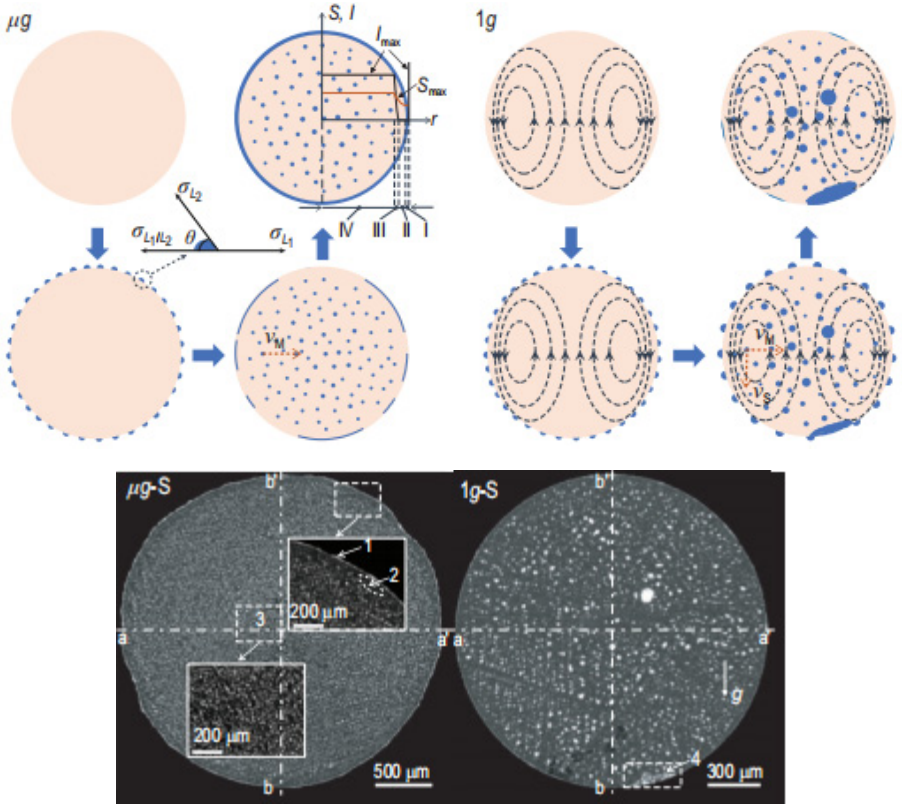

Fig.9 Schematics of the microstructure formation during liquid-liquid decomposition in space and on the ground[11].

2.2 Fundamental Physics

The ultracold atomic science rack and the cold atom interferometer provide opportunities for fundamental physics research on the space station. The former is a highly integrated experimental platform based on the principle of full optical trap evaporation cooling for ultracold atomic physics experiments. It can serve quantum simulation experiments based on optical lattice modulation of ultracold atoms. It will be expected to achieve the Bose-Einstein condensate. Thereafter, quantum simulation experiments on singular quantum states and dynamics will be conducted. The latter is a dual-species cold rubidium atom interferometer, installed in the microgravity scientific rack in Chinese space station to carry out such experiments with high-precision measurement as the weak equivalence principle test and so forth.

2.2.1 Testing the Equivalence Principle Based on the Space Cold Atom Interferometer

Atom interferometers offer a method for testing the Weak Equivalence Principle (WEP) at the microscopic level using atoms. Achieving high-precision WEP measurements involves measuring the differential acceleration of two atomic clouds with two types of atom interferometers. The atomic interferometer is an ^{85}Rb-^{87}Rb dual-type atomic interferometer developed by the Institute of Precision Measurement Science and Technology Innovation of the Chinese Academy of Sciences. It works in the microgravity science laboratory cabinet of the Chinese Space Station, and its scientific goal is to conduct in-orbit experiments on atom interferometry measurements. The use of an atomic interferometer for testing WEP not only enhances the accuracy of the test but also broadens its scope. Scientists have proposed a three-dimensional (3D) velocity selection method to efficiently lower the atomic ensemble temperature. Depending on the cooling process, the atomic cloud is allowed to expand freely, and the velocity of the atomic cloud in or perpendicular to the direction of the Raman laser is chosen[14]. The experimental scheme of the velocity selection method is shown in Figure 10.

The physical system contains a vacuum chamber, its accessories, the supporting structures, the optical components, and a magnetic shield, as shown in Figure 11.

To test WEP with high accuracy, the experimental process includes laser cooling, atom interference, and fluorescence detection stages. In the laser cooling experiment, images of the cold 85Rb atomic cloud in the 3D-MOT and time-of-flight images of the atomic clouds after the polarization gradient cooling process are shown in Figure 12. The number of the atoms was calculated to be more than 2×10^8 and the calculated atomic temperature was about 4 μK in one dimension.

To date, the atomic interference fringes of point source are realized up to 200 ms, and the on-orbit acceleration and rotation measurements are detected through the interference fringes. At the same time, by measuring the period of the point source interference fringe, the on-orbit Raman laser mirror angle coefficient calibration is obtained, and the systematic error evaluation of the rotation measurement value is carried out. The first measurement of on-orbit atomic interference rotation in the world is achieved with an accuracy of 1.71×10^{-5} rad·s^{-1}. The instrument is carrying out the in-orbit

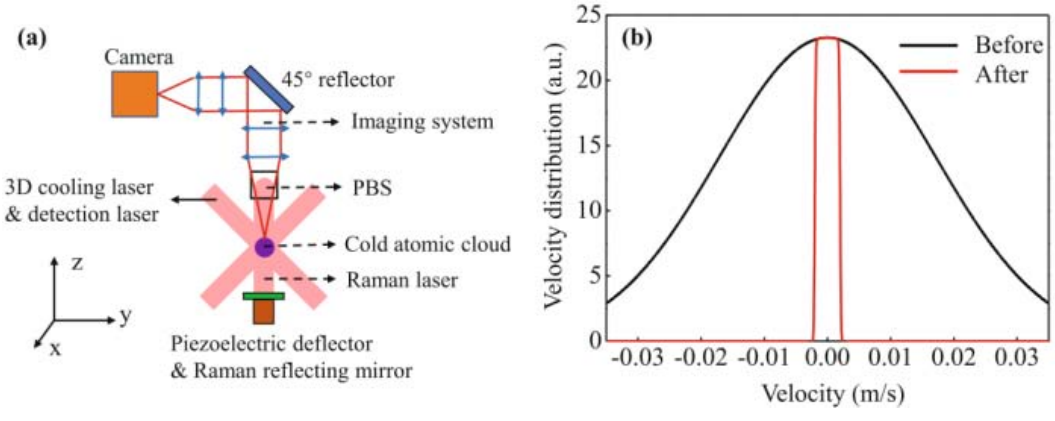

Fig.10 Scheme of the velocity selection and velocity distribution. a. 3D velocity selection. b velocity distribution of the atomic cloud before and after velocity selection[14]

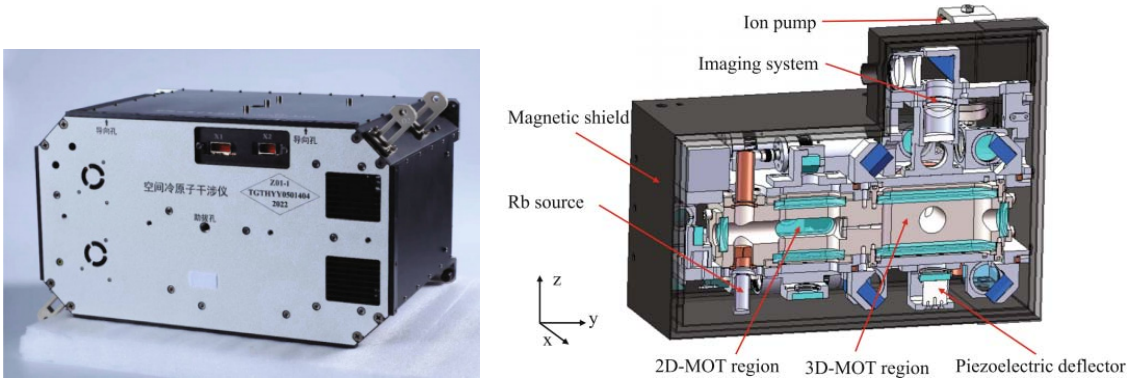

Fig.11 Space cold atom interferometer payload[14]

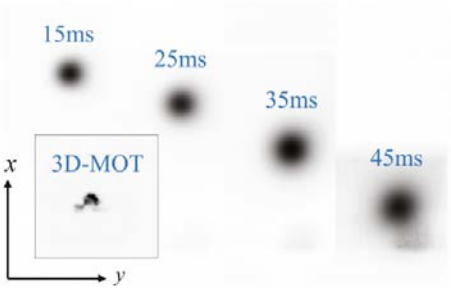

Fig.12 TOF fluorescence images of the 85Rb atomic cloud with different falling time[14]

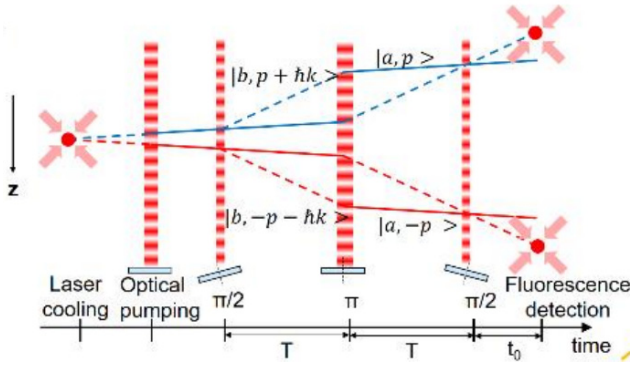

Fig.13 The principle of the double single diffraction scheme for Rb atom[15]

equivalence principle test experiment, and the dual component synchronous atomic interference of ^{87}Ru and ^{85}Ru in orbit has been accomplished.

2.2.2 High Precision Gyroscopes in Space

High-precision space gyroscope is of great significance for complex scientific experiments and deep space navigation. Microgravity in space provides an ideal condition for the operation of cold atom gyroscopes. The researchers implemented a cold atom gyroscope by using the atom interferometer whose evaluated rotation measurement is $(-115.64 \pm 1.71)\times10^{-5}$ rad·s^{-1} in space, and acceleration measurement resolution is 1.03×10^{-6} m·s^{-2} for a single image. This project is the first gyroscope based on the atom interferometer in space and paves the path for future related space-based experiments[15].

The gravity of the earth is a major disadvantage that limits the interference interrogation time and thus the resolution of the gyroscope. As the preliminary conditions, the cooling, state preparation, and fluorescence detection processes for the Chinese space station atom interferometer have been optimized, and the Mach-Zenden type interferometer for the ^{85}Rb and ^{87}Rb atoms has been constructed[15], see Figure 13.

The measurement data suggested that the angular velocity in orbit with an accuracy of 1.71×10^{-5} rad·s^{-1} can be obtained. The results are compared with the rotation values measured by the space station platform, and a good agreement is obtained. At the same time, the resolution of acceleration measurement is 1.03×10^{-6} m·s^{-2}.

2.3 Microgravity Fluid Physics

The research on fluid physics under micro-gravity on Chinese space station involves fluid dynamics, multiphase flow, and heat transfer, together with soft matter physics. The experiments of fluid storage and transportation in spherical and capsule tanks were carried out onboard. A theoretical model of bubbles in the tank was established, successfully verifying the fluid management performance of the tank, and supporting the development of novel plate tanks for spacecraft. Convection, evaporation, and phase transition heat transfer of the droplet and liquid layer were studied, finding the law of complex interface flow with heat and mass transfer. The glassy transition and rheology of the colloidal system were investigated, implying that the structure evolution of the three-dimensional colloid

system was coherent across scales in length. The gravity scaling law of heat transfer and bubble thermodynamic behavior in pool boiling is being studied, preliminary results demonstrate that boiling heat transfer performance rises instead of decreasing with the shrink of gravity, which seems intuitive and is expected to reveal the mechanism of gravity action in boiling phenomenon[20]. It provides direct instruction to fluid thermal management in multi-gravity environments for space exploration missions. The 3D trajectories of specific magnetic particles embedded in dense particles under various gravity conditions were measured precisely with Hall effect sensors, finding that the movement direction of particles with different sizes and density can be effectively controlled by the boundary geometry and motion conditions, and the abnormal 'Brazil nut' effect has been observed. This discovery is expected to improve the ability of space missions to manipulate particles under different gravity conditions and is expected to benefit particle mixing and separation engineering in pharmaceutical, food, chemical, and other industries.

2.3.1 Research on fluid Storage, Transport and Interface Behavior in Space

For spacecraft, to ensure the safety of the propellant management device, the tank that stores the propellant on the satellite usually has a central column. It is of great significance for fluid management under microgravity to explore the morphological characteristics of the bubbles in a tank with a central column and to study the various factors affecting them. However, the static shape and motion of bubbles under microgravity conditions have not been studied. The influence of geometry and liquid contact angle on the annular bubble profile is not clear. The research group of the Institute of Mechanics of the Chinese Academy of science has carried out a spherical tank model filling experiment on the Chinese Space Station. The liquid is pumped into the tank by an air pump.

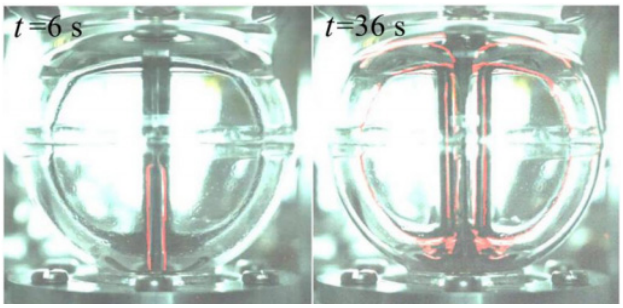

Fig.14 Liquid distribution vs time when filling tank[12]

An annular bubble surrounding the central column is formed inside the tank, see Figure 14. This kind of bubble under microgravity is observed for the first time, which will have important significance for the on-orbit liquid management and residual gauging. Annular bubbles are also observed in both experimental and numerical results. It can be seen in Figure 15 that the speed of liquid climbing along the guide vanes is faster than that in other areas; thus, a concave liquid surface is formed on the model wall, which is in good agreement with the experimental results in the CSS[12].

Different from the phenomena during the filling process, under this circumstance, the liquid is still spreading on the central column, forming another kind of bubble. Figure. 16 shows the results, there is an obvious large annular bubble in the middle of the tank model, the liquid distribution on the surface of the central column is clear to see, and the bulge is in the middle region of the central column.

In this experiment, the complete characteristics of the flow driven by surface tension in the fully managed or

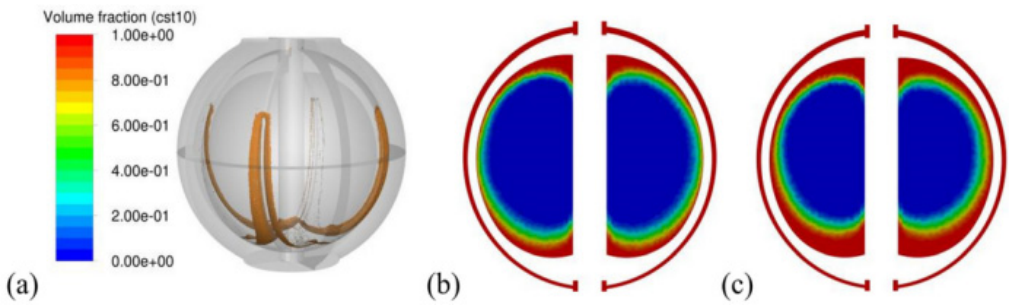

Fig.15 Liquid-gas interfaces when filling TA (a). Liquid distribution in the cross section when the liquid seal just forms (b), and liquid distribution in the cross section after further filling (c). The red region represents liquid and the blue region represents the gas[12]

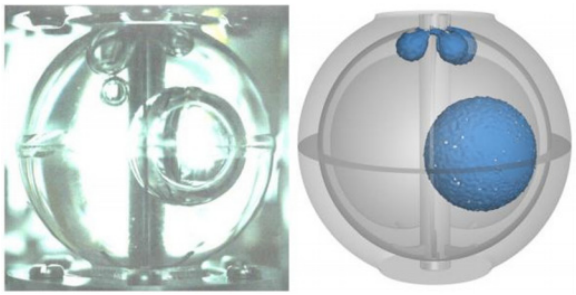

Fig.16 Comparison between experimental and numerical results[12]

semi-managed structure of the tank fluid were obtained, and the dynamical evolution roadmap of the bubble merging in the space large-scale structure was achieved. Based on the results, the theoretical model of an annular bubble contour in the tank is found. The law of bubble-shaped deformation and flow were revealed, and the fluid management performance of the tank in microgravity was confirmed. The liquid drainage rate of the semi-managed tank model exceeds 99%, which is a useful exploration for the in-orbit supply of spacecraft.

2.3.2 Vibration Fluidization Characteristics of Granular Materials under Variable Gravity Conditions

In various industrial processes and natural phenomena, particle segregation occurs when different shapes or sizes of particles are subjected to external vibrations or disturbances. Understanding and controlling this phenomenon is of significant importance in industries such as pharmaceuticals, where achieving a homogeneous distribution of components in powders is crucial, as well as in geological disasters such as earthquakes and landslides. Besides, granular systems provide valuable insights into nonequilibrium phenomena and are extensively studied in fundamental physics research.

Based on the centrifuge deployed on the Chinese Space Station, the scientists from the Institute of Physics, Chinese Academy of Science carried out experimental investigations on vibration fluidization of granular materials. Nevertheless, granular segregation faces challenges, particularly in three-dimensional systems. Traditional high-speed imaging techniques are limited to two-dimensional systems. In the experiment, a novel 3D particle tracking technique is utilized, i.e. the Hall-effect magnetic sensing technique, for high-precision trajectory tracking of a single magnetic sphere with varying densities within a granular bed[16] (see Figure 17).

A single large sphere acted as an intruder model system. The microscopic measuring of the dynamics of the intruder within the granular bed is obtained[17], see Figure 18.

They hunt for the relationship between the equilibrium position of the intruder and the vibration acceleration and density. The experiment reveals that the primary mechanism driving the upward motion of the intruder is the void-filling mechanism, while the effect of convection may play a limited role according to the observed phenomena since the intruder also exhibits upward motion near the container wall, confirming the Brazil nut effect, which is regarded as a critical conclusion for the dynamics of granular material.

Another extended experiment was carried out on the test bench to investigate the three-dimensional convection mode of fluidized particle materials through vibration in cube and cylindrical containers, which explains that convection mainly controls the motion dynamics of quasi-static shear particle media in cuboid containers,

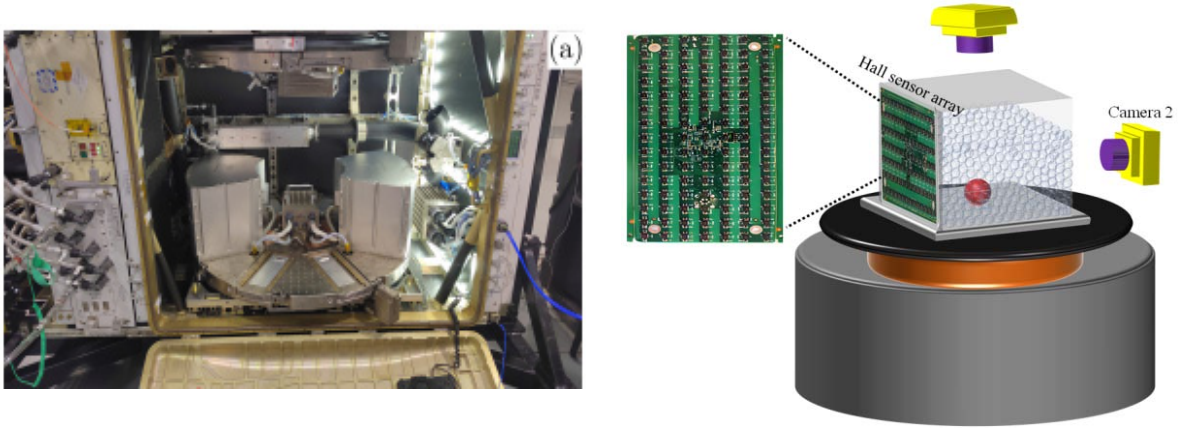

Fig.17 The assembly of test bed in centrifuge[16,17]

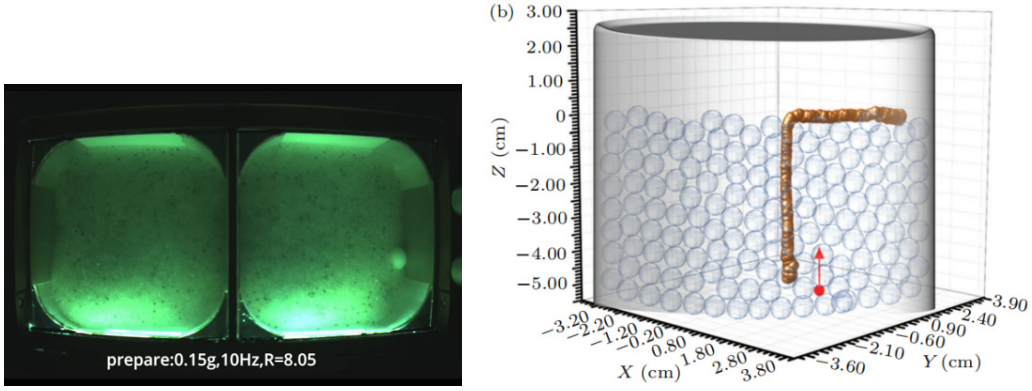

Fig.18 3D trajectory plot illustrating the path followed by the intruder throughout the experiment[17]

while its effect is less pronounced in cylindrical containers. These findings highlight the importance of vessel geometry in inducing periodic helical oscillatory motion, which needs to be considered in the engineering design of systems involving mixed particles.

2.4 Space Life Sciences and Biotechnology

Space stations provide suitable opportunities to carry out astrobiology experiments to explore the possibility of life beyond the earth and enable us to better understand the limits and requirements of life in different environments. Based on Chinese Space Station exo- ecosystem space experiment conducted onboard, the microorganisms will be exposed to space conditions, including microgravity, vacuum, UV radiation, and extreme temperatures.

2.4.1 Astroecology Experiment in Tiangong Space Station

The researchers set to examine whether methane- producing microorganism can survive in the environments inside and outside the space station at the first stage, validating methanogenic bacteria's adaptability to simulated environments (gravity, radiation) can provide indirect evidence for the process of generating methane on the planets such as Mars or Enceladus, which will help us understand whether the detected methane gas on these worlds may be a biological feature. Extraterrestrial exposure experiments will be conducted on standard sample cassettes equipped with UV filters provided on the external platform of the space station[19].

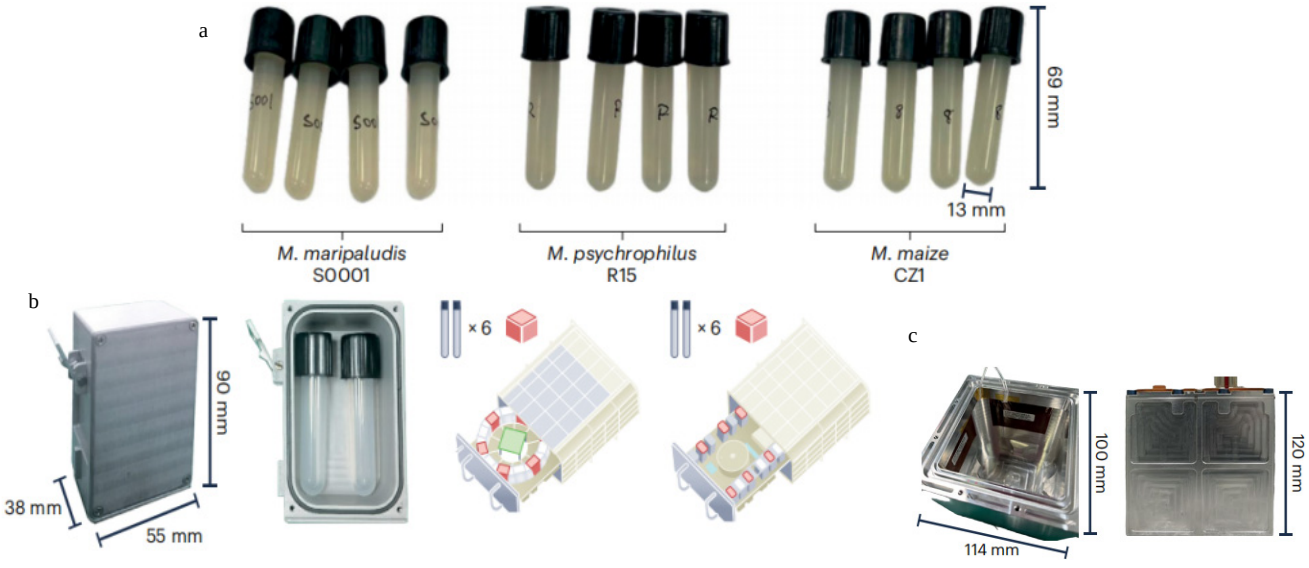

Fig.19 A schematic view of exo-ecosystem space experiment. (a) Space samples. (b) (c) The units for the simulated gravity experiments conducted in the Wentian module of Chinese space station. (c) The units for radiation experiments conducted at the exposure platform in the Mengtian module[19]

2.4.2 Human Embryonic Stem Cells into Hematopoietic Stem/Progenitor Cell

The inaugural in vitro study of human embryonic stem cell hematopoietic differentiation has been conducted aboard the Chinese Space Station. Microscopic images of cells collected and downlinked from orbit revealed that these human embryonic stem cells were successfully induced to differentiate into cobblestone-like Hematopoietic Progenitor Cells (HPCs). As development and differentiation progressed, these HPCs proliferated and formed grape-like clusters of hematopoietic cells. Subsequent analyses will involve the identification of the fixed samples returned from orbit, comparative analyses between space and Earth samples, and multi- omics studies. This mission establishes a foundation for future studies on early-stage hematopoiesis of stem cells in space and is anticipated to elucidate the mechanisms by which microgravity influences the differentiation of human pluripotent stem cells into early-stage hematopoietic cells.

2.4.3 Effects of Microgravity on Plant Growth and Development

The long-term cultivation of higher plants in space plays a substantial role in investigating the effects of microgravity on plant growth and development, acquiring valuable insights for developing a self-sustaining Biological Life-Supporting System (BLSS). In the studies on board, the researchers from the Center for Excellence in Molecular Plant Sciences, Chinese Academy of Science continued to conduct long-term plant research in space. Based on the so-called Biological Culture Module (GBCM), which was installed in the Wentian experimental Module of the CSS, was constructed to grow Arabidopsis thaliana and rice (Oryza sativa) plants a full life cycle in space. Dry seeds of Arabidopsis and rice were watered and germinated within a duration of 120 days. To this end, both Arabidopsis and rice plants completed a full life cycle in microgravity on the CSS. To date, this is the first space experiment achieving rice's complete life cycle from seed to seed in space. Some of these seeds have been used in a subsequent experiment to successfully produce a second generation after returning to Earth. Germination rates for space-produced seeds were about 90%, indicating that mature seeds developed in microgravity were healthy and viable. This result demonstrates the possibility of cultivating the important food crop rice throughout its entire life cycle under the spaceflight environment.

2.4.4 Microgravity Impairs Bone Formation by Inducing Gene Misregulation

Microgravity-related bone loss is affecting astronauts with long-term space travel due to decreased osteoblastic bone formation and increased osteoclastic bone resorption. A team from Zhejiang University, focuses on the impact of microgravity on osteogenesis at the cellular and molecular levels. Transcriptomic, proteomic, and genome-wide DNA methylation analysis was performed on pre-osteoblasts and osteoblasts derived from human Mesenchymal Stem Cells (hMSCs) cultured in space station or on Earth. The results showed that microgravity impairs osteoblast differentiation and drives adipogenesis from hMSCs by disrupting disease genes of "osteoporosis" and "osteoarthritis", as well as pathways related to glucose metabolism and extracellular matrix organization. The study also identified several potential extreme-microenvironment-sensitive molecules that could be targeted for improving osteogenesis, see Figure 20.

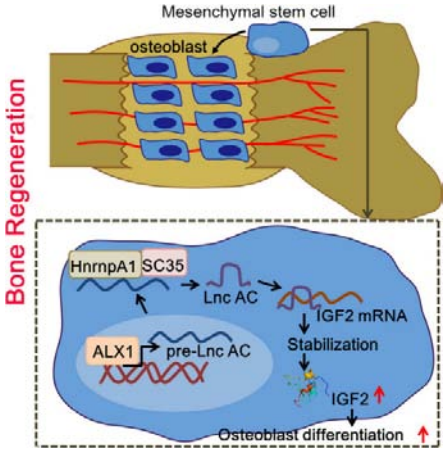

Fig.20 AC132217.4 promotes osteogenesis and bone healing

2.4.5 Space Radiation Biology Research

To study the molecular mechanisms of space radiation damage and genetic mutations, a systematic biological analysis is needed for model organisms exposed to space for long periods. However, because the individual sample in the long-term space exposure receives different high-energy heavy ions, traditional big data analysis methods cannot meet the big data analysis needs of space experiment samples. According to the necessaries. A scientific group from Dalian Maritime University has successfully developed Space radiation metrology and

biological damage assessment technology which overcomes key technologies such as microchannel structure design, fluid control, and biological matching. For the first time in the world, the automatic monitoring model of animal nematode individual horizontal growth, movement, tissue fluorescence protein labeling imaging was realized in orbit, and the whole-life tracking of various nematode species individuals was realized in situ. The results of the in-orbit analysis show that an animal experimental model of the biological effects of radiation and microgravity in orbit has been established. This work provides an experimental model for in-situ individual lifetime automatic analysis for space medicine and protection research in manned deep space exploration projects.

2.4.6 Survival Limits in Space of Microorganisms from Extreme Environments

The study on the tolerance and mechanism of microorganisms to space environments aims to explore the survival limits and interstellar transmission potential of microorganisms in space, to provide a basis for research on the origin of life and exploration of extraterrestrial life and data support for planetary protection technology research, and to evaluate the ability of pioneer microorganisms to expand into outer space. The tested/testing samples included 3 types of lithic microbial samples and 8 lichens collected from cold or arid regions from Northwestern China, 10 radiation-resistant strains isolated from deserts, glacial moraines, and 2 Bacillus strains, isolated from the spacecraft AIT environments, with different protection conditions by different spacecraft materials. The first batch of samples was returned at the end of October 2023, and the results indicated that most of the microbial samples could survive the extravehicular environment of the Mengtian module for three months.

3 Research Planning and Outlooks

To make critical scientific discoveries persistently, and transfer some of the achievements into applications in the next few years. It is planned to conduct innovative research in various fields of space science.

For instance, for bioscience, space breeding of mammals is going to be realized for the first time in the world, obtaining important new targets for aging and pathology, and making breakthroughs in stem cells, promoting pharmacological research and development.

For the physical science, many highlight studies will be carried out, for instance, high-quality semiconductor crystals, rare earth permanent magnet materials, biological and nanomaterials, *etc*. will be prepared in space and applied to the research and development of infrared detectors, scintillation crystals or other devices. Studies on space cold atom physics and their applications will become more in-depth and extensive, in particular, the research on quantum simulation and atom interferometer applications, *e.g.* ultra-cold temperature quantum gas preparation, exploring quantum decoherence mechanisms, topological quantum states studies, and expanding the in-orbit cold-atom interferometer applications on Earth science and fundamental physics testing.

The peculiar hydrodynamics under microgravity will be still of great importance to nonlinear mechanics investigation and engineering. The dynamics, especially for the evolution behavior of particulate matter in turbulence, the special flow of fluid caused by the thermal capillary phenomenon, and the rheological properties of non-Newtonian fluids will be deeply explored in the absence of gravity or low gravity conditions. In addition, the scientists who are interested in soft matter physics will have the opportunity to pursue the myths in three-dimensional collective behaviors of active matters (such as artificial active colloids, bacteria, *etc*.), investigating colloid and polymer self-assembly behavior and the other problems of statistical physics far from equilibrium. Moreover, more studies on fluid phase transition (*e.g.* evaporation, condensation, and boiling) and enhanced heat transfer mechanisms are planned, which directly strengthen the efficiency of fluid as well as thermal management in a large number of engineering fields, from ground-based applications to deep space exploration.

The studies of space combustion science will focus on basic combustion processes in the energy or power systems, such as ignition, flame propagation, flame stabilization, quenching, *etc*., committing to solving the key problems such as efficient and low-carbon combustion or performance improvement.

These interdisciplinary studies conducted on the experimental platform of Chinese Space Station, are greatly helpful to humanity's comprehension of the open scientific principles, driving the advancement of cutting-edge technologies, expanding the scope of human activities in space, and presenting substantial benefits from these endeavors.

References

[1] Press Conference for Shenzhou XVI Manned Flight Mission [EB/OL]. [2024-06-01]. https://www.cmse.gov.cn/xwzx/202305/t20230529_53634.html

[2] GU Yidong. Thoughts on space science development[J]. *Bulletin of Chinese Academy of Sciences*, 2022, **37**(8): 1031-1049

[3] GU Yidong. The China Space Station: a new opportunity for space science[J]. *National Science Review*, 2021. **9**(1), nwab219

[4] Announcement for the Call for Proposals for Space Science and Applications Projects of the Chinese Space Station[EB/OL]. [2024-06-03]. https://www.cmse.gov.cn/gfgg/202306/t20230616_53912.html

[5] WANG Haipeng, LIAO Hui, WEI Bingbo, *et al.* Freezing shrinkage dynamics and surface dendritic growth of floating refractory alloy droplets in outer space[J]. *Advanced Materials*, 2024, **36**: 2313162

[6] WANG Haipeng, HU Liang, XIE Wenjun, *et al.* Metastable liquid properties and surface flow patterns of ultrahigh temperature alloys explored in outer space[J]. A*ngewandte Chemie International Edition*, 2024, **63**: e202400312.

[7] WANG Haipeng, LIAO Hui, WEI Bingbo, *et al.* Decoupling effect stimulated independent dendrite growth of eutectic phases under microgravity and containerless states[J]. *Materials Today*, 2024, 74

[8] WANG Haipeng, LIU Dingnan, WEI Bingbo, *et al.* Spiral eutectic growth dynamics facilitated by space Marangoni convection and liquid surface wave[J]. *Physics of Fluids*, 2024, **36**: 047137

[9] CHANG Jian, WANG Haipeng, WEI Bingbo, *et al.* Remarkable undercooling capability and metastable thermophysical properties of liquid Nb84.1Si15.9 alloy revealed by electrostatic levitation in outer space[J]. *Review of Scientific Instruments*, 2024, **95**: 034501

[10] WANG Haipeng, LIAO Hui, WEI Bingbo, *et al.* Decoupling effect stimulated independent dendrite growth of eutectic phases under microgravity and containerless states[J]. *Materials Today*, 2024, 75

[11] ZHAO Jiuzhou, SUN Hao, ZHANG Lili, *et al.* In-situ composite microstructure formation of immiscible alloy solidified in space[J]. *National Science Review*, 2023 **10**: nwac261

[12] CHEN Shangtong, KANG Qi, *et al.* Study on the shape and motion of bubbles in the tank model with a central column aboard the Chinese Space Station [J]. *Physics of Fluids*, 2024, **36**: 012124

[13] CHEN S, DUAN L, LI W, CHEN S, KANG Q. Profiles of free surfaces in revolved containers under microgravity[J]. *Microgravity Science and Technology*, 2024, 36

[14] HE Meng, CHEN Xi, ZHAN Mingsheng, *et al.* The space cold atom interferometer for testing the equivalence principle in the China Space Station [J]. *NPJ Microgravity*, 2023, **9**: 58

[15] LI Jinting, CHEN Xi, ZHAN Mingsheng. Realization of a cold atom gyroscope in space [J]. arXiv:2405.20659

[16] CHENG Ke, HOU Meiying, *et al.* Tracking the motion of an intruder particle in a three-dimensional granular bed on-board the Chinese Space Station[J]. *Microgravity Science and Technology*, 2024 **36**:15

[17] LI Tuo, CHENG Ke, PENG Zheng, YANG Hui, HOU Meiying, Intruder trajectory tracking in a three-dimensional vibration-driven granular system: Unveiling the mechanism of the Brazil nut effect[J]. *Chin. Phys. B*, 2023, **32** (10): 104501

[18] LI Tuo, CHENG Ke, HOU Meiying, *et al.* The intruder motion in a cubic granular container[J]. *Physics of Fluids*, 2024(in pressing)

[19] CUI D, LI L, YANG S, *et al.* In pursuit of life beyond Earth[J]. *Nat. Astron*., 2023, 7: 1004-1005

[20] JIANG W, LI Z, ZHAO J, *et al.* The study of an integrated sensor for partial nucleate pool boiling at low heat flux[J]. *IEEE Sensors*, 2022, **22**(24): 23692-23698

[21] ZHANG C, *et al.* Cell Mol. Life Sci., 2022, **79**(6): 328

2 Lunar and Deep Space Exploration

XU Lin, LI Lei, LIU Jianzhong, LIN Honglei, LI Yang, LIU Yang, XIE Lianghai, ZHANG Jinhai, HU Teng, QIAO Fuhao, HAN Juanjuan, ZOU Yongliao. The Latest Scientific Results of China's Lunar and Deep Space Exploration (2022–2024). *Chinese Journal of Space Science*, 2024, **44**(4)

The Latest Scientific Results of China's Lunar and Deep Space Exploration (2022–2024)

XU Lin[1], LI Lei[2], LIU Jianzhong[3], LIN Honglei[4], LI Yang[3], LIU Yang[2], XIE Lianghai[2], ZHANG Jinhai[4], HU Teng[5], QIAO Fuhao[2], HAN Juanjuan[1], ZOU Yongliao[1,2]

1. General Office of the Lunar and Deep Space Exploration, Chinese Academy of Sciences/National Space Science Center, Chinese Academy of Sciences, Beijng 100190
2. State Key Laboratory of Space Weather, National Space Science Center, Chinese Academy of Sciences, Beijing 100190
3. Institute of Geochemistry, Chinese Academy of Sciences, Guiyang 550081
4. Institute of Geology and Geophysics, Chinese Academy of Sciences, Beijing 100029
5. China University of Geosciences, Beijing 100083

Abstract

China has successfully launched six lunar probes so far. From Chang'E-1 to Chang'E-4, they completed the circling, landing and roving exploration, of which Chang'E-4 was the first landing on the far side of the Moon in human history. Chang' E-5 was launched in December 2020, bringing back 1731 g of lunar soil samples. Through the detailed analysis of the samples, the scientists understand the history of late lunar volcanism, specifically extending lunar volcanism by about 800 million to 1 billion years, and proposed possible mechanisms. In addition, there are many new understandings of space weathering such as meteorite impacts and solar wind radiation on the moon. China's first Mars exploration mission "Tianwen-1" was successfully launched in May 2021. Through the study of scientific data, a number of important scientific achievements have been made in the topography, water environment and shallow surface structure of Mars. This paper introduces the main scientific achievements of Chang'E-4, Chang'E-5 and Tianwen-1 in the past two years, excluding technical and engineering contents. Due to the large number of articles involved, this paper only introduces part of the results.

Key words

Lunar and deep space exploration of China, Chang'E-4, Chang'E-5, Tianwen-1 mission

1 Introduction

This year marks the 20th anniversary of China's Lunar Exploration Project, from the launch of the first lunar exploration satellite Chang'E-1 in 2007 to the launch of Chang'E-6 in 2024 and the successful return of lunar samples, so far six lunar exploration missions have been successfully launched.

Chang'E-4 performs the first soft landing and exploration on the far side of the Moon, obtaining data on the

Received June 20, 2024

surface morphology, material composition, shallow structure, and the near-lunar space environment.

Launched in December 2020, Chang'E-5 brought back 1731 g of lunar soil samples from the moon, which is the first time humans have obtained samples of young volcanic regions on the lunar surface. Over the past three years, the China National Space Administration has distributed more than 80 grams of lunar samples seven times to more than 100 scientific teams in China. At present, more than 100 scientific and technological papers have been published, which delayed the end of lunar volcanic activity by about 800 million to 1 billion years through geological dating of samples, innovatively discovered the formation mechanism of solar wind, and also discovered the sixth new mineral on the moon "Chang'E stone" and other scientific achievements.

On April 24, 2020, the China National Space Administration announced that China's planetary exploration mission will be named Tianwen, and China's first Mars exploration mission will be named "Tianwen-1". Tianwan-1 will be launched in July 2020 and land on the Utopia Plain of Mars at 5° ~ 30° north latitude in May 2021 for landing and roving exploration. As the first mission of China's planetary exploration project, Tianwen-1 has achieved three goals of orbiting, landing and touring Mars through a single launch, which is unprecedented in the history of Mars exploration in the world. At present, the goal of China's first Mars exploration mission has been successfully accomplished. Through the study of scientific data, the scientific research team has achieved a number of scientific achievements in the topography, water environment, atmosphere and material composition, and shallow subsurface structure of Mars.

2 Chang'E-4 Mission

2.1 Lunar Topography and Geomorphology

The lunar regolith morphology is mainly acquired by imaging equipment including the Landing CAMera (LCAM) of Chang'E-4 lander, the ground Terrain CAMera (TCAM) image and the DEM of the Yutu-2 Panoramic CAMera (PCAM) validate the crater degradation levels from a qualitative and quantitative perspective, *etc*., which are suitable for acquiring images of centimeter-scale craters, rocks and ejecta to measure their shape, size, color, reflectance, roughness *etc*.[1]. Some of the craters contain high-reflectance materials at the bottom, suggesting secondary impact events, which hint at notable differences in the impact frequency between the lunar farside and nearside[2].

2.2 Characteristics and Composition of Lunar Regolith

Visible and Near-infrared Imaging Spectrometer (VNIS) is critical in constraining the accurate mineral proportions and composition of the lunar regolith[3]. Based on the mineral abundances retrieved from the VNIS data, the average plagioclase abundance (60.4 vol.%) is beyond the high-plagioclase end of the mineralogical range of SPA impact melt differentiation products and would require an additional contribution from potential ejecta[4]. VNIS also found iron-rich and magnesium-rich components, such as Finsen and Leibniz crater sputtering, requiring additional contributions from the lunar crust[5,6]; Rocks rich in low-Ca pyroxene and deficient in Mg-olivine have also been found, such as four special rocks encountered along the way, indicating that they were crystallized at a high temperature (980°~1300° C) and a rapid-cooling magmatic system produced by impact melt differentiation or volcanic resurfacing events[5,7]. These newly discovered compositional features combined with lunar rock minerals provide new insights into the origins of SPA.

The results show that the particle size of the lunar regolith at the Chang'E-4 landing site is similar to 15 μm on average over depth, which indicates an immature regolith below the surface[8], and the viscosity of the lunar regolith on the far side of the Moon is higher than that on the near side[9].

2.3 Sub-surface Structure

The layered structure of the upper 300 m of the lunar surface in the South Pole-Aitken Basin was discovered by using the measurements from the Lunar Penetrating Radar (LPR) onboard the Chang'E-4 rover Yutu-2[10]. The high-frequency radar observed a buried lens structure similar to 27 m below the lunar surface, interpreted as paleo regolith by previous studies[11]. Below the depth of 90 m, with thicknesses ranging from 20 m to larger than 70 m[12]. At least three strata basalt flows were speculated, while the shallowest stratum is composed of multiple thin lava flows[12]. Both the dielectric properties and the ilmenite content suggest a shallow sequence of basaltic layers overlaying a low-ilmenite

ejecta blanket[13]. The LPR also found a series of buried impact craters[14]. The smaller the impact craters are, the more likely they are to degenerate. The smaller the impact crater yield is, the closer it is to the removal rate, the more difficult it is to reach the equilibrium state[1]. The maximum penetrating depth of the low-frequency channel reaches 450 m, revealing multi-episode eruptions[15].

2.4 Lunar Space Environment

The Moon represents an airless body, where the lunar surface can directly interact with ambient space particles, and bring a space weathering effect. Some solar wind protons can be scattered as Energetic Neutral Atoms (ENAs) from the surface, which includes rich information of the solar wind-surface interaction. Sometimes, the interaction can be hindered by a magnetic anomaly, where a Lunar Mini-Magnetosphere (LMM) is formed. Due to the lack of in situ measurements on the lunar surface, people still know little about the ENA truth as well as the internal structure of LMM on the surface. The Chang'E-4 (Chang'E-4) mission is the first mission soft-landed on the lunar far side near strong magnetic anomalies. Moreover, the Advanced Small Analyzer for Neutrals (ASAN) instrument onboard the rover of Chang'E-4 can measure the backscattered ENAs from the surface. With the ENA data from Chang'E-4 mission and the solar wind data from ARTEMIS spacecraft, Xie *et al*.[16] reported a unique multi-point observation of the LMM, and found that there was no shock but just a boundary layer near the magnetic anomalies and the shock could only appear downstream from the magnetic anomalies known as the trailing shock. Zhong *et al*.[17] found that the ENA energy measured by Chang'E-4 showed a good relation with the solar wind energy, and the loss rate of ENA energy favored a higher solar wind energy and a lower solar zenith angle. Wieser *et al*.[18] presented a semi- empirical model to describe the energy spectra of the neutral emitted atoms, and found that the ENAs emitted from the lunar surface consist of two components: one is reflected and neutralized solar wind protons and the other is particles sputtered ENAs from the lunar regolith.

Apart from low-energy solar wind particles (with an energy of about 1 keV), there are also some high-energy space particles (with energies higher than several MeV), such as Solar Energetic Particles (SEPs) and Galactic Cosmic Rays (GCRs), which can directly bombard the lunar surface. The Lunar Lander Neutron and Dosimetry (LND) Experiment aboard the Chang'E-4 Lander can measure energetic charged and neutral particles and monitor the corresponding radiation levels. It is found that GCRs are the dominating component of charged particles on the lunar surface during solar quiet times. Moreover, the interaction of GCRs with the lunar regolith also results in upward-directed albedo protons which are measured by the LND[19]. Combined with the Radiation Environment and Dose at the Moon (REDMoon) mode, Xu *et al*.[19] have also provided the ratio of albedo protons to primary protons for measurements in the energy range of 64.7~76.7 MeV. In addition, Luo *et al*.[20] reported the first measurements of the low-energy (about 10 to 100 MeV/nuc) cosmic ray spectra on the lunar surface around the solar minimum 24/25, and found that the proton, helium, CNO, and heavy-ion groups, the ratios (ratio errors) of the Chang'E-4 fluxes to those from the near-earth spacecraft are 1.05 (0.15), 1.30 (0.18), 1.08 (0.16), and 1.24 (0.21), respectively. Moreover, a notable enhancement of $^{3}He/^{4}He$ ratio was observed at about 12 MeV/nuc, and the cosmic ray dawn-dusk symmetry was confirmed[20]. These results provide valuable insights into the cosmic rays on the lunar farside surface and will benefit future lunar exploration.

3 CHANG'E-5 Mission

Unlike the Apollo and Luna samples, the Chang'E-5 lunar samples were collected at middle to high latitudes and are the youngest lunar basalts to date (2.030 ± 0.004 Ga) and have higher FeO contents, with moderate TiO_2 and Al_2O_3[21-26]. There is evidence that Chang'E-5 lunar soils are mainly derived from spallation from the Xu Guangqi crater to the north-west of the landing site and have a higher lunar soil maturity, a feature probably due to the predominance of micrometeoroid impacts processes[27,28]. The study of the Chang'E-5 lunar samples by various analytical methods, including the newly developed Raman spectroscopy analysis, showed that the average particle size of the Chang'E-5 lunar soils was about 50 μm, with relatively low glass content, and that the basaltic fragments were mainly composed of clinopyroxene, plagioclase, olivine and ilmenite, with obvious textures diversity, including porphyritic, ophitic/ subophitic, poikilitic[22,23,26,27,29,30]. It is noteworthy that previous petrological analyses of late-stage basalts

based on remote sensing data have shown abundant olivine, but laboratory spectral analyses of the Chang'E-5 samples revealed iron-rich high-Ca pyroxene rather than olivine[31]. To present, the detailed chemical composition distribution of the lunar surface has been constrained[32].

3.1 Impact Glasses

Chang'E-5 glasses come in a wide variety of multitype and origins. The finding of indigenous ultra- elongated glass fibers and widely distributed ultra-thin amorphous layers without np-Fe^0 indicates the relatively moderate impact environment in the Chang'E-5 landing site[33]. The composition of the impact glass from the Chang'E-5 samples suggests a predominantly local origin, limiting transport distances to less than about 150 km, and U-Pb isotopic dates of the impact glasses indicate that the regional impact glass formed between a few million and two billion years ago, younger than the Chang'E-5 basalts[34]. Impact glass enriched in large KREEP material (>20 vol%) was found in the uniquely weathered lunar breccia returned by Chang'E 5 mission, suggesting a possible origin from a mixed region between the P58/Em4 mare unit and its contiguous eastern highlands[35].

The impact glasses in lunar breccias are enriched in a large KREEP material (>20 vol.%), suggesting a possible origin from a mixture of the Lunar Sea Unit and the Eastern Highlands[35].

3.2 Space Weathering

Chang'E-5 samples offer valuable insights into the study of space weathering processes. According to the research, space weathering in iron-rich basalts leads to a faster generation rate of np-Fe^0 and saturated aggregation to form larger particle sizes[28]. The discovery of np-Fe^0 caused by in situ thermal decomposition in the amorphous layer rims on the surface of fayalitic olivine provides new evidence for the mechanism of the formation of np-Fe^0[36]. Li *et al.*[37] found np-Fe^0 and Fe^{3+} in the amorphous mixture at the bottom of the microcraters on the surface of olivine, where high temperatures and pressures during the impact process drove the disproportionation reaction of Fe^{2+}, and the contribution of solar wind injection was very weak[37]. Lunar agglutinate glass formed and widely distributed by micrometeoroid impacts in the Chang'E-5 lunar samples contains a large amount of np-Fe^0 and Fe^{3+} produced by disproportionation reactions, and the content of Fe^{3+} increases continuously with the continuous micrometeoroid impacts[38].

In addition, a study reported for the first time the discovery of iron meteorite fragments in the lunar soil of Chang'E-5, the meteorite fragments are Ni- and P-rich, S-poor, and are classified as IID-group based on their mineral chemistry and overall composition. As this meteorite fragment experienced only limited partial melting followed by rapid cooling, suggesting formation by a low-velocity impact[39]. In addition, the natural nanophase new minerals trigonal Ti_2O and triclinic Ti_2O were found in micrometeorite impact craters on the surface of Chang'E-5 glass bead, as well as the seventh and eighth newly discovered minerals in lunar samples. This discovery not only acquires the response of Ti-oxides such as ilmenite to the micrometeorite impacts modification process and its effects, but also complements the understanding of the new products of space weathering, and suggests a new idea that space weathering can alter the photocatalytic properties of lunar regolith[40]. Nonetheless, the prolonged and persistent impact events resulted in extensive, uneven and complex thermal modification events in the Chang'E-5 landing site[41].

3.3 Sulfides

Although sulfides are less than 1% in the Chang'E-5 lunar samples, they still show abundant weathering modification features[23]. Guo *et al.*[42] discovered submicroscopic magnetite particles and np-Fe0 with impact-induced formation by eutectoid reaction for the first time in Chang'E-5 lunar soil, Magnetite and np-Fe0 particles embedded in oxygen-dissolved iron-sulfide particles from Chang'E-5 samples, representing large impact events on the lunar surface[42]. Furthermore, digenite mineral with characteristics of impact-induced evaporative deposition was reported for the first time in a lunar sample[43].

3.4 Solar Wind-derived Water

The Chang'E-5 lander performed in situ spectral measurements while collecting samples, and these observations revealed the presence of water on the lunar surface[44,45]. Solar wind-derived water is one of the major sources of lunar surface water, and recent studies have reported the presence of high levels of Solar wind-derived water (OH/H_2O) in the surface mineral layer, with the Chang'E-5 samples containing more than 170 ppm of water, consistent with lunar in situ spec-

troscopic measurements[44-46]. Moreover, the impact glasses from Chang'E-5 lunar soil are the major source of molecular H_2O in the lunar soil, with a content of up to 15 to 25 ppm. Due to the complexity of their formation mechanisms, impact glasses can preserve and record large sources of OH and molecular H_2O associated with the solar wind and a variety of other sources, including water derived from solar wind, deposited by water-bearing meteorites/micrometeorites, and inherited from lunar indigenous water[47]. Solar wind-derived water is preserved by diffusion into the impact glass beads, along with the ability to sustain the lunar surface water cycle. The abundance of solar wind-derived water in the impact glass beads can be as high as about 2000 ppm, with an average of about 500 ppm[48].

3.5 Petrogenesis and Volcanic Activity

The results of a comprehensive multi-method study of basaltic clasts in the Chang'E-5 lunar samples, including quantitative structural analysis, diffusion chronometry, clinopyroxene geothermobarometers, and crystallization simulations, show that the Chang'E-5 basalts originated in the olivine-bearing pyroxenite mantle source and that the source region has a pressure of 10~13 kbar and a temperature of about 1350 ± 50 °C. It is similar to the Apollo 12 low-Ti basalts[30]. Research suggests that the Moon is still magmatic at least 2 billion years ago and the presence of additional and yet-unrecognized lunar volcanic eruptions[49].

A study of the Chang'E-5 basalts revealed that most olivine grains have very short cooling timescales. Thermal modeling suggests that the minimum thickness of the lava flow bounded by most basalt grains is between 10~30 m. and the flat topography of the Chang'E-5 landing site suggests that large-scale magmatic eruptions continued into the late lunar period. Although lunar volcanism has generally declined over time, its late indirect eruptions still exhibit higher than average eruptive fluxes[26,50]. The Moon's youngest volcanism was not driven by abundant water in its mantle source[51], and further research is needed to clarify the causal mechanisms.

It has been reported that late-stage lunar magma ocean easily-melted cumulates in the lunar mantle source region lowered the melting point of the lunar mantle and triggered young volcanism on the Moon, with Chang'E-5 source magma having higher calcium and titanium dioxide contents than the Apollo counterparts[52]. The rapid cooling crystallization exhibited by the basalt debris and the smaller volume of vesicles observed in the Chang'E-5 samples indicate that the Chang'E-5 basalts have a lower degree of degassing compared to the Apollo basalts, and less volatile substances escape[53]. Two young basaltic lunar meteorites discovered in the Chang'E-5 lunar samples have similar source regions and formation mechanisms with Chang'E-5 basalts, suggesting that lunar volcanism shifted from KREEP-like dominance to non-KREEP dominance about 3 billion years ago[54].

4 Tianwen-1 Mission

4.1 Martian Aeolian Landforms

The Zhurong rover conducted observations of Aeolian landforms in the southern Utopia Planitia on Mars, revealing the dynamic changes in Martian Transverse Aeolian Ridges (TARs) and dunes. Studies indicate that these landforms were initially formed by northern winds and later re-worked by northeastern winds, showing significant aeolian reworking and climate change[55]. The analysis of Martian dunes suggests that wind direction changes coincided with the end of the recent "ice age" (roughly 0.4~2.1 million years ago), leading to the transformation of barchan dunes into longitudinal dunes, reflecting a major climatic transition from glacial to interglacial periods. This wind direction shift and the corresponding changes in dune morphology provide crucial evidence of Mars' dynamic climate history[56]. The transverse aeolian ridges are also analyzed[57], the presence of cones indicates a potential mud volcano origin[58], and the three-dimensional morphological features of rocks are analyzed[59,60].

4.2 Ancient and Modern Environments in Southern Utopia

MultiSpectral Camera (MSCam) onboard the Zhurong rover with its calibration target used to monitor dust deposition, providing a new ground observation, showing a low deposition rate in the first 110 sols, indicating clear weather, followed by an accumulation of dust[61]. Meteorological data show that wind speed and direction also exhibit significant seasonal characteristics, especially strong southern winds in the northern spring and summer mornings, indicating that wind speed is likely a key factor controlling the dust deposition rate—the

higher the wind speed, the faster the deposition[62].

The surface temperature analysis showed that thermal inertia and dust have the greatest impact on temperature. Fluctuations in atmospheric pressure and temperature affect the performance of surface thermal inertia, with increased dust storm activity thickening the dust cover and stabilizing surface temperature[63], consistent with the observed daily and seasonal temperature fluctuations in meteorological data[62]. Modeling the impact of daily and seasonal temperature variations on surface temperature suggested that the likelihood of shallow subsurface water ice is low[64]. This is corroborated by the radar data from the Mars Rover Penetrating Radar (RoPeR) of the Zhurong rover, which studied the dielectric properties of the Martian regolith, indicating that the regolith at the landing site likely consists of volcanic rocks and possible hydrated minerals or sediments[65].

4.3 Water Environment on Mars

The combination of radar and thermal simulation results suggests that liquid water, sulfate or carbonate brines are difficult to stabilize above 100m above the shallow surface. However, since the dielectric constant of sulfate or carbonate salt ice (2.5~8) is comparable to that of rocky materials, the presence of salty ice at shallow depths shows a possibility[66]. The Mars Climate Station (MCS) can record local wind speeds, temperatures, and barometric pressures, found that the meteorological conditions at the landing site were largely controlled by the seasonal variations on Mars. It was also found that water here frosts every morning and quickly sublimates and disappears after sunrise, and a brief period of liquid water may exist on the surface of the landing site around the summer solstice each year. The dissolution of salts in the soil can allow salt water to remain on the surface for a period of time. All these evidences suggest the existence of an active water vapor cycle at the soil-atmosphere interface in the landing site[67]. At the same time, using different cameras including the Navigation and Topography Cameras (NaTeCam), an in-depth study of the micro-morphological features and material composition characteristics of the surface of the dunes in the area, it found that the surface of the dunes shows crusts, cracks, agglomerations, polygonal ridges, banded watermarks and other surface features. Through spectral data analysis, it reveals that the dune's surface is rich in water-containing sulfate, opal, water-containing iron oxide and other substances, it was determined that these surface features are associated with frost or snowfall on the surface of saline dunes during cooling. This finding fills a gap in ground-based observational evidence for liquid water at low Martian latitudes, revealing that modern Martian climates can occur in wetter environments at low latitudes where surface temperatures are relatively warm and favorable[68].

The main rocks and soils in the landing site are basalts, and their chemical weathering index (CIA) is extremely low, revealing that the degree of aqueous alteration is low and that they may have been formed mainly by a mixture of widespread Martian dust and localized materials rich in calcium and poor in magnesium. The amorphous minerals found in Blessing may have been formed by the alteration of volcanic detrital material under conditions of low temperature, weak acidity, and low water-rock ratios, and it is estimated that the amount of water involved in water-rock interactions may have been low or short-lived[69]. Based on the spectroscopic studies, it can be inferred that the presence of a variety of water-bearing minerals in the landing site, such as polyhydric sulfates, gypsum, and water-bearing silicates, suggests that there was once water activity in the northern lowlands of Mars, which is consistent with speculation of the presence of subsurface glaciers or permafrost in the region, indicated by geomorphic features such as walled impact craters, pancake impact craters, and concave cones found in the Utopia Platinum. Based on the identification of sulfate minerals combined with dating results, it is suggested that groundwater or even surface water may have existed in the landing site 3.5 billion years ago[70]. The bright- colored rocks of the dunes found in the landing site are interpreted as locally developed crust layers, which require large amounts of liquid water to form and cannot be formed by atmospheric water vapor alone, and exclude the possibility of large-scale water activity on the surface before. The study deduces that these sulfate-rich crust layers may have been formed by the intermittent overflowing of groundwater, or by capillary action of evaporation and crystallization of salts crystallized minerals cemented to Martian soil The crusts were formed by petrogenesis, followed by erosive loss of the topsoil overlying the crusts, which ultimately exposed the crusts. It also found signs of water activity in landing sites of younger geologic age, suggesting that the Martian hydrosphere during the Amazonian period may have been more active than previously thought[71].

Analysis of the chemical composition and water content of the rocky crust using the Laser Induced Breakdown Spectrometer (LIBS) corroborated the hydrogen-rich signals found in Zhurong's short-wave infrared, and further confirmed the presence of groundwater activity in the Martian Amazonian over the vast area of the landing site. LIBS analysis of three other types of relatively loose material (dunes, soils and colluvium) found that the colluvium had similar elemental trends to the soils and dunes, indicating a similar material origin to the local soils and dunes, while its water content ordering indicated the presence of water-bearing magnesium salts. By analyzing the correspondence between water and other metal ions, it is also possible to determine that in these looser materials, water can be present in two forms, evaporated salts containing crystalline water (*e.g.*, hydrated magnesium sulfate) and adsorbed water molecules[67]. From the point of view of surface morphology, the possible causes of the polygonal fissures on the dunes: the exchange of water vapor between the surface and the atmosphere led to the formation of a hardened sandy crust layer on the surface, which broke up to form the polygonal fissures. The chronological characterization of the dunes suggests, they may be indicative of recent water activity and surfaChang'E-atmosphere water exchange processes on Mars, thus providing clues to the study of the water cycle on Mars under the current cold and arid climatic conditions[72].

4.4 Subsurface Structure and Physical Properties

Li *et al*.[66], using low-frequency radar data from the Zhurong rover, conducted detailed analyses and imaging to obtain the first high-resolution subsurface stratigraphy (<80 m) of a 1171m profile in the southern Utopia Planitia, They identified two fining-upward sedimentary sequences beneath a few meters of regolith, at depths of approximately 10~30 meters and 30~80 meters. These findings suggest multiple episodes of resurfacing events in southern Utopia Planitia since the late Hesperian period (3.5~3.2 billion years ago), with potential water-related geological processes persisting into the mid-to-late Amazonian period (around 1.6 billion years ago). Further, Zhang *et al*.[73] utilized high-resolution time-frequency analysis methods to discover alternating high- and low-frequency bands in the radar profile. This indicates significant changes in water activity and/or thermal conditions from the late Hesperian to early Amazonian periods, implying intense paleoclimate variations in the mid-to-low latitudes (about 25°N), potentially related to ancient Martian obliquity shifts. Chen *et al*.[74] conducted fine-scale investigations of the subsurface regolith structure up to 5 meters deep using high-frequency radar data from Zhurong rover. They did not find distinct stratification but identified residual impact craters and lenses, revealing the influences of Mars' thin atmosphere and other surface geological processes, such as wind erosion, on regolith layer formation and the degradation rate of small impact craters. In the southern Utopia region where Zhurong operates, Du *et al*.[75] detected extremely weak magnetic fields, with an average vector field strength of about 10 nT and spatial variation on the scale of hundreds of meters. These observations provide critical evidence on the cessation of Mars' magnetic dynamo: the weak magnetic field indicates complete demagnetization of the Utopia basin during its formation, supporting the idea that Mars' early dynamo ceased around 4.0 Ga. The absence of remagnetization in the subsequent early Hesperian lava flows suggests the dynamo might have stopped working between 3.6 and 3.7 Ga. Guo *et al*.[76] explored the potential of improving Phobos' gravity field estimates using Doppler tracking data from Tianwen-1 and Mars Express flybys. Their study examined different internal structure models for Phobos, indicating that incorporating more flyby data, especially under optimal conditions, could achieve a fifth-degree gravity field estimate.

4.5 Verification of in-situ Payload Performance of the Orbiter

Zhang *et al*.[77] and Fan *et al*.[78] utilized effective data on Tianwen-1's transfer orbit to Mars to confirm that MINPA's performance is reliable and stable. Wang *et al*.[79] found that 0.48% of ion observations at Mars were UV contaminated. A removal algorithm was proposed to reduce contamination while preserving valid signals, effectively improving data quality. Chi *et al*.[80] compared the magnetic field measurements from Tianwen-1/MOMAG and MAVEN/MAG during the ICME and SIR interval and found a generally good consistency between them.

4.6 The Interplanetary and Near Mars Space Environment

Fu *et al*.[81] reported the first MEPA measurements of the widespread SEP event when Tianwen-1 was in transit to Mars. Moreover, the decay phases of the time-

intensity profiles at Mars and Earth clearly show the reservoir effect. The double-power-law spectrum is likely generated at the acceleration site, and a small but finite cross-field diffusion is crucial to understanding the formation of the SEP reservoir phenomenon. Wang *et al*.[82] combined the upstream solar wind observations measured by MAVEN, ACE) and DSCOVR, successfully predicted the upstream solar wind conditions up to Mars. Zhong *et al*.[83] presented an accurate prediction for the arrival time and in-situ parameters of Corotating Interaction Regions (CIRs) when Earth and Mars have large longitudinal separations. Wang *et al*.[79] explored the Differential One-way Ranging (DOR) signals of Tianwen-1, observed by the China VLBI Network (CVN), to study the solar wind. The data catch the impact of the CME on the DOR signals when a CME passed across the ray paths of the telescope beams. The analysis indicates that multifrequency DOR signals observed by VLBI stations have great application in characterizing the density variations and propagation of the solar wind.

4.7 Impact of the Upstream Solar Wind on the Martian Space Environment

Cheng *et al*.[84] presented direct evidence of solar wind effects on the bow shock by analyzing Tianwen-1 and MAVEN data. The results indicate that the bow shock is rapidly compressed and then expanded during the dynamic pressure pulse in the solar wind, and is also oscillated during the IMF rotation. The superposition of variations in multiple solar wind parameters leads to more intensive bow shock oscillation. Protons in solar wind exchange electrons through collisions with neutral particles in the exosphere to produce Hydrogen Energetic Neutral Atoms (H-ENAs). Zhang *et al*.[85] developed an algorithm to invert the solar wind parameters from the H-ENAs measured in near-Mars space, suggesting the solar wind parameters inversed from H-ENA observation could be an important supplement to the dataset supporting studies on the Martian space environment.

Using Tianwen-1 and MAVEN, Su *et al*.[86] presented the first observation of significant modifications by a solar wind stream interaction region to the Martian foreshock waves. After the stream interface hit Mars, an unusual band of foreshock waves emerged, with a central frequency of about 0.4 Hz and a frequency width of about 0.2 Hz. These waves exhibited highly distorted waveforms and were approximately elliptically polarized, propagating highly obliquely to the background magnetic field. These waves differed greatly from the commonly known Martian foreshock 30 s waves and 1 Hz waves, but resembled, to some extent, the less frequently occurring terrestrial foreshock 3 s waves. From observations from the MINPA, Jin *et al*.[87] found the dominance of the field-aligned distribution type over the energy range from 188 to 6232 eV. Maps of the occurrence rate show the preferential presence of a trapped-like distribution at the lower altitudes of the surveyed nightside region. Chi *et al*.[88] presented two multipoint ICMEs detected by the Tianwen-1 and MAVEN at Mars and the BepiColombo upstream of Mercury. These findings highlight the importance of background solar wind in determining the interplanetary evolution and global morphology of ICMEs up to Mars distance. Yu *et al*.[89] utilized the simultaneous spacecraft observations from Tianwen-1/MOMAG in the solar wind and multiple instruments on board the MAVEN in the Martian upper atmosphere, to study the response of Mars to an ICME. During this event. The altitude of the Martian ionopause location was lowered. The depletion of the plasma density in the topside Martian ionosphere on the night side reveals the presence of substantial ion and electron escape to space. The column abundance of plasma dramatically decreased, with 34% e^-, 61% O_2^+, and 73% O^+ reduced.

Planetary heavy ions in the ionosphere are picked up by the solar wind, forming an important Martian ion escape channel known as a "plume". Ma *et al*.[90] took advantage of the joint observations of Tianwen-1 and MAVEN to study oxygen ion plumes, confirming the convection electric field acceleration as the energization mechanism of plume ions (up to >15 keV). Qiao *et al*.[91] delved into a Pick-Up Ion (PUI) event captured by the MINPA, revealing a faster acceleration than expected by the presence of an electric field region within the magnetosheath. The peak of the electric field strength is located at the upper edge or within the Magnetic Pileup Boundary. Hu *et al*.[92] conducted the Tianwen-1 radio-occultation experiment on 5 August 2021, retrieved excess Doppler frequency, bending angle, refractivity, electron density, neutral mass density, pressure and temperature profiles, exhibiting the ionosphere M1 (M2) layer peak, planetary boundary layer, troposphere and a stratosphere. The inversion system[93] developed for Tianwen-1 radio occultation observations enabled the derivation of neutral atmospheric density, pressure,

temperature, and electron density profiles of Mars. Importantly, these inversion results from Tianwen-1 maintained consistency with results from the Mars Express and the Chapman theory.

References

[1] HU T, YANG Z, KANG Z Z. Population of Degrading Small Impact Craters in the Chang'E-4 Landing Area Using Descent and Ground Images. *Remote Sensing* 2022, *14*

[2] DING L, ZHOU R, YUAN Y. A 2-year locomotive exploration and scientific investigation of the lunar farside by the Yutu-2 rover. *Science Robotics* 2022, *7*

[3] CHANG R, YANG W, LIN H L. Lunar Terrestrial Analog Experiment on the Spectral Interpretations of Rocks Observed by the Yutu-2 Rover. *Remote Sensing* 2022, *14*

[4] CHEN J, LING Z C, JOLLIFF B L. Radiative Transfer Modeling of Chang'E-4 Spectroscopic Observations and Interpretation of the South Pole-Aitken Compositional Anomaly. *Astrophysical Journal Letters* 2022, *931*

[5] LIU C, LIU L, CHEN J. Mafic mineralogy assemblages at the Chang'E-4 landing site: A combined laboratory and lunar in situ spectroscopic study. *Astronomy & Astrophysics* 2022, *658*

[6] WANG P Y, BUGIOLACCHI R, SU Y. A new compositional, mineralogical and chronological study of the Leibnitz crater within the SPA basin. *Planetary and Space Science* 2023, *227*

[7] WANG X, LIU J J, LIU D W. Dusty Mafic Rocks Alone the Path of Chang'E-4 Rover: Initial Analysis of the Image Cubes of the Onboard Visible and Near-Infrared Imaging Spectrometer. *Geophysical Research Letters* 2022, *49*

[8] XIAO X, YU S R, HUANG J. Thermophysical properties of the regolith on the lunar far side revealed by the in situ temperature probing of the Chang'E-4 mission. *National Science Review* 2022, *9*

[9] DING L, ZHOU R Y, YU T Y. Lunar rock investigation and tri-aspect characterization of lunar farside regolith by a digital twin. *Nature Communications* 2024, *15*

[10] CAO H Q, XU Y, XU L Y. From Schrodinger to Von Karman: An Intriguing New Geological Structure Revealed by the Chang'E-4 Lunar Penetrating Radar. *Geophysical Research Letters* 2023, *50*

[11] DING C Y, LI J, HU R. Moon-Based Ground-Penetrating Radar Observation of the Latest Volcanic Activity at the Chang'E-4 Landing Site. *Ieee Transactions on Geoscience and Remote Sensing* 2023, *61*

[12] FENG Y J, CHEN S R, TONG X H. Exploring the Lunar Regolith's Thickness and Dielectric Properties Using Band-Limited Impedance at Chang'E-4 anding Site. *Journal of Geophysical Research-Planets* 2023, *128*

[13] GIANNAKIS I, Martin-Torres J, SU Y. Evidence of shallow basaltic lava layers in Von Kármán crater from Yutu-2 Lunar enetrating Radar. *Icarus* 2024, *408*

[14] FENG J Q, SIEGLER M A, WHITE M N. Dielectric properties and stratigraphy of regolith in the lunar South Pole-Aitken basin: Observations from the Lunar Penetrating Radar. *Astronomy & Astrophysics* 2022, *661*

[15] ZHANG J H, ZHOU B, LIN Y T. Lunar regolith and substructure at Chang'E-4 landing site in South Pole-Aitken basin. *Nature Astronomy* 2021, *5*

[16] XIE L H, LI L, ZHANG A B. Multipoint Observation of the Solar Wind Interaction with Strong Lunar Magnetic Anomalies by ARTEMIS Spacecraft and Chang'E-4 Rover. *Astrophysical Journal Letters* 2022, *937*

[17] ZHONG T H, XIE L H, ZHANG A B. Dependences of Energetic Neutral Atoms Energy on the Solar Wind Energy and Solar Zenith Angle Observed by the Chang'E-4 Rover. *Astrophysical Journal Letters* 2024, *960*

[18] WIESER M, WILLIAMSON H, WIESER G S. Energy spectra of energetic neutral hydrogen backscattered and sputtered from the lunar regolith by the solar wind. *Astronomy & Astrophysics* 2024, *684*

[19] XU Z G, GUO J N, Wimmer-Schweingruber, R. F. Primary and albedo protons detected by the Lunar Lander Neutron and Dosimetry experiment on the lunar farside. *Frontiers in Astronomy and Space Sciences* 2022, *9*

[20] LUO P W, ZHANG X P, FU S. First measurements of low-energy cosmic rays on the surface of the lunar farside from Chang'E-4 mission. *Science Advances* 2022, *8*

[21] YAO Y G, XIAO C J, WANG P S. Instrumental Neutron Activation Analysis of Chang'E-5 Lunar Regolith Samples. *Journal of the American Chemical Society* 2022, *144*, 5478-5484

[22] CHE X C, NEMCHIN A, LIU D Y. Age and composition of young basalts on the Moon, measured from samples returned by Chang'E-5. *Science* 2021, *374*, 887-+

[23] LI C L, HU H, YANG M F. Characteristics of the lunar samples returned by the Chang'E-5 mission. *National Science Review* 2022, *9*

[24] LI Q L, ZHOU Q, LIU Y. Two-billion-year-old volcanism on the Moon from Chang'E-5 basalts. *Nature* 2021, *600*, 54-+

[25] YUE Z Y, DI K C, WAN W H. Updated lunar cratering chronology model with the radiometric age of Chang'E-5 samples (Feb, 10.1038/s41550-022-01604-3, 2022). *Nature Astronomy* 2022, *6*, 514-514

[26] QIAN Y Q, SHE Z B, He Q. Mineralogy and chronology of the young mare volcanism in the Procellarum-KREEP-Terrane. *Nature Astronomy* 2023, *7*, 287-+

[27] ZHANG H, ZHANG X, ZHANG G. Size, morphology, and composition of lunar samples returned by Chang'E-5 mission. *Science China-Physics Mechanics & Astronomy* 2022, *65*

[28] LU X J, CHEN J, LING Z C. Mature lunar soils from Fe-rich and young mare basalts in the Chang'E-5 regolith samples. *Nature Astronomy* 2023, *7*, 142-151

[29] TIAN H C, WANG H, CHEN Y. Non-KREEP origin for Chang'E-5 basalts in the Procellarum KREEP Terrane. *Nature* 2021, *600*, 59-+

[30] LUO B J, WANG Z C, SONG J L. The magmatic architecture and evolution of the Chang'e-5 lunar basalts. *Nature Geoscience* 2023, *16*, 301-+

[31] LIU D W, WANG X, LIU J J. Spectral interpretation of late-stage mare basalt mineralogy unveiled by Chang'E-5 samples. *Nature Communications* 2022, *13*

[32] YANG C, ZHANG X M, BRUZZONE L. Comprehensive mapping of lunar surface chemistry by adding Chang'E-5 samples with deep learning. *Nature Communications* 2023, *14*

[33] Zhao, R.; Shen, L. Q.; Xiao, D. D. Diverse glasses revealed from Chang'E-5 lunar regolith. *National Science Review* 2023, *10*

[34] LONG T, QIAN Y Q, NORMAN M D. Constraining the formation

and transport of lunar impact glasses using the ages and chemical compositions of Chang'E-5 glass beads. *Science Advances* 2022, *8*

[35] MEI A X, JIANG Y, LIAO S Y. KREEP-rich breccia in Chang'E-5 regolith and its implications. *Science China-Earth Sciences* 2023, *66*, 2473-2486

[36] GUO Z, LI C, LI Y. Nanophase Iron Particles Derived From Fayalitic Olivine Decomposition in Chang'E-5 Lunar Soil: Implications for Thermal Effects During Impacts. *Geophysical Research Letters* 2022, *49*

[37] LI C, GUO Z, LI Y. Impact-driven disproportionation origin of nanophase iron particles in Chang'E-5 lunar soil sample. *Nature Astronomy* 2022, *6*, 1156-1162

[38] XIAN H Y, ZHU J X, YANG Y P. Ubiquitous and progressively increasing ferric iron content on the lunar surfaces revealed by the Chang'E-5 sample. *Nature Astronomy* 2023, *7*, 280-+

[39] LIU X Y, GU L X, TIAN H C. First classification of iron meteorite fragment preserved in Chang'E-5 lunar soils. *Science Bulletin* 2024, *69*, 554-561

[40] ZENG X J, WU Y X, YU W. Unusual Ti minerals on the Moon produced by space weathering. *Nature Astronomy* 2024

[41] LI Y H, WANG Z C ZHANG W. Rb-Sr isotopes record complex thermal modification of Chang'E-5 lunar soils. *Science Bulletin* 2023, *68*, 2724-2728

[42] GUO Z, LI C, LI Y. Sub-microscopic magnetite and metallic iron particles formed by eutectic reaction in Chang'E-5 lunar soil. *Nature Communications* 2022, *13*

[43] GUO Z, LI C, LI Y. Vapor-deposited digenite in Chang'E-5 lunar soil. *Science Bulletin* 2023, *68*, 723-729

[44] LIN H L, LI S, XU R. In situ detection of water on the Moon by the Chang'E-5 lander. *Science Advances* 2022, *8*

[45] LIU J J, LIU B, REN X. Evidence of water on the lunar surface from Chang'E-5 in-situ spectra and returned samples. *Nature Communications* 2022, *13*

[46] ZHOU C J, TANG H, LI X Y. Chang'E-5 samples reveal high water content in lunar minerals. *Nature Communications* 2022, *13*

[47] ZHOU C J, MO B, Tang H. Multiple sources of water preserved in impact glasses from Chang'E-5 lunar soil. *Science Advances* 2024, *10*

[48] HE H C, JI J L, ZHANG Y. A solar wind-derived water reservoir on the Moon hosted by impact glass beads. *Nature Geoscience* 2023, *16*, 294-+

[49] ZENG X J, LI X Y, LIU J Z. Exotic clasts in Chang'e-5 regolith indicative of unexplored terrane on the Moon. *Nature Astronomy* 2023, *7*, 152-159

[50] TIAN H C, ZHANG C, YANG W. Surges in volcanic activity on the Moon about two billion years ago. *Nature Communications* 2023, *14*

[51] HU S, HEH C, JI J L. A dry lunar mantle reservoir for young mare basalts of Chang'E-5. *Nature* 2021, *600*, 49-+

[52] SU B, YUAN J Y, CHEN Y. Fusible mantle cumulates trigger young mare volcanism on the cooling Moon. *Science Advances* 2022, *8*

[53] WANG Z L, TIAN W, WANG W. Crystallization kinetics of a fastest-cooling young mare basalt of Chang'E-5. *Science Bulletin* 2023, *68*, 1621-1624

[54] XU J Y, LI Q L, LU K. Chang'E-5 basalt-like non-KREEP young lunar meteorite. *Science Bulletin* 2024, *69*, 601-605

[55] LU Y, EDGETT K S, WU B. Aeolian disruption and reworking of TARs at the Zhurong rover field site, southern Utopia Planitia, Mars. *Earth and Planetary Science Letters* 2022, *595*

[56] LIU J J, QIN X G, REN X. Martian dunes indicative of wind regime shift in line with end of ice age. *Nature* 2023, *620*, 303-+

[57] GOU S, YUE Z Y, DI K C. Transverse aeolian ridges in the landing area of the Tianwen-1 Zhurong rover on Utopia Planitia, Mars. *Earth and Planetary Science Letters* 2022, *595*

[58] WANG L, ZHAO J N, HUANG J. An explosive mud volcano origin for the pitted cones in southern Utopia Planitia, Mars. *Science China-Earth Sciences* 2023, *66*, 2045-2056

[59] CHEN Z Y, WU B, WANG Y R. Rock Abundance and Erosion Rate at the Zhurong Landing Site in Southern Utopia Planitia on Mars. *Earth and Space Science* 2022, *9*

[60] WANG B, GOU S, DI K C. Rock size-frequency distribution analysis at the Zhurong landing site based on Navigation and Terrain Camera images along the entire traverse. *Icarus* 2024, *413*

[61] ZHANG Q, LIU D W, REN X. Dust Deposition at Zhurong Landing Site From Multispectral Camera Observations. *Geophysical Research Letters* 2023, *50*

[62] JIANG C S, JIANG Y, LI H N. Initial results of the meteorological data from the first 325 sols of the Tianwen-1 mission. *Scientific Reports* 2023, *13*

[63] LUO Y W, YAN J G, LI F. Spatial Autocorrelation of Martian Surface Temperature and Its Spatio-Temporal Relationships with Near-Surface Environmental Factors across China's Tianwen-1 Landing Zone. *Remote Sensing* 2021, *13*

[64] ZHANG L, ZHANG J. H. Observation-based temperature field simulation at Zhurong landing site, Mars. *Frontiers in Astronomy and Space Sciences* 2022, *9*

[65] ZHANG L, XU Y, LIU R R. The Dielectric Properties of Martian Regolith at the Tianwen-1 Landing Site. *Geophysical Research Letters* 2023, *50*

[66] LI C, ZHENG Y K, WANG X. Layered subsurface in Utopia Basin of Mars revealed by Zhurong rover radar. *Nature* 2022, *610*, 308-+

[67] ZHAO Y Y S, YU J, WEI G F. In situ analysis of surface composition and meteorology at the Zhurong landing site on Mars. *National Science Review* 2023, *10*

[68] QIN X G, REN X, WANG X. Modern water at low latitudes on Mars: Potential evidence from dune surfaces. *Science Advances* 2023, *9*

[69] LIU C Q, LING Z C, WU Z C. Aqueous alteration of the Vastitas Borealis Formation at the Tianwen-1 landing site. *Communications Earth & Environment* 2022, *3*

[70] LIN H L, LIN Y T, WEI Y. Mineralogical evidence of water activity in the northern lowlands of Mars based on inflight-calibrated spectra from the Zhurong rover. *Science China-Earth Sciences* 2023, *66*, 2463-2472

[71] LIU Y, WU X, ZHAO Y Y S. Zhurong reveals recent aqueous activities in Utopia Planitia, Mars. *Science Advances* 2022, *8*

[72] WANG J, ZHAO J N, XIAO L. Recent Aqueous Activity on Mars Evidenced by Transverse Aeolian Ridges in the Zhurong Exploration Region of Utopia Planitia. *Geophysical Research Letters* 2023, *50*

[73] ZHANG L, LI C, ZHANG J H. Buried palaeo-polygonal terrain detected underneath Utopia Planitia on Mars by the Zhurong radar. *Nature Astronomy* 2024, *8*

[74] CHEN R A, ZHANG L, XU Y. Martian soil as revealed by ground-penetrating radar at the Tianwen-1 landing site. *Geology*

2023, *51*, 315-319

[75] DU A M, GE Y S, WANG H P. Ground magnetic survey on Mars from the Zhurong rover. *Nature Astronomy* 2023, *7*, 1037-+

[76] GUO X, YAN J G, YANG X. Simulation of Phobos gravity field estimation from Tianwen-1 flybys and implications for the modelling of Phobos' internal structure. *Monthly Notices of the Royal Astronomical Society* 2023, *520*, 925-934

[77] ZHANG A B, KONG L G, LI W Y. Tianwen-1 MINPA observations in the solar wind. *Earth Planet. Phys.*, 2022, *6*, 1-9

[78] FAN K, YAN L M, WEI Y. The solar wind plasma upstream of Mars observed by Tianwen-1: Comparison with Mars Express and MAVEN. *Science China-Earth Sciences* 2022, *65*, 759-768

[79] WANG Z C, MA M L, LIU Q H. Application of the Tianwen-1 DOR Signals Observed by Very Long Baseline Interferometry Radio Telescopes in the Study of Solar Wind Plasma and a Coronal Mass Ejection. *Astrophysical Journal Supplement Series* 2023, *269*

[80] CHI Y T, SHEN C L, CHENG L. Interplanetary Coronal Mass Ejections and Stream Interaction Regions Observed by Tianwen-1 and MAVEN at Mars. *Astrophysical Journal Supplement Series* 2023, *267*

[81] FU S, DING Z Y, ZHANG Y J. First Report of a Solar Energetic Particle Event Observed by China's Tianwen-1 Mission in Transit to Mars. *Astrophysical Journal Letters* 2022, *934*

[82] WANG J J, SHI Y R, LUO B X. Upstream Solar Wind Prediction up to Mars by an Operational Solar Wind Prediction System. *Space Weather-the International Journal of Research and Applications* 2023, *21*

[83] ZHONG Z H, SHEN C L, CHI Y T. Prediction for Arrival Time and Parameters of Corotation Interaction Regions using Earth-Mars Correlated Events from Tianwen-1, MAVEN, and Wind Observations. *Astrophysical Journal* 2024, *965*

[84] CHENG L, LILLIS R, WANG Y M. Martian Bow Shock Oscillations Driven by Solar Wind Variations: Simultaneous Observations From Tianwen-1 and MAVEN. *Geophysical Research Letters* 2023, *50*

[85] ZHANG Y T, LI L, XIE L H. Inversion of Upstream Solar Wind Parameters from ENA Observations at Mars. *Remote Sensing* 2023, *15*

[86] SU Z P, WANG Y M, ZHANG T L. Unusual Martian Foreshock Waves Triggered by a Solar Wind Stream Interaction Region. *Astrophysical Journal Letters* 2023, *947*

[87] JIN T F, NI B B, KONG L G. Proton pitch angle distributions in the Martian induced magnetosphere: A survey of Tianwen-1 Mars Ion and Neutral Particle Analyzer observations. *Earth Planet. Phys.*, 2023, *7*, 533-539

[88] CHI Y T, SHEN C L, LIU J Y. The Dynamic Evolution of Multipoint Interplanetary Coronal Mass Ejections Observed with Bepi-Colombo, Tianwen-1, and MAVEN. *Astrophysical Journal Letters* 2023, *951*

[89] YU B K, CHI Y T, OWENS M. Tianwen-1 and MAVEN Observations of the Response of Mars to an Interplanetary Coronal Mass Ejection. *Astrophysical Journal* 2023, *953*

[90] MA X, TIAN A M, GUO R L. Tianwen-1 and MAVEN observations of Martian oxygen ion plumes. *Icarus* 2023, *406*

[91] QIAO F H, LI L, XIE L H. Acceleration of Pick-Up Ions in the Martian Magnetosheath: A Tianwen-1 Case Study. *Journal of Geophysical Research-Space Physics* 2024, *129*

[92] HU X, WU X C, SONG S L. First Observations of Mars Atmosphere and Ionosphere with Tianwen-1 Radio-Occultation Technique on 5 August 2021. *Remote Sensing* 2022, *14*

[93] LIU M, CHEN L, JIAN N C. Preliminary Estimations of Mars Atmospheric and Ionospheric Profiles from Tianwen-1 Radio Occultation One-Way, Two-Way, and Three-Way Observations. *Remote Sensing* 2023, *15*

3 Achievement Highlight and Progress Update of Space Science Missions

CHANG Jin. Recent Progresses of the DAMPE Mission. *Chinese Journal of Space Science*, 2024, **44**(4)

Recent Progresses of the DAMPE Mission*

CHANG Jin

1. Key Laboratory of Dark Matter and Space Astronomy, Purple Mountain Observatory, Chinese Academy of Sciences, Nanjing 210033
2. School of Astronomy and Space Science, University of Science and Technology of China, Hefei 230026

Abstract

The DArk Matter Particle Explorer (DAMPE) is a space high-energy particle and γ-ray detector whose major scientific goals are the indirect detection of dark matter particles, the origin of cosmic rays and high-energy γ-ray astronomy. Since its successful launch in December 2015, the DAMPE has been operated smoothly in orbit for more than 8 years. The direct measurements of the boron-to-carbon and boron-to-oxygen flux ratios, and the proton+ Helium spectrum up to 316 TeV have been obtained, revealing new spectral features revealed with very high significances. The search results of γ-ray spectral line and fractionally charged particles indicate a good potential of DAMPE for indirect dark matter detection and new physical discovery in space. The DAMPE measurements are expected to significantly advance our understanding of the fundamental problems in astroparticle physics.

Key words

DAMPE, Dark matter, Indirect detection, Cosmic rays

1 Introduction

It has been well established that our Universe is made up of about 4.9% baryonic matter, 26.8% Dark Matter (DM), and 68.3% dark energy[1]. The physical nature of DM is one of the most important fundamental questions of modern physics. Many types of candidate DM models have been proposed, among which the leading one is a kind of Weakly Interacting Massive Particles (WIMPs) beyond the standard model of particle physics, as motivated by the relic abundance of DM and the bottom-up evolution pattern of the large scale structures of the Universe[2,3]. Many efforts have been made to search for the WIMP DM in laboratories, including the direct detection of the WIMP-nucleon scattering by underground detectors, the indirect detection of the annihilation or decay products in the cosmic radiation, and the collider detection of WIMP pairs produced in high- energy particle colliders[4]. After several decades of efforts, no convincing evidence has been found yet. Particularly, the direct detection experiments push the WIMP-nucleon scattering strength to a very low level[5], which has already severely constrained a series of WIMP models.

In recent years, some interesting anomalies have been found in Cosmic Ray (CR) and γ-ray observations, such as the positron excess discovered by PAMELA[6], Fermi-LAT[7], and AMS-02[8], and the associated total Cosmic Ray Electron plus positron (CRE) excess by ATIC[9], Fermi-LAT[10], and AMS-02[11]. The excesses of positrons and CREs can be explained by either the astrophysical sources such as pulsars and the DM annihilation or decay[12-17]. There are still debates on the astrophysical or DM origin of the positron and/or CRE excesses, in particular, that the most recent HAWC ob-

* Supported by the National Key Research and Development Program of China (2016YFA0400200), and the National Natural Science Foundation of China (U1738205, U1738206)
Received May 15, 2024

servations of two nearby pulsars tend to disfavor the pulsar interpretation[18]. Higher precision measurements in a wider energy band are crucial to identifying their physical origin. Other anomalies include the γ-ray excess in the Galactic center[19], and the potential excess of CR antiprotons [20,21].

The purpose of the DArk Matter Particle Explorer (DAMPE) is to search for possible annihilation/decay relics of DM in CREs, with unprecedentedly high energy resolution and low background[22,23]. DAMPE is also a general purpose high-energy particle detector for observations of γ-rays and CR nuclei, which can be particularly helpful in the study of high-energy astrophysical phenomena and CR physics[23]. The DAMPE mission was launched into a 500 km Sun-synchronous orbit on 17 December 2015, with an inclination angle of 97°. It orbits the Earth every 95 minutes. All the detectors perform excellently in space. The daily event rate of DAMPE is about 5 million. It has recorded in total over 8 billion CR events as of May 2020, most of which are CR nuclei. There are about 1% CREs and 3×10^{-5} γ-ray photons in the DAMPE data.

2 Detector

DAMPE is made of 4 sub-detectors, which are, from top to bottom, the Plastic Scintillator strip Detector (PSD[24]), the Silicon-Tungsten tracKer-converter (STK[25]), the BGO imaging calorimeter[26], and the NeUtron Detector (NUD[27]). A schematic plot of the DAMPE detector is shown in Figure 1[23]. The total weight of the payload (satellite) is about 1.5 (1.9) tons, and the power consumption is 300 (500) W. The size of the satellite is about 1.2 m×1.2 m×1.0 m.

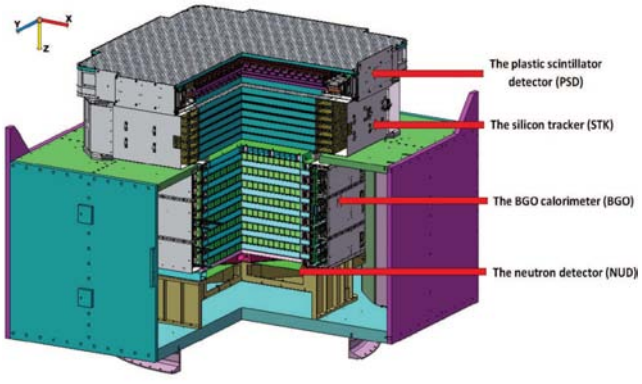

Fig.1 Schematic plot of the DAMPE detectors

The PSD is to measure the (absolute) charge of incident particles up to Z=30 via the ionization effect (dE/dx). It also serves as an anticoincidence detector for γ-rays. The PSD consists of two layers of orthogonally placed plastic scintillator bars. For each layer, 41 plastic scintillator bars are further placed in two sub-layers with a shift of 0.8 cm between them to reduce the gaps. The effective area of the PSD is 82.5 cm×82.5 cm[23]. The weight of the PSD is about 103 kg, and the power is 8.5 W.

The main function of STK is to measure the trajectory of a particle. The charge of light nuclei (Z<8) can also be measured by the STK. The STK consists of 12 layers (6 for x direction and 6 for y direction) of silicon trackers, each with two sub-layers arranged orthogonally to measure the x and y positions of a track. The STK is also a g-ray converter by means of three 1 mm thick tungsten plates inserted in the second, third, and fourth planes. Each silicon layer is made of 16 ladders, each formed by 4 silicon micro-strip detectors. Every ladder is segmented into 768 strips, half of which are readout strips and the other half are floating strips. In total, there are 384×16×12=73728 readout channels of the STK. The effective detection area of STK is 76 cm×76 cm. The STK has a weight of 154 kg and a power consumption of 82 W.

The BGO calorimeter is the major instrument of DAMPE. It has three functions: (i) measuring the energy deposition of incident particles, (ii) imaging the 3D profile of the shower development, and providing electron/hadron discrimination, and (iii) providing the level 0 trigger for the DAMPE data acquisition system. The BGO calorimeter is made of 308 BGO bars, each is read out at two ends by PhotoMultiplier Tubes (PMTs). The BGO crystals are placed orthogonally in 14 layers, with a total depth of about 32 radiation lengths and about 1.6 nuclear interaction lengths. The length of the BGO crystal is 60 cm, which is the longest in the world. The calorimeter has an effective area of 60 cm×60 cm, a total weight of 1052 kg, and a power consumption of 42 W.

The NUD is at the bottom of the detector. The main purpose of the NUD is to perform electron/hadron discrimination by means of the fact that neutrons are much more abundant in hadronic showers than in electromagnetic ones. Once the neutrons are created, they are quickly thermalized in the BGO calorimeter, and then get captured by Boron-doped plastic scintillators. The

NUD is made of four 30 cm×30 cm×1 cm plastic scintillators with 5% (weight) Boron element. The NUD has an effective area of 61 cm×61 cm, a mass of 12 kg, and a power of 0.5 W.

Table 1 summarizes the expected detector performance of DAMPE, for observations of electrons, g-rays, and protons[23]. With good measurements of the charge, direction, and energy of various types of particles, DAMPE is expected to play a significant role in exploring the high-energy Universe.

Table 1 Expected performance of DAMPE

Parameter	Value
Energy range (e/γ)	5 GeV to 10 TeV
Energy resolution (e/γ)	1.5% at 800 GeV
Energy range (p)	50 GeV to 500 TeV
Energy resolution (p)	40% at 800 GeV
Effective area (vertical γ)	1100 cm^2 at 100 GeV
Geometry factor (e)	0.3 m^2 sr above 30 GeV
Angular resolution (γ)	0.1° at 100 GeV
Field of view	1.0 sr

3 On-orbit Performance

Dedicated calibration of each unit of the detector has been done using the on-orbit data, which enables precise measurements of the physical quantities of each event[28]. Figure 2 gives the charge measurements by the PSD[29]. The absolute charge resolution is about 0.20e for Z=8 (*Oxy*gen) and 0.30e for Z=26 (Iron). Such a good charge resolution is the basis of precise spectral measurements of each species. Using the bright γ-ray sources we can calibrate the angular resolution of the STK, which results in about 0.5° for energies higher than 5 GeV.

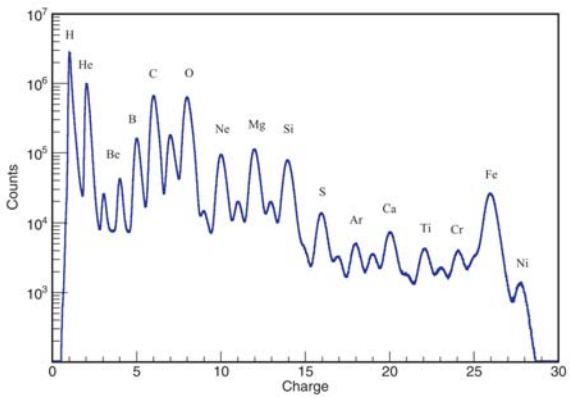

Fig.2 Charge spectrum obtained using two years of on-orbit data

The very thick BGO calorimeter enables that there is no significant leakage of electromagnetic showers from the bottom for energies as high as TeV. There is, however, a few percent of energy loss due to the dead materials of the calorimeter. An event-level energy correction method was developed and verified by MC simulations and the beam test data[30]. The beam test data and the MC simulations show that the energy resolution for CREs is better than 1.2% for energies above 100 GeV. DAMPE also has P- and N-side readouts for each BGO crystal, which have different gains. These two-side readouts give a consistency check of the energy measurement. We find that the energies measured by both sides agree with each other very well. Figure 3 presents the ratios of energies measured by the two sides, together with a Gaussian fit that gives a mean of 1.005±0.005 and a width of 0.016±0.001[31]. Such a result further supports the quoted energy resolution of about 1%.

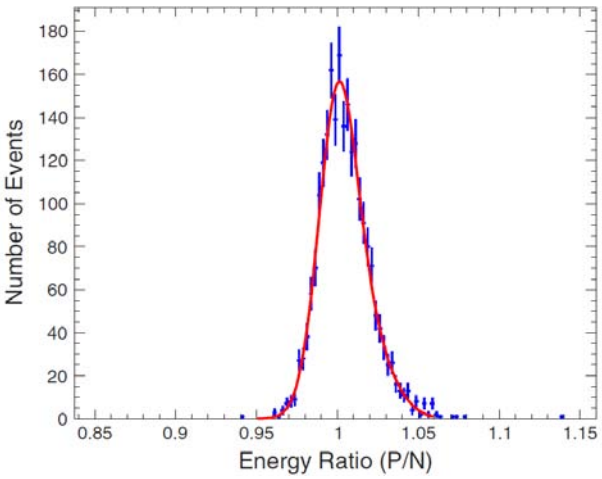

Fig.3 Ratios of energies reconstructed with P- and N-side data

Particle identification is one of the most challenging things for the observations of CREs. The background of CREs is CR protons (heavier nuclei can be effectively rejected *via* the charge measurement in PSD). The fluxes of CREs are about three orders of magnitude lower than that of protons. Therefore, a high rejection power of protons is essential for reliable measurements of the CRE fluxes. DAMPE uses the morphology difference between CREs and protons in the calorimeter to distinguish them[32,33]. This is basically due to different developments of hadronic and electromagnetic showers in the calorimeter. A simple two-parameter method was adopted to describe the longitude and latitude develop-

ments of the showers. They are: (i) an energy-weighted root-mean-square (RMS) value of hit positions in the calorimeter (shower spread), and (ii) the deposited energy fraction of the last BGO layer ($F_{\rm last}$). The left panel of Fig. 5 shows the distributions of these two parameters for the flight data with BGO energies between 500 GeV and 1 TeV[31]. We can see clearly two populations of events in this plot, with the upper population being proton candidates and the lower one being CRE candidates. To better quantify the separation between these two populations, we further define a shape parameter, $\zeta = F_{\rm last}\times(\text{shower spread/mm})^4/(8\times10^6)$, which projects these two parameters into one dimension. The distributions of the ζ parameter for the flight data and Monte Carlo (MC) simulations for CREs and protons are shown in the right panel of Figure 4. We select CREs with $\zeta\leqslant8.5$, which gives only about 2% proton background in this energy range[31]. For energies below TeV, the proton background is lower than 3%. The highest background in the energy range from 25 GeV to 4.6 TeV is estimated to be about 18%[31].

The NUD provides additional help of the electron-proton discrimination, since the neutron yields for hadronic showers are much higher than those of the electromagnetic showers. Simulations show that using the NUD alone the proton background can be suppressed by a factor of about 25 when keeping a CRE efficiency of 95%, for 1~5 TeV deposited energies[34]. Together with the calorimeter, the total suppression power improves by a factor of about 2[34]. The NUD capability is expected to be more important at higher energies.

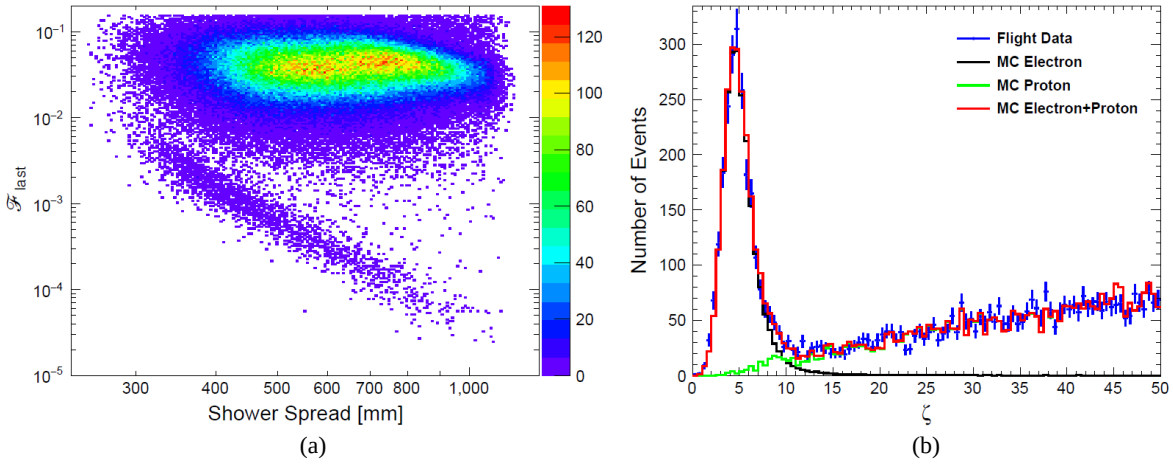

Fig.4 (a) Shower spread versus the last layer energy fraction for selected events with BGO energies between 500 GeV and 1 TeV. (b) one-dimensional distributions of the shape parameter ζ, compared with MC simulations

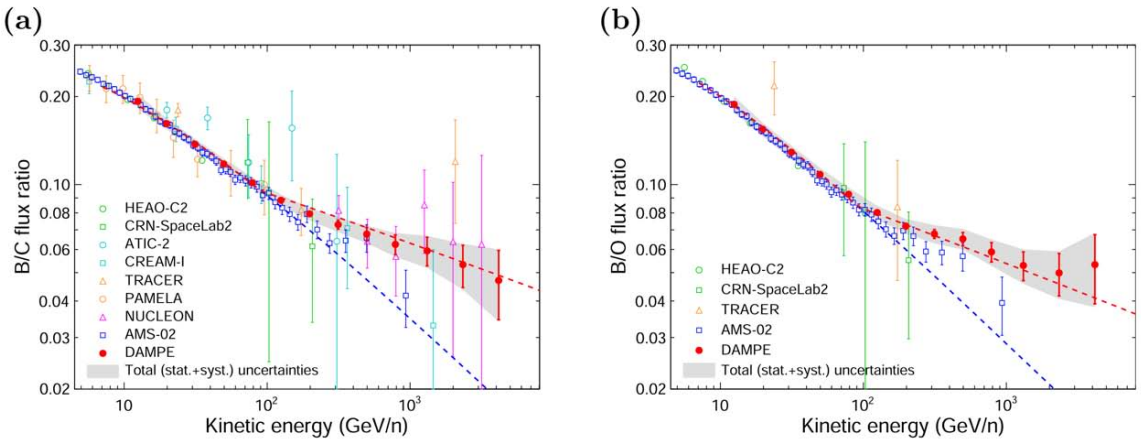

Fig.5 Boron-to-carbon (a) and boron-to-oxygen (b) flux ratios as functions of kinetic energy per nucleon measured by DAMPE [35] (Red filled dots), compared with measurements from other experiments [37-44]

4 Scientific Results

Figure 5 shows the direct measurements of boron-to-carbon (B/C) and boron-to-oxygen (B/O) flux ratios in the energy range from 10 GeV/n to 5.6 TeV/n with 6 years of on-orbit data collected by DAMPE, with high statistics and well-controlled systematic uncertainties[35]. Boron nuclei in cosmic rays are believed to be mainly produced by the fragmentation of heavier nuclei, such as carbon and oxygen, via collisions with the interstellar matter. Therefore, the precise measurements of the B/C and B/O ratios are very essential probes of the CR propagation. The energy dependence of both the B/C and B/O ratios measured by DAMPE can be well fitted by a broken power-law model rather than a single power-law model, suggesting the existence in both flux ratios of a spectral hardening at about 100 GeV/n. The significance of the break is about 5.6σ and 6.9σ for the GEANT4 simulation, and 4.46σ and 6.9σ for the alternative FLUKA simulation, for B/C and B/O, respectively. These latest measurements deviate from the predictions of conventional turbulence theories of the interstellar medium (ISM), which point toward a change of turbulence properties of the ISM at different scales or novel propagation effects of CRs, and should be properly incorporated in the indirect detection of dark matter via anti-matter particles. Improved measurements of the B/C, B/O, and other secondary-to- primary ratios in cosmic rays with higher statistics and lower systematics by DAMPE and future direct detection experiments such as HERD[36] are expected to eventually uncover the fundamental problems of the origin and propagation of CRs and shed new light on the indirect detection of dark matter particles.

Figure 6 shows the direct measurement of the CR proton+Helium (p+He) spectrum from 46 GeV to 316 TeV with 6 years of on-orbit data collected by DAMPE[45]. The selection of proton+helium, instead of individual proton and helium contributions, allows the collection of additional statistics, thus reaching higher energies with low background. The DAMPE p+He spectrum is in agreement with other direct/indirect-detection experiments, within the systematic uncertainties. The DAMPE measurement thus provides a link between direct and indirect CR measurements, exhibiting a good general agreement among very different techniques. The p+He spectrum in such a wide energy range deviates from a simple power-law behavior, and shows the presence of a spectral hardening around about 600 GeV followed by a softening at 28.8 ± 4.5 TeV. The softening features revealed in both the individual proton[46] and helium[47] spectra measured by DAMPE are further confirmed by the p+He spectrum, with an unprecedented significance of 6.6σ. Moreover, The p+He spectrum shows a novel hint regarding a possible direct detection of a second hardening around 150 TeV, for the first time in space.

Figure 7 shows the results of the Fractionally Charged Particle (FCP) search based on the on-orbit data of the DAMPE experiment[55]. Unlike underground experiments, which require an FCP energy of the order of hundreds of GeV, the FCP search with DAMPE starts at only a few GeV. Based on the analysis using 5 years ofcomic-ray events recorded by DAMPE, no FCP signal

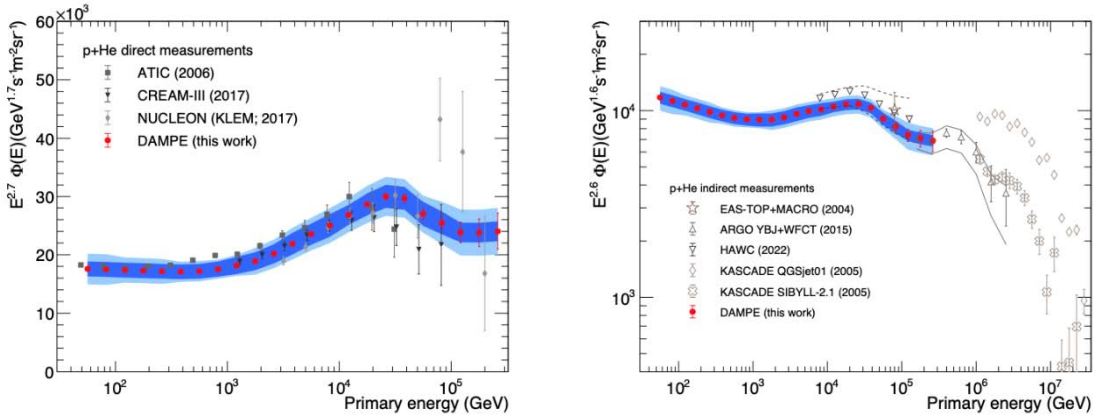

Fig.6 P+He spectrum from 46 GeV to 316 TeV measured by DAMPE[45] (red fill dots), compared with direct measurements of p+He made by ATIC-02 [48], NUCLEON[49] and CREAM[50] (left), and indirect measurements from ARGO-YBJ+WFCT[51], HAWC[52], KASCADE[53] and EAS-TOP+MACRO[54] (right)

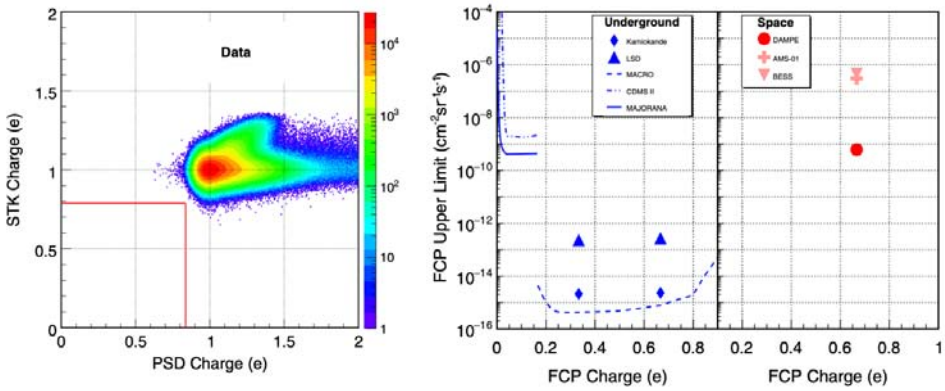

Fig.7 (left) Distribution of PSD-STK charge for the on-orbit data of DAMPE, the red lines indicate the signal region for FCPs. (right) FCP flux upper limit of DAMPE[55] (red dots), compared with the other space experiments [56,57] and underground experiments[58-62]

is observed (Figure 7 left) and the flux upper limit of $\frac{2}{1}e$ FCP is found to be $\Phi < 6.2 \times 10^{-10}$ cm^{-2}·sr^{-1} s^{-1} at the 90% CL (Figure 7 right). Our results demonstrate that DAMPE exhibits higher sensitivity than experiments of similar types by three orders of magnitude that more stringently restricts the conditions for the existence of FCP in primary cosmic rays. In the future, with the accumulation of more on-orbit data, DAMPE is expected to perform even more sensitive FCP searches.

Thanks to the unprecedented high energy resolution, DAMPE is well-suitable for searching for monochromatic and sharp γ-ray structures in the GeV–TeV. With the first 5 years of DAMPE data, we carry out the search for spectral γ-ray lines from 10 to 300 GeV[63]. To improve the sensitivity, we develop two types of dedicated data and adopt the signal-to-noise ratio optimized regions of interest (ROIs) for different DM density profiles. No line signals or candidates with TS value $\geqslant 9$ are detected between 10 and 300 GeV in the Galaxy. The 95% C.L. constraints on the annihilation cross section for $\chi\chi \to \gamma\gamma$ and the decay lifetime for $\chi \to \gamma\nu$, with proper addressing of the systematic uncertainties, are presented in Figure 8. Most of our constraints are comparable to the 5.8-year results of

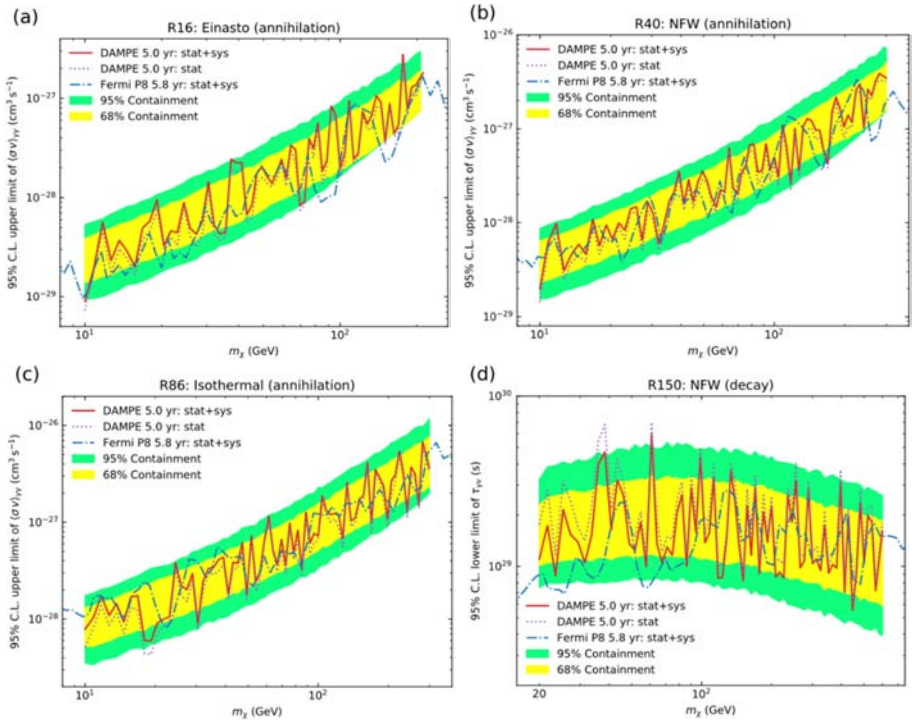

Fig.8 95% C.L. constraints for different DM density profiles with the DAMPE experiment[63]. The blue dot-dashed lines show the 5.8-year Fermi-LAT constraints[64]

Fermi-LAT thanks to the better energy resolution and the smaller influence of the systematic uncertainties. For the decaying DM, the DAMPE lower limits on the decay lifetime are stronger for DM with mass $\leqslant$100 GeV by a factor of about 2. In view of the fact that the DAMPE data set is about ten times smaller than that of Fermi-LAT, our findings demonstrate the potential of high-energy-resolution observations on dark matter detection.

Figure 9 shows the all-sky γ-ray map above 2 GeV along with the identified point-like sources obtained using 7.2 years of the DAMPE data[65]. The luminous Galactic plane and some bright sources can be clearly seen. Using the blind search method based on the Li-Ma formula[66], 248 point sources in total are detected with TS values larger than 25 and their locations are shown in Figure 10. By associating the observed sources with the Fermi-LAT 4FGL-DR3 catalog[67], the types of these sources are determined. The analysis reveals that a significant portion of the sources are associated with Active Galactic Nuclei (AGNs) and pulsars, indicating their origin in high-energy astrophysical processes associated with these objects.

Figure 10 shows the preliminary spectral measurement of the Galactic Center Excess (GCE) by DAMPE and the preferred DM parameter space for the annihilation channel $\chi\chi \to b\bar{b}$ [68]. The GCE is searched with 7.2 years of the DAMPE photon data. It is detected with a TS value of 81.3, which corresponds to a significance of 7.9σ with 6 degrees of freedom. The spatial distribution is fitted with the DM annihilation distribution of the generalized NFW profile $\rho_{nfw}(r) = \rho_0 / [(r/r_s)^{\gamma}(1+r/r_s)^{3-\gamma}]$ and the optimal inner slope is γ = 1.16 ± 0.10, which is consistent with that of the Fermi-LAT[69]. If the excess is explained with the DM annihilation into $b\bar{b}$, DM particles with mass m_{χ} = 45±11 GeV and cross section $\langle\sigma v\rangle = (2.2 \pm 0.3) \times 10^{-26}\,\mathrm{cm}^3 \cdot \mathrm{s}^{-1}$ is required. The DM parameter space is also consistent with the Fermi-LAT[70,71].

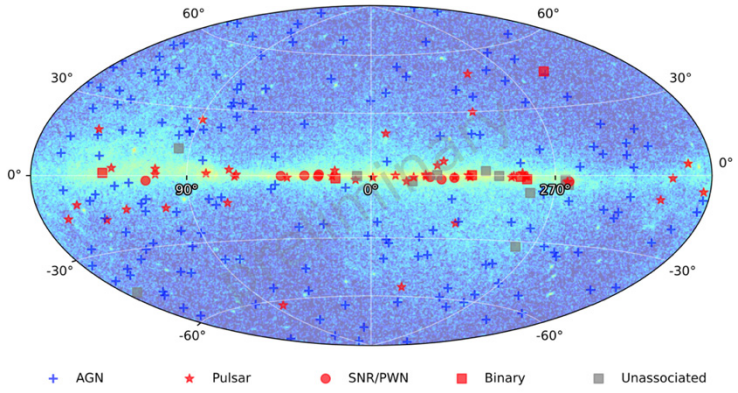

Source Type	Number
AGN	175
Pulsar	46
SNR/PWN	10
Binary	6
Unassociated	11
Total	248

Fig.9 Significant point sources (TS ≥ 25) detected in 7.2-yr DAMPE data [65]. The markers present the types of the associated sources. The numbers of different source types are listed in the right table

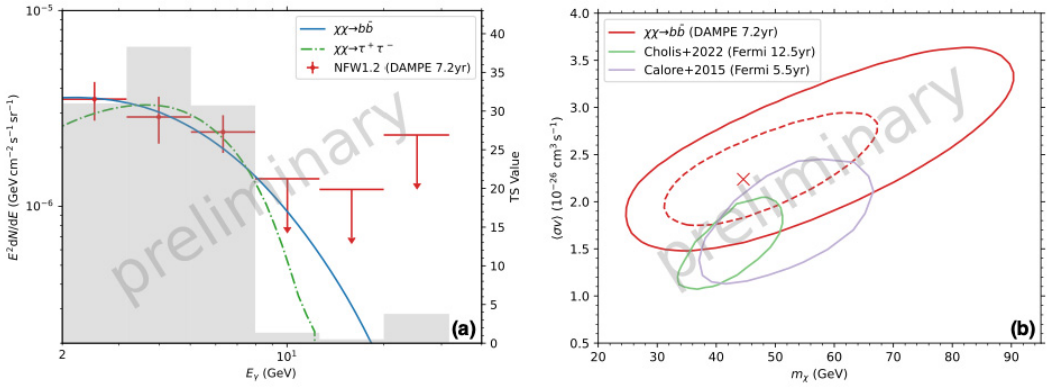

Fig.10 Preliminary spectral measurement of the Galactic center excess (GCE) by DAMPE (a) and the preferred DM parameter space for the annihilation channel $\chi\chi \to b\bar{b}$ (b)[68]

5 Summary

DAMPE has been operating smoothly in orbit for more than eight years. Based on the accumulated high-quality data recorded by DAMPE, multiple latest scientific results have been obtained, regarding CR physics, indirect DM detection and γ-ray astronomy. The precise measurements of the B/C and B/O ratios reveal a common spectral hardening at about 100 GeV/n with very high significances, which provides important implications in understanding the CR propagation. The latest measurements of the p+He spectrum up to 316 TeV suggest a hint of hardening structure at about 150 TeV for the first time in space. The FCP search provides the strictest restriction in space for the existence of FCP in primary cosmic rays. Benefiting from the unprecedented high energy resolution of DAMPE, the γ-ray line search achieves even stronger DM constraints for the lower limits on the decay lifetime below 100 GeV. In the near future, more scientific progresses from DAMPE are expected to shed new light on our understandings of DM and the high-energy Universe.

Acknowledgements

The DAMPE mission was funded by the strategic priority science and technology projects in space science of the Chinese Academy of Sciences.

References

[1] ADE P, AGHANIM N, ARNAUD M *et al*. (PLANCK collaboration), Planck 2015 results. XIII. Cosmological parameters[J]. Astron. Astrophys., 2016, 594: A13
[2] JUNGMAN G, KAMIONKOWSKI M, GRIEST K., Supersymmetric dark matter[J]. Phys. Rept., 1996, 267: 195-373
[3] BERTONE G, HOOPER D, SILK J. Particle dark matter: evidence, candidates and constraints[J]. Phys. Rept., 2005, 405: 279-390
[4] BI X J, YIN P F, YUAN Q. Status of dark matter detection[J]. Frontiers of Physics, 2013, 8: 794-827
[5] LI Z, LIU J. Experimental search for dark matter in China[J]. Frontiers of Physics, 2020, 15: 44301
[6] ADRINAN O,BARBARINO G, BAZILEVSKAYA G *et al*. (PAMELA collaboration). An anomalous positron abundance in cosmic rays with energies 1.5-100 GeV[J]. Nature, 2009, 458: 607-609
[7] ACKERMANN M, AJELLO M, ALLAFORT A *et al*. (Fermi-LAT collaboration). Measurement of separate cosmic ray electron and positron spectra with the Fermi Large Area Telescope[J]. Phys. Rev. Lett., 2012, 108: 011103
[8] AGUILAR M, ALBERTI G, ALPAT B *et al*. (AMS collaboration). First result from the Alpha Magnetic Spectrometer on the International Space Station: precision measurement of the positron fraction in primary cosmic rays of 0.5-350 GeV[J]. Phys. Rev. Lett., 2013, 110: 141102
[9] CHANG J, ADAMS J, AHN H S *et al*. (ATIC collaboration). An excess of cosmic ray electrons at energies of 300-800 GeV[J]. Nature, 2008, 456: 362-365
[10] ABDO A A, ACKERMANN M, AJELLO M *et al*. (Fermi-LAT collaboration). Measurement of the cosmic ray e++e- spectrum from 20 GeV to 1 TeV with the Fermi Large Area Telescope[J]. Phys. Rev. Lett., 2009, 102: 181101
[11] AGUILAR M, ALBERTI G, ALPAT B *et al*. (AMS collaboration). Precision measurements of the e++e- flux of the primary cosmic rays from 0.5 GeV to 1 TeV with the Alpha Magnetic Spectrometer on the International Space Station[J]. Phys. Rev. Lett., 2014, 113: 221102
[12] SHEN C S, Pulsars and Very High-Energy Cosmic-Ray Electrons [J]. Astrophys. J. Lett., 1970, 162: L181
[13] HOOPER D, BLASI P, SERPICO P D. Pulsars as the sources of high energy cosmic ray positrons[J]. J. Cosmol. Astropart. Phys., 2009, 1: 25
[14] YUKSEL H, KISTLER M D, STANEV T. TeV gamma rays from Geminga and the origin of the GeV positron excess[J]. Phys. Rev. Lett., 2009, 103: 051101
[15] BERGSTROM L, BRINGMANN T, EDSJO J. New positron spectral features from supersymmetric dark matter - a way to explain the PAMELA data?[J] Phys. Rev. D, 2008, 78: 103520
[16] CIRELLI M, KADASTIK M, RAIDAL M *et al*. Model- independent implications of the e+/–, pbar cosmic ray spectra on properties of dark matter [J]. Nucl. Phys. B, 2009, 813: 1-21
[17] YIN P F, YUAN Q, LIU J *et al*. PAMELA data and leptonically decaying dark matter[J]. Phys. Rev. D, 2009, 79: 023512
[18] ABEYSEKARA A U, ALBERT A, ALFARO R *et al*. (HAWC collaboration). Extended gamma-ray sources around pulsars constrain the origin of the positron flux at Earth[J]. Science, 2017, 358: 911-914
[19] HOOPER D, GOODENOUGH L. Dark matter annihilation in the Galactic center as seen by the Fermi gamma ray telescope[J]. Phys. Lett. B, 2011, 697: 412-428
[20] CUI M Y, YUAN Q, TSAI Y L S *et al*. Possible dark matter annihilation signal in the AMS-02 antiproton data[J]. Phys. Rev. Lett., 2017, 118: 191101
[21] CUOCO A, KRAMER M, KORSMEIER M. Novel dark matter constraints from antiprotons in light of AMS-02[J]. Phys. Rev. Lett., 2017, 118: 191102
[22] CHANG J. Dark Matter Particle Explorer: The First Chinese Cosmic Ray and Hard γ-ray Detector in Space[J]. Chin. J. Space Sci., 2014, 34: 550-557
[23] CHANG J, AMBROSI G, AN Q *et al*. (DAMPE collaboration). The dark matter particle explorer mission[J]. Astropart. Phys., 2017, 95: 6-24
[24] YU Y, SUN Z, SU H *et al*. The plastic scintillator detector for DAMPE [J]. Astropart. Phys., 2017, 94, 1-10
[25] AZZZARELLO P, AMBROSI G, ASFANDIYAROV R *et al*. The DAMPE silicon-tungsten tracker[J]. Nuclear Instruments and Methods in Physics Research A, 2016, 831: 378-384
[26] ZHANG Z, ZHANG Y, DONG J *et al*. Design of a high dynamic range photomultiplier base board for the BGO ECAL of DAMPE [J]. Nuclear Instruments and Methods in Physics Research A, 2015, 780: 21-26
[27] HE M, MA T, CHANG J *et al*. GEANT4 simulation of neutron detector for DAMPE[J]. Acta Astronomica Sinica, 2016, 57: 1-8
[28] AMBROSI G, AN Q, ASFANDIYAROV R *et al*. (DAMPE collaboration). The on-orbit calibration of dark matter particle explorer [J]. Astropart. Phys., 2019, 106, 18-34
[29] DONG T K, ZHANG Y, MA P *et al*. Charge measurement of cosmic ray nuclei with the plastic scintillator detector of DAMPE[J]. Astropart. Phys., 2019, 105: 31-36
[30] YUE C, ZANG J, DONG T *et al*. A parameterized energy correc-

tion method for electromagnetic showers in BGO-ECAL of DAMPE[J]. Nuclear Instruments and Methods in Physics Research A, 2017, 856: 11-16
[31] AMBROSI G, AN Q, ASFANDIYAROV R *et al*. (DAMPE collaboration). Direct detection of a break in the teraelectronvolt cosmic-ray spectrum of electrons and positrons[J]. Nature, 2017, 552: 63-66
[32] CHANG J. On the detection and identification of cosmic gamma-rays in a cosmic ray detector[J]. International Cosmic Ray Conference, 1999, 5: 37
[33] CHANG J, ADAMS J, AHN H *et al*. Resolving electrons from protons in ATIC[J]. Advances in Space Research, 2008, 42: 431-436
[34] HUANG Y Y, MA T, YUE C *et al*. Calibration and performance of the neutron detector onboard of the DAMPE mission[J]. Res. Astron. Astrophys., 2020, 20: 153
[35] DAMPE collaboration. Detection of spectral hardenings in cosmic-ray boron-to-carbon and boron-to-oxygen flux ratios with DAMPE[J]. Science Bulletin. 2022, 67: 2162–2166
[36] ZHANG S N *et al*. (HERD collaboration). The high energy cosmic-radiation detection (HERD) facility onboard China's Space Station[J]. Proc SPIE, 2014, 9144: 91440X
[37] ENGELMANN J J, FERRANDO P, SOUTOUL A *et al*. Charge composition and energy spectra of cosmic-ray nuclei for elements from Be to Ni - Results from HEAO-3-C2[J]. Astron. Astrophys., 1990, 233: 96
[38] SWORDY S P, MUELLER D, MEYER P *et al*. Relative bundances of secondary and primary cosmic rays at high energies[J]. Astrophys. J., 1990, 349: 625
[39] PANOV A D, SOKOLSKAYA N V, ADAMS J H *et al*. Relative abundances of cosmic ray nuclei B-C-N-O in the energy region from 10 GeV/n to 300 GeV/n - Results from ATIC-2 (the science flight of ATIC)[J]. International Cosmic Ray Conference 2008, 2: 3.
[40] AHN H S, ALLISON P S, BAGLIESIE M G *et al*. Measurements of cosmic-ray secondary nuclei at high energies with the first flight of the CREAM balloon-borne experiment[J]. Astropart. Phys., 2008, 30: 133.
[41] OBERMEIER A, AVE M, BOYLE P *et al*. Energy spectra of primary and secondary cosmic-ray nuclei measured with TRACER[J]. Astrophys. J., 2011, 742: 14.
[42] ADRIANI O, BARBARINO G C, BAZILEVSKAYA G A *et al*. Measurement of boron and carbon fluxes in cosmic rays with the PAMELA experiment[J]. Astrophys. J., 2014, 791: 93
[43] GREBENYUK V, KARMANOV D, KOVALEV I *et al*. Secondary cosmic rays in the NUCLEON space experiment[J]. Adv. Space. Res., 2019, 64: 2559.
[44] AGUILAR M *et al*. (AMS collaboration). The Alpha Magnetic Spectrometer (AMS) on the International Space Station: Part II - results from the first seven years[J]. Phys. Rep., 2021, 894:1.
[45] ALEMANNO F *et al*. (DAMPE collaboration). Measurement of the cosmic p+He energy spectrum from 46 GeV to 316 TeV with the DAMPE space mission[J]. arXiv: 2304.00137.
[46] AN Q, ASFANDIYAROV R, AZZARELLO P *et al*. (DAMPE collaboration). Measurement of the cosmic ray proton spectrum from 40 GeV to 100 TeV with the DAMPE satellite[J]. Sci. Adv., 2019, 5: eaax3793.
[47] ALEMANNO F *et al*. (DAMPE collaboration). Measurement of the Cosmic Ray Helium Energy Spectrum from 70 GeV to 80 TeV with the DAMPE Space Mission[J]. Phys. Rev. Lett., 2021, 126: 201102
[48] AHN H *et al*. (ATIC collaboration). The energy spectra of protons and helium measured with the ATIC experiment[J]. Adv. Space. Res., 2006, 37: 1950
[49] ATKIN E *et al*. (NUCLEON collaboration). First results of the cosmic ray NUCLEON experiment[J]. J. Cosmol. Astropart. Phys., 2017, 7: 20
[50] AHN H S *et al*. (CREAM collaboration). Discrepant hardening observed in cosmic-ray elemental spectra[J]. Astrophys. J. Lett., 2010, 714: L89
[51] BARTOLI B *et al*. (ARGO-YBJ collaboration, LHAASO collaboration). Knee of the cosmic hydrogen and helium spectrum below 1 PeV measured by ARGO-YBJ and a Cherenkov telescope of LHAASO[J]. Phys. Rev. D, 2015, 92: 092005
[52] ALBERT A *et al*. (HAWC collaboration). Cosmic ray spectrum of protons plus helium nuclei between 6 and 158 TeV from HAWC data [J]. Phys. Rev. D, 2022, 105: 063021
[53] ANTONI T *et al*. (KASCADE collaboration). KASCADE measurements of energy spectra for elemental groups of cosmic rays: Results and open problems[J]. Astropart. Phys., 2005, 24: 1
[54] AGLIETTA M *et al*. (MACRO collaboration and EAS-TOP collaboration). The cosmic ray proton, helium and CNO fluxes in the 100 TeV energy region from TeV muons and EAS atmospheric Cherenkov light observations of MACRO and EAS-TOP[J]. Astropart. Phys., 2005, 21: 223
[55] ALEMANNO F *et al*. (DAMPE collaboration). Search for relativistic fractionally charged particles in space[J]. Phys. Rev. D, 2022, 106: 063026
[56] SBARRA C *et al*. Search for Fractional Charges in Cosmic Rays with Ams[J]. arXiv: astro-ph/0304192
[57] FUKE H *et al*. Search for fractionally charged particles in cosmic rays with the BESS spectrometer[J]. Adv. Space Res., 2008, 41: 2050
[58] MORI M *et al*. Search for fractionally charged particles in Kamiokande II[J]. Phys. Rev. D, 1991, 43: 2843
[59] AGLIETTA M *et al*. Search for fractionally charged particles in the Mont Blanc LSD scintillation detector[J]. Astropart. Phys., 1994, 2: 29
[60] AMBROSIO M *et al*. Search for lightly ionizing particles with the MACRO detector[J]. Phys. Rev. D, 2000, 62: 052003
[61] AGNESE R *et al*. First Direct Limits on Lightly Ionizing Particles with Electric Charge Less than e/6[J]. Phys. Rev. Lett., 2015, 114: 111302
[62] ALVIS S L *et al*. First Limit on the Direct Detection of Lightly Ionizing Particles for Electric Charge as Low as e/1000 with the Majorana Demonstrator[J]. Phys. Rev. Lett., 2018, 120: 211804
[63] DAMPE collaboration and LIANG Y F. Search for gamma-ray spectral lines with the DArk Matter Particle Explorer[J]. Science Bulletin, 2022, 67: 679–684
[64] ACKERMANN M, AJELLO M, ALBERT A *et al*. Updated search for spectral lines from Galactic dark matter interactions with pass 8 data from the Fermi Large Area Telescope[J]. Phys. Rev. D., 2015, 91: 122002
[65] DUAN K K *et al*., Point-like source catalog observed by DAMPE [J]. Proc. ICRC, 2023, 670
[66] LI T P and Ma Y Q. Analysis methods for results in gamma-ray astronomy[J]. Astrophys. J., 1983, 272: 317
[67] Fermi-LAT collaboration. Incremental Fermi Large Area Telescope Fourth Source Catalog[J]. Astrophys. J. Suppl. Ser., 2022, 260: 53
[68] Shen Z Q *et al*. Analysis of the Galactic center excess with DAMPE[J]. Proc. ICRC, 2023, 671
[69] DAYLAN T, FINKBEINER D P, HOOPER D *et al*. The characterization of the gamma-ray signal from the central Milky Way: A case for annihilating dark matter[J]. Phys. Dark Univ., 2016, 12: 1
[70] CALORE F, CHOLIS I and WENIGER C. Background model systematics for the Fermi GeV excess[J]. J. Cosmol. Astropart. Phys., 2015, 2015: 038
[71] CHOLIS I, ZHONG Y M, MCDERMOTT SD *et al*. Return of the templates: Revisiting the Galactic Center excess with multimessenger observations[J]. Phys. Rev. D, 2022, 105: 103023

ZHANG Shu, ZHANG Shuangnan. Insight-HXMT Research Progress Since 2023. *Chinese Journal of Space Science*, 2024, **44**(4)

Insight-HXMT Research Progress Since 2023

ZHANG Shu, ZHANG Shuangnan

Key Laboratory for Particle Astrophysics, Institute of High Energy Physics, Chinese Academy of Sciences, Beijing 100049

Abstract

Since the launch in 2017 June, Insight-HXMT has been in service smoothly in orbit and particularly productive in 2023 and 2024. Among a total number of 238 papers published so far based on Insight-HXMT data, 63 were published in 2023, and 32 in the early 2024 (till 2024 April), accounting for 40% of the total. These studies cover a variety of scientific subjects including the basic properties of black holes and neutron stars, the outburst of accreting black holes and neutron X-ray binaries, thermal nuclear burst probes, isolated pulsars, quasi periodical oscillations, cyclotron resonant scattering features, fast radio bursts and gamma-ray bursts, *etc*. This paper introduces the overall progress with focus on some potential breakthroughs.

Key words

Insight-HXMT, Black hole, Neutron star, Outburst

1 Introduction

The Hard X-ray Modulation Telescope (HXMT) is China's first Chinese X-ray astronomy satellite and was launched in June 2017, dubbed as Insight-HXMT in memory of the Chinese scientist Prof. Zehui He. Insight-HXMT has already demonstrated itself with a large amount of important discoveries even during the early mission phase. Only after two months in orbit, Insight-HXMT joined the global campaign of observing the historical event of the first neutron star merging event GW 170817, and reported the strongest constraint on the flux limit at hard X-rays[1]. Insight-HXMT observed the outbursts of MAXI J1820+070 roughly nine months in orbit and of the first galactic Ultra Luminous Source (ULX) Swift J0243.6+6124 roughly three months in orbit, and obtained so far the unique data in high cadence monitoring of the outbursts of the two important sources. With these data, breakthroughs have been made on understanding Quasi Periodic Oscillations (QPOs), disk and jet properties; compared to the QPOs detected by other missions prior to Insight-HXMT, QPOs with the highest energy of about 250 keV was discovered during the long-lasting Low Hard State (LHS) of MAX J 1820+070[2] and, accordingly, a twisted jet scenario was first proposed. From the measurement of the evolution of the disk reflection feature, it was found that the jet moved outward acceleratively when its size contracts toward the central Black Hole (BH)[3]. The first observational evidence of radiation pressure dominated disk was obtained from the data of MAXI J0243.6+6124[4]. The most interesting result was obtained from Swift J0243.6+6124 five years after the outburst data were collected: during peak phase of the outburst, with a spin-phase-resolved analysis the highest energy of the Cyclotron Resonant Scattering Feature (CRSF) at 146 keV was detected from Swift J0243.6+6124 during peak phase of the outburst[5], compared to

Received June 20, 2024

the previous record of 80 keV from the data of GRO J1008-57 during the early Insight-HXMT mission phase[6]. As the time goes on, more important discoveries are kept being produced from either the Insight-HXMT data archive or the Insight-HXMT observations on the later activities of some compact objects. This paper summaries the latest results of the Insight-HXMT research progress conducted since 2023.

2 Instrument and Performance

There are three slat-collimated instruments onboard Insight-HXMT (Figure 1). HE consists of 18 NaI/CsI phoswich modules (main detectors) with a total geometrical area of about 5000 cm^2 in 20~250 keV. The Field of Views (FoVs) for HE are 1.1°×5.7° (for fifteen modules), 5.7°×5.7° for two modules, and one blind for measuring the background. ME takes 1728 Si-PIN pixels which cover an energy range of 5~30 keV with a total geometrical area of 952 cm^2. ME has FoVs of 4°×1°, 4°×4° and blind. LE adopts the swept charge device (SCD) as its detectors, which is sensitive in 1~15 keV with a total geometrical area of 384 cm^2. The FoVs of LE are 6°×1.6°; 6°×4°,60°×3° and blind. For the details of the three telescopes and the mission, please refer to Liu *et al.*[7], Cao *et al.*[8], Chen *et al.*[9] and Zhang *et al.*[10].

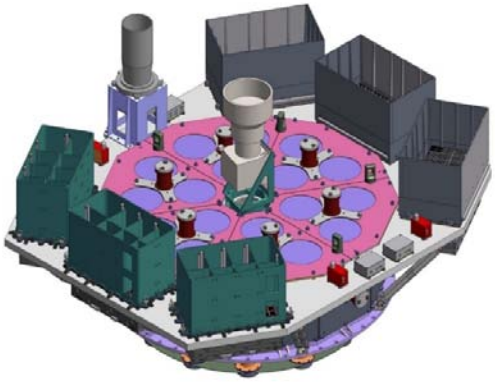

Fig.1 Insight-HXMT payload configuration

Insight-HXMT has been operating well since its launch in June 2017. During the last more than six years of operation, the altitude of Insight-HXMT orbit dropped by roughly 15 km, and two re-boosts were carried out in March and May 2023, respectively (Figure 2). All of the 18 HE modules work well and the detector elements dropped by 298 for ME and 7 for LE, accounting for 17% and 8% of the total numbers, respectively.

The Insight-HXMT telescopes were well calibrated

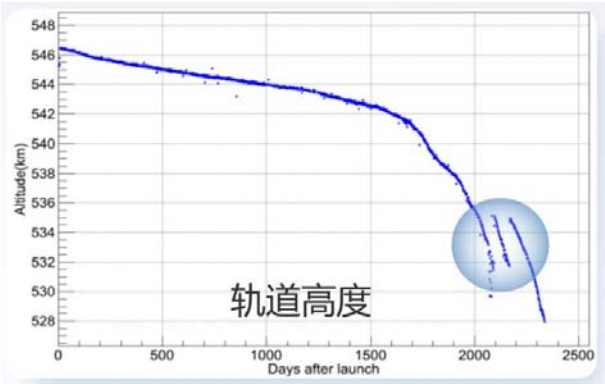

Fig.2 Maintenances of the orbit

on ground before launch. There are two calibration facilities built specially for the Insight-HXMT[11, 12, 13] (Figure 3), one in 15~100 keV built for HE, and one in 0.8~30 keV for ME and LE. For both the mono-energy X-ray beams are produced from the double crystal monochromators, with an intrinsic energy dispersion of roughly 0.1%~1%. The one for HE works in the air under room temperature, while the one for ME/LE is rather complex since supplementary devices like the vacuum chamber and cooling system have to be constructed to satisfy the working conditions of ME/LE.

After launch, Insight-HXMT has been being calibrated in orbit[14]. The annual calibration consumes about 5% exposure *via* observations of the Crab *etc*. and cross calibration campaigns with other contemporary space X-ray missions for timing and the instrumental response calibrations. Specifically, in 2023 with the dedicated work for subtle correction of the dead time, QPO detection significance can be moderately promoted[15].

The background models of Insight-HXMT are essential for producing reliable scientific results from the observed celestial sources. However, as a collimated telescope with configuration of different field of views, the background models are completely different from those adopted previously by the collimated telescopes, *e.g.* RXTE. The Insight-HXMT background models are built *via* frequently observing the blank sky, and by taking the advantage of having blind detectors for measuring the instantaneous particle background. The current background models are as precise as 2.1%, 1.6%, and 4.6% for HE, ME and LE, respectively, for a typical exposure[16]. In the meanwhile, background models were also developed for Insight-HXMT by following the traditional way adopted by the previous RXTE mission, used as the backup in case of losing the blind

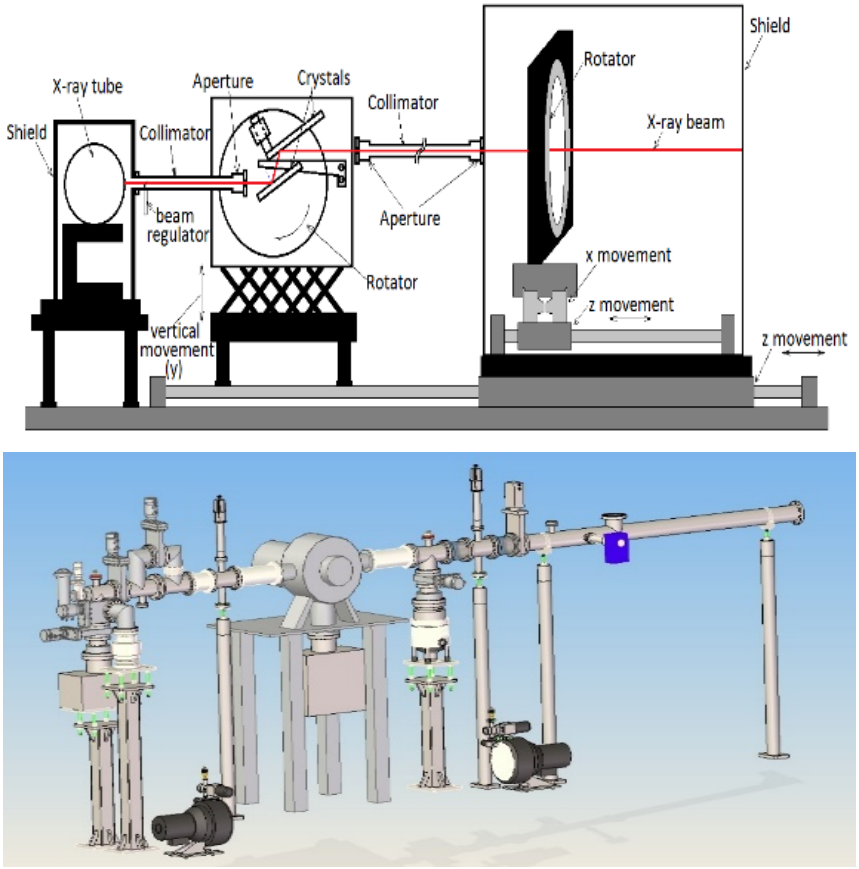

Fig.3 Ground calibration facilities implemented for HE at hard X-rays (upper) and for ME/LE at soft X-rays (lower)[12]

detectors[17]. The blank sky observations consume roughly 7% of the annual total exposure budget.

The scientific observations of Insight-HXMT are organized by the so-called Science Ground Segment (SGS), at the Institute of High Energy Physics (IHEP) of the Chinese Academy of Sciences (CAS)[13]. Insight-HXMT releases the Announcement of Opportunity (AO) annually to call for the proposals of the scientific observation for each year. It ran into AO 6 in 2023 with a total proposal number of 50. These proposals were submitted by users spreading over the whole world and, accordingly, Insight-HXMT long-term and short-term observational plans are constructed. Insight-HXMT can carry out a triggered Target of Opportunity (ToO) observation within five hours.

Data will be subjected to a proprietary period of one year for regular observations, three months for pre-approved ToOs, and none for *Ad Hoc* ToOs. SGS processes the raw data with the software developed for Insight-HXMT and produces the standard data products ready for the inputs of Heasoft, a common software maintained by NASA Heasarc for timing and spectral analyses. Please refer to the following links for the Insight-HXMT data archive, web page for proposal submission and Insight-HXMT analysis software: http://hxmten.ihep.ac.cn/.

3 Scientific Results

The core sciences of Insight-HXMT are: (1) Monitoring survey for more weak and short transient sources in a very wide energy band (1~250 keV); (2) High statistics study of bright sources and long-term high cadence monitoring of XRB outbursts; (3) All sky monitoring for GRBs and pulsars in 0.2~3 MeV. Accordingly, the corresponding observational modes are Galactic plane survey, pointed observation and GRB mode.

So far a total number of 238 papers have been published based on Insight-HXMT data, including 63 in 2023, and 32 in the early 2024. These studies cover a variety of scientific subjects, such as the basic properties of black holes and neutron stars, the outburst of accreting black holes and neutron X-ray binaries, thermal nuclear burst probes, isolated pulsars, quasi periodical

oscillations, cyclotron resonant scattering features, fast radio bursts and gamma-ray bursts, solar flares, terrestrial gamma-ray flashes, *etc*., as well as the instrumental performance.

3.1 Outburst of Black Hole X-ray Binaries

A Black Hole X-ray Binary (BHXRB) consists of a BH as the compact object and a stellar star as the companion. The accretion matter overflows through the Roche robe and forms an accretion disk around the BH. The instability of the accumulated matter can lead to ionization of the outer part of the disk and thus causes an outburst: the matter moves inward *via* transforming the angular momentum outward through viscosity that heats the gas to radiate away part of the gravitational power in X-rays in the vicinity of the BH. An outburst behaves a variety of observational features in both the temporal and spectral domains. Usually, the outburst will start with a LHS, and evolves through a Hard Intermediate State (HIMS), a Soft Intermediate State (SIMS), a High Soft State (HSS) and finally returns to a LHS again but at a luminosity level lower than the initial LHS, forming the so-called hysteresis in a typical q shape in the Hardness-Intensity Diagram (HID). Low Frequency Quasi Periodic Oscillations (LFQPOs) usually show up in the LHS and HIMS (type-C QPO) and SIMS (type-B and type-A QPO).

Since the X-rays are released at the inner most region of the accretion disk where the strong gravitational field takes effect, the outbursts of BHXRBs are regarded as one of the ideal labs to test the General Relativity (GR). Testing the fundamental theories of GR under the extremes of gravity is the key objective of the future mission eXTP (enhanced X-ray Timing and Polarimetry Mission) beyond Insight-HXMT. As we know, BHXRB outburst evolution is generally believed as the changing balance between thermal emission from the disk and the non-thermal emission from either the hot corona or moderately relativistic jet. Obviously, to better understand such labs, one has to perform sufficient high cadence observations of the outbursts and investigate in much more details at least the basic properties of each of the key elements (disk, corona, jet, and magnetic field *etc*.) and the roles they play in governing the outburst evolution.

MAXI J1820+070 underwent a huge outburst in 2018. In the late decay phase of this outburst, You *et al*.[18] found the most direct evidence for the existence of the so-called magnetic arrested disk (MAD), a phenomena theoretically predicted long time ago. The joint Insight-HXMT, radio and optical observations show the unprecedented long-term time lags of the latter with respect to the X-rays. This reveals for the first time the observational evidence of magnetic transportation within the accretion flow, and as well the whole process of forming a MAD (Figure 4).

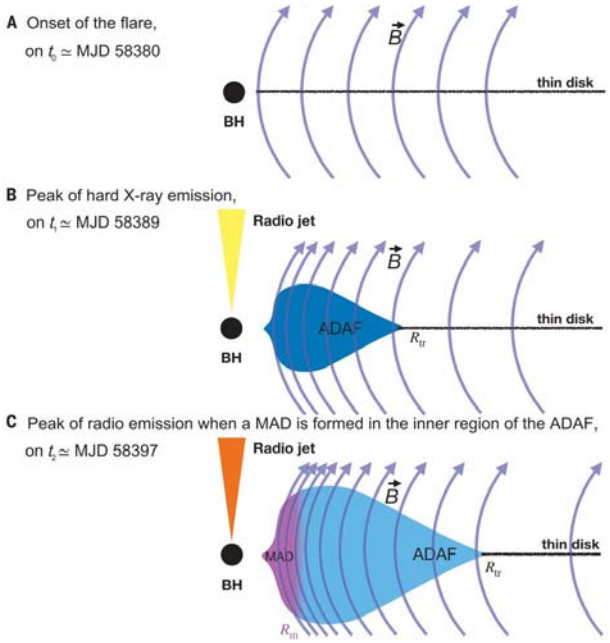

Fig.4 MAD discovered during the decay phase of MAXI J1820+030[18]

The spectral and temporal properties of the black hole X-ray transient binary MAXI J1820+070 during the 2018 outburst are studied systematically with Insight-HXMT observations. The outburst of MAXI J1820+070 can be divided into three intervals. For the two intervals of the outburst, we find that low-energy (below 140 keV) photons lag high-energy (140~170 keV) ones, while in the decay of the outburst, high-energy photons lag low-energy photons, both with a time-scale of the order of days. Based on these results, the canonical hysteresis effect of the “q” shape in the HID can be reformed into a roughly linear shape by considering the lag corrections between different energy bands (Figure 5). Timing analysis shows that the high-frequency break of hard X-rays, derived from the power-density spectrum of the first interval of the outburst, is in general higher and more variable than that of soft X-rays. The spectral fitting shows that the coverage fraction of the hard X-rays drops sharply at the beginning of the

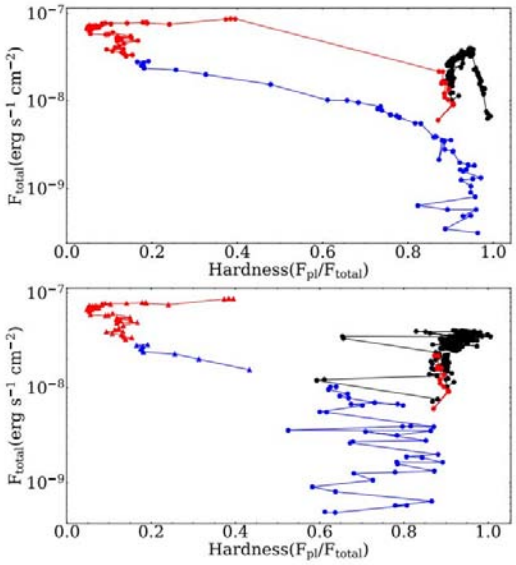

Fig.5 HID modification by accounting for the lag corrections between different energy bands for the outburst of MAXI J1820+070[19]

outburst to about 0.5, and then increases slightly. The coverage fraction drops to roughly zero once the source steps into the soft state and increases gradually to unity when the source returns to the low-hard state. These provide a possible overall scenario for the outburst evolution of MAXI J1820+070 revealed by Insight-HXMT[19].

Further investigations on the 2018 outburst of MAXI J1820+070 bring us more interesting results. By introducing a scenario that the inner part of the disk provides variability of the soft seed photons, which feed into the outer part of the hot corona and results in the soft comptonization, and the inner part of the hot corona provides the hard Comptonization with the local seed photons, the energy spectrum, power spectrum and the time lag spectrum are jointly fitted[20]. As shown in Figure 6, the joint fit cannot reproduce the data at energies above 50 keV, suggesting the necessity of introducing an additional component, *e.g.*, a jet to account for the emission at the high energy part. A complicated corona structure is also indicated in Wang *et al.*[21] in their study of the correlation between noise rms and flux: they found that along with the decay during the initial LHS, apart from a slab one, a vertical corona emerged and continuously expanded.

The black hole candidate system SLX 1746-331 was back to business in 2023, after a long silence of roughly 13 years. An outburst was observed thoroughly by Insight-HXMT and NICER. The outburst is characterized by spectral dominance of the soft state, where the joint Insight-HXMT and NICER spectral analysis shows the temperature dependence of the disk flux follows aboutT^4 and thus suggests that the inner disk reached to the Inner Most Stable Orbit (ISCO) during almost the entire outburst[22, 23] (Figure 7). No low hard state and intermediate states may mean the disk evaporation is very low during the entire outburst. The 2023 outburst of SLX 1746-331 differs from those of normal black hole transient X-ray binaries in their evolution patterns in HID: instead of a low-hard state toward a soft state, SLX 1746-331 stayed around the ISCO during the whole outburst. Although such an outburst phenomenon is relatively rare, we notice that so far a similar case was also observed in the outburst of another black hole X-ray binary system MAXI J0637-430[24]. Peng *et al.*[22] compared SLX 1746-331 with MAXI J0637-430, and suggested that such peculiar outburst could be related to the special configuration of the binary system. Unlike MAXI J0637-430, which had a peak luminosity of about 0.08 L_{Edd} and a soft-to-hard transition at about 0.007 L_{Edd}, SLX 1746-331 remains in the soft state, with no state transition observed even at a luminosity <500 times lower than the peak luminosity of the outburst.

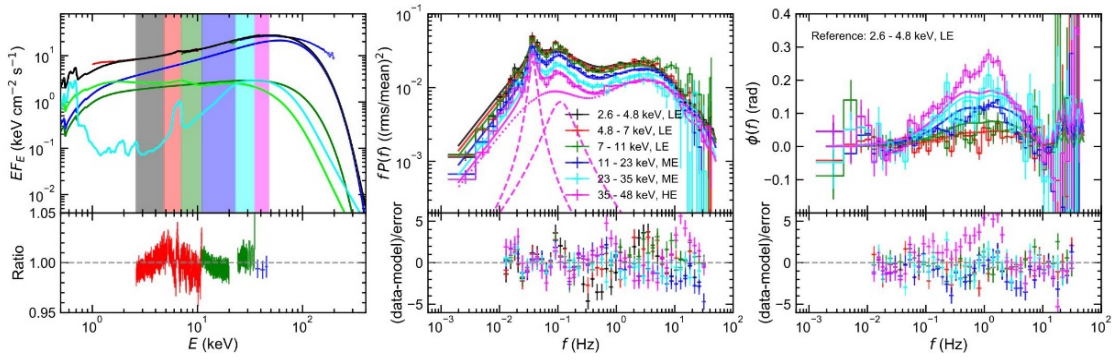

Fig.6 Joint fits to she spectra in energy, frequency and time lag domains for the outburst of MAXI J1820+070[20]

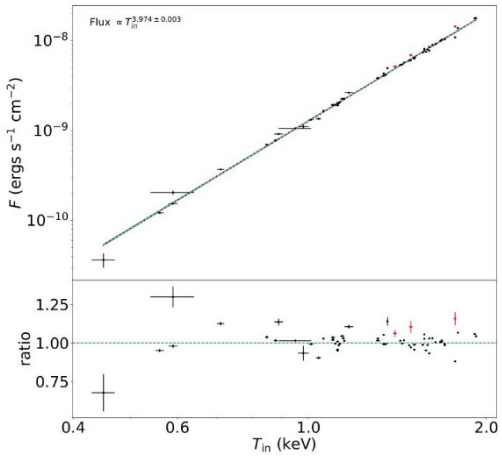

Fig.7 A standard accretion disk exists during the whole outburst of SLX 1746-331[23]

Swift J1727.8-1613 is a black hole X-ray binary newly discovered in 2023. The joint Insight-HXMT, NICER and NuSTAR observations during LHS reveal an additional hard component apart from the normally observed hard component with reflection in the spectrum, indicating a distinguished outburst of Swift J1727.8-1613. A hybrid jet/corona configuration is adopted to account for the spectral fitting with different model trials[25] (Figure 8).

The latest results from Insight-HXMT observations of the outbursts from MAXI J1348-630 in 2019, GRS 1915+105 in 2017–2021, MAXI J1535-571 in 2017, 4U 1543-47 in 2021 also bring us interesting findings. Analysis of the joint NuSTAR and Insight-HXMT observations of the reflare 4 months later than the major outburst of MAXI J1348-630 in 2019 shows the disk-corona behavior at low Eddington luminosity: it seems that there exists a critical luminosity to govern the balance between heating up the corona and forming a disk which needs efficient transfer of the angular momentum outward *via* viscosity[26]. Yu *et al.* performed a spectral-timing study of the inner flow geometry in MAXI J1535-571 during an outburst observed with Insight-HXMT and NICER in 2017[27]. The reverberation mapping shows that the soft lag evolves to about zero at a specific frequency, which might denote the connection point between the inner disk and the corona. Thus, the evolution of such frequency can serve as a new viewer on if the inner disk is truncated during the outburst. The outburst of 4U 1543-47 in 2021 serves as a nice example for investigation of the accretion disk at luminosity around Eddington level. The analyses carried out by Zhao *et al.*[28] based on the joint Insight-HXMT and NuSTAR observations result in a self-irradiation inner disk, highly consistent with the theoretical prediction of having a slim disk under a high accretion rate. The same outburst was also studied by Jin *et al.*[29] but with focus on the decay phase based on only the Insight-HXMT high cadence observations. It turns out that the source can experience a state transition to LHS at luminosity around Eddington limit and the aforementioned self-disk-illumination feature disappeared after the state transition, thus proofs the possibility for existence of a LHS at an accretion rate of as high as around Eddington limit. The exploration of the timing and spectral properties of GRS 1915+105 based on X-ray observations of NICER and Insight-HXMT during the long outburst from 2017 to 2021 revealed new class of variability in the rising stage of the outburst that differs from the previously reported patterns of light curves, which helps to understand the class transition mechanism in GRS 1915+105[30].

3.2 Black Hole Mass and Spin

As a peculiar theoretical singularity BH can be probed

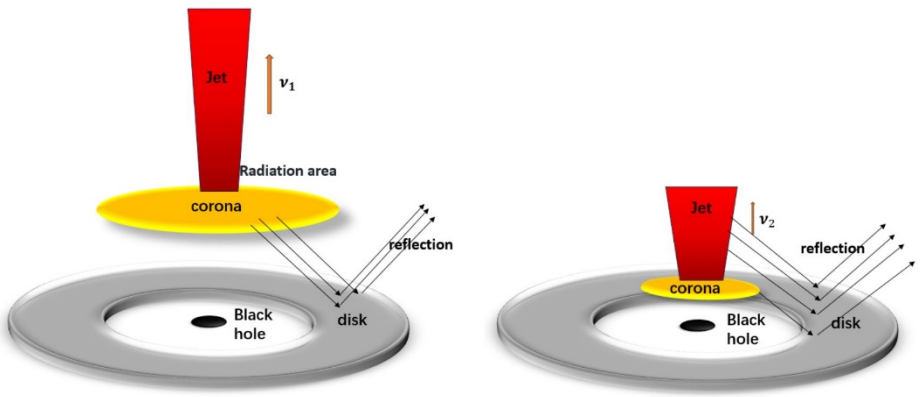

Fig.8 A hybrid jet/corona scenario introduced to the outburst evolution of Swift J1727.8-1613[25]

with only two observables of mass and spin. The interests in the measurements of BH spin and mass are not only about understanding BH, but also relevant to the evolution of the stars in their processes of collapsing into BHs and probably as well the formation and evolution of the X-ray binary systems. The Gravitational Wave (GW) experiments measure the BH masses *via* observing the GW from the compact merger events, and put forward a new puzzle regarding to the BH mass distribution (Figure 9): it seems that there exists a mass gap of 2.5~5 solar mass where only two GW-detected BHs and one XRB system GRO J0422+32 are currently in, which is not consistent with the theoretical expectations of either having a lot or none[31]. To solve this problem, Gao *et al.*[32] proposed a scenario that, with specific system configuration, a neutron star hosted in a Pulsating Ultra-Luminous X-ray (PULX) source can grow up in mass *via* accreting the material from the companion in a super-Eddington manner and finally turns into BH with relatively small mass. Such a theory is supported by the Insight-HXMT discovery of the highest CRSF line at 146 keV[5] which in turn proves that the PULX should really have an accretion rate beyond Eddington limit. Here we find that one more BH candidate may fall into this mass gap: the outburst from SLX 1746-331 was observed by Insight-HXMT to keep in disk-dominated state covering a luminosity range roughly 500 times lower than the maximum, wider than the canonical 0.001~0.3 Eddington ratio and thus results in a reasonable assumption for the peak flux of the outburst around 0.3% Eddington ratio. From fitting the reflection component with the joint Insight-HXMT and NuSTAR observations, the BH spin is first measured as 0.85±0.03 and an inclination angle can be constrained as 53°±0.5°. With a distance of 10.81 ± 3.52 kpc measured by Yan *et al.* with an outburst samples[33], the BH mass is estimated as 5.5 ± 3.6$M_{\odot}$ for SLX 1746-331[22] which, albeit with relatively large error bar inherited from the larger uncertainty in distance, is consistent with 5.2 ± 4.5$M_{\odot}$ obtained from the empirical correlation between the disk peak temperature and BH mass established from a sample BH outburst[22] (Figure 10). We notice that SLX 1746-331 shares similar characters with MAXI J0637-430 in aspects that their outbursts are short of the clear spectral states prior to HSS and dominated by disk emissions at rather low accretion rates[34]. Interestingly, the BH mass was measured as 5.1 ± 1.6 $M_{\odot}$ for MAXI J0637-430, and thus makes MAXI J0637-430 another candidate with a small BH mass falling into the BH mass gap. The peculiar outburst behaviors of SLX 1746-331 and MAXI J0637-430 require the systems have rather small accretion disks, which is in line with the small BH mass held by these systems and as well so far the shortest orbital period of 2.2. hours reported in MAXI J0637-430[35]. We speculate that both sources may constitute low mass BHs in the BH ZOO (Figure 11).

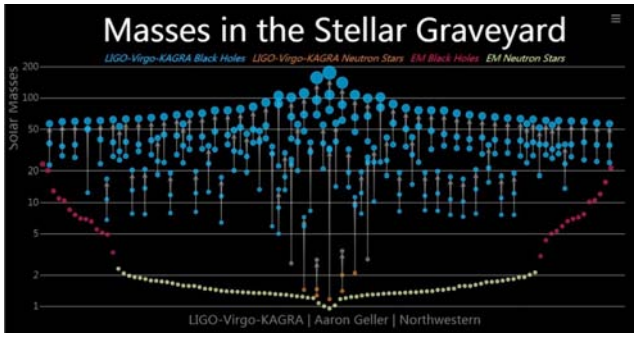

Fig.9 The mass gap puzzle

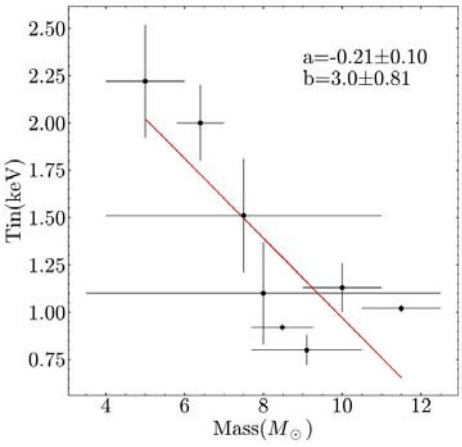

Fig.10 BH mass estimated from an empirical correlation between disk temperature and BH mass from a BH outburst sample[22]

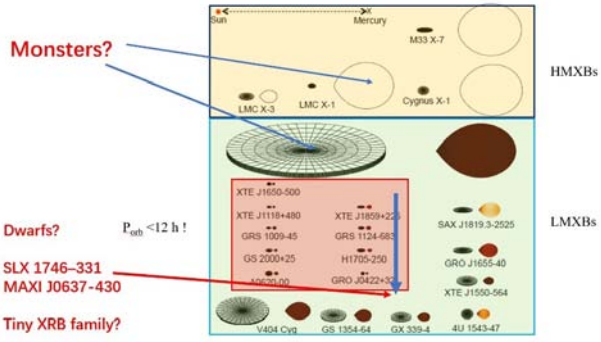

Fig.11 The BH zoo

Since 2023 more BH spins have been measured by Insight-HXMT with the canonical methods of disentangling disk reflection component in energy spectrum or fitting the continuum dominated by the standard disk emission, under assumption that the inner disk stays around the ISCO. MAXI J1348-630 was discovered by the MAXI/GSC instrument during the outburst in 2019, and the follow-up observations from Insight-HXMT covered the spectral states from LHS to HSS. Song *et al.*[36] analyzed the Insight-HXMT data with the reflection models and found that a moderate spin of $0.82^{+0.04}_{-0.03}$ can be derived in all the spectral states covered by Insight-HMXT observations. Wu *et al.*[37] instead took the continuum-fitting method to estimate the BH spin with the Insight-HXMT HSS data, and reported a BH spin of $0.42^{+0.13}_{-0.50}$, significantly lower than that derived by the disk-reflection method. Interestingly, BH spin was reported as $0.78^{+0.04}_{-0.04}$ with NuSTAR data[38] and 0.80±0.02 with NICER data[39], by adopting the methods of reflection and continuum fitting, respectively. Although the source of the discrepancies for measurements of the BH spin with different methods remains unclear, it is probably due to the different ways the spin estimation is made: based on the GR effect on the broadened iron line or purely the ISCO radius. Obviously, the latter is highly dependent on the precisions of the input parameters of BH mass, system distance and disk inclination angle, which may cause the differences in BH spin estimation with NICER or Insight-HXMT observations. 4U 1543-47 is another example that previous spin measurements are largely inconsistent with each other. 4U 1543-47 underwent a huge outburst in 2021, reaching a peak intensity of about 9 Crab. By taking the Insight-HXMT observations with the source luminosity staying within f about 0.28~0.31 $L_{\rm Edd}$, and the state-of-art parameters of BH mass, distance and inclination angle, Chen *et al.*[40] reported a BH spin of 0.46 ± 0.12. Since most part of the outburst exceeded the thin-disk luminosity limit, Yorgancioglu *et al.*[41] picked up the Insight-HXMT and NICER observations dominated by the disk thermal emission with a low/stable disk inner radius, which end up with a dataset covering luminosity up to about 1 $L_{\rm Edd}$. They instead tried for the first time a slim disk model to account for the continuum disk emission and derived an overall BH spin of $0.65^{+0.14}_{-0.24}$, roughly consistent with that reported by Chen *et al.*[40].

3.3 Quasi Periodic Oscillation

QPOs remain a puzzle since its discovery in the last century, although the previous RXTE telescope has accumulated great amount detections for QPOs of different types. The LFQPOs, subdivided into type-C, type-B and type-A, mainly reside in the initial different spectral states of the BH outbursts on their ways entering into the HSS. The current popular models on the LFQPOs are either the pure geometry effect, caused by the relativistic Lense-Thirring (LT) procession of the inner disk, corona or jet due to the frame dragging effect for a BH system where the BH spin is not aligned with the disk[42], or the intrinsic properties of the accretion flow. The latter concerns the instability of the accretion rate and includes trapped corrugation modes[43], the accretion-ejection instability model[44], and the two-component advection flow model[45], *etc*. However, none of them can fully account for all the properties discovered so far for the LFQPOs. Obviously, a breakthrough requires further observational clues in at least the following aspects: (1) QPO phase-resolved spectrum; (2) the QPO properties beyond the energy limit of RXTE around 30 keV; (3) QPO phase-resolved polarization, and probably as well others that cannot be foreseen at the moment.

Recovering the QPO waveform is a tough task and thus carrying out QPO phase-resolved spectral analysis is extremely difficult, due to that QPO in definition is a phenomenon of a rather broad peak component showing up in the power spectrum, which means that it covers a series of frequencies. The early effort of recovering the QPO waveform and the QPO phase-resolved analysis was performed by Ingram & van der Klis[46] using the statistical phase difference of QPO between the fundamental and harmonic components. This Fourier method, as will be discussed later, depends on the existence of an obvious harmonic component and handle the QPO phases in a statistically averaged way. An empirically chosen peak and trough of QPO in a specific light curve during the hard state of the bright outburst from MAXI J1820+030 revealed that the spectral difference between the peak and trough phases[47]. The wavelet technique was also tried on the LHS of the MAXI J1820+030 outburst, and found that the QPOs have an averaged lifetime of around 5 oscillation cycles[48] (Figure12).

As a non-traditional temporal analysis technique, Hilbert–Huang Transform (HHT)[49] is a powerful tool

for analyzing phenomena with nonstationary periodicity and has been successfully applied in astronomical research. HHT enables us to not only trace the variation in frequency in the QPO but also to process phase-resolved analyses even though the periodicity is unstable. HHT consists of two main components: mode decomposition and Hilbert Spectral Analysis (HSA). The mode decomposition aims to decompose a time series into several Intrinsic Mode Functions (IMFs), while the HSA allows obtaining both the frequency and phase functions of the desired IMFs, such as the QPO component. Shui *et al.*[50] replaced the original Empirical Mode Decomposition (EMD) proposed by Huang *et al.*[49], which directly operates in the temporal space and adaptively decomposes the input signal into several IMFs, with a novel Variational Mode Decomposition (VMD) that surpasses traditional decomposition approaches such as EMD[51]. By employing the HHT method, Shui *et al.*[50] extracted the intrinsic QPO variability, and obtained the corresponding instantaneous amplitude, phase, and frequency functions for each data point. With well-defined phases, the QPO waveforms and phase-resolved spectra are constructed. By comparing the phase-folded waveform with that obtained from the Fourier method adopted in Ingram & van der Klis[46], they found that phase folded on the phase of the QPO fundamental frequency leads to a slight reduction in the contribution of the harmonic component (Figure 13). This suggests that the phase difference between QPO harmonics exhibits time variability. Phase resolved spectral analysis reveals strong concurrent modulations of the spectral index and flux across the bright hard state (Figure 14). The modulation of the spectral index could potentially be explained by both the corona and jet precession models, with the latter requiring efficient acceleration within the jet. Furthermore, significant modulations in the reflection fraction are detected exclusively during the later stages of the bright hard state. These findings provide support for the geometric origin of LFQPOs and offer valuable insights into the evolution of the accretion geometry during the outburst in MAXI J1820+070.

QPO signals at energies above 30 keV are one of the major discoveries from BHXRB outbursts observed by Insight-HXMT. For MAXI J1820+070 the large detection area of CsI onboard Insight-HXMT allows for the QPO detection up to energies around 250 keV with a traditional FFT analysis tool[2]. As demonstrated in Shui *et al.*[52], with a HHT technique QPO waveform can be reconstructed at even high energies. An example to demonstrate such power is the recovery of the QPO

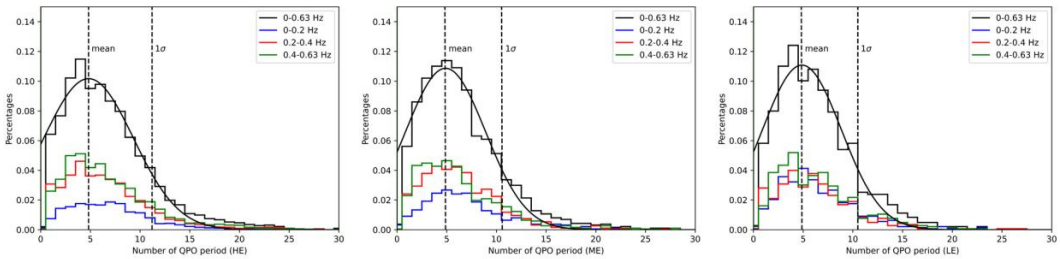

Fig.12 QPO lifetime distribution over all the March to June 2018 Insight-HXMT observations in units of cycles[48]

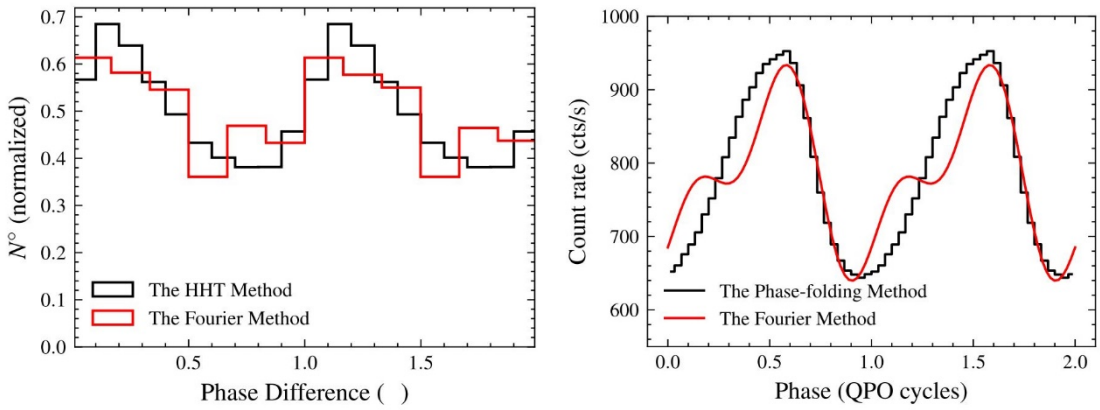

Fig.13 Left: histogram of measured values of the phase difference between harmonics obtained using the HHT (black) and Fourier (red) methods. To show a clear peak, we repeat the data from 0 to π. Right: reconstructed QPO waveform derived from the HHT phase-folding (black) and Fourier (red) methods[50]

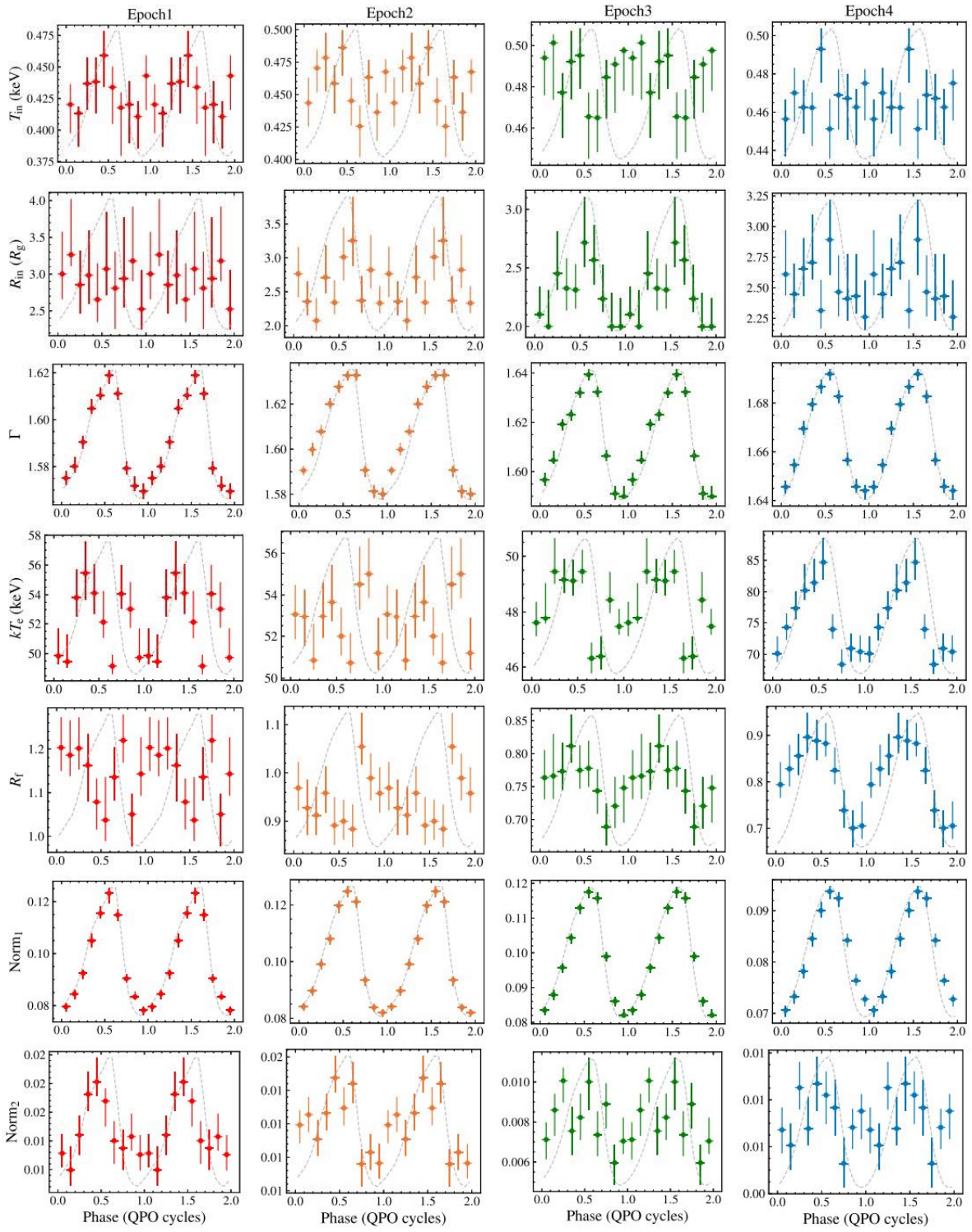

Fig.14 Phase dependence of the seven free spectral parameters, including the temperature of the inner radius of the disk (T_{in}), inner radius (R_{in}), spectral index (Γ), electron temperature (kT_e), reflection fraction (R_f), and the normalization of relxillCp (Norm1) and xillverCp (Norm2), across the four epochs[50]

waveform for MAXI J1535-571 with HHT at energies above 170 keV (Figure 15), significantly higher than 100 keV reported for the same Insight-HXMT data but with a traditional Fourier method[53]. Although QPO in polarimetry view goes beyond the scope of this paper since it is probed by IXPE but not Insight-HXMT, recent IXPE/NICER investigation on the phase-resolved QPO polarization from the outburst of Swift

J1727.8-1613, with HHT technique developed by Shui *et al.*[50], revealed polarization degree lower than the predication of LT procession model[54].

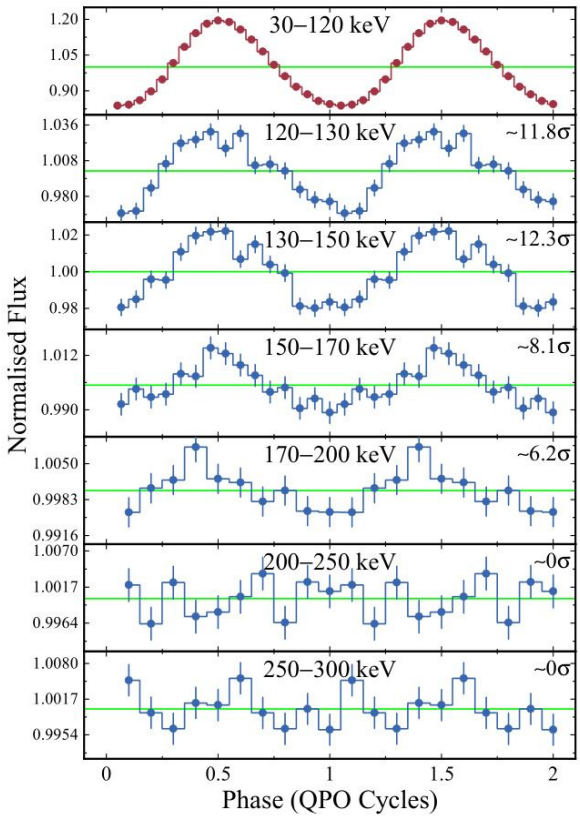

Fig.15 HHT phase-folded QPO waveforms of MAXI J1535-571 from Insight-HXMT/HE light curves[52]

The other QPO research progresses from Insight-HXMT since 2023 are listed as follows. A thorough timing analysis was carried out by Yu *et al.*[55] based on the Insight-HXMT observations of the outburst from Swift J1727.8-1613. Apart from the canonical type-C QPOs they found the peaked noise oscillation which correlates with the LFQPO in a manner of Psaltis-Belloni-van der Klis (PBK) relationship[56]. This finding helps to diagnostic the QPO origin in the context of investigating the instability in a rather broad frequency range. They also took the HHT technique to investigate the QPO time lags in the outburst of MAXI J1820+070 and got results consistent with Ma *et al.* who estimated the QPO time lag by subtracting off the underlined noise contribution in the cross spectrum[2,57]. Ma *et al.* supplemented their previous QPO report based purely on the Insight-HXMT observations of the MAXI J1820+070 outburst by enclosing as well the contemporary NICER observations at soft X-rays, and found that a twisted jet scenario still holds[58]. Timing analysis of the new black hole candidate MAXI J1803-298 with Insight-HXMT and NICER revealed type-C and type-B QPOs[59]. While the rms and time lag behaviors of type-C QPO can be understood in LT precession model, those for type-B are rather peculiar which may be explained with a dual-corona model. The fast transitions of X-ray variability in the black hole transient GX 339–4 was compared with MAXI J1820+070 and MAXI J1348-630 by Yang *et al.*[60]. They found transitions between band-limited noise-dominated PDS and type-B QPOs, accompanied with rapid appearance or disappearance. A detailed comparison between the fast transitions in GX 339-4 with those seen in MAXI J1820+070 and MAXI J1348-630 was conducted. They argued that there may exist possible change of the geometry of the inner accretion flow and/or jet during the transitions. QPOs in GX 339-4 during the 2021 outburst observed with Insight-HXMT were also studied by Jin *et al.*[61]. They reported the first findings of the type-C QPOs and their rms/time-lag properties during state transitions from LHS to HIMS. The bicoherence can be used to measure the phase coupling at different Fourier frequencies. With this technique, Ding *et al.*[62] presented the timing analysis of the nonlinear variability in two BHXRBs MAXI J1820 +070 and MAXI J1535-571. They found the different patterns, *e.g.*, “cross” and “hypotenuse”, for LFQPOs in different outburst states can be shared to some extent with the type-C and type-B QPOs. Thus, they suggested that different types of QPOs may originate from similar underlying mechanisms and the nonlinear variability may be a promising approach to disentangle different QPO models which assume different interactions between the broadband noise and QPO components.

While the QPOs are relatively rare in outburst of the accretion NSXRB systems, unlike those showing up in BHXRBs which suffer from degeneracy in models of geometric and accretion instability, it is generally the consensus that QPOs in accretion pulsar NSXRBs can inherit the information of the accretion instability in the inner region of the accretion disk. Progresses made in this aspect come from Li *et al.* in their studies on the outbursts from two accreting pulsar systems RX J0440.9+4431 and MAXI J1816-195[63,64]. A strong 2.5 Hz periodic oscillation was detected from the newly

discovered accretion millisecond pulsar MAXI J1816-195, which is likely attributed to an unstable corona[63]. The timing analysis on the Be/X-ray binary pulsar RX J0440.9+4431 using observations from NICER and Insight-HXMT during the 2022–2023 outburst resulted in discover of QPOs at 0.2~0.5 Hz, characterized with the accompanied short flares. Again, they argued that the origin of QPOs is related to the instabilities within the accretion flow[64].

3.4 Outburst of Neutron Star X-ray Binaries

The X-ray outbursts caused by matter accreted to the NSs can be classified into two categories: high mass and low mass XRBs. In high mass XRBs the accretion matters are channeled by their strong magnetic field lines onto the magnetic poles of NSs, forming the so-called Accretion-Powered Pulsars (APP). In low mass XRBs, typically observed as Atoll and Z sources, the accretion matters are accreted on the entire surfaces of NSs, behaving persistent emission for Z sources, and outbursts resembling BHXRB but with only the Island (hard) and banana (soft) states for Atoll sources. Because of such similarity, the type-I burst of the thermal nuclear burning on the surface of a NS provides a nice probe into the accretion environment surrounding the NS during the outbursts, and the research progresses will be introduced in the following section of “burst probe”. Thus, here we mainly focus on the outbursts observed by Insight-HXMT in APP systems.

One major interest regarding to the outbursts from APP systems is the region around the co-rotation radius, where the angular velocity of accretion matter controlled by the magnetic field of the NS becomes comparable to that of Keplerian velocity maintained by the gravitational force of the NS. The angular velocity of the former depends on the NS spin and hence is independent of the magnetic radius which can be compressed by the accretion matter. At radius beyond the co-rotation one the accretion will in principle be stopped *via* the propeller effect, and otherwise an outburst usually shows up *via* releasing the gravitational power at the magnetic poles, along with the inner part of a truncated disk located always around the co-rotation radius. Therefore, the instability inherited around this particular region will leave footprint in its temporal behaviors for emissions observed around the magnetic poles. For example, the early Insight-HXMT reported a transition from gas to radiation dominated disk emissions form the first Galactic ULX Swift J0243.6+6124[4], mainly based on the detection of two breaks in the power spectrum. The QPO features, as introduced in the last section, detected by Insight-HXMT in the outbursts from the accreting millisecond pulsar MAXI J1816-195 and Be APP system RXJ0440.9+4431 strengthen again that the intrinsic temporal features as observed around the magnetic poles are highly relevant to the instability for the accretion flow residing outside of the NS magnetosphere[63,64].

The other major interest regarding to the outbursts from APP systems is the region around the magnetic poles, where the gravitational power is released and radiates away mainly in X-rays. The general consensus on the physical process in this region is that, the accretion matter channeled to the top of the NS surface can form a shock due to either the local radiation pressure at high luminosity or the gas pressure at low accretion rate. In the former case, the accretion matter heated by the shock will sink toward the NS surface and forms an accretion column, where the emission is released manly from the lateral side of the column in a so-called fan-mode. The hot materials will be cooled *via* inverse Compton scatterings off the seed photons from either outside of the column or the internal synchrotron emissions on their way settling on the NS surface. In case of low accretion rate, a pencil mode is foreseen, where the shocked materials will heat directly the NS magnetic poles and radiate away along the magnetic file lines. However, a great amount of the details is still in debate. For example, in which region of the column do the hard X-rays come from? Is the height of column comparable to its base where a hot spot is expected to exist? How does the emission region evolve from fan to pencil mode? What will happen in case of the co-existence of both dipole and multipole magnetic fields? Are the emissions from PULX systems beamed or intrinsic? To answer these questions, one needs thorough observational information in both the energy and time domains. To this end one of the key parameters is the critical luminosities under which the transitions between different modes occur. Previous results obtained by Kong *et al.*[65] with Insight-HXMT observations of the outburst from the PULX Swift J0243.6+6124 present the first complete sample to describe how the spectral parameters evolve within a wide scope of luminosity. The critical luminosity responsible for the mode transition to fan-mode turns out consistent with a strong magnetic

field discovered by the detected CRSF with a centroid energy as high as 146 keV[5].

The latest results from Insight-HXMT about this ULX come from the investigation of the pulsed iron line[66]. The phase-resolved spectral results show, for the first time, the pulsed characteristics of the broad iron line in a PULX Swift J0243.6+6124. The variation in the width and intensity of this iron line has a phase offset of about 0.25 from the pulse phase. They suggest that the uneven irradiation of the thick inner disk by the accretion column produces the modulated variation of the broad iron line. In addition, the non-pulsed narrow line is suggested to come from the outer disk region (Figure 16)[66]. 1A 0535+262 is another example with the high cadence observations of Insight-HXMT during a huge outburst in 2020. The latest results about this outburst come from the investigation of the beam pattern by Hu *et al.*[67] and a deep search in gamma-ray with Fermi gamma-ray observatory by Hou *et al.*[68]. With a decomposition technique, the pulse profile of 1A 0535+262 during a giant outburst observed by Insight-HXMT in 2020 can be described with a geometry consisting of a distorted dipole magnetic field[67]. 1A 0535+262 has been monitored by Fermi for over than 13 years and the deep search in gamma-rays resulted in no significant detection during its previous outbursts[68]. This is not of surprise since the neutron star in this system has a spin much slower than that held in the accretion millisecond pulsar and the gamma-rays beyond 511 keV, if any, would be absorbed locally in a compact emission region of the accretion column.

Other studies carried out since 2023 are listed in what follows. The Centaurus X-3 orbital ephemerides was improved using Insight-HXMT, RXTE, Swift/BAT and NuSTAR observations[69]. A hard tail was detected from Sco X-1 with Insight-HXMT observations[70], which requires a non-thermal component in addition to a normal corona. 4U 1700-37 is an eclipsing high-mass X-ray binary holding a compact object of 2.44 ± 0.27 solar mass. Although a NS or BH nature of this compact object is not clear, the studies carried out by Xiao *et al.*[71] based on Insight-HXMT observations found short flares with stable spectral hardness, which resembles to the superfast giant X-ray transients (SgXBs) observed with flares produced by the clumpy stellar wind of the companion. Furthermore, hint for detection of CRSFs also point to the NS nature of this compact object[71]. Broadband X-ray timing and spectral characteristics of the accretion-powered millisecond X-ray pulsar MAXI J1816-195 were analyzed by Li *et al.* with a report of the stable X-ray pulsations above about 95 keV detected in a combination of Insight-HXMT HE observations[72].

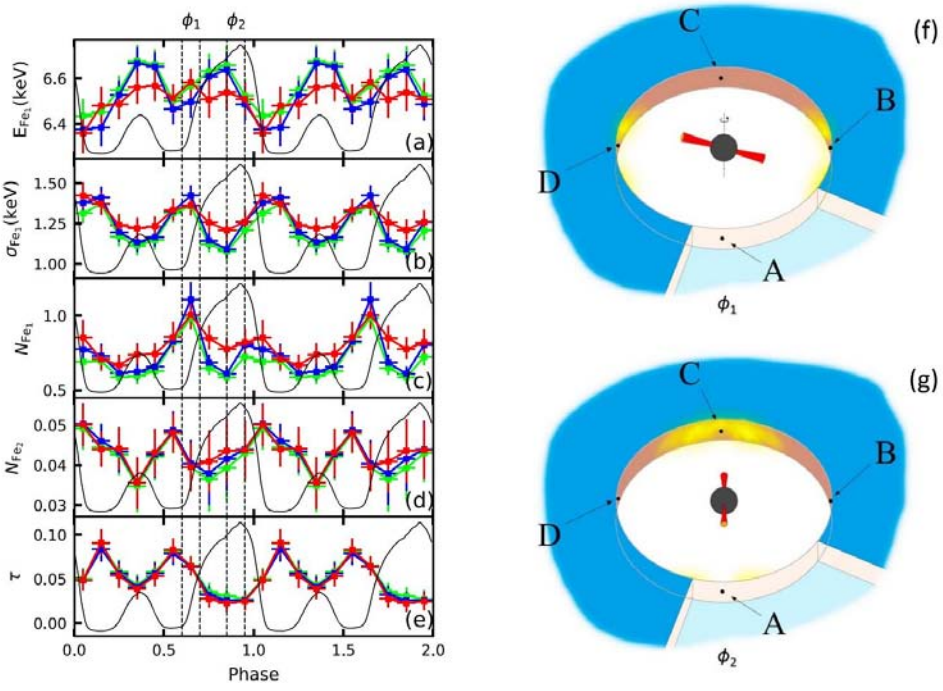

Fig.16 Geometric sketch of the broad iron line emission region on the accretion disk of two specific phase intervals from the observer's perspective. The accretion disk is divided equally into regions A, B, C, and D toroidally, with the region A being on the side closest to the line of sight of the observer[66]

As an atoll source, 4U 1730-22 underwent two outbursts in 2021 and 2022 after 49 years of silence. The joint Insight-HXMT and NICER observations showed a transition to LHS during the decay phase which, if a propeller effect is at work, can be used to estimate the magnetic field of the NS as (1.8~2.2) × 10^8 G[73].

4 Cyclotron Resonant Scattering Features

Strong magnetic field can quantize the movement of the hot electrons confined in the emission region around the magnetic poles into the Landau levels, and hence CRSFs can show up in the observed energy spectrum at the specific energies needed for the electron to stay at different quantum status. The centroid energy of CRSF E_{cyc} is correlated to the magnetic field in form of $E_{cyc} \approx 11.6 \times B_{12}$ keV, where B_{12} is the magnetic field strength in units of 10^{12} G, providing the only manner to estimate directly the magnetic fields of NSs. A NS's magnetic field is highly relevant to many issues regarding to understanding the accretion process of a NS XRB system which is governed jointly by accretion rate and the NS's magnetic field. For example, the discovery of the highest CRSF centroid energy of 146 keV has already proved that the PULX should have the super-Eddington luminosity intrinsically instead of beamed[5]. Since the CRSFs are generally thought to be produced at the site where the hard X-rays are produced, evolution of the CRSF E_{cyc} against luminosity serves as a probe to investigate how the emission region could evolve between different emission modes, and discriminate the different models at work. For example, the E_{cyc}-luminosity correlation will change from positive to negative once the luminosity increases across the critical one. Thus, measurement of such a critical luminosity may discriminate the popular models at work currently[74]. However, as shown in Mushtukov *et al.*[74], the sporadic observational results for E_{cyc}-luminosity correlation are far from sufficient for fulfilling this task. A possible breakthrough may come from Insight-HXMT observation of the outburst from 1A0535+262, where a clear change in E_{cyc}-luminosity correlation at a critical luminosity seems to be consistent with model prediction of Becker *et al.*[75]. Recently, by taking a pulse-to-pulse method, Shui *et al.*[76] obtained more detailed results which refined the fine structures of the E_{cyc}-luminosity correlation from 1A0535+262. As shown in Figure 17, three critical luminosities (denoted as L1, L2 and L3) are found in the E_{cyc}-luminosity diagram, which subdivides the entire E_{cyc}-luminosity evolution into four regions: the correlation changes from negative to positive at L1 (from regions I to II), remains flat after L2 (region III) and finally turns into negative across L3 (region IV). Apart from the positive and negative correlations as predicted by the current models at high luminosities, the new components of region III located between L2 and L3, and region I at below L1 definitely put new/strong constraints on the current popular models. Specifically, the flat region III may suggest a smooth transition between modes dominated by radiation and Coulomb pressures in deceleration process of the infalling material after the shock. Moreover, if region I below L1 could be responsible to the gas shock dominated mode, where a pencil beam is expected, the continuous evolution of E_{cyc} can put for the first time a very strong constraint on the evolution manner of the emission site. For example, Figure 17 requires that, if the CRSF in region I is produced from the accretion mound on the surface of the NS, the column in fan-mode in region IV should have a size comparable to the mound since all the regions (I~IV) share the similar variation range of E_{cyc}.

Other CRSF research progresses since 2023 are summarized in what follows. From two observations of the NSXRB system Cen X-3 performed by Insight-HXMT during 2017 and 2018, Yang *et al.* reported for the first time both fundamental and harmonic lines, located at 27 KeV and 48 keV in the energy spectrum, respectively[77]. However, during the Insight-HXMT observations of this source in 2022, only the fundamental line of 29 keV was detected with a weak correlation against the luminosity[78]. These may denote some episodes that the source has experienced different evolutional behaviors. For the Be XRB system XTE J1946 +274, Ashwin Devaraj *et al.* analyzed the AstroSat and Insight-HXMT observations during the rising and peak phases of the 2018 outburst, respectively. They confirmed for the first time the previously debated reports on the existence of CRSF around 40~50 keV (Figure 18), and clarified its dependences on the luminosity and pulse phase[79]. These discoveries contribute the complementary patches which help to build a complete

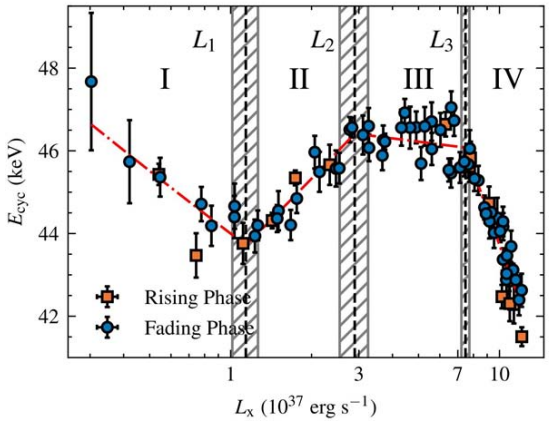

Fig.17 Luminosity dependence of cyclotron line centroid energy with the linear energy drift of $\dot{E}_{cyc}$ = 0.047 keV·d^{-1} taken into account. The red dashed line represents the best fitting result with the broken power-law model which has three break luminosities (L1, L2, and L3). These three vertical dashed lines and shaded areas are the best fitting break luminosities and corresponding uncertainties, respectively. These transitional luminosities suggest the division of the E_{cyc}–L_X relation into four zones (regions I, II, III, and IV) with different types of the E_{cyc}–L_X correlation[76]

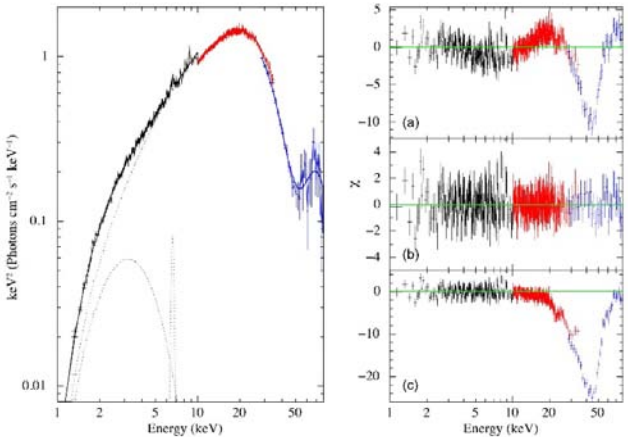

Fig.18 Unfolded spectrum of the HXMT 2018 observation with the best fit of NPEX model is shown on the left panel. The right panel shows the residues[79]

scenario for understanding the E_{cyc}-luminosity correlation.

4.1 Type-I Burst Probe

The spectral state transitions are almost the unique processes for understanding the basic elements of the BHXRB systems: disk, corona and jet, *etc*. Particularly, the nature of the corona still remains a puzzle since in definition it is a radiation-inefficient hot flow which is in principle hard to be observed directly unless with seed photons lighting it up. However, the intrinsic properties of the corona cannot be readily recovered from an outburst since the state transitions and the recovery of the corona in the initial and delayed LHSs are governed by the viscos time scales of the disk accretion which may not be intrinsic to the corona itself. Type-I burst is the explosive thermal nuclear burning on the surface of NS and can serve as a probe to corona due to its well known properties of location, luminosity, spectrum and duration. It provides an intense shower of the soft X-rays which can be reminiscent to the effect of the accretion rate changes of the disk and hence the possible influences on the evolution of the corona and probably as well the jet. In fact, such a burst probe was adopted to investigate the accretion environment and a series of burst-induced effects were discovered: during type-I burst, the accretion rate can be enhanced[80]; the corona can be cooled and recovered with a few tens of seconds[81]; jet can be produced by the type-I burst[82].

Prior to the launch of Insight-HXMT, the persistent emission from the corona was observed to have shortage during type-I burst *via* stacking tens of burst samples due to the relative small detection area of the previous hard X-ray missions, *e.g.*, RTXE (see the series of reports from Chen *et al.*[83] and Ji *et al.*[84], *etc*.). Obviously, Insight-HXMT demonstrated its power and advantage to this end, initially *via* detecting a burst-induced corona cooling event from a single normal type-I burst in the early Insight-HXMT phase[86]. Recently more studies were carried out on the burst influences on the corona and jet by observing the spectrum of the persistent emission at hard X-rays, as are introduced in what follows.

Wang *et al.* found that the newly discovered millisecond pulsar MAXI J1816-195 shows a rare likely clocked-burst behavior it its outburst observed by Insight-HXMT in 2022[86]. Chen *et al.* investigated the energy spectrum of the hard X-ray deficit during these bursts, and reported that the energy spectrum for Deficit Fraction (DF) of the hard X-rays becomes more or less saturated at higher energies[87] (Figure 19). DF was obtained in other systems observed by Insight-HXMT: in 4U 1608-52 the hard X-ray shortage remains around 50% of the persistent emission at energies above 50 keV[88] (Figure 20), while in 4U 1636-536 it shows a positive correlation between DF and energy[89] (Figure 21). We speculate that these results may be relevant to how a hybrid corona/jet population contributes the persistent emission at hard X-rays, where the jet is relatively harder to be cooled down by the burst shower than the

corona. The outburst of MAXI J1816-195 presents the accretion-produced pulsation originated around the magnetic pole of the NS harbored in this system and, during the clocked-burst events, Ji *et al.* found that the strength and profile of the pulsations remained unchanged, which means that the accretion matters channeled onto the magnetic poles are not influenced by the explosive burning on the NS surface[90]. They therefore suggested that the interaction with burst photons can be used as a direct diagnostic to distinguish contributions from the hot plasma near polar caps and the corona around the accretion disk, which are highly degenerate in their spectral shapes. Yan *et al.* conducted an analysis of 45 bursts observed from 4U 1636-53 and they

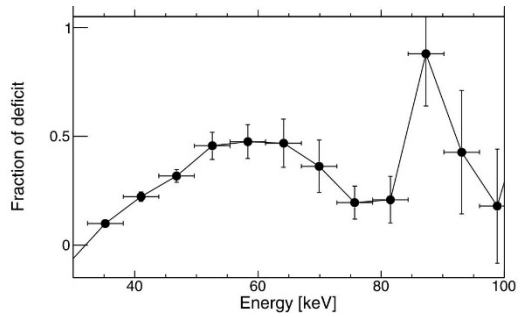

Fig.19 Deficit fraction versus energy during the bursts detected by HE in MAXI J1816-195[87]

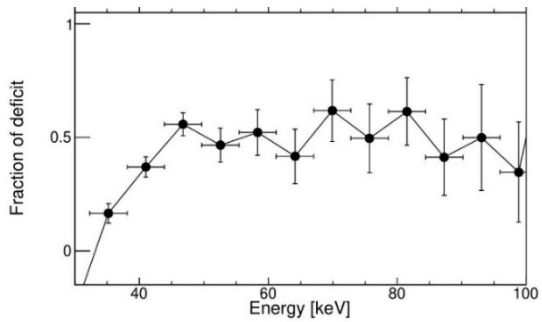

Fig.20 Deficit fraction versus energy during the bursts detected by HE in 4U 1608-52[88]

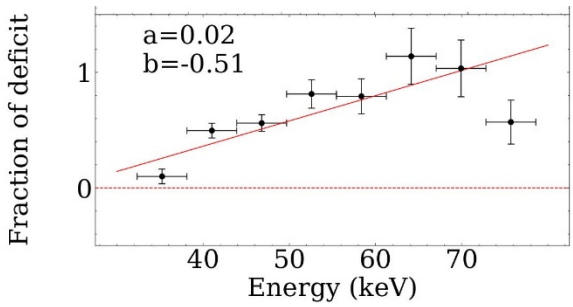

Fig.21 Deficit fraction versus energy during the bursts detected by HE in 4U 1636-536[89]

observed an inverse correlation between the maximum increase of the persistent emission flux during the non-PRE bursts[91]. By analyzing the profiles of the Photospheric Radius Expansion (PRE) events during the outbursts of 4U 1730-22, Lu *et al.* proposed the pure helium as the fuel and updated the source distance[92].

4.2 Galactic Plane Scanning Survey

Galactic plane survey is one of the core sciences of Insight-HXMT. Roughly 20%~30% of the Insight- exposure was spent on the Galactic plane survey in order to investigate the variability of the X-ray sources. A Galactic region enclosed with $0° < l < 360°$, $-10° < b < 10°$ is subdivided into small patches on which the survey is carried in a scanning mode. The schematic diagram of the scanning method of a small sky area is shown in Figure 22. The source information can be extracted from the scanned data with either fitting the triangle response of the telescope as adopted in Wang *et al.*[93], or a modified direct demodulation method which can handle the variable source *via* setting in the detector response matrix with an additional column dedicated to the target source[94]. The preliminary results from the Insight-HXMT Galactic plane survey were reported by Sai *et al.*[95], and Wang *et al.*[93] presented the long- term monitoring results of Insight-HXMT in the first 4 years of its Galactic plane scanning survey (GPSS). It is shown that, the 4-year limit sensitivities at main energy bands can reach 8.2×10^{-12} erg·s^{-1}·cm^{-2} (2~6 keV), 4.21×10^{-11} erg·s^{-1}·cm^{-2} (7~40 keV), and 2.78×10^{-11} erg·s^{-1}·cm^{-2} (25 ~100 keV). More than 1300 sources have been monitored in a wide band (1~100 keV), of which 223 sources have a signal-to-noise ratio greater than 5. By combining the GPSS data of Insight-HXMT and MAXI,

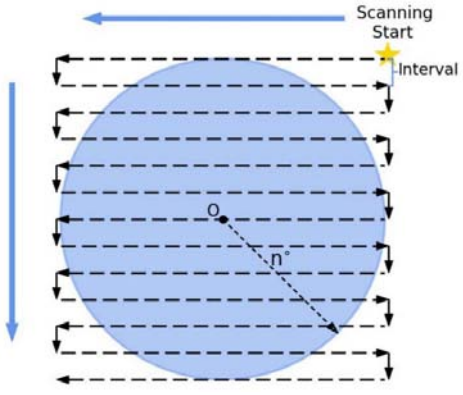

Fig.22 Schematic diagram of the scanning method of a small sky area[93]

long-term light curves established are used to study the flux variabilities at different energy bands for 223 bright sources. The first Insight-HXMT catalogue of X-ray sources of different types was released and the detailed investigations with parameters, *e.g.*, the hardness ratio and variability *etc*., show distinguished differences between different source types, in line with the specific intrinsic properties known for each of the individual source types[96].

4.3 Isolated Pulsars

Isolated pulsars are mainly used for in-orbit timing calibrations and Insight-HXMT spent over 4 M_s on Crab observations. The long-term evolution of Crab as monitored by Insight-HXMT demonstrated a correlation in the form of $L_x \propto L^{\alpha}_{sd}$ between the pulsed flux L_x and the spin down flux L^{α}_{sd}., where α is constant across the Insight-HXMT energy band. The hard X-ray flux evolution shows that the performance of HE, such as effective area, keeps stable[97]. As an exploration of the non-thermal emission, a sample of MeV pulsars observed by different high energy telescopes including Insight-HXMT were studied with findings of a harder spectrum and a higher radiation efficiency in 0.3~10 keV energy bands compared to the Fermi pulsars. Such a difference may be attributed to either the different viewing angle of the spin axis or the different inclination angle of the magnetic axis[98]. Isolated pulsars can also be observational targets for navigation; a review and an updated research were given by Wang *et al.*[99,100].

4.4 Fast Radio Bursts

A Fast Radio Burst (FRB) was first reported in 2007[101] with characteristics of bright millisecond radio pulses, random arrival direction and time, some repeating and even periodic, but remained a puzzle with counterpart or radiation at any other wavelengths not known until 28 April 2020, when an identification the counterpart of the FRB 200428 with a magnetar SGR J1935+2145 was reported by Insight-HXMT[102]. A series of studies were carried out since 2023 based on the Insight-HXMT observation on this unique FRB-SGR association event and the bursts from SGR J1935+2145 monitored by Insight-HXMT and GECAM *etc*.

Refined information was reconstructed by Ge *et al.* from Insight-HXMT observations of the flares from FRB200428, with improved temporal and spectral analyses. Accordingly, the measurements for the properties of the accompanied X-ray bursts were updated[103]. In Cai *et al.*[4], 75 X-ray bursts produced by magnetar SGR J1935+2154 during an active period in 2020 were published. The cumulative distributions of the parameters of this burst sample can be interpreted by a self-organizing criticality theory, supporting a possible magnetic reconnection scenario in magnetars[105]. With the same sample, the phase distribution of the bursts is found to correlate with the type of the burst spectrum[106]. To account for the light curves and spectra measured by Insight-HXMT in association with the FRB 200428, Xie *et al.* proposed a model that the FRB-associated X-ray bursts originate from QED magnetic reconnections[107]. As shown in Figure 23, individual magnetic islands will be created in the magnetosphere due to magnetic reconnections, where the QED will take effects on the particle acceleration and cooling. With such a scenario, adjustments of the QED parameters can recover the light curves and energy spectra as observed by Insight-HXMT (Figure 24). About five months later, radio pulses from SGR 1915+105 were detected by FAST,

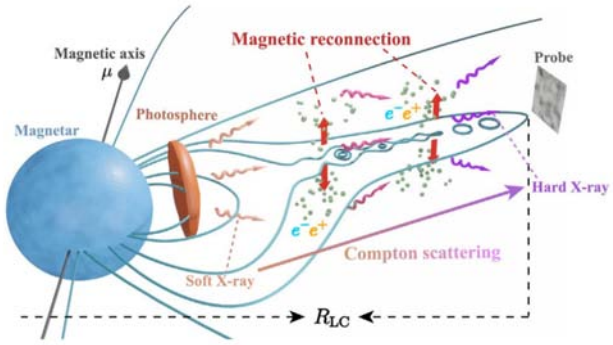

Fig.23 Schematic of the proposed origin model for the FRB 200428-associated X-ray burst[105]

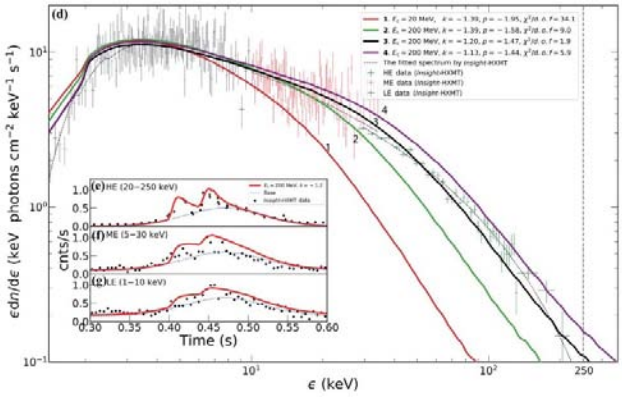

Fig.24 Insight-HXMT X-ray light curves and energy spectrum fitted by the model configured in a QED scenario[105]

with profiles anti-aligned with the X-rays. The observed difference in phase distributions of the radio and X-rays suggest fixed emission region for radio but random for X-rays[108].

SGR J1935+21 was active in 2020–2022, and hundreds of bursts were detected by Insight-HXMT, GECAM Fermi/GBM. With this burst sample, Xiao *et al.* carried out a series of studies. They found that the Minimum Variation Timescale (MVT) of the X-ray bursts associated with FRB 200428 is significantly longer than that of most bursts and implies its special radiation mechanism[109]. No obvious QPO exists for the sample but for some individual bursts a feature of 40 Hz is hinted to resemble the X-ray burst associated with FRB 200428[110]. About 61 percent bursts from SGR J1935+2154 have spectral lags that are linearly dependent on the photon energy[111]. The differential and cumulative distributions for the parameters of MVT and spectral lag follow a power law shape. The distributions of fluctuations in both parameters follow the Tsallis q-Gaussian distributions[112] and the q values are consistent for different scale intervals, thus indicating a scale-invariant nature for both parameters[113].

4.5 Gamma-Ray Bursts

Gamma-Ray Bursts (GRBs) are among the core sciences of Insight-HXMT and there are normal mode and GRB mode for GRB observations. For the latter, the high electric voltage of PMTs will be lowered so that the band passes for both NaI and CsI detectors can be promoted to higher energies and the corresponding FoVs can be enlarged to more than half of the whole sky unblocked by the earth. Particularly, CsI detectors can cover energies from 200 keV up to several MeV with a rather large detection area. The first Insight-HXMT GRB catalogue was released[114]. The capability of Insight-HXMT GRB detection is about 80 events per year. The brightest GRB 221009A was detected and the joint GECAM and Insight-HXMT observations present almost unique data covering the main peak phases by the unsaturated detections of GECAM and the precursor/afterglow jointly by Insight-HXMT.

The unconventional precursor of GRB 221009A detected by Insight-HXMT may provide a peculiar case study for GRB precursor phenomena. A two-stage collapsar scenario is proposed by Song *et al.*[115] as the most likely origin for GRB 221009A: the jet for the precursor is produced during the initial core-collapse phase, and should be weak enough not to disrupt the star when it breaks out of the envelope (relevant to the gap after the precursor), so that the fallback accretion process could continue to form the main GRB phase (Figure 25). Zheng *et al.* analyzed the energy spectrum of the early afterglow observed by Insight-HXMT, GECAM and Fermi/GBM. They found that the spectrum of the early afterglow in 20 keV~20 MeV can be well described by a cutoff power law with an extra power law that dominates the low- and high-energy bands, respectively. The spectral index changed at time around the jet break[116]. The optical afterglow of GRB

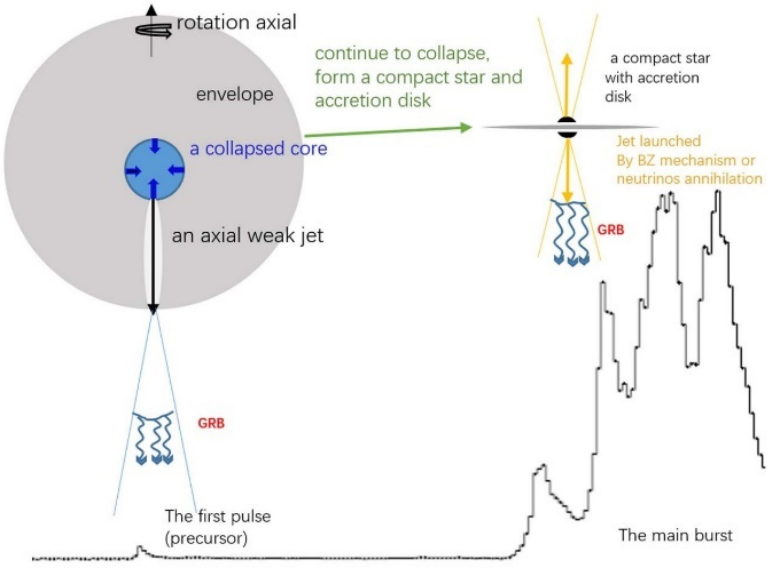

Fig.25 A scenario for the "two-stage" model of precursors for GRB221009A[115]

221009A was investigated by Kann *et al.* together with the contemporary Insight-HXMT and Swift-XRT data. The results they derived suggest that the observed afterglow is produced by synchrotron radiation at the forward external shock during the deceleration of a top-hat relativistic jet by a uniform medium, with a tension between the observed temporal and spectral evolution[117].

Together with the Insight-HXMT GRB catalogue, the GRB catalogues built so far from different detectors make it feasible for comprehensively investigating the GRB properties by studying their fine structures. Camisasca *et al.* took the catalogues produced from Insight-HXMT and Swift/BAT, and used the peak detection algorithm *mepsa* to identify the shortest pulse within a GRB light curve. They confirmed that short GRBs have significantly shorter MVTs than long GRBs, which is important because it provides a new clue concerning the progenitor's nature[118]. With two more catalogues from CGRO/BATSE and BeppoSAX/GRBM, Guidorzi *et al.* analyzed the stochastic process by extracting and modelling for the first time the distribution of the number of peaks within a GRB profile, and grouped the long duration GRBs into two classes: peak poor and peak rich, which account for 80% and 20% of the total GRB sample, respectively. They associated the class of peak-rich GRBs with the presence of sub-second variability and suggested two different regimes for the inner engines to release energy[119].

5 Summary and Outlook

The rich scientific results of Insight-HXMT since 2023, as highlighted in this paper, show the scientific capability and power of Insight-HXMT. Among these results, one notices that the potential breakthroughs were accomplished with either the multi-wavelength campaigns or the development of new analysis techniques. Actually, these may serve as the main interests in future to better use Insight-HXMT, which is open to the international community for observations and data archives. The mission currently is still operating quite well and will be available to the world-wide community for years to come. Please visit hxmt.org for further information about Insight-HXMT and downloading data.

References

[1] LI Tipei, XIONG Shaolin, ZHANG Shuangnan, *et al.* Insight-HXMT observations of the first binary neutron star merger GW170817[J]. *Science China Physics, Mechanics & Astronomy*, 2018, **61**(3): 1011-1018. DOI: 10.1007/s11433-017-9107-5

[2] MA Xiang, TAO Lian, ZHANG Shuangnan, *et al.* Discovery of oscillations above 200 keV in a black hole X-ray binary with Insight-HXMT [J]. *Nature Astronomy*, 2021, **5**: 94-102

[3] YOU Bei, TUO Youli, LI Chengzhe, *et al.* Insight-HXMT observations of jet-like corona in a black hole X-ray binary MAXI J1820+070 [J]. *Nature Communications*, 2021, **12**: 1025

[4] DOROSHENKO V, ZHANG S N, SANTANGELO A, *et al.* Hot disc of the Swift J0243.6+6124 revealed by Insight-HXMT [J]. *Monthly Notices of the Royal Astronomical Society*, 2021, **491**: 1857-1867. DOI: 10.1093/mnras/stz2879

[5] KONG Lingda, ZHANG Shu, ZHANG Shuangnan, *et al.* Insight-HXMT Discovery of the Highest-energy CRSF from the First Galactic Ultraluminous X-Ray Pulsar Swift J0243.6+6124 [J]. *The Astrophysical Journal Letters*, 2022, **933**: 3-10. DOI: 10.3847/2041-8213/ac7711

[6] GE M Y, JI L, ZHANG S N, *et al.* Insight-HXMT firm detection of the highest-energy fundamental cyclotron resonance scattering feature in the spectrum of GRO J1008-57[J]. *The Astrophysical Journal Letters*, 2020, **899**: 19-23. DOI: 10.3847/2041-8213/abac05

[7] LIU Congzhan, ZHANG Yifei, LI Xufang, *et al.* The High Energy X-ray telescope (HE) onboard the Insight-HXMT astronomy satellite[J]. *Science China Physics, Mechanics & Astronomy*, 2020, **63**, 249503

[8] CAO Xuelei, JIANG Weichun, MENG Bin, *et al.* The Medium Energy X-ray telescope (ME) onboard the Insight-HXMT astronomy satellite[J]. *Science China Physics, Mechanics & Astronomy*, 2020, **63**, 249504

[9] CHEN Yong, CUI Weiwei, LI Wei, *et al.* The Low Energy X-ray telescope (LE) onboard the Insight-HXMT astronomy satellite[J]. *Science China Physics, Mechanics & Astronomy*, 2020, **63**, 249505

[10] ZHANG Shuangnan, LI Tipei, LU Fangjun, *et al.* Overview to the Hard X-ray Modulation Telescope (Insight-HXMT) Satellite [J]. *Science China Physics, Mechanics & Astronomy*, 2020, **63**, 249502

[11] ZHOU X, LI X Q, XIE Y N, *et al.* Introduction to a calibration facility for hard X-ray detectors[J]. *Experimental Astronomy*, 2014, **38**: 433-441

[12] ZHANG S, CHEN Y P, XIE Y N, *et al.* The X-ray facilities in-building for calibrations of HXMT[J]. *Proc. SPIE*, 2014, **9144**, 55

[13] ZHANG S, ZHANG S N, LU F J, *et al.* The insight-HXMT mission and its recent progresses[J]. *Proc. SPIE*, 2018, 106991U. DOI: 10.1117/12.2311835

[14] LI Xiaobo, LI Xufang, TAN Ying, *et al.* In-flight calibration of the Insight-Hard X-ray Modulation Telescope[J]. *Journal of High Energy Astrophysics*, 2020, **27**: 64-76

[15] TUO Youli, LI Xiaobo, GE Mingyu, *et al.* In-orbit timing calibration of the Insight-Hard X-Ray Modulation Telescope[J]. *The Astrophysical Journal Supplement Series*, 2022, **259**: 14-26

[16] LIAO Jinyuan, ZHANG Shu, LU Xuefeng, *et al.* Background model for the high-energy telescope of Insight-HXMT[J]. *Journal of High Energy Astrophysics*, 2020, **27**: 14-23

[17] YOU Yuan, LIAO Jinyuan, ZHANG Shuangnan, *et al.* A Parametric model to reproduce the background of the Insight-HXMT/HE blind detector[J]. *The Astrophysical Journal Supplement Series*, 2021, **256**: 47-61

[18] YOU Bei, CAO Xinwu, YAN Zhen, *et al.* Observations of a black hole X-ray binary indicate formation of a magnetically arrested

disk[J]. *Science*, 2023, **381**: 961

[19] PENG J Q, ZHANG S, CHEN Y P, *et al.* A possible overall scenario for the outburst evolution of MAXI J1820+070 revealed by Insight-HXMT[J]. *Monthly Notices of the Royal Astronomical Society*, 2023, **518**: 2521-2528

[20] KAWAMURA Tenyo, DONE Chris, AXELSSON Magnus, *et al.* MAXI J1820+070 X-ray spectral-timing reveals the nature of the accretion flow in black hole binaries [J]. *Monthly Notices of the Royal Astronomical Society*, 2023, **519**: 4434-4453

[21] WANG Yanan, ZHANG Shuangnan. RMS-flux slope in MAXI J1820+070: a measure of the disk-corona coupling[J]. *The Astrophysical Journal*, 2024, **962**: 53-61

[22] PENG Jingqiang, ZHANG Shu, WANG Pengju, *et al.* Back to Business: SLX 1746-331 after 13 Years of Silence[J]. *The Astrophysical Journal*, 2023, **955**: 96-105

[23] PENG Jingqiang, ZHANG Shu, SHUI Qingcang, *et al.* NICER, NuSTAR and Insight-HXMT views to black hole X-ray binary SLX 1746-331[J]. *The Astrophysical Journal Letters*, 2024 (in press)

[24] MA R C, SORIA R, TAO L, *et al.* The peculiar spectral evolution of the new X-ray transient MAXI J0637-430[J]. *Monthly Notices of the Royal Astronomical Society*, 2022, **514**: 5238-5256

[25] PENG Jingqiang, ZHANG Shu, SHUI Qingcang, *et al.* NICER, NuSTAR, and Insight-HXMT Views to the Newly Discovered Black Hole X-Ray Binary Swift J1727.8-1613[J]. *The Astrophysical Journal Letters*, 2024, **960**: 17-26

[26] DAI Xiaohang, KONG Lingda, BU Qingcui, *et al.* Evolution of disc and corona in MAXI J1348-630 during the 2019 reflare: NICER and Insight-HXMT view[J]. *Monthly Notices of the Royal Astronomical Society*, 2023, **521**: 2692-2703

[27] YU Wei, BU Qingcui, LIU Hexin, *et al.* A Spectral-timing study of the inner flow geometry in MAXI J1535-571 with Insight-HXMT and NICER[J]. *The Astrophysical Journa*l, 2023, **953**: 191-202

[28] ZHAO S J, TAO L, LI, P P, *et al.* The bright black hole X-ray binary 4U 1543-47 during 2021 outburst: a thick accretion disk inflated by high luminosity [J] . *Astronomy and Astrophysics*, 2024 (in press)

[29] JIN Pei, ZHANG Guobao, ZHANG Yuexin, *et al.* The bright black hole X-ray binary 4U 1543-47 during 2021 outburst. A clear state transition from super-Eddington to sub-Eddington accretion revealed by Insight-HXMT[J]. *Monthly Notices of the Royal Astronomical Society*, 2024 (in press)

[30] SHI Zhihong, WU Qingwen, YAN Zhen, *et al.* A new variability pattern in GRS 1915+105 with NICER and Insight-HXMT observations[J]. *Monthly Notices of the Royal Astronomical Society*, 2023, **525**: 1431-1442

[31] BELCZYNSKI Krzysztof, WIKTOROWICZ Grzegorz, FRYER Chris L, *et al.* Missing Black Holes Unveil the Supernova Explosion Mechanism[J]. *The Astrophysical Journal*, 2012, **757**: 91-96

[32] GAO Shijie, LI Xiangdong, SHAO Yong. Formation of mass-gap black holes from neutron star X-ray binaries with super-Eddington accretion[J]. *Monthly Notices of the Royal Astronomical Society*, 2022, **514**: 1054-1070

[33] YAN Zhen, YU Wenfei. X-Ray Outbursts of low-mass X-Ray binary transients observed in the RXTE era[J]. *The Astrophysical Journal*, 2015, **805**: 87-108

[34] MA R C, SORIA R, TAO L, *et al.* The peculiar spectral evolution of the new X-ray transient MAXI J0637-430[J]. *Monthly Notices of the Royal Astronomical Society*, 2022, **514**: 5238-5256

[35] SORIA Roberto, MA Ruican, TAO Lian, *et al.* A 2-hr binary period for the black hole transient MAXI J0637-430[J]. *Monthly Notices of the Royal Astronomical Society*, 2022, **515**: 3105-3112

[36] SONG Yujia, JIA Nan, YANG Jun, *et al.* The spin measurement of MAXI J1348-630 using the Insight-HXMT data[J]. *Monthly Notices of the Royal Astronomical Society*, 2023, **524**: 6041-6051

[37] WU Hanji, WANG Wei, SAI Na, *et al.* A moderate spin for the black hole in X-ray binary MAXI J1348-630 revealed by Insight-HXMT[J]. *Monthly Notices of the Royal Astronomical Society*, 2023, **522**: 4323-4331

[38] JIA Nan, ZHAO Xueshan, GOU Lijun, *et al.* Detailed analysis on the reflection component for the black hole candidate MAXI J1348-630[J]. *Monthly Notices of the Royal Astronomical Society*, 2022, **511**: 3125-3132

[39] KUMAR Raj, BHATTACHARYYA Subir, BHATT Nilay, *et al.* Estimation of spin and mass of the black hole in MAXI J1348-630 from the soft state using NICER and NuSTAR observations[J]. *Monthly Notices of the Royal Astronomical Society*, 2022, **513**: 4869-4874

[40] CHEN Jiashi, WANG Wei. The spin of a stellar black hole 4U 1543-47 determined by Insight-HXMT[J]. *Monthly Notices of the Royal Astronomical Society*, 2024, **527**: 238-248

[41] YORGANCIOGLU E S, BU Q C, SANTANGELO A, *et al.* Spin measurement of 4U 1543-47 with Insight-HXMT and NICER from its 2021 outburst A test of accretion disk models at high luminosities[J]. *Astronomy and Astrophysics*, 2023, **677**: 79-88

[42] STELLA Luigi, VIETRI Mario. Lense-thirring precession and quasi-periodic oscillations in low-mass X-ray binaries[J]. *The Astrophysical Journal Letters*, 1998, **492**: 59-62

[43] KATO Shoji. Trapped one-armed corrugation waves and QPO's[J]. *Publications of the Astronomical Society of Japan*, 1990, **42**: 99-113

[44] TAGGER M, PELLAT R. An accretion-ejection instability in magnetized disks[J]. *Astronomy and Astrophysics*, 1999, **349**: 1003-1016

[45] MOLTENI Diego, SPONHOLZ Hanno, CHAKRABARTI Sandip K. Resonance Oscillation of Radiative Shock Waves in Accretion Disks around Compact Objects[J]. *The Astrophysical Journal*, 1996, **457**: 805-812

[46] INGRAM Adam, VAN DER Klis Michiel. Phase-resolved spectroscopy of low-frequency quasi-periodic oscillations in GRS 1915+105[J]. *Monthly Notices of the Royal Astronomical Society*, 2015, **446**: 3516-3525

[47] GAO Chenxu, YAN Zhen, YU Wenfei. Low-frequency quasi-periodic oscillation in MAXI J1820+070: Revealing distinct Compton and reflection contributions[J]. *Monthly Notices of the Royal Astronomical Society*, 2023, **520**: 5544-5551

[48] ZHANG P, SORIA R, ZHANG S, *et al.* Intermittent properties of the quasi-periodic oscillations of MAXI J1820+070 revealed by Insight-HXMT[J]. *Astronomy and Astrophysics*, 2023, **677**: 178-185

[49] HUANG N E, SHEN Z, LONG S R, *et al.*, The empirical mode decomposition and the Hilbert spectrum for nonlinear and non-stationary time series analysis [J]. *RSPSA*, 1998, **454**: 903

[50] SHUI Qingcang, ZHANG Shu, ZHANG Shuangnan, *et al.* A phase-resolved view of the low-frequency quasiperiodic oscillations from the black hole binary MAXI J1820+070 [J]. *The Astrophysical Journal*, 2023, **957**: 84-98

[51] DRAGOMIRETSKIY Konstantin, ZOSSO Dominique. Variational mode decomposition[J]. *IEEE Transactions on Signal Processing*, 2014, **62**(3): 531-547

[52] SHUI Qingcang, ZHANG Shu, ZHANG Shuangnan, *et al.* Recovery of High-energy Low-frequency Quasi-periodic Oscillations

from Black Hole X-ray Binary MAXI J1535-571 with a Hilbert-Huang Transform Method[J]. *The Astrophysical Journal Letters*, 2024 (in press)

[53] HUANG Y, QU J L, ZHANG S N, *et al.* INSIGHT-HXMT observations of the new black hole candidate MAXI J1535-571: timing analysis [J]. *The Astrophysical Journal*, 2018, **866**: 122-131

[54] ZHAO Qingchang, TAO Lian, LI Hancheng, *et al.* The first polarimetric view on quasiperiodic oscillations in a black hole X-ray binary [J]. *The Astrophysical Journal Letters*, 2024, **961**: 42-48

[55] YU Wei, BU Qingcui, ZHANG Shuangnan, *et al.* Timing analysis of the newly discovered black hole candidate Swift J1727.8-1613 with Insight-HXMT[J]. *Monthly Notices of the Royal Astronomical Society*, 2024, **529**: 4624-4632

[56] PSALTIS D, BELLONI T, VAN DER Klis M. Correlations in quasi-periodic oscillation and noise frequencies among neutron star and black hole X-Ray binaries[J]. *The Astrophysical Journal*, 1999, **520**: 763-775

[57] YU Wei, BU Qingcui, YANG Zixu, *et al.* Hilbert-Huang Transform analysis of quasi-periodic oscillations in MAXI J1820+070 [J]. *The Astrophysical Journal*, 2023, **951**: 130-138

[58] MA X, ZHANG L, TAO L, *et al.* A detailed view of low-frequency quasi-periodic oscillation in the broadband 0.2-200 keV with Insight-HXMT and NICER[J]. *The Astrophysical Journal*, 2023, **948**: 116-120

[59] ZHU Haifan, CHEN Xiao, WANG Wei. Timing analysis of the new black hole candidate MAXI J1803-298 with Insight-HXMT and NICER[J]. *Monthly Notices of the Royal Astronomical Society*, 2023, **523**: 4394-4404

[60] YANG Zixu, ZHANG Liang, ZHANG Shuangnan, *et al.* Fast transitions of X-ray variability in the black hole transient GX 339-4: comparison with MAXI J1820+070 and MAXI J1348-630 [J]. *Monthly Notices of the Royal Astronomical Society*, 2023, **521**: 3570-3584

[61] JIN Y J, WANG W, CHEN X, *et al.* Quasi-periodic Oscillations in GX 339-4 during the 2021 outburst observed with Insight-HXMT [J]. *The Astrophysical Journal*, 2023, **953**: 33-43

[62] DING Qi, JI Long, BU Qingcui, *et al.* Nonlinear variability observed with Insight-HXMT in MAXI J1820+070 and MAXI J1535-571 [J]. *Research in Astronomy and Astrophysics*, 2023, **23**: 85024-85032

[63] LI P P, TAO L, ZHANG L, *et al.* Detection of a strong ~2.5 Hz modulation in the newly discovered millisecond pulsar MAXI J1816-195 [J]. *Monthly Notices of the Royal Astronomical Society*, 2023, **525**: 595-606

[64] LI P P, TAO L, TUO Y L, *et al.* Broadband noise and quasi-periodic oscillation characteristics of the X-ray pulsar RX J0440.9+4431 [J]. *Monthly Notices of the Royal Astronomical Society*, 2024, **529**: 1187-1194

[65] KONG L D, ZHANG S, CHEN Y P, *et al.* Two Complete Spectral Transitions of Swift J0243.6+6124 Observed by Insight-HXMT [J]. *The Astrophysical Journal*, 2020, **902**: 18-26

[66] XIAO Y X, XU Y J, GE M Y. Pulsed iron line emission from the first galactic ultraluminous X-ray pulsar swift J0243.6+6124 [J]. *The Astrophysical Journal*, 2024, **965**: 18-29

[67] HU Y F, JI L, YU C, *et al.* Beam pattern evolution of accreting X-ray pulsar 1A 0535+262 during its 2020 giant outburst [J]. *The Astrophysical Journal*, 2023, **945**: 138-149

[68] HOU X, ZHANG W, TORRES D F, *et al.* Deep Search for Gamma-Ray Emission from the Accreting X-Ray Pulsar 1A 0535+262 [J]. *The Astrophysical Journal*, 2023, **944**: 57-64

[69] KLAWIN Moritz, DOROSHENKO Victor, SANTANGELO Andrea, *et al.* Improving Centaurus X-3 orbital ephemerides using Insight-HXMT, RXTE, Swift/BAT and NuSTAR observations [J]. *Astronomy and Astrophysics*, 2023, **675**: 135-141

[70] DING G Q, QU J L, SONG L M, *et al.* Insight-HXMT Detections of Hard X-ray Tails in Scorpius X-1[J]. *The Astrophysical Journal*, 2023, **950**: 69-79

[71] XIAO Hua, JI Long, ZHANG Peng, *et al.* Timing and spectral analysis of the HMXB 4U 1700-37 observed with Insight-HXMT [J]. *The Astrophysical Journal*, 2024, **963**: 18-27

[72] LI Zhaosheng, KUIPER Lucien, GE Mingyu, *et al.* Broadband X-ray timing and spectral characteristics of the accretion-powered millisecond X-ray pulsar MAXI J1816-195 [J]. *The Astrophysical Journal*, 2023, **958**: 177-186

[73] CHEN Yupeng, ZHANG Shu, ZHANG Shuangnan, *et al.* Return of 4U 1730-22 after 49 yr silence: the outburst properties observed by NICER and Insight-HXMT [J]. *The Astrophysical Journal Letters*, 2023, **942**: 12-28

[74] MUSHTUKOV Alexander A, SULEIMANOV Valery F, TSYGANKOV Sergey S, *et al.* The critical accretion luminosity for magnetized neutron stars [J]. *Monthly Notices of the Royal Astronomical Society*, 2015, **447**: 1847-1856

[75] BECKER P A, KLOCHKOV D, SCHÖNHERR G, *et al.* Spectral formation in accreting X-ray pulsars: bimodal variation of the cyclotron energy with luminosity [J]. *Astronomy and Astrophysics*, 2012, **544**: 123-135

[76] SHUI Q C, ZHANG S, WANG P J, *et al.* Cyclotron line evolution revealed with pulse-to-pulse analysis in the 2020 outburst of 1A 0535+262 [J]. *Monthly Notices of the Royal Astronomical Society*, 2024, **528**: 7320-7332

[77] YANG W, WANG W, LIU Q, *et al.* Discovery of two cyclotron resonance scattering features in X-ray pulsar cen X-3 by Insight-HXMT [J]. *Monthly Notices of the Royal Astronomical Society*, 2023, **519**: 5402-5409

[78] LIU Qi, WANG Wei, YANG Wen, *et al.* Studying the variations of the cyclotron line in Cen X-3 using Insight-HXMT [J]. *Journal of High Energy Astrophysics*, 2024, **41**: 22-29

[79] DEVARAJ Ashwin, SHARMA Rahul, NAGESH Shwetha, *et al.* Insights into the phase-dependent cyclotron line feature in XTE J1946+274: an AstroSat and Insight-HXMT view [J]. *Monthly Notices of the Royal Astronomical Society*, 2024, **527**: 11015-11025

[80] DEGENAAR Nathalie, BALLANTYNE David R, BELLONI Tomaso, *et al.* Accretion Disks and Coronae in the X-Ray Flashlight [J]. *Space Science Reviews*, 2018, **214**: 15-75

[81] FRAGILE P Chris, BALLANTYNE David R, BLANKENSHIP Aidan. Interactions of type I X-ray bursts with thin accretion disks [J]. *Nature Astronomy*, 2020, **4**: 541-546

[82] RUSSELL Thomas D, DEGENAAR Nathalie, VAN DEN Eijnden Jakob, *et al.* Thermonuclear explosions on neutron stars reveal the speed of their jets [J]. *Nature*, 2024, **627**: 763-766

[83] CHEN Yupeng, ZHANG Shu, ZHANG Shuangnan, *et al.* Type-I X-Ray Bursts Reveal a Fast Co-evolving Behavior of the Corona in an X-Ray Binary [J]. *The Astrophysical Journal Letters*, 2012, **752**: 34-37

[84] JI Long, ZHANG Shu, CHEN Yupeng, *et al.* Diagnosing the Burst Influence on Accretion in the Clocked Burster GS 1826-238 [J]. *The Astrophysical Journal*, 2015, **806**: 89-97

[85] CHEN Y P, ZHANG S, QU J L, *et al.* Insight-HXMT observations of 4U 1636-536: corona cooling revealed with single short Type-I X-ray burst[J]. *The Astrophysical Journal Letters*, 2018, **864**: 30-34

[86] WANG P J, CHEN Y P, JI L, *et al.* Type-I X-ray burst evolution of the new millisecond pulsar MAXI J1816-195 revealed by Insight-HXMT[J]. *Journal of High Energy Astrophysics*, 2024, **41**: 106-113

[87] CHEN Yupeng, ZHANG Shu, JI Long, *et al.* The prolific thermonuclear X-ray bursts from the outburst of the newly discovered millisecond pulsar MAXI J1816-195 observed by Insight-HXMT and NICER[J]. *The Astrophysical Journal Letters*, 2022, **936**: 21-31

[88] CHEN Yupeng, ZHANG Shu, JI Long, *et al.* Insight-HX MT observations on thermonuclear X-ray bursts from 4U 1608-52 in the low/hard state: the energy-dependent hard X-ray shortage and cooling saturation of the corona [J]. *Monthly Notices of the Royal Astronomical Society*, 2024 (submitted)

[89] PENG Jingqiang, ZHANG Shu, CHEN Yupeng, *et al.* New insight into the hard X-ray emission influenced by the type-I bursts observed by Insight-HXMT during outburst of 4U 1636-536 [J]. *Astronomy and Astrophysics*, 2024 (in press)

[90] JI Long, GE Mingyu, CHEN Yupeng, *et al.* The influence of thermonuclear bursts on polar caps of accreting X-ray millisecond pulsar MAXI J1816-195[J]. *The Astrophysical Journal Letters*, 2024 (in press)

[91] YAN Zhe, ZHANG Guobao, CHEN Yupeng, *et al.* Insight-HXMT observations of thermonuclear X-ray bursts in 4U 1636-53 [J]. *Monthly Notices of the Royal Astronomical Society*, 2024, **529**: 1585-1596

[92] LU Yongqi, LI Zhaosheng, PAN Yuanyue, *et al.* Type I X-ray bursts' spectra and fuel composition from the atoll and transient source 4U 1730-22[J]. *Astronomy and Astrophysics*, 2023, **670**: 87-96

[93] WANG Chen, LIAO Jinyuan, GUAN Ju, *et al.* The long-term monitoring results of Insight-HXMT in the first 4 yr galactic plane scanning survey[J]. *The Astrophysical Journal Supplement Series*, 2023, **265**: 52-82

[94] GUAN Ju, LU Fangjun, ZHANG Shu, *et al.* A modified direct demodulation method applied to Insight-HXMT Galactic plane scanning survey [J]. *Journal of High Energy Astrophysics*, 2020, **26**: 11-20

[95] SAI Na, LIAO Jinyuan, LI Chengkui, *et al.* Methodology and performance of the two-year galactic plane scanning survey of Insight-HXMT [J]. *Journal of High Energy Astrophysics*, 2020, **26**: 1-10

[96] WANG Chen, LIAO Jinyuan, GUAN Ju, *et al.* Analysis of bright source hardness ratios in the 4 yr Insight-HXMT galactic plane scanning survey catalog[J]. *Research in Astronomy and Astrophysics*, 2024, **24**: 025013-025029

[97] ZHAO Haisheng, GE Mingyu, LI Xiaobo, *et al.* Long-term evolution of the X-ray flux of the Crab pulsar[J]. *Radiation Detection Technology and Methods*, 2023, **7**: 48-55

[98] TAKATA J, WANG H H, LIN L C C , *et al.* Efficiency of non-thermal pulsed emission from eight MeV pulsars[J]. *The Astrophysical Journal*, 2024 (in press)

[99] WANG Yidi, ZHENG Wei, ZHANG Shuangnan, *et al.* Review of X-ray pulsar spacecraft autonomous navigation [J]. *Chinese Journal of Aeronautics*, 2023, **36** (10): 44-63

[100] WANG Yidi, ZHANG Shuangnan, GE Minyu, *et al.* On-orbit pulse phase estimation of X-ray crab pulsar for XNAV flight experiments [J]. *IEEE Transactions on Aerospace and Electronic Systems*, 2023, **59**: 3395-3404

[101] LORIMER D R, BAILES M, McLaughlin M A, A bright millisecond radio burst of extragalactic origin[J]. *Science*, 2007, **318**: 777-780

[102] LI C K, LIN L, XIONG S L. HXMT identification of a non-thermal X-ray burst from SGR J1935+2154 and with FRB 200428[J]. *Nature Astronomy*, 2021, **5**: 378-384

[103] GE M Y, LIU C Z, ZHANG S N, *et al.* Reanalysis of the X-ray burst associated FRB 200428 with Insight-HXMT observations[J]. *The Astrophysical Journal*, 2023, **953**: 67-75

[104] CAI Ce, XUE Wangchen, LI Chengkui, *et al.* An Insight-HXMT dedicated 33-day observation of SGR J1935+2154. I. burst catalog [J]. *The Astrophysical Journal Supplement Series*, 2022, **260**: 24-35

[105] ZHANG Wenlong, LI Xiujuan, YANG Yupeng, *et al.* Statistical properties of X-ray bursts from SGR J1935+2154 detected by Insight-HXMT [J]. *Research in Astronomy and Astrophysics*, 2023, **23**: 5013-5018

[106] LU Xuefeng, SONG Liming, GE Mingyu, *et al.* Burst Phase Distribution of SGR J1935+2154 Based on Insight-HXMT[J]. *Research in Astronomy and Astrophysics*, 2023, **23**: 5007-5013

[107] XIE Yu, GENG Jinjun, ZHU Xiwei *et al.* Origin of FRB-associated X-ray burst: QED magnetic reconnection[J]. *Science Bulletin*, 2023, **68**: 1857-1861

[108] ZHU Weiwei, XU Heng, ZHOU Dejiang, *et al.* A radio pulsar phase from SGR J1935+2154 provides clues to the magnetar FRB mechanism[J]. *Science Advances*, 2023, 9, 30: 6198-6209

[109] XIAO Shuo, YANG Jiaojiao, LUO Xihong, *et al.* The minimum variation timescales of X-Ray bursts from SGR J1935+2154[J]. *The Astrophysical Journal Supplement Series*, 2023, **268**: 5-13

[110] XIAO Shuo, LI Xiaobo, XUE Wangchen, *et al.* Individual and averaged power density spectra of X-ray bursts from SGR J1935+2154: quasi-periodic oscillation search and slopes[J]. *Monthly Notices of the Royal Astronomical Society*, 2024, **527**: 11915-11924

[111] XIAO Shuo, TUO Youli, ZHANG Shuangnan, *et al.* Discovery of the linear energy-dependence of the spectral lag of X-ray bursts from SGR J1935+2154 [J]. *Monthly Notices of the Royal Astronomical Society*, 2023, **521**: 5308-5333

[112] TSALLIS Constantino. Possible generalization of Boltzmann-Gibbs statistics[J]. *Journal of Statistical Physics*, 1988, **52**: 479-487

[113] XIAO Shuo, ZHANG Shuangnan, XIONG Shaolin, *et al.* The Self-organized Criticality Behaviors of Two New Parameters in SGR J1935+2154[J]. *Monthly Notices of the Royal Astronomical Society*, 2024, **528**: 1388-1392

[114] SONG Xinying, XIONG Shaolin, ZHANG Shuangnan, *et al.* The First Insight-HXMT Gamma-Ray Burst Catalog: The First Four Years[J]. *The Astrophysical Journal Supplement Series*, 2022, **259**: 46-61

[115] SONG Xinying, ZHANG Shuangnan. GRB 221009A with an unconventional precursor: a typical two-stage collapsar scenario? [J]. *The Astrophysical Journal*, 2023, **957**: 31-39

[116] ZHENG Chao, ZHANG Yanqiu, XIONG Shaolin, *et al.* Observation of GRB 221009A early afterglow in X-ray/gamma-ray energy bands[J]. *The Astrophysical Journal Letters*, 2024, **962**: 2-10

[117] KANN D A, AGAYEVA S, AIVAZYAN V, *et al.* GRANDMA and HXMT Observations of GRB 221009A - the Standard-Luminosity Afterglow of a Hyper-Luminous Gamma-Ray Burst[J]. *The Astrophysical Journal Letters*, 2023, **948**: 12-45

[118] CAMISASCA A E, GUIDORZI C, AMATI L, *et al.* GRB minimum variability timescale with Insight-HXMT and Swift: implications for progenitor models, dissipation physics and GRB classifications[J]. *Astronomy and Astrophysics*, 2023, **671**: 112-131

[119] GUIDORZI C, SARTORI M, MACCARY R, *et al.* Distribution of number of peaks within a long gamma-ray burst[J]. *Astronomy and Astrophysics*, 2024 (in press)

WANG Chenwei, XIONG Shaolin. Progress of GECAM Observation Research. *Chinese Journal of Space Science*, 2024, **44**(4)

Progress of GECAM Observation Research

WANG Chenwei[1,2], XIONG Shaolin[1,2]

1. Key Laboratory of Particle Astrophysics, Institute of High Energy Physics, Chinese Academy of Sciences, Beijing 100049
2. University of Chinese Academy of Sciences, Beijing 100049, China

Abstract

Gravitational wave high-energy Electromagnetic Counterpart All-sky Monitor (GECAM) is a constellation with four instruments (launch date): GECAM-A/B (December 10, 2020), GECAM-C (July 27, 2022) and GECAM-D (March 13, 2024), which are dedicated to monitoring gamma-ray transients in all-sky. The primary science objectives of GECAM include Gamma-Ray Bursts (GRBs), Soft Gamma-ray Repeaters (SGRs), high energy counterparts of Gravitation Wave (GW) and Fast Radio Burst (FRB), Solar Flares (SFLs), as well as Terrestrial Gamma-ray Flashes (TGFs) and Terrestrial Electron Beams (TEBs). A series of observations and research have been made since the launch of GECAM-A/B. GECAM observations provide new insights into these high-energy transients, demonstrating the unique role of GECAM in the "multi-wavelength, multi-messenger" era.

Key words

GECAM, Gravitational wave electromagnetic counterpart, High energy transients

1 Introduction

Gamma-ray transients are phenomena with a sudden increase in gamma-ray flux from celestial objects in the distant universe. Since the first observation of a Gamma-Ray Burst (GRB) in 1967, various gamma-ray transient sources have been discovered. Especially in recent years, the operation of advanced gamma-ray instruments has enabled rapid progress in the study of gamma-ray transients and related phenomena. A milestone event is the observation of the Gravitational Wave (GW) produced by the merger of binary neutron stars (GW170817) and the GW-associated Gamma-Ray Burst (GWGRB), GRB 170817A, heralding a new era in "multi-messenger, multi-wavelength" time-domain astronomy[1,2]. The pursuit of the GWGRB is the primary motivation of GECAM mission.

GECAM is originally a constellation of two small X-ray and gamma-ray all-sky space telescopes funded and built by the Chinese Academy of Sciences. These two microsatellites, denoted as GECAM-A and GECAM-B, were launched on December 10, 2022 (Beijing Time). GECAM-C is the 3rd GECAM monitor on board the SATech-01 satellite launched on July 27, 2022. GECAM-D is the 4th instrument in GECAM series which was launched on March 13, 2024 on board the DRO-A satellite. Currently, GECAM has established the capability of monitoring the full sky all the time in a wide energy range (*i.e.* 6 keV to 5 MeV).

The primary science objectives of GECAM are various types of gamma-ray transients, including GWGRBs, GRBs, SGRs and high-energy counterparts of Fast Radio Bursts (FRBs). Moreover, SFLs, TGFs and TEBs are also important targets of GECAM.

Received June 20, 2024

GECAM data and analysis software have been released at: http://gecam.ihep.ac.cn/grbDataAnalysisSoftware. jhtml.

2 GRB

GRB is the most violent stellar explosive phenomenon in the universe which can last from a few milliseconds to hours. Long GRBs, whose duration is over 2 seconds, originate from the collapse of massive stars, while short GRBs, lasting less than 2 seconds, are believed to result from the merger of binary neutron stars or a neutron star and a black hole. GRBs from the compact merger are likely associated with GW signal.

2.1 "BOAT"—GRB 221009A

GRB 221009A, as the brightest gamma-ray Burst Of All Time (BOAT), was detected by many instruments in multi-wavelength. Most space gamma-ray telescopes suffered severe data saturation and instrumental effects during the main emission of GRB 221009A. Remarkably, GECAM-C provided the best measurement of this burst with accurate and high-resolution data without any instrumental effects[3].

Based on the joint analysis of GECAM-C and *Insight*/HXMT, a comprehensive and precise measurement of the BOAT GRB was achieved, including precursor, main burst, flare and the early afterglow. Especially GECAM-C provided the most precise observations of the extremely bright main burst[4]. The observations of GECAM-C and *Insight*/HXMT revealed that GRB 221009A has a record-breaking isotropic equivalent energy E_{iso} up to 10^{55} erg. In addition, a break in the flux light curve of the early afterglow was also discovered and is considered to be a jet break. Based on the time of this break, E_{iso}, and redshift of this GRB, the jet opening angle of the GRB 221009A was found to be only about 0.73 degrees[4].

Zheng *et al*. conducted a detailed joint analysis of the early afterglow of GRB 221009A from 660 to 1860 seconds after the trigger with the data from *Insight*/HXMT, GECAM-C, and *Fermi*/GBM[5]. They found that the early afterglow spectrum of GRB221009A has two components—a cutoff power- law with an additional power-law, forming a V shape. Additionally, by fitting the flux light curves in different energy bands, the break time is well consistent from keV to TeV, *i.e.* achromatic break feature, further confirming that it is a jet break. Interestingly, the analysis indicates that the slopes of the flux light curves before and after the break vary with energy, and tend to be consistent as the energy decreases. These observational results provide strong evidence that the jet of GRB 221009A is structured with an extremely narrow and bright core.

By taking the advantage of the unsaturated data of GECAM-C, Zhang *et al*. performed a comprehensive spectral analysis of GRB 221009A jointly with GECAM-C and *Fermi*/GBM data and found a series of emission lines up to about 37 MeV with a nearly constant ratio of the line width and line central energy in multiple time intervals including the brightest part of this burst[6]. Remarkably, they discovered that the central energy and the energy flux of emission lines follow a power-law decay with time, with power-law indices of

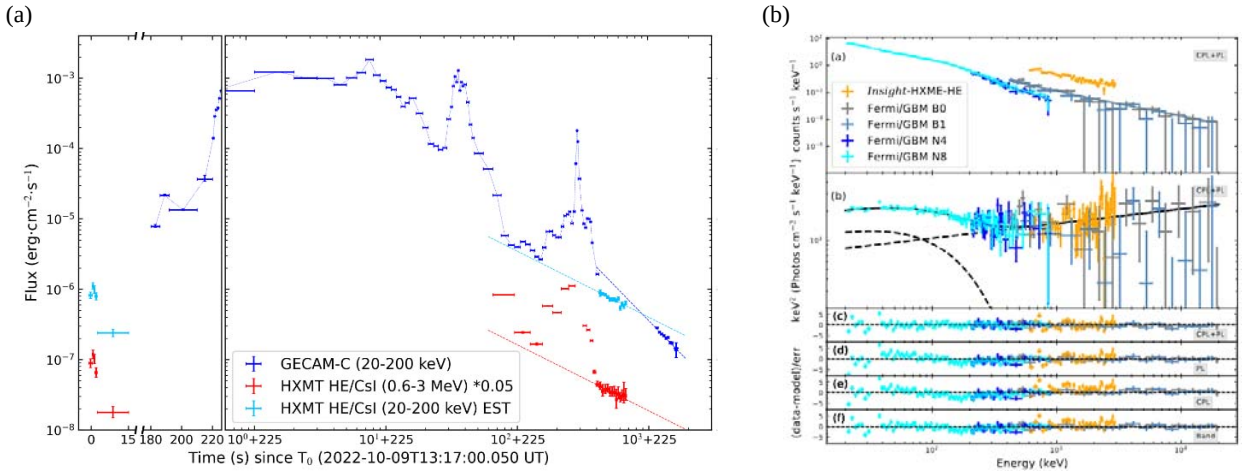

Fig.1 Left: The light curves of GRB 221009A[4]. Right: The spectra of the early afterglow of GRB 221009A[5]

–1 and –2, respectively. They suggest that the observed emission line could be explained as the blue-shifted of electron positron pair annihilation 511 keV line in the jet, thus the bulk Lorentz factor of the jet could be measured directly from the emission line for the first time during the prompt emission. They also reported a low significant absorption line in the GECAM data in this GRB. These discoveries of the spectral line features provide new insights into the physics of GRB and relativistic jets.

To investigate the time-resolved spectra of GRB 221009A, Yang *et al*. fit the GECAM-C and *Fermi*/GBM data with a synchrotron radiation model, assuming an expanding emission region with relativistic speed and a global magnetic field decaying with radius[7]. The results indicate that the spectra of this burst are consistent with a synchrotron origin from relativistic electrons accelerated at a large emission radius. The lack of thermal emission in the prompt emission spectra supports a Poynting flux-dominated jet composition.

2.2 The Second Brightest GRB—GRB 230307A

GRB 230307A is another important GRB, not only because it has the second-highest brightness[8], but also because it is a long-duration burst with merger origin. As an atypical long-short burst, GRB 230307A, along with GRB 211211A, represents a new type of type I GRB which could be associated with a GW event. The extremely high brightness also caused data saturation in other instruments, however, thanks to the dedicated design, both GECAM-B and GECAM-C accurately and completely recorded this profound burst without data problems, resulting in a series of important and interesting discoveries.

Sun *et al*. conducted a comprehensive analysis of the broad-band prompt emission of GRB 230307A based on the data from GECAM and LEIA[8]. They show that, despite of its apparently long duration, the properties of prompt emission and host galaxy suggest this GRB has a compact star merger origin, which is consistent with its association with a kilonova. Another interesting phenomenon was discovered in this peculiar GRB: as the gamma-ray radiation disappears, an extended X-ray radiation component appears, indicating the emergence of a magnetar central engine. Additionally, an achromatic temporal break in the hard x-ray light curves of GECAM during the prompt emission phase is identified, which is considered as an edge effect of the jet. This is the first time that such an effect is seen in the prompt emission phase and could be used to constrain the geometry of the jet.

In another study of this burst, Yi *et al*. noticed that the complex multi-peak structure in the light curve of GRB 230307A can be well-fitted by a Fast Rise Exponential Decay (FRED) function, and the spectrum shows a regular time evolution[9]. By fitting the light curves in different energy bands with FRED function, a clear spectral lag of the full FRED shape is found, while the spectral lag of the narrow pulses is negligible. Additionally, it was also discovered that the overall light curve exhibits self-similarity. These behaviors are difficult to be explained by the internal shock model, lending strong support to the ICMART model.

3 SGR

SGRs are repeated, intense bursts in the X-ray and soft gamma-ray bands from a special type of neutron stars with extremely strong magnetic fields (*i.e.* magnetar). Among those SGRs monitored by GECAM, SGR J1935+2154 is peculiar and well-known for its prolific bursts (also called X-Ray Burst, XRB) and for the first identification as the source of an FRB (*i.e.* FRB 200428). Importantly, GECAM also detected an XRB on Oct. 14, 2022 from SGR J1935+2154 which is associated with a radio burst[10], confirming the association between XRB and FRB.

Xie *et al*. collected an updated burst sample from SGR J1935+2154, including all bursts reported by *Fermi*/GBM and GECAM till 2022 January and the targeted-search bursts in the *Fermi*/GBM data from 2008 August to 2014 December[11]. They found that the bursts of SGR J1935+2154 exhibit a periodicity of about 126 days. Moreover, they suggest that this periodicity may be interpreted as the precession of the magnetar.

By using the Li-CCF, a novel cross-correlation function method, Xiao *et al*. conducted a spectral lag analysis of the burst sample from SGR J1935+2154 detected by several instruments including GECAM, and found that there is a linear relationship between the time lag and photon energy (the higher-energy photons arrive earlier)[12]. They also found that the distribution of the slopes of the linear relationship can be fitted with three Gaussians. This research shows that spectral lag analysis could serve as an important tool for understanding the radiation mechanism of SGRs.

The Minimum Variation Timescale (MVT) is an important probe for the physical mechanisms of SGR. Xiao *et al*. noticed that the peak of the MVT of SGR J1935+2154 is about 2 ms, based on data from GECAM, *Fermi*/GBM and *Insight*-HXMT[13]. This time scale corresponds to the emission region of about 600 km, which is comparable to the scale of the magnetosphere of a pulsar, lending supports to the magnetosphere origin of a magnetar burst. Just like spectral lag, the energy dependence of MVT of SGR is also different from that of GRB. These findings are very helpful to distinguish whether a burst originates from a magnetar or GRB.

Quasi-Periodic Oscillations (QPOs) have been reported in some magnetars. Xiao *et al*. employed a Power Density Spectrum (PDS) method to search for the QPOs in hundreds of XRBs from SGR J1935+2154 observed by GECAM, *Insight*-HXMT and *Fermi*/GBM from 2014 July to 2022 January[14]. Although no definitive QPO signal (significance >3σ) was detected in individual bursts or in the averaged periodogram of bursts grouped by duration, several bursts were identified as exhibiting features at about 40 Hz, which could be explained as the proximity intervals between adjacent pulses of XRB. This study also found that the distribution of the slopes of the PDS of this XRB sample peaks at about 2.5, which is consistent with other magnetars but higher than the commonly observed 5/3 in GRB.

In another study, Xiao *et al*. combined the above research results and found that the differential and cumulative distributions of MVT and spectral lag of SGR J1935+2154 follow the power-law model and the fluctuations in both parameters follow the Tsallis q-Gaussian distributions, with consistent q value across different scale intervals[15]. These results suggest that both the MVT and spectral lag are scale-invariant, providing new parameters for studying the Self-Organized Criticality (SOC) systems.

4 SFL and TGF

Thanks to its large field of view, GECAM can provide a nearly continuous monitoring of the Sun in hard X-ray and soft gamma-ray band. Besides, the usage of Charged Particle Detectors (CPD) makes GECAM has the ability to distinguish charged particles and high-energy photons, which is vital to observing the TGFs and TEBs from the Earth.

4.1 SFL

As a high-energy monitor for the Sun, GECAM features a very high temporal resolution (0.1 microseconds) and wide energy band (about 6 keV to 5 MeV). In addition, GECAM itself has the capability of localization to determine whether a burst comes from the Sun.

By investigating the high-time resolution data from GECAM of the M9.6 solar flare event on 2022 April 21 at 01:52 UTC, Zhao *et al*. discovered significant paired QPP with a short period in the precursor phase in hard X-ray band, which is very rare in the precursor phase[16]. The joint analysis of GECAM data and microwave data from NoRP and RSTN indicates that the precursor and impulsive phases of this eruption were generated by non-thermal electrons. Combining the image data of the Sun, the authors found that the observed properties of paired QPP are in good agreement with the scenario of the current loop coalescence model.

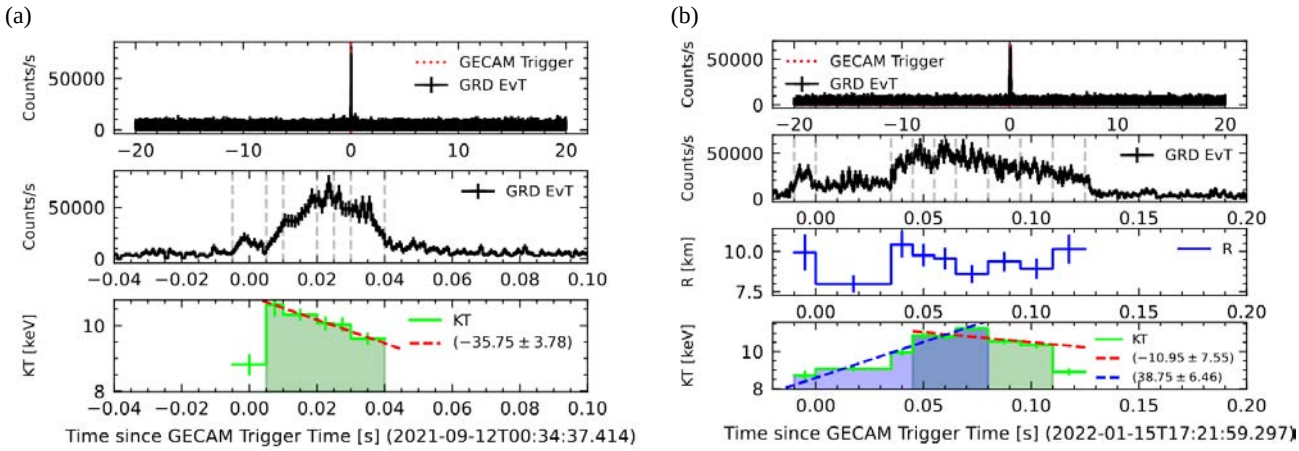

Fig.2 The light curves and the evolution of the Blackbody temperature (KT) with time of two bursts from SGR J1935+2154[12]: trigger time of burst is 2021-09-12T00:34:37.414 UTC for panel (a) and 2022-01-15T17:21:59.297 UTC for panel (b)

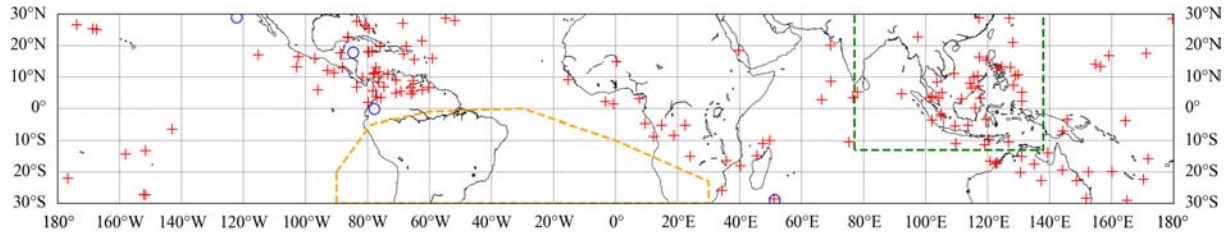

Fig.3 Geographical distribution of GECAM TGFs[17].

4.2 TGF

To measure and distinguish the TGFs and TEBs, dedicated designs have been implemented to GECAM, including the usage of both the Gamma-Ray Detector (GRD) and Charged Particle Detector (CPD) with high temporal resolution and short dead time.

Zhao *et al*. conducted a systematic search in the GECAM-B data from December 2020 to September 2022, and found 147 bright TGFs, 2 typical TEB events, and 2 special TEB-like events, corresponding to a discovery rate of about 200 TGFs per year for GECAM-B. The statistical properties such as the lightning- association ratio, duration, and hardness ratio were systematically investigated[17]. They found that there are some unique and interesting events, such as the double-peaked TGFs characterized by two about 100 μs pulses with very similar temporal and spectral structures, and the quadruple-peaked TEB-like events, which pose challenges in the understanding of such phenomena.

5 Summary

To monitor the gamma-ray transients especially the GWGRBs, GECAM was originally designed to be composed of two microsatellites to cover the full sky, *i.e*. GECAM-A and GECAM-B, which were launched on December 10, 2020. Now GECAM has grown to be a constellation of four instruments on different spacecrafts. Thanks to the dedicated design in the detector and electronics, GECAM showed its unique role in measuring the bright bursts with very high time resolution in a wide energy band. Indeed, GECAM has successfully and accurately measured the two brightest GRBs (GRB 221009A and GRB 230307A) without data saturation and other instrumental effects, resulting in fruitful achievements in understanding these two amazing events and GRB physics. Importantly, GECAM detected many SGR bursts including those associated with radio bursts from SGR J1935+2154. GECAM also made great contributions to the observation and study of SFL, TGF and TEB. Looking into the future, GECAM is expected to play an important role in the "multi- wavelength, multi-messenger" astronomy era.

References

[1] ABBOTT B P, ABBOTT R, ABBOTT T D, *et al*. Gravitational Waves and Gamma-Rays from a Binary Neutron Star Merger: GW170817 and GRB 170817A[J]. The Astrophysical Journal Letters,2017, 848, L13

[2] https://gcn.nasa.gov/circulars/21520

[3] https://gcn.nasa.gov/circulars/32751

[4] AN Z H, ANTIER S, BI X Z, *et al*. 2023, arXiv:2303.01203. doi:10.48550/arXiv.2303.01203

[5] ZHENG C, ZHANG Y Q, XIONG S L, *et al*. Observation of GRB 221009A Early Afterglow in X-Ray/Gamma-Ray Energy Bands[J]. The Astrophysical Journal Letters, 2024, 962, L2

[6] ZHANG Y Q, LIN H X, XIONG S L, *et al*. Observation of spectral lines in the exceptional GRB 221009A[J], Science China Physics, Mechanics, and Astronomy, 2024, 67, 289511

[7] YANG J, ZHAO X H, YAN Z, *et al*. Synchrotron Radiation Dominates the Extremely Bright GRB 221009A[J], The Astrophysical Journal Letters, 2023, 947, L11

[8] SUN H, WANG C W, YANG J, *et al*. 2023, arXiv:2307.05689. doi:10.48550/arXiv.2307.05689

[9] YI S X, WANG C W, SHAO X Y, *et al*. 2023, arXiv:2310.07205. doi:10.48550/arXiv.2310.07205

[10] WANG C W, XIONG S L, ZHANG Y Q, *et al*. 2022, The Astronomer's Telegram, 15682

[11] XIE S L, CAI C, XIONG S L, *et al*. Revisit the periodicity of SGR J1935+2154 bursts with updated sample[J]. Monthly Notices of the Royal Astronomical Society, 2022, 517, 3854

[12] XIAO S, TUO YL, ZHANG S N, *et al*. Discovery of the linear energy dependence of the spectral lag of X-ray bursts from SGR J1935+2154[J]. Monthly Notices of the Royal Astronomical Society, 2023, 521, 5308

[13] XIAO S, YANG J J, LUO X H, *et al*. The Minimum Variation Timescales of X-Ray Bursts from SGR J1935+2154[J]. The Astrophysical Journal Supplement Series, 2023, 268, 5

[14] XIAO S, LI X B, XUE W C, *et al*. Individual and averaged power density spectra of X-ray bursts from SGR J1935+2154: quasi-periodic oscillation search and slopes[J], Monthly Notices of the Royal Astronomical Society, 2024, 527, 11915

[15] XIAO S, ZHANG S N, XIONG S L, *et al*. The self-organized criticality behaviours of two new parameters in SGR J1935+2154[J]. Monthly Notices of the Royal Astronomical Society, 2024, 528, 1388

[16] ZHAO H S, LI D, XIONG SL, *et al*. Paired quasi-periodic pulsations of hard X-ray emission in a solar flare[J]. Science China Physics, Mechanics, and Astronomy, 2023, 66, 259611

[17] ZHAO Y, LIU J C, XIONG S L, *et al*. The First GECAM Observation Results on Terrestrial Gamma-Ray Flashes and Terrestrial Electron Beams[J]. Geophysical Research Letters, 2023, 50, 14

LUO Ziren, ZHANG Min, WANG Jianyu, WU Yueliang. Progress of Taiji-2 Project. *Chinese Journal of Space Science*, 2024, **44**(4)

Progress of Taiji-2 Project

LUO Ziren[1,2,3], ZHANG Min[1,2,4], WANG Jianyu[2,5], WU Yueliang[1,2,4]

1. Taiji laboratory for Gravitational Universe, University of Chinese Academy of Sciences, Beijing 100049
2. Hangzhou Institute for Advanced Study, University of Chinese Academy of Sciences, Hangzhou 310024
3. Institute of Mechanics, Chinese Academy of Sciences, Beijing 100190
4. International Center for Theoretical Physics Asia-Pacific, University of Chinese Academy of Sciences, Beijing 100190
5. Shanghai Institute of Technical Physics, Chinese Academy of Sciences, Shanghai 200083

Abstract

Taiji-2 project is the second step of Taiji program, which is to verify the required technology for Taiji-3 mission. The feasibility study of Taiji-2 is successfully finished, and some of the main progress is introduced here.

Key words

Gravitational wave, Taiji program, Taiji-2 project

Taiji is a Chinese space-borne Gravitational Wave (GW) detection program led by Chinese Academy of Sciences[1,2,3] and planned to be launched in 2030s. Taiji-1 satellite mission is the first step of Taiji program which was launched in 2019 [4]. The second step is to launch the Taiji pathfinder (also called Taiji-2) no later than 2030. The final step is to launch Taiji (also called Taiji-3), which is similar to the LISA constellation (see Figure 1). The purpose of Taiji-2 project is to verify thoroughly the required technology for Taiji-3 and may also produce limited scientific outcomes.

Taiji-2 is initially proposed to build a pair of satellite to test the whole key technology. These two satellites will be deployed in the heliocentric orbit, same as Taiji-3. The architecture of the platform and the design of the payload of Taiji-2 satellite will be made to be the same to Taiji-3 satellite for inheritance. On the other hand, if there could be a second party that can contribute another satellite, Taiji-2 would have the potential to form a 3-satellite-constellation as a mini Taiji-3. In that case, Taiji-2 could possess the capability to detect some supermassive black hole mergers, although it is designed to have a relaxed requirement of sensitivity.

The feasibility study of Taiji-2 was begun on 2020 and it was successfully completed on 2022. Taiji-2 now is ready to be approved for engineering phase. Some results of this feasibility study were gradually being published.

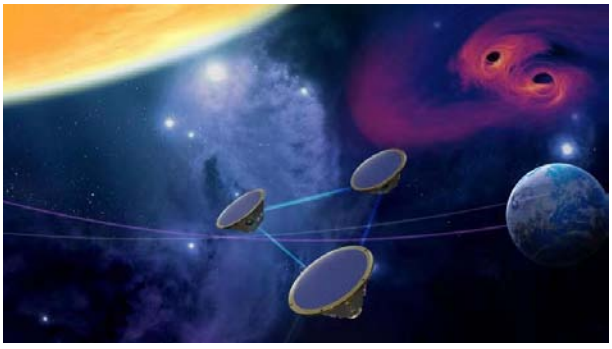

Fig.1 Taiji-3 constellation. Taiji-3 consists of 3 identical satellites which form a gigantic equilateral triangle. Each of the satellite takes an Earth-like heliocentric orbit. The constellation will be leading or trailing earth for about 18 degrees. Taiji-3 has the ability to detect the GW from intermediate or supermassive black hole mergers

Received June 20, 2024

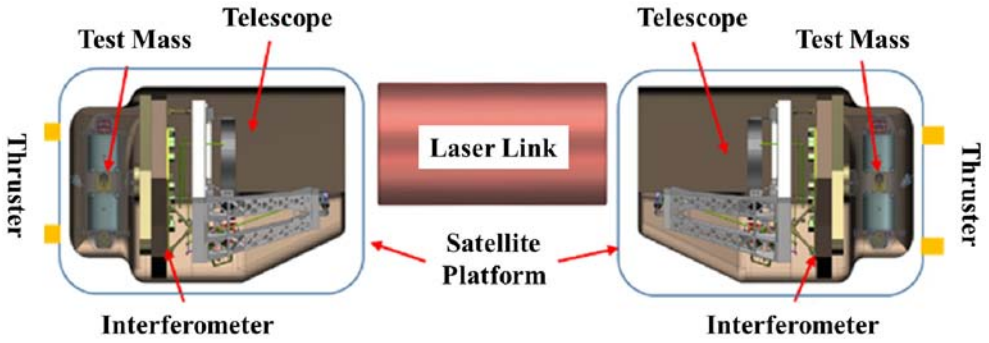

Fig.2 Taiji-2 satellites. The payload configuration of Taiji-2 satellite is designed to be the same as Taiji-3 in order to expand to 3-satellite constellation when there's second party to contribute additional satellite.

One of the significant progress of Taiji-2 feasibility study is parameter estimation of GW sources for space-borne gravitational wave detection missions such as LISA[5], Taiji[1,2,3] and Tianqin[6]. The team of Taiji data analysis has for the first time demonstrate the application of machine learning techniques, specifically the normalizing flows, in parameter estimation of massive black hole binary events[7]. Compare to traditional techniques, this method has remarkable speed that could be several orders faster (see Table 1). Notably, this approach remains resilient against challenges such as confusion noise and the intricacies of varying reference times, underscoring its reliability and potential for broader applications.

Table 1 Comparison of computational time required by different posterior sampling approaches to generate their respective samples

Sampling method	Numbers of samples	Run time/s	Time per sample/s
Nest sampling	11215	3000	0.26750
Normalization flow	10000	2.7	0.00027

The second progress is Taiji-2 payload integration scheme and its verification. During the feasibility study project, the team of Taiji-2 payload research had built and tested the prototype of laser interferometer, inter-satellite laser acquisition sub-system, inertial sensor, stable structure of satellite platform, micro-thruster and drag-free control unit (some of the prototypes were shown in Figure 3). One of the most challenging tasks is to evaluate the performance of inertial sensor due to its extreme sensitivity and complex disturbances on ground. To tackle this problem, a novel design of torsion balance with differential wave front sensing (DWS for short, see Figure 3b) was proposed[8] which can measure the test mass's acceleration to 3×10^{-13} m·s^{-2}·Hz$^{-1/2}$. Besides, an integration scheme for Taiji-2 payload was also studied (see Figure 3c). In order to test the integrate payload, a test bed was built and put into use in 2023[9]. It consists of two vacuum tanks that can fully test the inter-satellite interferometric ranging for Taiji-2 laser interferometer (see Figure 3d) with displacement and laser pointing jitter measurement ability to 100 pm·Hz$^{-1/2}$ and 100 nrad·Hz$^{-1/2}$ respectively.

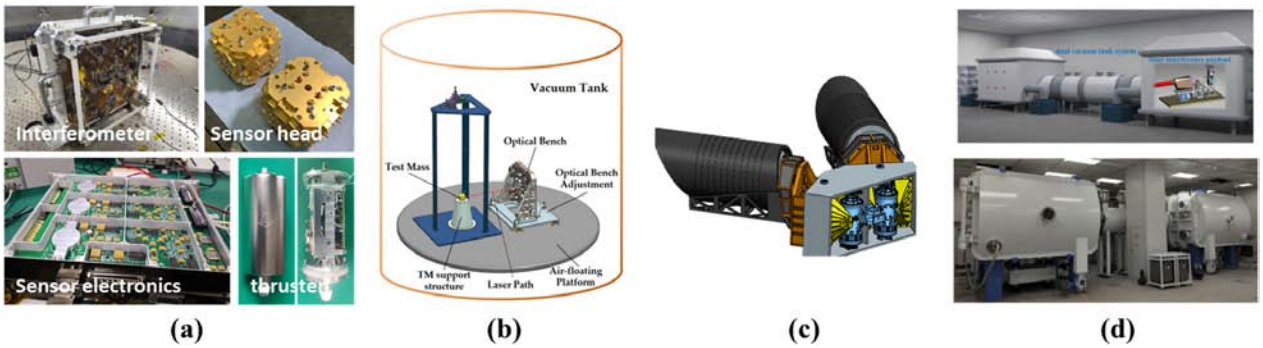

Fig. 3 (a) Taiji-2 payload prototypes. (b) The torsion balance with DWS technique. (c) The payload integration scheme. (d) The test bed for Taiji-2 inter-satellite laser interferometric ranging

Acknowledgements

The work was funded by the "Strategic Priority Research Program of the Chinese Academy of Science" (XDA15021100), the National Natural Science Foundation of China (NSFC) under Grant No. 12147103 and the Fundamental Research Funds for the Central Universities.

References

[1] HU W R, WU Y L. The Taiji Program in Space for gravitational wave physics and the nature of gravity [J]. *Natl. Sci. Rev.*, 2017, 4: 685-686

[2] LUO Z R, GUO Z K, JIN G, *et al*. A brief analysis to Taiji: Science and technology [J]. *Results in Physics*, 2020, **16**, 102918

[3] LUO Z R, JIN G, WU Y L, *et al*. The Taiji program: a concise overview[J]. *Progress of Theoretical and Experimental Physics*, 2020. DOI: 10.1093/ptep/ptaa083

[4] The Taiji Scientific Collaboration. China's first step towards probing the expanding universe and the nature of gravity using a space borne gravitational wave antenna[J]. *Communications Physics*, 2021, 4, 34

[5] AMARO-SEOANE, P, AUDLEY H, BABAK S, *et al*. Laser interferometer space antenna[J]. ArXiv preprint, 2017, 1702: 00786. https://arxiv.org/abs/1702.00786

[6] LUO J, CHEN L S, DUAN H Z, *et al*. TianQin: A space-borne gravitational wave detector. *Classical and Quantum Gravity*, 2016, **33**, 035010. DOI: 10.1088/0264-9381/33/3/035010

[7] DU M, LIANG B, WANG H, *et al*. Advancing space-based gravitational wave astronomy: Rapid parameter estimation via normalizing flows [J]. *Sci. China-Phys. Mech. Astron.*, (2024, **67**, 230412

[8] WANG S, LIU H, DAI L, *et al*. Using DWS Optical Readout to Improve the Sensitivity of Torsion Pendulum[J]. *Sensors*, 2023, **23**, 8087

[9] WANG Y, MENG L, XU X, *et al*. Research on semi-physical simulation testing of inter-satellite laser interference in the China Taiji space gravitational wave detection program[J]. *Appl. Sci.*, 2021, **11**, 7872

GUO Huadong, DOU Changyong, LIANG Dong, JIANG Nijun, TANG Yunwei, MA Wenyong. SDGSAT-1: Capabilities for Monitoring and Evaluating SDG Indicators. *Chinese Journal of Space Science*, 2024, **44**(4)

SDGSAT-1: Capabilities for Monitoring and Evaluating SDG Indicators

GUO Huadong[1,2,3*], DOU Changyong[1,2], LIANG Dong[1,2], JIANG Nijun[1,2], TANG Yunwei[1,2], MA Wenyong[1,2]

1. International Research Center for Big Data for Sustainable Development, Beijing 100094
2. Key Laboratory of Digital Earth Science, Aerospace Information Research Institute, Chinese Academy of Sciences, Beijing 100094
3. University of Chinese Academy of Sciences, Beijing 100049

Abstract

SDGSAT-1, the world's first science satellite dedicated to assisting the United Nations 2030 Sustainable Development Agenda, has been operational for over two and a half years. It provides valuable data to aid in implementing the Sustainable Development Goals internationally. Through its Open Science Program, the satellite has maintained consistent operations and delivered free data to scientific and technological users from 88 countries. This program has produced a wealth of scientific output, with 72 papers, including 28 on data processing methods and 44 on applications for monitoring progress toward SDGs related to sustainable cities, clean energy, life underwater, climate action, and clean water and sanitation. SDGSAT-1 is equipped with three key instruments: a multispectral imager, a thermal infrared spectrometer, and a glimmer imager, which have enabled ground-breaking research in a variety of domains such as water quality analysis, identification of industrial heat sources, assessment of environmental disaster impacts, and detection of forest fires. The precise measurements and ongoing monitoring made possible by this invaluable data significantly advance our understanding of various environmental phenomena. They are essential for making well-informed decisions on a local and global scale. Beyond its application to academic research, SDGSAT-1 promotes global cooperation and strengthens developing countries' capacity to accomplish their sustainable development goals. As the satellite continues to gather and distribute data, it plays a pivotal role in developing strategies for environmental protection, disaster management and relief, and resource allocation. These initiatives highlight the satellite's vital role in fostering international collaboration and technical innovation to advance scientific knowledge and promote a sustainable future.

Key words

SDGSAT-1, Earth observation, Remote sensing, SDGs

1 Introduction

In 2015, the United Nations (UN) established an ambitious development roadmap for global society, the 2030 Agenda for Sustainable Development, which contains 17 Sustainable Development Goals (SDGs). To achieve them by 2030, this framework includes a wide range of broad goals and related targets that promote peace, prosperity, and sustainability for both people and the planet. Lack of data on SDG indicators still remains an important limitation, as only 138 of the 168 SDG indicators have sufficient data for their assessment. It is es-

Received June 20, 2024

timated that approximately 85% of the monitored indicators do not meet their defined schedules or show deterioration[1]. Without sufficient data, it has been difficult to understand the full scope of sustainability challenges, and all stakeholders, from governments to NGOs, struggle to make informed decisions and effective policies for the SDGs. For example, the lack of precise data on emissions and environmental changes makes it difficult to gauge the real impact of sustainability initiatives on climate action. Access to accurate, real-time data is therefore important to bridging the data gap and empowering stakeholders to make substantial efforts toward the SDGs.

Over the past several decades, Earth observation (EO) technology has improved the coverage and quality of reliable, structured data, offering critical data beyond the reach of standard ground monitoring methods. Particularly, continuous monitoring of Earth's surface through various satellite observation systems over several decades has proven to be very useful in tracking changes over time and provides continuous temporal data, critical for tracking long-term trends in climate change, urban development, deforestation, and other key indicators required by the SDGs[2]. The development of Earth observation satellite platforms is a specialized domain. However, research and development efforts aimed at improving spatial, radiometric, and temporal resolutions of these platforms offer cost-effective solutions to global data challenges. These advancements enhance capabilities and opportunities for adding value to datasets through multi-source data integration, providing novel ways to study and understand complex global issues, and facilitating more targeted and realistic sustainability plans[3].

The United Nations General Assembly approved the 2030 Agenda for Space, recognizing the importance of space technology and emphasizing its strategic importance for sustainable development. The Space2030 agenda explicitly emphasizes the importance of EO technology as a critical tool for monitoring and assessing worldwide environmental and development changes[4]. It encourages countries worldwide to invest in and use these modern tools to fulfill their sustainability goals. China took decisive actions to address data and implementation challenges for SDGs and in November 2021 launched the first science satellite dedicated to serving the 2030 Agenda and SDGs: Sustainable Development Science Satellite 1 (SDGSAT-1). China also set up the International Research Center of Big Data for Sustainable Development Goals (CBAS) in September 2021, following its announcement by President Xi Jinping during the 75th Session of The United Nations General Assembly. Building upon these achievements, China also expressed a strong commitment to facilitate global efforts toward developing a constellation of SDG satellites in collaboration with partners. This was highlighted as one of the deliverables of the multilateral High-level Dialogue on Global Development (2022): "Launching a Sustainable Development Satellite Constellation Plan, developing and sharing data and information for Sustainable Development Goal monitoring"

Operating SDGSAT-1, CBAS has been at the forefront of utilizing space-based tools to advance global efforts in deploying modern technology for sustainable development. CBAS has demonstrated successful use cases of SDGSAT-1 to monitor SDGs. Equipped with advanced sensing technology, SDGSAT-1 is tailored to monitor the interaction between human activity and Earth's environment[2] and has been used to analyze environmental change, urban expansion, agricultural productivity, and other SDG-related issues. CBAS, through its SDGSAT-1 programs and research efforts, has expanded the availability of high-quality data and made significant contributions to support global efforts to accomplish the SDGs by providing stakeholders with the knowledge to make informed decisions and properly monitor their impact.

2 SDGSAT-1 Mission Overview

SDGSAT-1 has maintained a stable operation status since its launch, providing a steady stream of data daily. With a sun-synchronous orbit at an altitude of 505 km and an inclination angle of 97.5°, the revisit period of SDGSAT-1 is approximately 11 days. The swath width of the imagery acquired by all three sensors is 300 km. The spatial resolution for the Thermal Infrared Spectrometer (TIS) is 30 m, while the MSI provides a spatial resolution of 10 m. GLI has three RGB bands at a spatial resolution of 40 m and one high-resolution panchromatic band at a spatial resolution of 10 m. The primary technical parameters of all three SDGSAT-1 sensors are in Table 1. For a more detailed description of

Table 1 Technical parameters of three instruments onboard SDGSAT-1

Instrument	Parameter	Specification and unit
Multispectral imager	Swath width	300 km
	Spatial resolution	10 m
	Bands and central wavelengths	Band 1 (deep blue): 400.63 nm Band 2 (deep blue): 438.47 nm Band 3 (blue): 495.10 nm Band 4 (green): 553.23 nm Band 5 (red): 656.75 nm Band 6 (red edge): 776.12 nm Band 7 (near-infrared): 854.02 nm
Thermal infrared spectrometer	Swath width	300 km
	Spatial resolution	30 m
	Bands and central wavelengths	Band 1: 9.35 μm Band 2: 10.73 μm Band 3: 11.72 μm
Glimmer imager	Swath width	300 km
	Spatial resolution	Panchromatic: 10 m, RGB: 40 m
	Bands and central wavelengths	Blue band: 478.87 nm Green band: 561.20 nm Red band: 734.25 nm Panchromatic band: 680.72 nm

the satellite platform and subsystems, refer to the corresponding chapters by Guo *et al*.[5,6] in previous Space Science Activities in China National Reports.

The data quality of all three data types has been routinely evaluated and improved after the successful launch of SDGSAT-1 on November 5, 2021. Relying on the accurate imaging of the Earth's surface, MSI has been used for various SDG applications. MSI absolute calibration coefficients for converting Digital Number (DN) data to apparent radiance were derived by a field radiometric calibration experiment conducted at the Dunhuang calibration site. They were cross-validated against Sentinel-2A Multispectral Instrument and Landsat 8 Operational Land Imager data[7]. The SDGSAT-1 Data Users Handbook[8] clearly states the procedures, parameters, and other considerations required to further transform the radiance to apparent reflectance.

Thermal infrared data sourced from SDGSAT-1 can accurately depict the thermal environments of ground cover and is crucial for deriving Land Surface Temperature (LST) and Land Surface Emissivity (LSE). The radiometric calibration conditions of TIS have been systematically evaluated[9] and measures have been developed to improve the TIS data quality, including on-orbit image quality evaluation[10], an enhanced image stitching method that mitigates geometric distortion present in the wide-swath TIS image[11]. Researchers have also developed an upgraded image restoration method improving its efficiency and standing out among other state-of-the-art methods[12]. The LSE retrieved from TIS data was empirically proven to have a quality consistent with LSEs retrieved from Landsat 8 and MODIS data[13]. Considering the well-established applications of thermal infrared data provided by Landsat 8 and MODIS, high-resolution SDGSAT-1 thermal infrared data has the potential to advance the research on regional energy balance, urban heat islands, retrieval of evapotranspiration, and land surface materials analysis.

Researchers have also thoroughly structured the calibration of DN values of GLI data into radiance, leading to a good correlation between GLI data and the Day-Night Band (DNB) data of the Visible Infrared Imaging Radiometer Suite (VIIRS)[14]. GLI data provides an important source of observations for nighttime human activity. Furthermore, de-noising and de-striping algorithms were proposed to address the high background noise and stripes in the GLI data[15-17]. Additionally, selecting an appropriate pan-sharpening method for GLI data has also been in development[18].

3 Advancing SDG Applications through the SDGSAT-1 Open Science Program

3.1 SDGSAT-1 Open Science Program

In September 2022, CBAS launched the SDGSAT-1 Open Science Program (www.sdgsat.ac.cn), offering

free access to SDGSAT-1 data to support global progress toward the SDGs. The program fosters multidisciplinary SDG research and addresses data gaps that hinder the implementation of the SDGs. As of April 2024, the program has accumulated 1,500 data users across 88 countries, resulting in over 16,000 image downloads. In addition to accessing archived data of past missions, users can submit observation plans corresponding to specific mission needs, with the SDGSAT-1 operation team adjusting the satellite operation accordingly.

As shown in Figure 1, the SDGSAT program has produced numerous publications in various areas of sustainable development, which aligns with the satellite's broad impact on academic research. As of the end of April 2024, there are 72 articles related to SDGSAT-1, including 28 articles on data processing and 44 on SDG monitoring and evaluation applications. More than half of the articles were published in "Remote Sensing", "Remote Sensing of Environment", and "International Journal of Digital Earth". Among the data processing articles, over 50% focus on data preprocessing techniques, registration, and correction techniques, followed by data calibration and validation, as well as quality enhancement. In the SDG monitoring and evaluation articles, research on SDG 11 receives the most attention. It covers the broadest range of objectives, followed by studies on SDG 7 and SDG 14, with SDG 13 and SDG 6 closely following. In terms of payload usage in published articles, the GLI sensor receives the most attention, accounting for 57%, which underscores its potential for sustainable cities (SDG 11), clean energy (SDG 7), and underwater life (SDG 14). Next is the thermal infrared sensor, primarily showcasing its ability to finely characterize heat sources.

3.2 Emerging SDG Applications

As of April 2024, research projects utilizing SDGSAT-1 imagery are gaining increasing influence in the study of SDGs, particularly within the research communities focused on SDG 6 (Clean water and sanitation), SDG 9 (Industry, innovation, and infrastructure), SDG 11 (Sustainable cities and communities), and SDG 13 (Climate action).

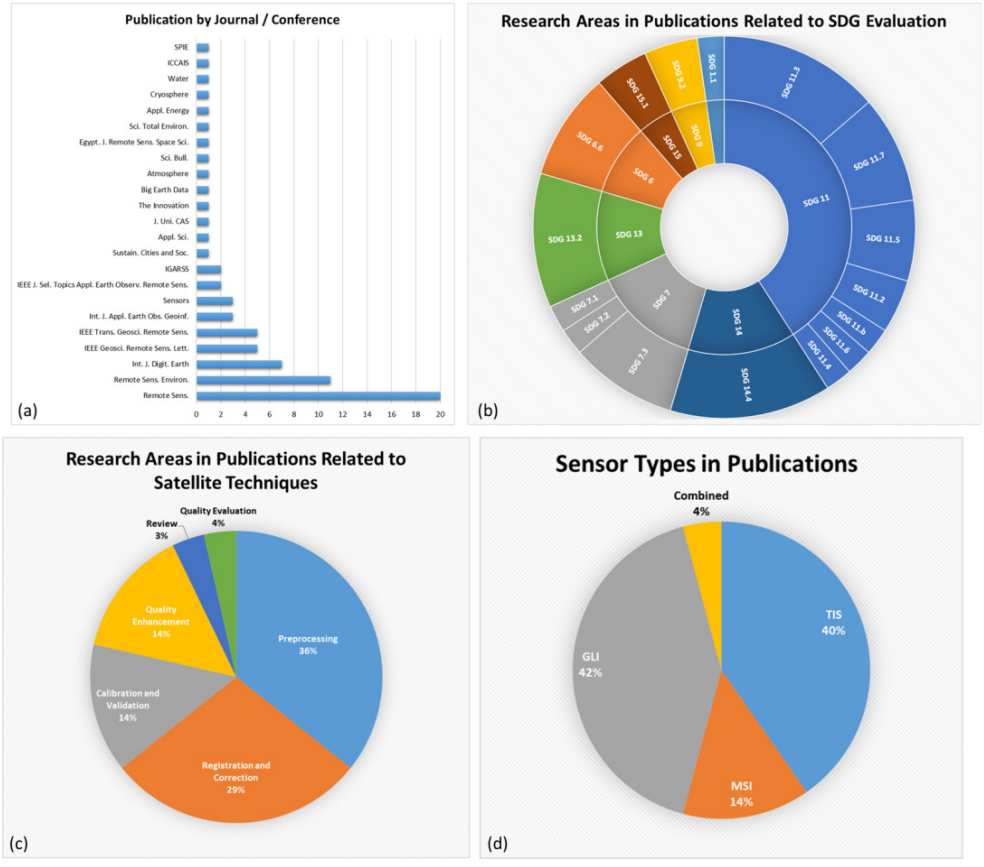

Fig. 1 Statistics of public articles

3.2.1 SDG 6 Clean water and sanitation

SDGSAT-1 MSI and TIS data have proven valuable proxies for water quality analysis, supporting the implementation of SDG target 6.1 (Safe and affordable drinking water). Figure 2 depicts the red tide near the coast of Huizhong City from a study on red tide index using SDGSAT-1 MSI data conducted by Wang *et al*.[19]. Additionally, MSI-based studies on water quality parameters such as Suspended Sediment Concentration (SSC)[20], Optical Water Type (OWT)[21], and suspended matter concentration (C_{tsm})[22], along with TIS-based sea surface temperature retrieval[23], have introduced methods for water quality analysis using SDGSAT-1 data.

3.2.2 SDG 9 Industry, Innovation, and Infrastructure

To address the significant environmental challenges posed by industrial activities, SDG target 9.4 (Upgrade all industries and infrastructures for sustainability) appeals to the monitoring of industrial processes and emissions. However, in situ surveillance of factories may encounter challenges such as high costs of materials and human resources and inconclusive or false results due to deliberate evasion of inspection. SDGSAT-1 offers an effective alternative for capturing distinctive industrial thermal signals using its TIS. Figure 3 shows a cluster of factories in Tangshan City, China, which have high thermal signals compared with the landmass and the sea surface. In a study locating industrial heat sources in the Beijing–Tianjin–Hebei Region, high- resolution TIS data helps identify industrial heat sources with low heat emissions and small spatial coverage[24]. Furthermore, the sensitivity of TIS data to heat anomalies has facilitated its application in detecting thermal discharge from nuclear power stations[23].

3.2.3 SDG 11 Sustainable Cities and Communities

With more than half of the global population residing in cities and the concentration of socioeconomic activities in urban centers, it is crucial to trace human activity within these areas accurately. Disasters, air and light pollution, and climate changes can have disproportionately large impacts on the urban population, underscoring the importance of SDG target 11.5, “Reduce the adverse effects of natural disasters”.

Fig. 2 SDGSAT-1 MSI true RGB image (band combination: 5-4-3) of the red tide observed off the coast of Huizhou City, Guangdong Province, China, captured on Mar. 11, 2022

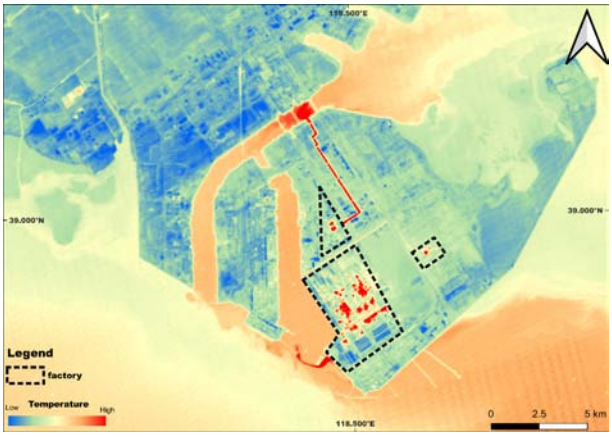

Fig. 3 SDGSAT-1 TIS Band 2 nighttime imagery showing coastal factories in Tangshan City, Hebei Province, China, on Jan. 10, 2024. Heat sources within the factory perimeters are visible in the imagery. Water bodies around factories also have an elevated temperature relative to their surrounding environments

Damage to power grids and buildings caused by earthquakes, flooding, and other natural disasters can be assessed by comparing pre-disaster and post-disaster glimmer images. Previous generations of nighttime light sensors, such as the VIIRS with a spatial resolution of 500 m, cannot capture nighttime light dynamics at a fine scale. In contrast, SDGSAT-1 GLI has a maximum resolution of 10 m, the highest among contemporary freely available data sources, enabling it to capture the status of nighttime light at a neighborhood level. The ability of SDGSAT-1 glimmer data to assess the destruction of disasters has been proven in damage assessment research and reports of the 2023 Turkey-Syria earthquake[25,26], the 2023 Libya flooding[27], the 2023 Sudan

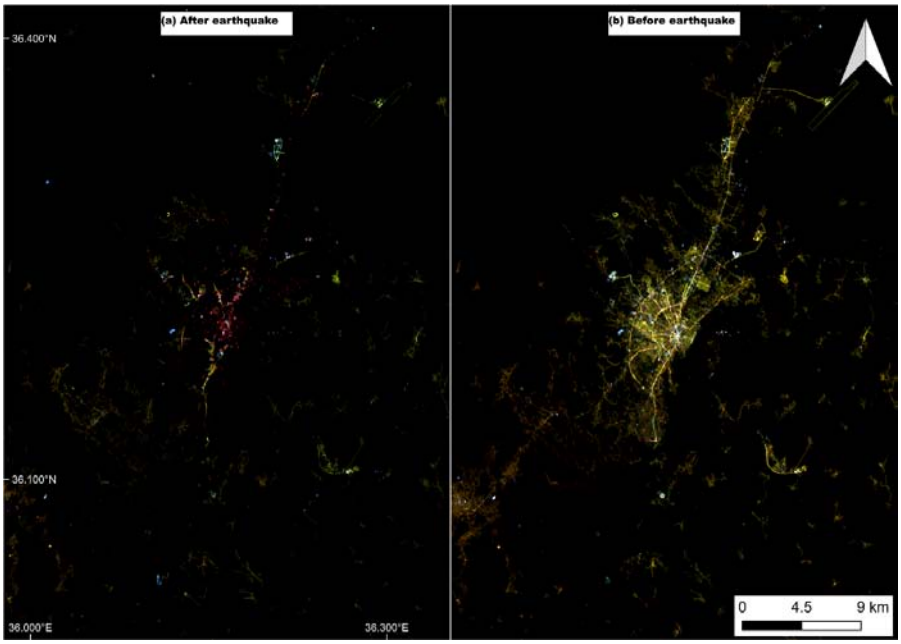

Fig. 4 The comparison between SDGSAT-1 GLI imagery of Antakya, Hatay Province, Turkey, before and after the 2023 Turkey-Syria earthquakes. (a) RGB (band combination: 1-2-3) nighttime GLI imagery captured on Feb. 12, 2023, after the earthquake, (b) RGB (band combination: 1-2-3) nighttime GLI imagery captured on Aug. 22, 2022, before the earthquake, depicting bright nighttime light from roads and urban areas with precise details

conflicts[28], and the 2023 Gansu earthquake[29]. For example, Figure 4 shows that Antakya, Turkey, experienced a significant light loss after the 2023 Turkey-Syria earthquakes that occurred on Feb. 6, 2023.

The RGB band configuration of the GLI facilitates in-depth analysis of the distribution of different artificial light sources and Correlated Color Temperature (CCK). Thus, extensive applications of SDGSAT-1 for light pollution and light source studies[30-33] have been conducted, and a light pollution map of the Iberian Peninsula, Canary Islands, Balearic Islands, and Madeira has been published through cooperation between the Complutense University of Madrid and CBAS[34].

3.2.4 SDG 13 Climate Action

The accumulation of greenhouse gases has warmed and altered Earth's climate significantly over the course of a century. As temperature and climate become increasingly unpredictable, the disasters associated with climate change, such as wildfires and flooding, become more frequent and severe[35,36]. Building a comprehensive mechanism to record the severity of climate-related disasters, climate change phenomena, and their impacts on population can contribute to SDG targets 13.1 (Strengthen resilience and adaptive capacity to climate-related disasters) and 13.2 (Integrate climate change measures into policy and planning).

Sea ice dynamics in the polar regions are closely associated with global warming in a positive feedback loop[37]. SDGSAT-1 wide-swath high-resolution TIS data has the capability to detect previously hard-to-trace small ice leads in polar regions, contributing additional insights for monitoring sea ice changes[38]. In Figure 5, the considerable temperature difference between ice sheets and seawater makes gaps and fractures between sea ice obvious.

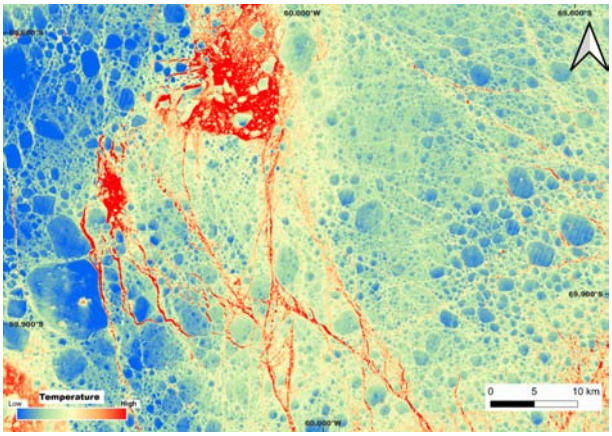

Fig. 5 SDGSAT-1 TIS Band 2 imagery of the sea ice distribution near the Antarctic Peninsula. Imaging date: Feb. 16, 2023

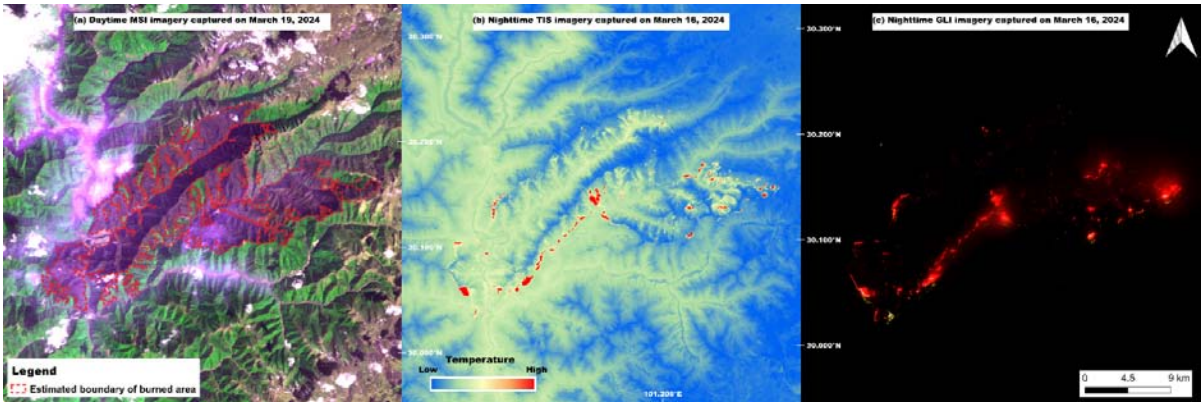

Fig. 6 SDGSAT-1 three-sensor synergetic observation of the 2024 Ganzi forest fire. (a) MSI pseudo-RGB image (band combination: 5-6-3) captured on Mar. 19, 2024, of burned areas near Yajiang County, Ganzi Prefecture, Sichuan Province, China. (b) TIS Band 2 nighttime imagery of the same area was captured on Mar 16, 2024. (c) GLI nighttime imagery (band combination: 1-2-3) captured on Mar. 16, 2024, of the same location.

CBAS has conducted an experimental study applying synergetic observation of three SDGSAT-1 sensors to observe the spread of a forest fire. Figure 6 illustrates the observation of the 2024 Ganzi forest fire using all three sensors. In the daytime MSI imagery (Figure 6a), burned areas differ from their surrounding environments. The nighttime observation of the regions around Yajiang County on March 16, 2024 (Figure 6b), shows that TIS data is sensitive to high temperatures. GLI images (Figure 6c) captured synchronously with the TIS data were clearly able to delineate fire locations for observing nighttime forest fires.

4 Conclusion

SDGSAT-1 has played a pioneering role in addressing the data gaps that have impeded advancements in the United Nations Sustainable Development Goals (SDGs). Being the first scientific satellite to facilitate progress toward the 2030 Agenda, SDGSAT-1 has showcased the significant capabilities of Earth observation technology in tracking and assessing efforts toward sustainable development across various sectors. The Open Science Program of SDGSAT-1 has cultivated a worldwide network of researchers who are actively employing its data to create new techniques and solutions for different SDG targets and indicators. This initiative has produced numerous scientific papers demonstrating the satellite's adaptability in analyzing water quality, identifying industrial heat sources, evaluating disasters, examining light pollution, and monitoring climate change.

The ability to successfully integrate space technology with sustainable development goals is demonstrated by SDGSAT-1's ongoing success. The information acquired from this mission is essential for developing policies and plans that address disaster risk reduction, environmental preservation, and socioeconomic inequality. Moreover, the data and methods developed are critical in supporting international innovation and collaboration, strengthening international efforts to accomplish the SDGs. The ability to improve and broaden these strategies as we use the data supplied by SDGSAT-1 will enable more focused and efficient actions, thereby reinforcing satellite technology's position as a key component in the worldwide effort to achieve sustainability. SDGSAT-1's legacy will be used to demonstrate the advancements in satellite and Earth observation technology and provide guidance for other missions that will deepen our knowledge and improve our ability to manage Earth's resources. Developing space-based observational capabilities provides countries worldwide with the essential instruments needed to manage sustainable development challenges in a dynamic world.

Acknowledgments

The authors wish to thank the CASEarth Small Satellite research teams of the CASEarth project and SDGSAT-1 Engineering Project teams for their continuous efforts and contributions.

References

[1] United Nations. Sustainable Development Goals Progress Chart 2023[R]. New York: United Nations, 2023

[2] GUO H, DOU C, CHEN H, LIU J, FU B, LI X, *et al*. SDGSAT-1: The world's first scientific satellite for sustainable development goals[J]. *Science Bulletin*. 2023, 68(1): 34-8
[3] ESA. Earth observation for SDG: Compendium of Earth Observation contributions to the SDG targets and Indicators[R]. Frascati: ESA Centre for Earth Observation, 2021
[4] United Nations. The "Space2030" Agenda: space as a driver of sustainable development[R]. New York: United Nations, 2021
[5] GUO H, CHEN H, CHEN L, FU B. Progress on CASEarth Satellite Development[J]. *Chinese Journal of Space Science*. 2020, 40(5): 120-30
[6] GUO H, DOU C, CHEN H, FU B. Progress of SDGSAT-1 Mission[J]. *Chinese Journal of Space Science*. 2022, 42(4): 44-8
[7] CUI Z, MA C, ZHANG H, HU Y, YAN L, DOU C, *et al*. Vicarious Radiometric Calibration of the Multispectral Imager Onboard SDGSAT-1 over the Dunhuang Calibration Site, China[J]. *Remote Sensing*. 2023, 15(10): 2578
[8] CBAS. SDGSAT-1 Data Users Handbook[OL]. Beijing: CBAS, [cited 2024 April 26]. Available from: https://www.sdgsat.ac.cn/userGuide/document
[9] HU Y, LI XM, DOU C, JIA G, HU Z, XU A, *et al*. Absolute radiometric calibration evaluation of the thermal infrared spectrometer onboard SDGSAT-1[J]. *International Journal of Digital Earth*. 2023, 16(2): 4492-511
[10] QI L, LI L, NI X, ZHOU X, CHEN F. On-Orbit Spatial Quality Evaluation of SDGSAT-1 Thermal Infrared Spectrometer[J]. *IEEE Geoscience and Remote Sensing Letters*. 2022, 19: 1-5
[11] YANG L, LI X, JIANG L, ZENG F, PAN W, CHEN F. Resolution-Normalizing Image Stitching for Long-Linear-Array and Wide-Swath Whiskbroom Payloads[J]. I*EEE Geoscience and Remote Sensing Letters*. 2022, 19: 1-5
[12] QI L, ZHANG R, HU Z, LI L, WANG Q, NI X, *et al*. Fast Thermal Infrared Image Restoration Method Based on On-Orbit Invariant Modulation Transfer Function[J]. *IEEE Transactions on Geoscience and Remote Sensing*. 2024, 62: 5001015
[13] ZHONG X, ZHAO L, REN P, WANG J, LI Y, ZHANG X, *et al*. Land surface emissivity retrieval from SDGSAT-1: comparison of LSE products with different spatial resolutions[J]. *International Journal of Digital Earth*. 2024, 17(1): 2297940
[14] YAN L, HU Y, DOU C, LI X M. Radiometric Calibration of SDGSAT-1 Nighttime Light Payload[J]. *IEEE Transactions on Geoscience and Remote Sensing*. 2024, 62: 1-15
[15] LIU S, WANG C, CHEN Z, LI W, ZHANG L, WU B, *et al*. Efficacy of the SDGSAT-1 glimmer imagery in measuring sustainable development goal indicators 7.1. 1, 11.5. 2, and target 7.3. *Remote Sensing of Environment*[J]. 2024, 305: 114079
[16] WANG N, HU Y, LI XM, LAN Y, KANG C, YAN L, *et al*. Enhancing SDGSAT-1 night light images using a panchromatic guidance denoising algorithm[J]. *International Journal of Applied Earth Observation and Geoinformation*. 2024, 128: 103748
[17] ZHANG D, CHENG B, SHI L, GAO J, LONG T, CHEN B, *et al*. A Destriping Algorithm for SDGSAT-1 Nighttime Light Images Based on Anomaly Detection and Spectral Similarity Restoration[J]. *Remote Sensing*. 2022, 14(21): 5544
[18] LI H, JING L, DOU C, DING H. A Comprehensive Assessment of the Pansharpening of the Nighttime Light Imagery of the Glimmer Imager of the Sustainable Development Science Satellite 1[J]. *Remote Sensing*. 2024, 16(2): 245
[19] WU J, YE H, LIU Y, SHI J, WANG F, CHEN C, *et al*. The Evaluation of MII/SDGSAT-1 in Red Tide Detection Along the Guangdong Middle Coast[J]. *IEEE Geoscience and Remote Sensing Letters*. 2023, 21: 1500305
[20] HOU Y, XING Q, ZHENG X, SHENG D, WANG F. Monitoring Suspended Sediment Concentration in the Yellow River Estuary and Its Vicinity Waters on the Basis of SDGSAT-1 Multispectral Imager[J]. *Water*. 2023, 15(19): 3522
[21] SANG R, WANG Y, ZHANG F, WANG S, LI J. A novel water optical types framework for Chinese inland waters with the application of multitype satellite sensor[J]. *International Journal of Digital Earth*. 2024, 17(1): 2327834
[22] HU X, LI J, SUN Y, BAO Y, SUN Y, CHEN X, *et al*. Retrieval of Total Suspended Matter Concentration Based on the Iterative Analysis of Multiple Equations: A Case Study of a Lake Taihu Image from the First Sustainable Development Goals Science Satellite's Multispectral Imager for Inshore[J]. *Remote Sensing*. 2024, 16(8): 1385
[23] HUANG W, JIAO J, ZHAO L, HU Z, PENG X, YANG L, et al. Thermal Discharge Temperature Retrieval and Monitoring of NPPs Based on SDGSAT-1 Images[J]. *Remote Sensing*. 2023, 15(9): 2298
[24] WANG D, XIE Y, MA C, ZHAO Y, YAN D, CHEN H, *et al*. Identification of Industrial Heat Source Production Areas Based on SDGSAT-1 Thermal Infrared Imager[J]. *Applied Sciences*. 2024, 14(6): 2450
[25] LEVIN N. Using Night Lights from Space to Assess Areas Impacted by the 2023 Turkey Earthquake[J]. *Remote Sensing*. 2023, 15(8): 2120
[26] YU B, CHEN F, WANG N, WANG L, GUO H. Assessing changes in nighttime lighting in the aftermath of the Turkey-Syria earthquake using SDGSAT-1 satellite data[J]. *The Innovation*. 2023, 4(3): 100419
[27] CBAS, UNOSAT. Night-Time Light Loss Assessment in Derna & Al Bayda (Libya) using Nighttime Light Imagery[OL]. Geneva: UNOSAT, [cited 2024 April 26]. Available from: https://unosat.org/products/3678
[28] UNOSAT. Power Outage Assessment in Sudan using Night-time Light Imagery[OL]. Geneva: UNOSAT, [cited 2024 April 26]. Available from: https://unosat.org/products/3625
[29] CBAS, IRDR. Analysis of Gansu Jishishan earthquake based on nighttime light[OL]. Geneva: UNDRR, [cited 2024 April 26]. Available from: https://www.preventionweb.net/publication/analysis-gansu-jishishan-earthquake-based-nighttime-light
[30] JIA M, ZENG H, CHEN Z, WANG Z, REN C, MAO D, *et al*. Nighttime light in China's coastal zone: The type classification approach using SDGSAT-1 Glimmer Imager[J]. *Remote Sensing of Environment*. 2024, 305:114104
[31] GUO B, HU D, ZHENG Q. Potentiality of SDGSAT-1 glimmer imagery to investigate the spatial variability in nighttime lights[J]. *International Journal of Applied Earth Observation and Geoinformation*. 2023, 119: 103313
[32] LIN Z, JIAO W, LIU H, LONG T, LIU Y, WEI S, et al. Modelling the public perception of urban public space lighting based on sdgsat-1 glimmer imagery: A case study in Beijing, China[J]. *Sustainable Cities and Society*. 2023,88:104272
[33] LIU S, ZHOU Y, WANG F, WANG S, WANG Z, WANG Y, et al. Lighting characteristics of public space in urban functional areas based on SDGSAT-1 glimmer imagery: A case study in Beijing, China[J]. *Remote Sensing of Environment*. 2024,306:114137
[34] Complutense University of Madrid, CBAS. High-resolution calibrated light pollution map of the Iberian Peninsula[OL]. Madrid: Complutense University of Madrid, [cited 2024 April 26]. Available from: https://pmisson.users.earthengine.app/view/sdgsat-1-p- iberica
[35] SENANDE-RIVERA M, INSUA-COSTA D, Miguez-Macho G. Spatial and temporal expansion of global wildland fire activity in response to climate change[J]. *Nature Communications*. 2022, 13(1): 1208
[36] TABARI H. Climate change impact on flood and extreme precipitation increases with water availability[J]. *Scientific reports*. 2020, 10(1): 13768
[37] WUNDERLING N, WILLEIT M, DONGES J F, Winkelmann R. Global warming due to loss of large ice masses and Arctic summer sea ice[J]. *Nature Communications*. 2020, 11(1): 5177.
[38] QIU Y, LI XM, GUO H. Spaceborne thermal infrared observations of Arctic sea ice leads at 30 m resolution[J]. *The Cryosphere*. 2023, 17: 2829-49

GAN Weiqun. Progress Report on ASO-S: 2022–2024. *Chinese Journal of Space Science*, 2024, **44**(4)

Progress Report on ASO-S: 2022–2024*

GAN Weiqun

Key Laboratory of Dark Matter and Space Astronomy, Purple Mountain Observatory, Chinese Academy of Sciences, Nanjing 210023

Abstract

The Advanced Space-based Solar Observatory (ASO-S) marked China's first comprehensive solar mission in space. Drawing upon the previous reports covering 2018–2020 and 2020–2022, we present here an update on the ASO-S made from 2022 to 2024. In August 2022, ASO-S completed its Phase D study and was successfully launched on October 9, 2022. The commissioning phase was carried out and concluded within the first nine months following the launch. The data and associated analysis software have been opened to the community and the research on the early ASO-S data has been well developed. We anticipate also the achievements in data research pertaining to ASO-S in the near future.

Key words

Space astronomy, Solar physics, Spacecraft

1 Introduction

As a part of the CNCOSPAR national report series, this is the third report dedicated to detailing the advancements of the ASO-S project. Our first report[1] provided an overview of ASO-S's history, the Phase-B study, and aspects of the Phase-C study. In our second report[2], we elaborated on the later stages of the Phase-C study and portions of the Phase-D study. This report continues to document briefly the progress of ASO-S from 2022 to 2024, encompassing the conclusion of Phase-D, the launch, commissioning, and early observational research linked to ASO-S. For more detailed descriptions of the ASO-S, readers are encouraged to refer to references [3]~[7].

2 Late Phase-D Study

The official Phase-D study ran from September 2021 to August 2022. The last report[2] outlined the progress of Phase D until March 2022. As per the plan, after the delivery of each of well-established subsystems, in May 2022 the integration of the entire system commenced smoothly. Subsequently, the final tests encompassing the environment, performance, communication, and so on were successfully conducted. By the end of August 2022, the mission successfully concluded its Phase-D study and was packaged, and ready for transportation to the launch site in Jiuquan, Gansu province. Shortly after, in early September 2022, ASO-S was safely flown to Jiuquan.

3 Launch and Commissioning Phase

After approximately one month of regular preparation and testing at the launch site, the ASO-S was success-

* Supported by the Strategic Priority Research Program of the Chinese Academy of Sciences (XDB0560000, XDA15320000), the National Key R&D Program of China (2022YFF0503002), and the National Natural Science Foundation of China (12233012, 12333010, 11921003)

Received May 6, 2024

fully launched at 07:43 Beijing time on October 9, 2022. Following the launch, the ASO-S was given a Chinese nickname, "Kuafu-1", named after a character in a well-known Chinese mythological story who pursued the Sun in an attempt to capture it. On November 23, 2022, the national media reported the first hard X-ray images of solar flares captured by HXI. Then, on December 13, 2022, all the initial images obtained by FMG, HXI, and LST were collectively displayed in the national media. Gan *et al.*[7] described the final status of the mission just before the launch as well as the first light images obtained by ASO-S.

The commissioning lasted over 9 months, longer than anticipated. The performance of the platform and HXI exhibited an excellent correlation with the designed and expected outcomes. For the FMG and LST, although they fulfilled almost all requirements, the FMG exhibited a dark region in its full-disc image and a loss of functionality in one of the liquid crystal components; on the other hand, the LST displayed a light leakage in the SCI and had a spatial resolution lower than expected for both the SDI and WST. Addressing these issues and determining their root causes took considerable time.

By the end of July 2023, when the commissioning was officially completed, the final status of all three payloads was as follows: the FMG provided routinely longitudinal magnetic field data for the local region, with accuracy comparable to or even exceeding that of the HMI; the HXI offers currently unique solar hard X-ray images from Earth's perspective, ranking among the top in the world in image quality; the LST, for the first time, captured routinely Lyman-alpha images of the entire disc, extending to 2.5 solar radius.

The details related to the commissioning for the FMG, HXI, and LST can be found in the papers by Bai *et al.*[8], Su *et al.*[9], and Chen, *et al.*[10], respectively. The latest status for Science Operation and Data Analysis Center (SODC) of ASO-S was presented by Huang *et al.*[11].

4 Research Organisation and Early Results

The scientific organization is a crucial component of the ASO-S project. Alongside the work surrounding SDOC and the release of the first ASO-S images to the public, on April 11~12, 2023, an international tutorial on ASO-S data was conducted online. Over 400 participants from 25 countries attended this meeting. During the event, Dr. Weiqun Gan, the Principal Investigator of the mission, presented the status of all three payloads in orbit and addressed relevant scientific issues such as data release and limitations, data policy, the ASO-S Guest Investigator Program (AGIP), and the ASO-S special issue on Solar Physics. Additionally, three payload data scientists, Drs. Yang Su, Li Feng, and Suo Liu (representing Jiangtao Su), demonstrated the data and software for HXI, LST, and FMG, respectively. A half-day practice session with a Q&A segment completed the tutorial in a closed loop. Since April 1, 2023, the entire data set from HXI, the local longitudinal magnetic field data from FMG, and the data of SDI and WST from LST have been freely accessible to the research community.

To encourage users to utilize ASO-S data, enhance scientific output, and foster closer international collaboration, the ASO-S team has launched the ASO-S Guest Investigator Program (AGIP) to the global solar community via the homepage at http://aso-s.pmo.ac.cn/english/science/asos_gip.jsp. Additionally, the first announcement was issued in international community media in April 2023. As of April 2024, approximately 11 proposals have been received, with 8 being approved. Successful applicants have visited or will visit, the Solar Data Operation Center (SDOC) at Purple Mountain Observatory since October 2023 for several months to conduct independent or collaborative research based on or related to ASO-S data. The program's effectiveness has been evaluated and has proven to be positive. The AGIP is expected to remain available at least until the end of 2025.

To foster analysis of ASO-S data among researchers, a joint science assembly between ASO-S and CHASE was successfully held in October 2023. Over 200 domestic participants attended the event, and approximately 100 oral presentations were made, covering topics related to ASO-S, CHASE, or both. Some of these talks were later submitted to a special issue on Solar Physics, entitled "ASO-S Mission: Inflight Performance and its Early Results", which opened in February 2023. By the deadline of March 15, 2024, a total of 31 papers had been submitted to the special issue. As of April 30, 2024, about 10 papers have been published or accepted, while the remaining are still under review. Additionally, over other ten papers related to ASO-S

data have been submitted to other journals, which are either published or under review. Among these early results, beyond calibration and orbital testing, we can see some noteworthy findings, like the work on the WLFs observed by the WST of LST[12], together with the hard X-ray observations by the HXI. This work, marked by the editor's choice, revealed that WLFs are not as rare as previously thought, with about 25% of solar flares exhibiting enhanced continuum emission at 360 nm. Another significant study focuses on hard X-ray imaging of slipping reconnection and Quasi-Periodic Pulsations (QPP) in a solar flare[13], which sheds light on a new QPP mechanism that is associated with energetic electrons accelerated by quasi-periodic energy release from slipping reconnection process with periodic magnetic flux input. Gan and Huang[14] comprehensively summarized all of the early achievements of ASO-S.

In order to better organize research based on ASO-S data, several national research projects have been granted funding, as highlighted in this report. These grants include funding from the Strategic Priority Research Program of the Chinese Academy of Sciences, the National Key R&D Program of China, and the National Natural Science Foundation of China. Although these research grants do not exclusively support work related to ASO-S, they indeed provide significant support for research involving ASO-S observations.

5 Conclusions

As China's first comprehensive solar-dedicated spacecraft, ASO-S is currently operating smoothly in orbit. Approximately 500GB of primary data is processed daily at SDOC and transformed into high-level data, enabling users to download events of interest from the mission's homepage. Although the data from the SCI of LST have not yet been opened to the community, both the ultraviolet (Lyman-alpha) and visible light waveband observations sometimes capture excellent observations of CMEs. However, personalized processing is required, which hinders the public release of this data. For the FMG, the vector magnetic field can be obtained by rotating the platform, which can be performed in the user mode. The close cooperation with the science team members is obviously beneficial for making full use of the data from ASO-S. We sincerely hope that more and more colleagues will become interested in the ASO-S mission and utilize its data, ensuring that the scientific objectives of ASO-S are fully realized.

References

[1] GAN W Q, Status of the Advanced Space-based Solar Observatory [J]. *Chin. J. Space Sci.*, 2020, 40, 704-706

[2] GAN W Q, Progress Report on ASO-S[J]. *Chin. J. Space Sci.*, 2022, 42, 565-567

[3] GAN W Q, FENG L, SU Y, A Chinese Solar Observatory in Space [J]. *Nature Astronomy*, 2022, 6, 165

[4] GAN W Q, DING M D, HUANG Y, *et al*. Preface: Advanced Space-based Solar Observatory (ASO-S)[J]. *Res. Astron. Astrophys.*, 2019, 19: 155

[5] GAN W Q, ZHU C, DENG Y Y, *et al*. Advanced Space-based Solar Observatory (ASO-S): An Overview[J]. *Res. Astron. Astrophys.*, 2019, 19: 156

[6] GAN W Q, ZHU C, CHEN B, HUANG Y, China's First Comprehensive Space Solar Observatory[J]. *Chin. Astron. Astrophys.*, 2023, 47, 441-445

[7] GAN W Q, ZHU C, DENG Y Y, *et al*. Advanced Space-based Solar Observatory (ASO-S)[J]. *Solar Physics*, 2023, 298: 68

[8] BAI X Y, DENG Y Y, ZHANG H Y, *et al*. Calibration and Performance of the Full-Disc vector Magnetograph (FMG) onboard the Advanced Space-based Solar Observatory (ASO-S)[J]. *Solar Physics*, 2024, submitted

[9] SU Y, ZHANG Z, CHEN W, *et al*. The tests and calibrations of the Hard X-ray Imager onboard ASO-S[J]. *Solar Physics*, 2024, submitted

[10] CHEN B, FENG L, ZHANG G, *et al*. LST inflight performances and Calibrations[J]. *Solar Physics*, 2024, submitted

[11] HUANG Y, LI Y P, LIU S, *et al*. Science Operation and Data Analysis Center of the Advanced Space-based Solar Observatory (ASO-S) Mission[J]. *Solar Physics*, 2024, submitted

[12] JING Z C, LI Y., FENG L, *et al*. A Statistical Study of Solar White-Light Flares Observed by the White-Light Solar Telescope of the Lyman-Alpha Solar Telescope on the Advanced Space-Based Solar Observatory (ASO-S/LST/WST) at 360 nm[J]. *Solar Physics*, 2024, 299: 11

[13] CHEN C X, SU Y, GUO Y, *et al*. Hard X-ray imaging of slipping reconnection and quasi-periodic pulsations in a solar flare[J]. *Nature Communication*, 2024, submitted

[14] 甘为群, 黄宇, "夸父一号"卫星及早期观测研究概述, 《空间物理学进展》丛书第九卷(主编王赤、叶永烜、史建魁), 2024, 待发表

ZHANG Chen. Updates on the Einstein Probe Mission. *Chinese Journal of Space Science*, 2024, **44**(4)

Updates on the Einstein Probe Mission

ZHANG Chen (On behalf of the Einstein Probe team)

National Astronomical Observatories, Chinese Academy of Sciences, Beijing 100012

Abstract

The Einstein Probe (EP) is a mission dedicated to time-domain astronomy to monitor the sky in the soft X-ray band, led by the Chinese Academy of Sciences with participation from ESA, MPE Germany and CNES France. There are two payloads on board EP, the Wide Field X-ray Telescope (WXT) and the Follow-up X-ray Telescope (FXT). WXT makes use of micro-pore lobster-eye X-ray focusing optics, which can achieve a focusing imaging field-of-view of about 3850 square degrees to discover transient sources. FXT is of the Wolter-I type X-ray optics, which can observe the discovered transient in detail. EP is also capable of fast transient alerts triggering and down-linking, aiming at multi-wavelength follow-up observations by the worldwide community. EP will enable systematic survey and characterization of high-energy transients at unprecedented sensitivity, spatial resolution, grasp, and monitoring cadence. EP was launched on January 9, 2024, and the first light results were released at the end of Apr. 2024.

Key words

X-ray all-sky monitor, Time-domain astronomy, High-energy astrophysics, X-ray transients, Lobster-eye MPO

1 Mission Overview

The Einstein Probe (EP) is a dedicated time-domain high-energy astrophysics mission of the Chinese Academy of Sciences (CAS). Its primary goals are to discover high-energy transients and monitor variable objects. The main payload of EP, the so-called Wide Field X-ray Telescope (WXT), has a very large instantaneous field-of-view (about 3850 square degrees) with moderate spatial resolution (FWHM <5 arcmin), achieved by novel lobster-eye optics. Compared to previous all-sky monitors in operation, WXT offers unprecedentedly high sensitivity due to focusing imaging capability all over the FOV. The other payload, the so-called Follow-up X-ray Telescope (FXT), is a conventional Wolter-I X-ray telescope with a larger effective area (>600 cm^2 @ 1 keV) to perform follow-up characterization and precise localization of newly-discovered transients. Public transient alerts will be issued rapidly to the worldwide community for multi-wavelength follow-up observations.

The primary science objectives are as follows. (1) Discover and characterize cosmic X-ray transients, particularly faint, distant and rare X-ray transients, in large numbers. (2) Discover and characterize X-ray outbursts from otherwise normally dormant black holes. (3) Search for X-ray sources associated with gravitational-wave events and precisely locate them. The mission will address some of the key questions in astrophysics and cosmology, and details of the physics that operates in extreme conditions of strong gravity.

Launched on January 9, 2024, EP orbits at a height of approximately 590 km with an inclination angle of about 29 degrees. In the normal survey mode, three fields are observed on the night side of the sky, with each

* More information about the EP project can be found at https://ep.bao.ac.cn/ep/.

Received June 20, 2024

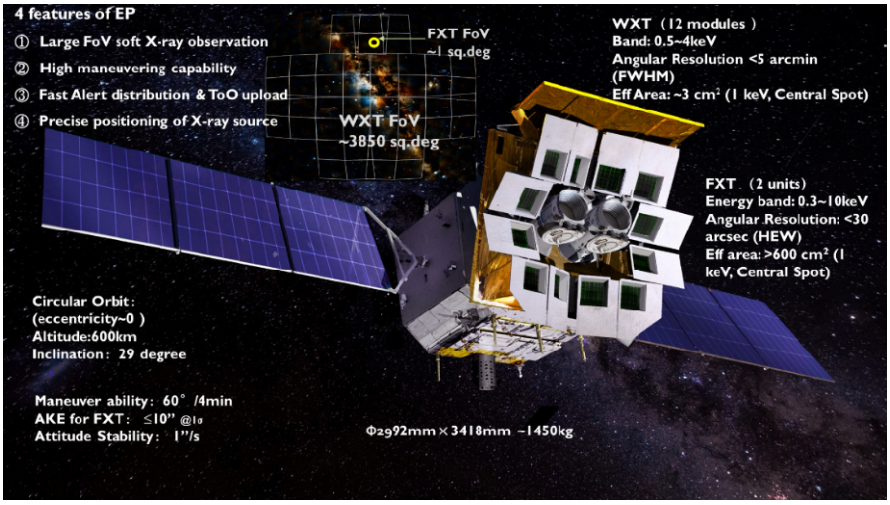

Fig.1 Layout and key performances of the Einstein Probe spacecraft and scientific payloads, which include 12 modules of WXT aligned to cover about 1/12 sky and 2 coaligned modules of FXT (Satellite rendering image credit: IAMCAS)

pointing for roughly 20 min, over the duration of a single 97-minute orbit (the survey strategy may change due to optimization). Over three orbits almost the entire night sky will be sampled, with visit cadences ranging from several to a few tens per day, depending on the location in the sky. EP is currently in commissioning phase until July 2024, with a nominal lifetime of 3 years (5 years as a goal). Figure 1 provides detailed information about the basic facts and performances of the EP satellite.

2 Review of EP Mission Activities in Phase D

2.1 Satellite Platform

The EP satellite system was developed by the Innovation Academy for Microsatellites of CAS (IAMCAS). EP passed the Mission Critical Design Review (MCDR) on March 25 (Figure 2), 2022. This milestone marked the beginning of phase D.

In the next two months, the EP satellite platform confirmed its requirements and completed the detailed design of software components. In November 2022, IAMCAS received the key units of the satellite platform, including the Satellite Management Unit (SMU), Payload Data Processing Unit (PDPU), power supply grid, GNSS, momentum wheels, and attitude control units. Standalone function tests of these units started in October 2022. By January 2023, all platform software components had been tested and verified.

Fig.2 EP MCDR meeting on March 25, 2022

In March, all subsystems of the satellite platform, along with control units for two payloads (WXT and FXT), were wired together in a test room for flight simulations and testing. All functions performed properly.

By June 2023, all units as well as the payloads were integrated onto the satellite platform (Figure 3), after which extensive end-to-end simulated flight tests were performed. A lot of efforts were spent to verify the observation managements onboard and resolve any software issues. Minor issues of software were identified and promptly addressed, but no major issues were found.

From July 21 to August 8, 2023, the satellite was undergoing thermal vacuum tests (Figure 4). The thermal control system of the satellite was demonstrated to be capable of maintaining the onboard instruments within the working temperature range in different external heat

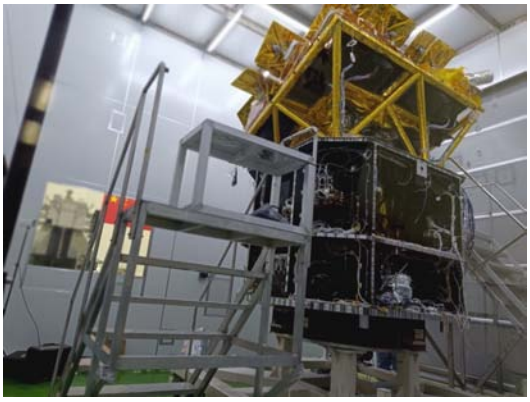

Fig.3 EP satellite integrated for end-to-end testing

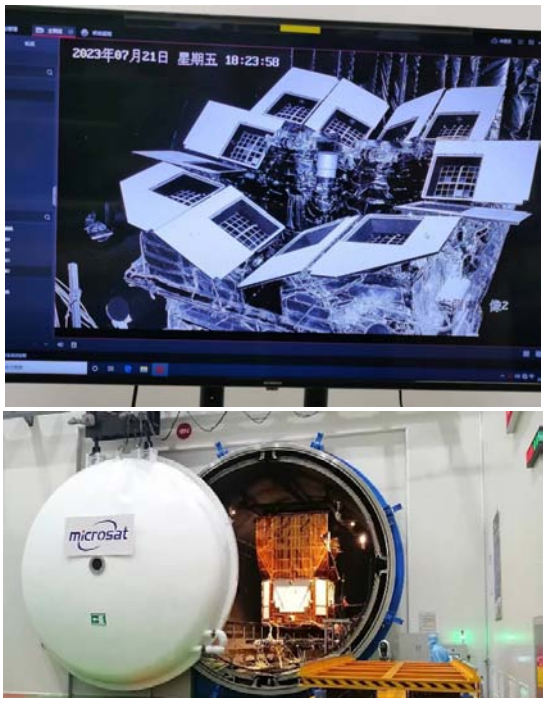

Fig.4 EP satellite flight model under thermal-balancing tests in Shanghai

flux environments, indicating a correct and reasonable energy balance design. During thermal tests, all the focal plane sensors, including CMOS arrays of WXT and PN-CCDs of FXT, were powered on, which was the only chance to verify their performances under working conditions after satellite integration before launch. All the sensors performed as expected.

In September 2023, the EP satellite successfully passed the mechanical tests. The responses to vibrations for different units, including the WXT and FXT payloads, were verified to meet specifications. The acoustic testing results confirmed that the satellite can generate a suitable random mechanical environment for all units onboard.

Then, the deployment and illumination tests of the solar panels were performed and passed. The magnetic tests include the measurement of the magnetic moment of the satellites in both static and energized states were carried out, and finally the magnetic compensation of the satellite was performed. The satellite's residual magnetic moment was successfully reduced to meet the specified range. Finally, in September, the ElectroMagnetic Compatibility (EMC) test results confirmed excellent radio frequency compatibility and electromagnetic compatibility among the subsystems and units.

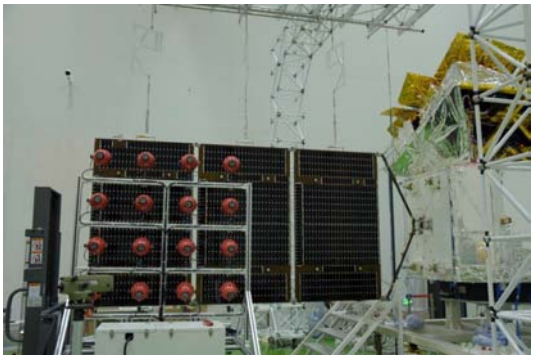

Fig.5 Deployment and illumination tests of the solar panels

After passing major tests and addressing minor issues, the product quality assurance reviews for EP were carried out in October 2023, and then all the units onboard completed the stand-alone software soldering. The acceptance review for the satellite delivery by CAS was held at NSSC on November 29, 2023, and the satellite successfully passed the delivery acceptance review, fully meeting the launch conditions. On November 27, 2023, the EP satellite was delivered to the launch site.

After arriving at the launch site, the EP satellite was assembled and subjected to a series of pre-launch tests. Following these tests, the satellite was deemed ready for launch.

During the building of EP satellites, great efforts were spent on the contamination control, due to the soft X-ray which the payloads worked at was quite sensitive to contamination. To prevent particle contamination, all key components, such as the focal plane cameras and the optics assemblies, were handled and stored in a clean room (better than ISO Class 6). The environments were strictly controlled and monitored. A moveable Class 6 clean room was constructed for the satellite, even at the launch site (Figure 6). All components and

Fig. 6 EP satellite was being assembled within the specially-built EP clean chamber at the launch center in December 2023

materials were carefully selected and degassed in a vacuum to prevent molecular contamination. During transportation, clean air or nitrogen was used to fill the containers of the payload and the components to ensure they remained clean. Monitoring data before the launch showed that the satellite met the requirements of the contamination control, and no performance degradation has been observed so far in operation.

2.2 Developments of WXT

The WXT payload was jointly developed by the Shanghai Institute of Technical Physics (SITP) of CAS and National Astronomical Observatories (NAOC) of CAS, with key components provided by North Night Vision Technology (NVN).

In February 2022, the design reviews of WXT Flight Model (FM) were performed at SITP Shanghai. The construction of WXT FM was kicked off. WXT payload has 12 modules labeled as WXT-FM1~12, each of which has an optics assembly label as OA-FM1~12 and a focal plane camera with a sensor array of 4 CMOSs.

In February 2022, the first batch of MPO devices for flight was delivered to NAOC from NVN. The first optics assembly, labeled OA-FM1, began construction in February 2022 and was delivered to SITP in May 2022 for further integration (Figure 7). The mounting facility at NAOC had the capacity to produce two optics assemblies simultaneously, each requiring about 70 days for MPO device mounting, optics assembly X-ray tests, mechanic vibration tests, and beamline calibrations. That means about each month since May 2022, one optics assembly could be delivered to SITP. By August 2022, all 13 batches of the MPO devices for flight had been tested and delivered to NAOC. Totally NAOC built 13 optics assemblies, 12 of which were launched with WXT and 1 was stored in NAOC as a flight spare (OA-FM11). The last optics assembly, labeled OA-FM13, was delivered to SITP in March 2023.

The electron diverters, one component of the optics assembly that deflect electrons to reach the CMOS sensors, were designed and fabricated by the Institute of Electrical Engineering (IEE) of CAS. In March 2023, all 13 including 1 flight spare divertors were delivered to NAOC.

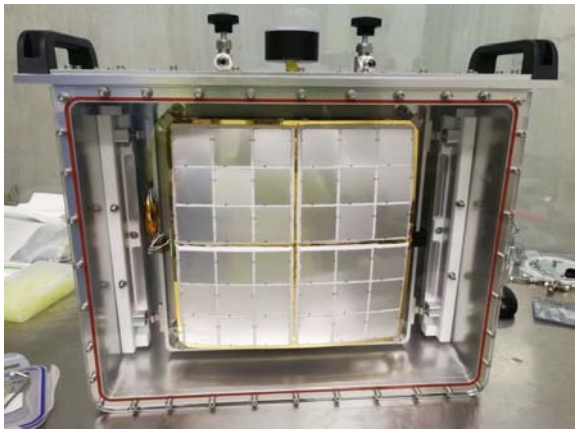

Fig.7 The first WXT Mirror Assembly for flight labeled as OA-FM1 built at NAOC

The CMOS sensors were delivered to SITP in batches for acceptance tests and then calibrated for gain, quantum efficiency as well as bias map at NAOC. Calibrations for each sensor took almost one week. All 48 CMOS sensors, along with 6 extra sensors for flight spares, were received, calibrated, and ultimately delivered back to SITP in October 2022.

SITP was responsible for fabricating the main structure and front electronics for WXT. Once SITP received all components of a WXT module, integration of that module started. The first flight module of WXT, labeled as WXT-FM1 (Figure 8), was completed in May 2022 after passing the vibration tests, and the last module was completed in April 2023. Thermal balancing tests of the modules were performed three times, with 4 modules tested each time in December 2022, February 2023 and April 2023. All modules were delivered to IAMCAS in June 2023, and integrated into the satellite platform on June 24, 2023.

The calibration campaigns of WXT were performed on CMOS sensors, optics assemblies as well as modules.

Fig.8 The first complete module (WXT-FM1) of the WXT Flight Model (developed at SITP)

At NAOC there was a small multi-target beamline facility with two CMOS sensors exposed to X-ray photons simultaneously. One CMOS was used as the reference sensor and was mounted on the facility throughout the entire calibration campaigns of CMOS sensors. The other one was the flight sensor, which tested for gain, relative quantum efficiency (QE) relative to the reference sensor, and uniformity across the entrance window. After all the flight sensors were tested on that facility, the reference sensors underwent absolute QE calibration at Leicester University. The test data shows that the QE of all the flight sensors at different energies were nearly identical and matched the theoretical values predicted by the structure of the sensors.

11 MPO Optics Assemblies (MPO-OAs) except OA-FM5 for flight were calibrated after the assembly vibration test at NAOC's X-ray Imaging Beamline facility (XIB). The X-ray tube was about 13.5 m away from the test chamber and had a Ti target with an electron spot diameter of about 1 mm. A calibration module with a similar mechanical configuration to the flight module was mounted on positioning hexapods to precisely control the module pointing inside the facility. The calibration module was equipped with a focal plane camera with 2*2 CMOS sensors, and a quick release adjustable supporting structure that allowed to mount of an MPO-OA and to adjust of the distance between the MPO-OA and the camera based on focal length. After mounting, 484 pointings inside the FOV were performed by hexapods for each MPO-OA. At each point, the focused X-ray photons by MPO-OA were measured by CMOS sensors such as energy and flux. Then the MPO-OA was removed from the beamline, and the X-ray beam was measured again as a reference. An SDD detector was applied all the time to monitor the flux variation. By comparing the flux measured by the CMOS sensor with and without MPO-OAs, the response of the optics could be calculated. For each MPO-OA, it took almost 14 days for calibration.

Based on the collaboration between ESA and CAS, OA-FM5 was sent directly to the Panter Facility at MPE Germany for calibration in August 2022. The Panter facility had performed a sophisticated calibration plan on OA-FM5, which concluded on Nov. 30, 2022. After NAOC received OA-FM5, it was calibrated again at XIB with the same plan as the other assemblies.

The calibration data from CMOS sensors and MPO-OAs were used to compile a calibration database for each module. 3 modules were also sent to a 100-meter facility at IHEP for end-to-end calibrations. WXT-FM1 with OA-FM1 was calibrated at IHEP in August 2022, WXT-FM5 with OA-FM5 in May 2023, and WXT-FM11 with OA-FM13 in May 2023.

OA-FM5 was calibrated at Panter, NAOC and IHEP after being integrated into WXT-FM5. All calibration data obtained from these campaigns of OA-FM5 were consistent with each other, demonstrating the effectiveness and reliability of the WXT ground calibration procedures.

2.3 Pathfinder of WXT

To verify the reliability of the MPO optics as well as CMOS sensors, one of the WXT qualification modules, labeled as WXT-QM4, was sent into space with satellite SY-01 as the pathfinder of WXT, named LEIA (Figure 9). The SY-01 satellite was an experimental mission designed to verify and test new space technologies, with a sun-synchronous orbit at 500 km. SY-01 was launched on July 27, 2022, with a nominal lifetime of approximately 2 years.

Fig.9 Leia (WXT-QM4) on SY-01 satellite

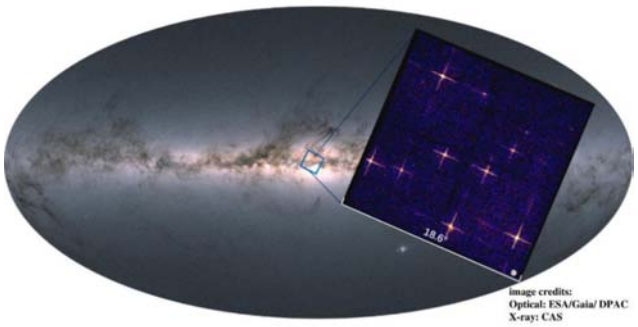

Fig.10 An image of the central sky zone of the Milky Way obtained by the lobster-eye telescope in August 2022

LEIA observed the Crab nebula and CAS A SNR then performed the all-sky survey as pathfinding procedures, which would also be performed for EP-WXT. The EPSC/NAOC successfully processed and handled the observation data from LEIA immediately after the instruments were powered on. When LEIA pointed to the galaxy center (Figure 10), all bright X-ray sources with cruciform-like spots were clearly identified, marking the first wide field-of-view X-ray observations by a Lobster-eye focusing telescope in orbit. LEIA also discovered several new X-ray transients, which led to proposals and approvals for Target-of-Opportunity (ToO) observations by Swift/XRT.

There are two main issues noticed by WXT team when operating LEIA. Firstly, the onboard processing and triggering unit could frequently be mis-triggered by energetically charged particles, which would cause signals at a bunch of pixels in a single frame. If these pixels were clustered together within a small region, the trigger algorithm would treat it as a very fast ‘transient’. The other issue was related to thermal control of the front-end electronics, where two loop heat pipes were applied to conduct heat to the main structure. Unfortunately, both loop heat pipes failed. LEIA could only powered on for 15 min per orbit to keep the proper temperature of the electronics. The WXT team optimized the algorithm for LEIA and EP and replaced all 24-loop heat pipes with ordinary ones on WXT FM.

Despite these challenges, LEIA has successfully identified tens of transients and remains in operation.

2.4 Developments of FXT

The FXT payload was developed at the Institute for High Energy Physics (IHEP), CAS, and includes two nearly identical telescope units. Each unit comprises of an optics assembly, a thermal baffle, an electron deflector, a contamination shield, a filter wheel, a pnCCD camera, a cooling system and a front-end electronics box.

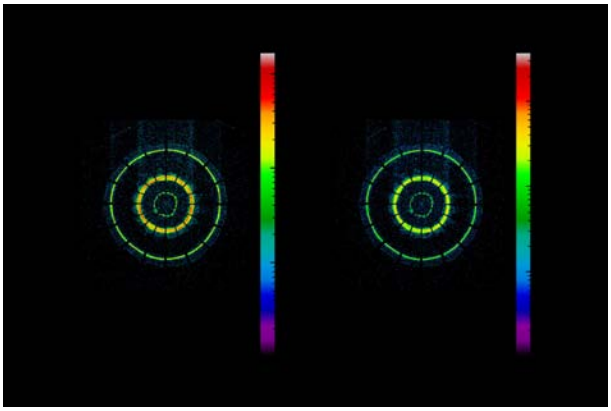

Fig.11 Thermo-optical test of the FXT STM

One mirror assembly was produced by ESA (FXTOA-A), while the other was contributed by MPE Germany, which is the flight spare model of the eROSITA mission (FXTOA-B). Both focal plane sensors were contributed by MPE too.

In March 2022, all key components were delivered to IHEP, and the design reviews of several FXT subsystems (load motion mechanism controller single machine, structural subsystem, thermal control subsystem, optical subsystem) flight models were completed. The thermo-optical experiment of the FXTOA-A STM (Figure 11) started at the IHEP 100m X-ray facility on April 24. The thermal control test and the thermo-optical experiment of FXTOA-B were conducted at the same facility from May 24 to 26. The test results showed that there were no significant changes in the PSF for temperatures between 18℃ and 22℃, indicating the good thermal stability of the optics assemblies.

In July 2023, the tests of FXTOA-A and FXTOA-B were completed with pnCCD camera flight model respectively at the IHEP 100 m X-ray facility. All the test results were consistent with those measured at the Panter facility MPE before delivery to IHEP (Figure 12, Figure 13).

Unfortunately, the main supporting structure connecting the mirror assembly and focal plane camera was accidentally contaminated during machining. Manufacturing a new supporting structure caused several months of delay to the overall schedule of the FXT FM delivery of and the satellite’s AIT.

Fig.12 FXTOA-B (eROSITA FS) at IHEP 100 m X-ray facility

In December 2022, IHEP received all components for both FXT units. In January 2023, the FXT-A unit (with mirror assembly FXTOA-A and pnCCD FM1) was assembled and calibrated at the IHEP 100m X-ray facility. The function, performance test and calibration of FXT-A started at IHEP 100m X-ray facility on January 9 and concluded on February 15. The function, performance test and calibration of FXT-B (with FXTOA-B mirror assembly and pnCCD FM2) started at IHEP 100m X-ray facility on February 22 and concluded in March.

On April 8, the integration of all mirror assemblies, focal plane cameras, and the main structure of the FXT was completed at IHEP. End-to-end tests were performed to verify the functionality and performance of the FXT subsystem in April. The satellite's PDPU, which hosted the online data process software components, also participated in these tests to verify the online source detection function. On May 21, the FXT completed AIT (Figure 15) and was delivered to IAMCAS on May 26. The FXT was then integrated into the satellite on June 5, 2023.

2.5 Activities of EP Science Center

In July 2022, the EP Science Center (EPSC) deployed and adapted the core components of the WXT processing pipeline to support the operation of LEIA. After LEIA powered on, the LEIA pipeline processed the first batch of data and generated the first scientific products successfully. The WXT data processing pipeline was subsequently verified. The EPSC has been operating LEIA ever since, which has facilitated optimizing and debugging the WXT data processing pipeline, the CALDB, as well as transient handling and identification tools through practical experience gained. On November 7, 2022, a bright X-ray transient, LXT 221107A – the first by LEIA, was detected. Several Swift/XRT and NICER ToO observations were proposed and approved, with two ATel alerts posted by EPSC. This transient was later identified as a giant X-ray flare from a known variable star. The scientific users of EPSC analyzed the data products using tools developed for WXT.

In October 2022, the EPSC started to build the whole software system with core components compiled and tested. The ground calibration data for both payloads was analyzed using the first compiled CalDBs version.

After one year of coding and testing, EPSC systematically tested its interfaces, functions, performance, and processes of the EPSC based on the actual flow of scientific operations with simulation data. The functions, performance and reliability of the hardware and software of each sub-system met the requirements. The working flow of each process was confirmed to be able to be executed normally. The test results indicate that the EPSC is generally capable of completing the daily

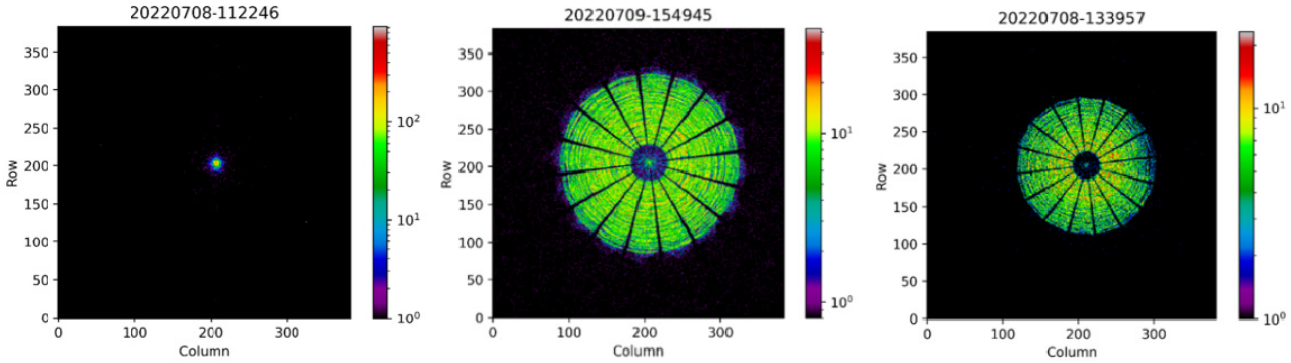

Fig.13 Left: first-light X-ray image obtained with the FXTOA-A, at the Al-K line energy. Middle: The X-ray image with the FXTOA-A, 80mm extra-focal at the Al-K energy. Right: The X-ray image 60mm intra-focal at the Al-K energy

scientific operation. The ground segments passed the acceptance review and were ready for EP operation.

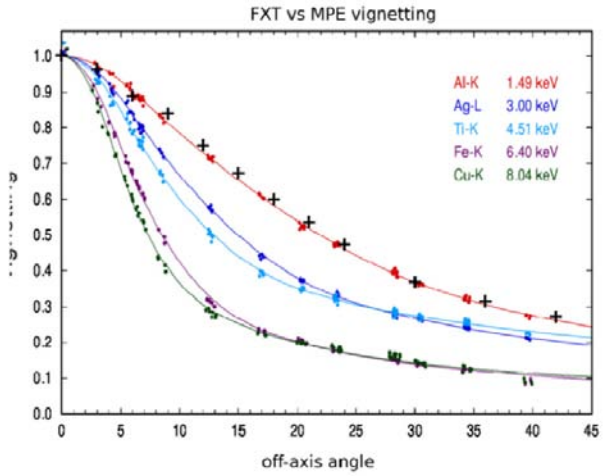

Fig.14 Measured vignetting of the FXTOA-A, at IHEP (crosses) at various energies and comparison with the MPE results (dots and curves)

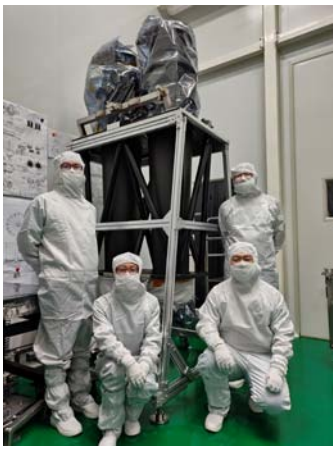

Fig. 15 Overall integration of the FXT telescopes

On April 19, 2023, the kick-off meeting of the Einstein Probe Science Topical Panels (STP) was held online. Over 130 researchers from China (including Hong Kong and Taiwan) and six European countries attended the conference, with STP formally approved members. EP Satellite First General Meeting STPs held in Beijing Xiangshan Hotel from June 6 to 7, 2023. In August 2023, EPSC issued the invitation to STP members to propose the targets of performance verification (PV) observations, which were applied to demonstrate to the community the satellite's performance and scientific capabilities. In October, the observation plan for the PV phase was approved.

3 Commissioning Phase

In two days after launch, the basic satellite functions were confirmed, and the satellite platform was in good condition. The satellite could achieve energy balance with solar panels as well as the batteries worked as expected. The attitude control stability and maneuvering speed met scientific requirements. The transmission of links between satellite and ground channels was stable, the thermal environments could support the operation of the payloads.

The WXT in-orbit calibration was initiated on January 19. As of the end of May, WXT successfully completed the first round of calibrations of all 12 modules. The performances were consistent with ground calibrations. Angular resolutions of these modules were tested and attained (3.3~4.4 arcmin), meeting the performance requirement (<5 arcmin@1keV) and validating the efficacy of WXT's calibration database. Up to the end of May 2024, WXT has detected 2,548 known sources, 7 burst sources, 20 X-ray transient sources, and more than 180 stellar flares. The onboard transient triggering was verified by the discovery of the EP240315a.

FXT has initiated in-orbit performance testing and

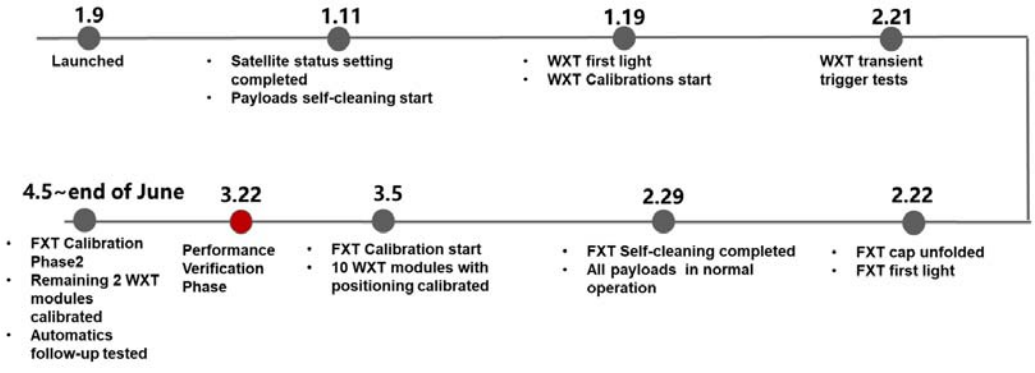

Fig.16 Timeline of in orbit tests and calibrations

calibration since March 5th. From March 5 to 19, FXT conducted various in-orbit observations on targets such as M87, NGC2516, Omega Cen, 3C 273, Crab, Puppis A, and Puppis A East Knot for calibration purposes, and data analysis is currently ongoing. Beginning on April 5th, FXT continued in-orbit calibration and continued observing a variety of targets such as 1RXS J170849.0-400910, 1RXS J185635.1-375433, PSR B1937+21, 3C 273, and the Moon accordingly. FXT will advance its calibration activities with primary calibration sources such as Sco X-1, the Moon, and RX J1856, as well as joint calibration with HXMT. The calibration work is expected to be completed before July 10th.

Between March 24 and April 5, WXT and FXT conducted PV observations jointly. Even in the calibration observations, FXT was also conducted to ToO observations by EPSC, such as EP240222a, EP240315a, and EP240414a, resulting in significant gains. The onboard triggering and automatic follow-up observation were tested in June 2024. On June 2, a transient source was detected by the WXT triggering unit onboard, which triggered automated follow-up observation with FXT approximately 2 minutes after the WXT detection, with an exposure time of approximately 3000 seconds, validating the function of FXT automated follow-up. The FXT data suggested that the WXT transient was a stellar flare. The preliminary performances estimated by calibration observations are shown in Figure 1.

Since February 6, EPSC has been conducting daily in-orbit operations from the operation rooms at NAOC and IHEP and providing support for in-orbit calibration work and PV observations. On March 21, EPSC released FXTDAS and CalDB (v1.05) for PV data analysis. On April 5, the second phase of calibration observations began with updates to CalDB. From April, EPSC started to support ToO-MM observations during LIGO O4b. EPSC provided support for EP Cycle 1 scientific proposal submission, collecting 115 proposals, including teams from ESA, MPE, and CNES. Of these, 68 proposals have been evaluated. Additionally, support was provided for PV proposals, in-orbit calibration proposals, and ToO proposals.

4 First Light

At the end of April, the EP consortium formally released EP's first light images acquired in orbit.

The very first target of WXT was the Cassiopeia A (Cas A) supernova remnant (SNR) around 11,000 light-years away. Figure 17 was obtained with an exposure time of 21564 sec with ObId 13600000042, and the cruciform shape spot with the color cyan in the center is Cas A. The SNR CTB 109 can be also seen in this image (red). The red color represents X-ray photons with energy 450 to 1000 eV, green represents 1000 to 2000 eV and blue represents 2000 to 5000 eV. Figure 17 also indicated that the X-ray photons emitted by Cas A have higher energy than that of STB 109.

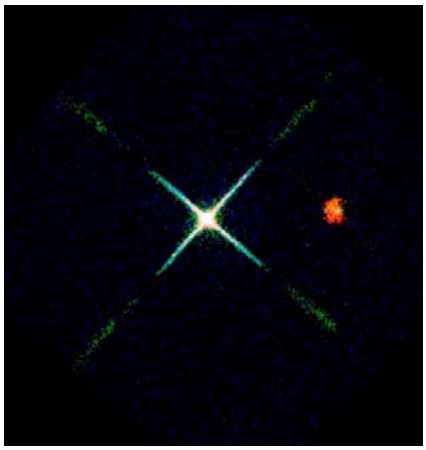

Fig.17 Very first observation of WXT pointed to Cassiopeia A, with SNR CTB 109

Figure 18 shows the observation of WXT pointed to the center of the Milky Way Galaxy with an exposure time of about 40 ksec with ObId as 13600005157. The X-ray sources are drawn with color purple, which is stacked with a Digitized Sky Surveys image provided by the European Southern Observatory. Almost all the bright X-ray sources can be clearly identified with cruciform shape spots by Lobster-eye optics (purple). And the blue cloud-like structures are the foreground emission of hot gas surrounding the galaxy. Figure 18 clearly demonstrates that WXT has the largest focusing Field-Of-View (FOV) and covers almost 1/10 of the whole sky. A newly discovered transients labeled as Swift J151857.0-572147 as reported in GCN Circular 35853 can be clearly observed in this observation.

The EP240219a is one of the earliest transients discovered by WXT on February 19, 2024, and the first reported transient on Astronomer's Telegram ((#16463), as shown in Figure 19. EP240219a was a Gamma-Ray

Burst (GRB) candidate, which suddenly appeared, lasted about 100 seconds and then vanished from WXT's view. The bright source in the center of the image is the most famous X-ray source Crab nebula, which is the positioning calibration source of WXT.

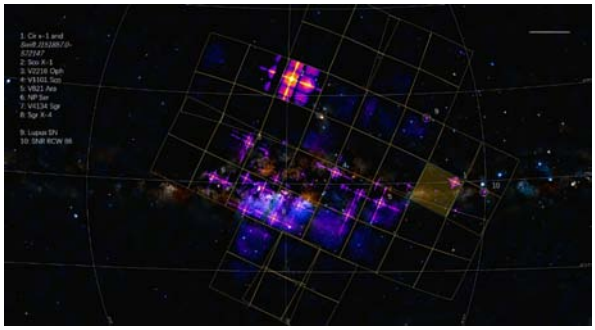

Fig.18 Observation of WXT pointed to the center of the Milky Way Galaxy with an exposure time of about 40 ksec. The X-ray sources are drawn with the color purple, which is stacked with a Digitized Sky Surveys image provided by European Southern Observatory (ESO). (DSS image credit: ESO)

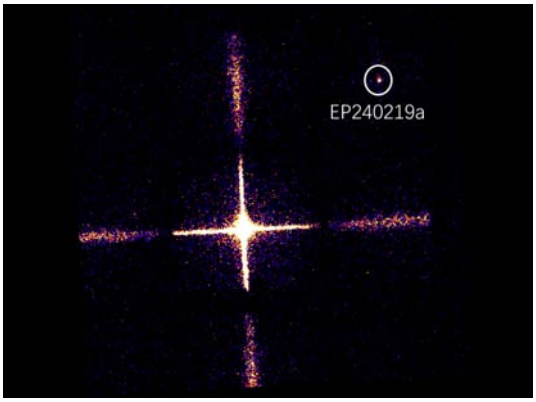

Fig.19 Transient EP240219a with Crab nebular in the center

Crab is a famous supernova remnant, whose precursor star exploded in 1054 and was observed and recorded in detail by Chinese astronomers during the Song Dynasty. FXT observed pulsars and peripheral pulsar wind nebula using Partial-Window Mode as shown in Figure 20, obtained pulsar pulse profiles using Timing Mode, and fitted the accurate period and phase.

M87 is a bright giant elliptical galaxy in the Virgo galaxy cluster. Unlike optical images, FXT observed a large amount of dispersed hot gas within M87 in the X-ray energy range. There are two arm structures in the central region, which are formed by the jets generated by the central massive black hole, which carry out the cold gas originally located in the central region. At the same time, a cold front with sharp changes of surface brightness was observed clearly around M87 (Figure 21).

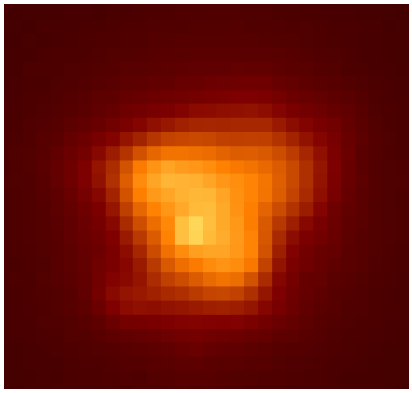

Fig.20 Crab SNR taken by FXT in Partial-Window Mode

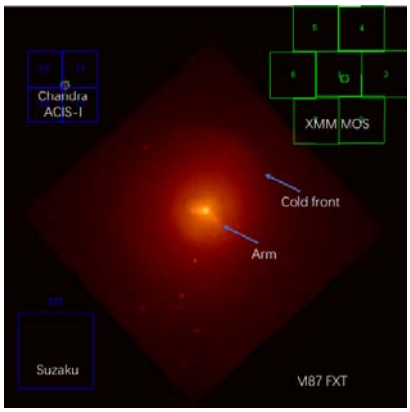

Fig.21 M87, a bright giant elliptical galaxy in the Virgo galaxy cluster, observed with FXT

5 Conclusions

After a successful launch, the EP is now in operation for calibrations. The performance of the satellite has met all the requirements for scientific observations. After the commissioning phase is over, the EP will be handed over to the EP science team in July 2024 to begin nominal science operations. Overall, these events represent a significant milestone in the mission and a major step forward in our ability to conduct impactful scientific research.

WEI Jianyan. Progress on SVOM Satellite Development. *Chinese Journal of Space Science*, 2024, **44**(4)

Progress on SVOM Satellite Development

WEI Jianyan

National Astronomical Observatories, Chinese Academy of Sciences, Beijing 100101

Abstract

SVOM (Space-based multiband Variable Object Monitor) is a Chinese-French space mission mainly designed to study gamma-Ray Bursts. The satellite carries four instruments to detect and localize the prompt GRB emission and measure the evolution of the afterglow in the visible band and in soft X-rays, and a VHF communication system enabling the fast transmission of SVOM alerts to the ground. The ground segment includes an array of wide-angle cameras and two follow-up telescopes. It was launched into an orbit of about 635km on 22 June 2024, with three years of nominal operations and an extension of two years.

Key words

Chinese-French space mission，SVOM Satellite，Gamma-Ray Bursts

SVOM (Space-based multiband Variable Object Monitor) is a mission dedicated to study Gamma-Ray Bursts (GRBs)[1], approved jointly by both Chinese and French space agencies. The satellite has an orbit with an altitude of 635km and an inclination of 29°. The system Final Acceptance Review (FAR) was carried out by CNSA and CNES in January 2024. It was launched at Xichang Satellite Launch Center by Long March 2C on 22 June 2024.

GRBs are extremely luminous transient sources appearing when a newborn stellar mass black hole or magnetar emits an ultra-relativistic jet towards the Earth. Consequently, the study of GRBs not only has the potential to expand or revolutionize our understanding of key astrophysical issues on the mechanisms driving stellar explosions and the radiation processes of relativistic jets. In the next years GRBs will also undoubtedly shed new light on the evolution of the young universe, particularly on the history of star formation, the metal enrichment of galaxies, and the reionization of the intergalactic medium[2]. GRB 170817A, a normal short GRB detected by Fermi-GBM, was the first confirmed counterpart of gravitational-wave transients, which made GRBs even hotter topic[3].

The scientific objectives of SVOM put a special emphasis on two categories of GRBs: very distant GRBs at $z > 5$ which constitute exceptional cosmological probes, and faint/soft nearby GRBs which allow probing the nature of the progenitors and the physics at work in the explosion. These goals have a major impact on the design of the mission: the on-board hard X-ray imager is sensitive down to 4 keV and computes online image and rate triggers, and the follow-up telescopes on the ground are sensitive in the NIR.

In order to take advantage of the astrophysical potential of GRBs, SVOM is designed to (i) permit the detection of all known types of GRBs; (ii) provide fast, reliable GRB positions; (iii) measure the spectral shape of the GRB prompt emission from visible to MeV; (iv) measure the temporal properties of the GRB prompt emission from visible to MeV; (v) identify quickly the afterglows of detected GRBs at both X-ray and visible bands, including the ones that are highly redshifted ($z > 5$); (vi) measure the spectral shape of the early and late GRB afterglow from visible to X-rays; (vii) measure the

Received June 20, 2024

temporal evolution of the early and late GRB afterglow from visible to X-rays.

SVOM mission is designed to consist of a set of scientific instruments to implement the synergy between space and ground observations. The space-based instruments include: (i) ECLAIRs, a wide field-of-view hard X-ray imager and spectrometer; (ii) GRM, a wide field-of-view soft gamma-ray spectrometer; (iii) MXT, a narrow field-of-view low-energy X-ray telescope; (iv) VT, a narrow field-of-view visible/near infrared (NIR) telescope. An artist view of the SVOM satellite is showed in Figure 1. And the ground-based instruments include: (i) GFTs, two follow-up telescopes (one of which featuring efficient NIR capabilities); (ii) GWAC, an array of wide field-of-view cameras in visible band. A network of about 45 VHF receiving stations, and a Beidou short-message system as supplement, are designed for real-time downlink communication.

SVOM is a unique multi-wavelength observatory with rapid slew capability and quick command up-link capability. Therefore, SVOM will also be a powerful target-of-opportunity observatory for the whole astronomy community beyond the specific objectives linked to GRBs. For example, the SVOM mission has been conceived to promptly point to the celestial fields where sources have been detected by wide field of view astronomical devices such as the upgraded generation of gravitational wave detectors (LIGO, VIRGO, GEO and KAGRA) and high-energy neutrino detectors (IceCube, KM3NeT).

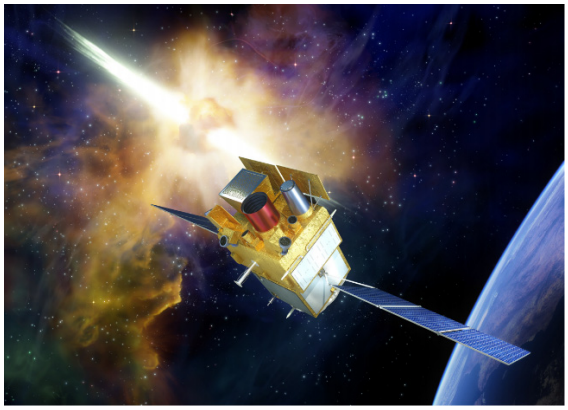

Fig.1 Artistic view of the SVOM satellite

References

[1] WEI J, CORDIER B, ANTIER S, *et al*. The deep and transient universe in the SVOM era: new challenges and opportunities– scientific prospects of the SVOM mission[J]. arXiv161006892W, 2016

[2] GEHRELS N, RAMIREZ-RUIZ E, FOX D B. Gamma-ray bursts in the swift era [J]. *Ann. Re. Astron. Astrophys*., 2009, **47**(1): 567-617

[3] GOLDSTEIN A, VERES P, BURNS E, *et al*. An ordinary short gamma-ray burst with extraordinary implications: fermi-GBM detection of GRB 170817A [J]. *Astrophys. J. Lett*., 2017, **848**(2):14

WANG Chi, ESCOUBET C Philippe, Colin Forsyth, LI Jing, David Agnolon. Recent Progress of the Solar Wind Magnetosphere Ionosphere Link Explorer (SMILE) Mission. *Chinese Journal of Space Science*, 2024, **44**(4)

Recent Progress of the Solar Wind Magnetosphere Ionosphere Link Explorer (SMILE) Mission

WANG Chi[1], ESCOUBET C Philippe[2], Colin Forsyth[3], LI Jing[1], David Agnolon[2]

1. State Key Laboratory of Space Weather, National Space Science Center, Chinese Academy of Sciences, Beijing 100190
2. European Space Agency/European Space Research and Technology Centre, Noordwijk 2201 AZ
3. Mullard Space Science Laboratory, University College London, London RH5 6NT

Abstract

The SMILE (Solar wind Magnetosphere Ionosphere Link Explorer) mission is a joint space science mission between the Chinese Academy of Sciences (CAS) and the European Space Agency (ESA), aiming to understand the interaction of the solar wind with the Earth's magnetosphere in a global manner. As of May 2024, the SMILE mission is in phase-D with an expected launch date of September 2025. This report summarizes developments in the mission during the past two years.

Key words

SMILE, Soft X-ray imager, ultra-violet imager, light ion analyzer, MAGnetometer

1 Introduction

The SMILE[1] mission is the first all-around ESA-CAS joint mission in the framework of the Chinese Academy of Sciences (CAS) Strategic Priority Program on Space Science. The mission aims to deepen our understanding of the interaction of the solar wind with the Earth's magnetosphere. The primary scientific objectives of SMILE are to answer three main questions: (i) What are the fundamental modes of the dayside solar wind/ magnetosphere interaction? (ii) What defines the substorm cycles? (iii) How do CME-driven storms arise and what is their relationship to substorms?

To answer these questions, SMILE hosts a payload that comprises four scientific instruments: Magnetometer (MAG), Light Ion Analyzer (LIA), Soft X-ray Imager (SXI) and Ultraviolet Imager (UVI). SXI will spectrally image the Earth's magnetopause, magnetosheath and magnetospheric cusps. UVI will capture images of the aurora borealis, LIA will measure the in-situ distribution function of the ions, and MAG will measure the in-situ vector magnetic field.

SMILE is a single spacecraft mission consisting of two main parts:

(1) A 3-axis stabilized Platform (PF), consisting of a Service Module (SVM) and a Propulsion Module (PM) that provides the spacecraft resources, will raise the orbit from the Launcher insertion orbit to the Highly Elliptical Orbit (HEO). It also hosts the two LIA sensors to enable them to synthesize a full-sky field of view.

Received June 20, 2024

(2) The Payload Module (PLM) hosts the other three instruments, SXI, UVI and MAG, the equipment and instrument control unit, and the X-band science data downlink subsystem. Figure 1 shows the SMILE satellite structure.

The joint Mission Preliminary Design Review (M-PDR) was completed successfully in January 2020 in the Netherlands. This was the third critical joint review of the SMILE mission, marking the kick-off of Phase-C activities. After two and a half years of phase C including the development and testing of structural and thermal models, electrical models, avionics tests and complete platform qualification, the fourth critical joint review, the Mission Critical Design Review (M-CDR), was successfully completed in Shanghai in June 2023 (see Figure 2), marking the kick-off of Phase-D activities. Since then, the mission has been developing the Flight Models (FMs).

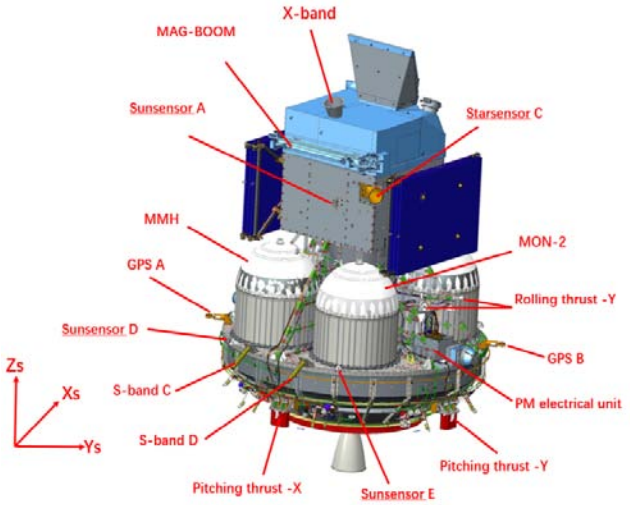

Fig.1 SMILE satellite structure

In the previous progress report[2] in 2022, the respective responsibilities of CAS and ESA, as well as the Phase-B study and the early Phase-C study were introduced in detail. In this report, the progress in the last two years, *i.e*. late Phase-C and Phase-D stages is elaborated.

2 Advances in Scientific Research

2.1 A New Mechanism for Driving Planetary Magnetosphere Convection

Plasma convection induced by the interaction between planetary magnetic fields and the impinging solar wind is a fundamental and prominent feature of planetary magnetosphere dynamics. A global-scale pattern of magnetospheric convection in Earth's magnetosphere, known as the Dungey cycle[3], provides a basic understanding of solar-wind-magnetosphere coupling and has been used to explain day-to-day convection processes. In the Dungey cycle, reconnection between the IMF and the magnetosphere drives the convection of open magnetic field lines through the polar cap and magnetotail lobes, whereas nightside reconnection closes this open flux and drives the convection of closed field lines through the magnetosphere and back to the dayside. The dynamics of magnetosphere convection are crucial in the occurrence of geomagnetic storms and substorms. Differing from the Dungey cycle, Dai *et al*[4] provide direct evidence supporting a scenario whereby reconnection on the dayside enhances the Region 1 and Region 2 current systems, resulting in enhanced convection within the closed magnetosphere towards the dayside as well as the expected convection of open field-lines towards the nightside. This new finding was published in *Nature*

Fig.2 SMILE M-CDR group photo in Shanghai

Communications with the title of "Global-scale magnetosphere convection driven by dayside magnetic reconnection", and was featured on the homepage and cover of the Nature Communications official website. This important finding provides valuable insights into the mechanisms driving planetary magnetosphere convection, which may be tested by the observation of the upcoming SMILE mission.

2.2 Modelling Working Group

The SMILE Modelling Working Group (MWG) provides modeling supports for the SMILE mission, such as Magneto-Hydro-Dynamical (MHD) model comparison, validation of the SXI requirements and goals, boundary tracing from simulated SXI data, and the development of techniques to reconstruct the 3D magnetopause from X-ray images. The main progress of MWG has been published recently in the journal Earth and Planetary Physics (EPP) as a special issue [5]. This special issue, comprised of 22 articles, covers the following seven topics: (ⅰ) instrument descriptions of the Soft X-ray Imager (SXI), (ⅱ) numerical modeling of the X-ray signals, (ⅲ) data processing of the X-ray images, (ⅳ) boundary tracing methods from the simulated images, (ⅴ) physical phenomena and a mission concept related to the scientific goals of SMILE-SXI, (ⅵ) studies of the aurora, and (ⅶ) ground-based support for SMILE.

Guo J *et al.*[6] and Yang ZW *et al.*[7] performed hybrid simulations to reproduce refined structures in the magnetosheath, such as waves and High-Speed Jets (HSJs). According to simulation results, although local X-ray emissivity in the magnetosheath can have large amplitude fluctuations (up to 160%), the accuracy of magnetopause boundary detection is not significantly affected while analyzing line-of-sight integration of X-ray emissivity. Deformation of the magnetopause caused by HSJs can reach about 1 RE in spatial scale and can last for minutes as illustrated in Figure 3. Their results suggest that the impact of HSJ's may be visible to SMILE.

Jorgensen *et al.*[8] studied the reconstruction method of the subsolar magnetopause from multiple Soft X-ray images to be observed by different missions in space at the same time. It is concluded that real-time CT reconstruction of the subsolar magnetopause position can be achieved with images observed by two hypothetical satellites from different viewing geometries.

Careful removal of background X-ray noise is imperative in order to derive the magnetopause position accurately. Zhang *et al.* [9] use two methods to remove the X-ray background superposed on the magnetosheath signal in XMM-Newton data. It demonstrates that both

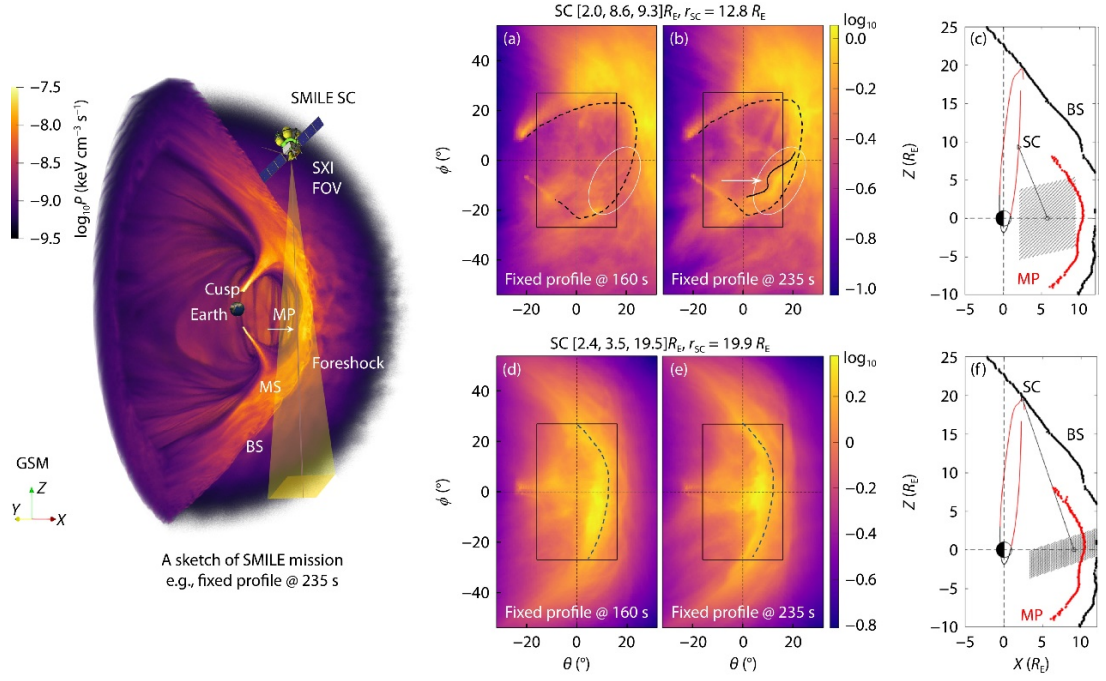

Fig.3 Deformation of the magnetopause caused by high-speed jets as revealed by the X-ray emissivity (upper panel) and X-ray images (lower panel)[7]

methods are robust and reliable. Wang *et al*. [10] developed an image restoration algorithm based on deep learning to remove background noises and highlight the magnetosheath signals. They demonstrated that the image restoration algorithm significantly improves the accuracy of the magnetopause position derived from noisy X-ray images.

Combining global detection from SMILE with observations from other missions and observatories could be important to understanding the solar wind-magnetosphere-ionosphere coupling system. Zhang *et al*. [11] provide analyses of the joint detection capability of SMILE and the European Incoherent Scatter Sciences Association's (EISCAT)-3D radar. Opportunities for joint studies using SMILE and EISCAT-3D data are presented.

3 Mission Update

3.1 Platform

The PF structure is a stacked structure, including the PM structure comprised of a large Carbon Fiber Reinforced Polymer (CFRP) primary structure and four propellant tanks, and the cubical-shaped SVM structure featuring several honeycomb panels and CFRP frames. There are two solar arrays mounted on the SVM +*Y* and -*Y* lateral panels as shown in Figure 4, which are installed and deployed by two solar array mechanisms. The assembly of SVM and PM flight models has now been completed.

3.2 Payload Module

The PLM, hosting the SXI, UVI, MAG, the equipment and instrument control unit and the X-band science data downlink transmitter, has successfully passed CDR in May 2023. Currently, the PLM is on track for integration of the instruments. After receiving the FM of SXI, MAG and LIA as well as QM of UVI, the PLM will complete the last steps of its Assembly, Integration and Tests (AIT) phase.

Fig.4 The Assembly of the SVM with PM

3.3 Instruments

3.3.1 SXI

SXI will use novel soft X-ray imaging technology to obtain global images of the large-scale structures of the magnetosheath for the first time. This is critical to understand the key features of magnetospheric global dynamics. SXI consists of a main telescope, an SXI electronics box and the front-end electronics. The telescope uses a Lobster-eye technique based on micropore optics to focus the X-rays onto the two very large CCD arrays located on the focal plane. The focal plane is protected from potential radiation damage by a shutter mechanism. Figure 5 shows the SXI Telescope Proto-Flight Model (PFM) during a vibration Test conducted at Rutherford Appleton Laboratory (RAL) Space. SXI is now going through its PFM Qualification and Acceptance Review (QAR) and will be delivered to Airbus shortly thereafter.

Fig.5 SXI Telescope PFM during Vibration Test Conducted at RAL Space (credit to S. Sembay, Leicester U., UK)

3.3.2 UVI

UVI will capture global images of the aurora borealis with high spatial resolution. UVI consists of two key sub-assemblies: the optical module (UVI Camera, UVI-C), which is the heart of the instrument; and the electrical control unit (UVI-E). Following programmatic difficulties in 2021, the responsibilities for the development of this instrument, originally led by the Canadian Space Agency, were taken on by CAS with contributions from ESA. This caused a delay in the development of UVI, however, CAS and ESA are doing their utmost to minimize the schedule impact. The UVI-C Qualification Model (QM) has completed delivery acceptance testing, and QM Pre-Shipment Review (PSR) will follow. The FM of UVI will be tested at acceptance levels, cali-

brated, and delivered to ESA by September 2024.

3.3.3 MAG

The MAG instrument will measure the in-situ magnetic field using a digital fluxgate magnetometer system consisting of two individual tri-axial fluxgate sensor heads mounted on a 3-meter-long deployable boom. In March 2024, MAG FM passed the QAR and PSR organized by CAS and ESA. It has now been delivered to Airbus, which is the first instrument of SMILE that has been delivered to ESA.

3.3.4 LIA

Two identical LIA sensors are designed on the basis of a top-cap electrostatic analyzer for large dynamic flux range, wide Field of View (FOV) and high-resolution ion measurement. Since each LIA has 2π FOV, a large 4π FOV for the ion measurement can be achieved overall by the two LIAs. The FMs of LIA have been calibrated at the National Space Science Center (NSSC) and further calibration will take place at the Mullard Space Science Laboratory (MSSL) in August 2024. LIA has now completed its QAR.

3.4 Ground Segment

The Ground Segment (GS) of the SMILE mission is jointly established by CAS and ESA. The GS architecture is illustrated in Figure 9 to demonstrate the respective

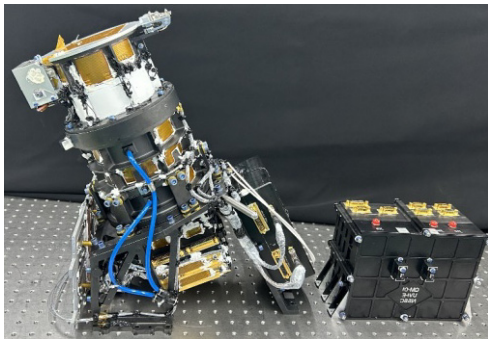

Fig.6 QM of UVI

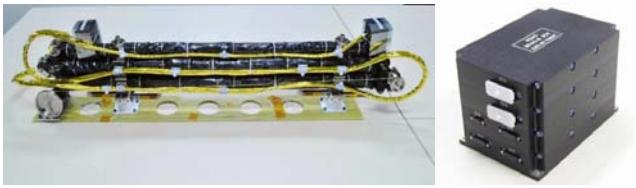

Fig.7 FM of MAG boom (left) and electronic box (right)

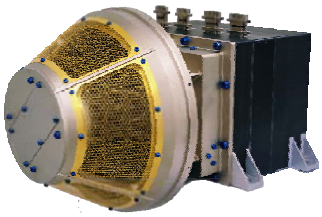

Fig.8 FM of LIA

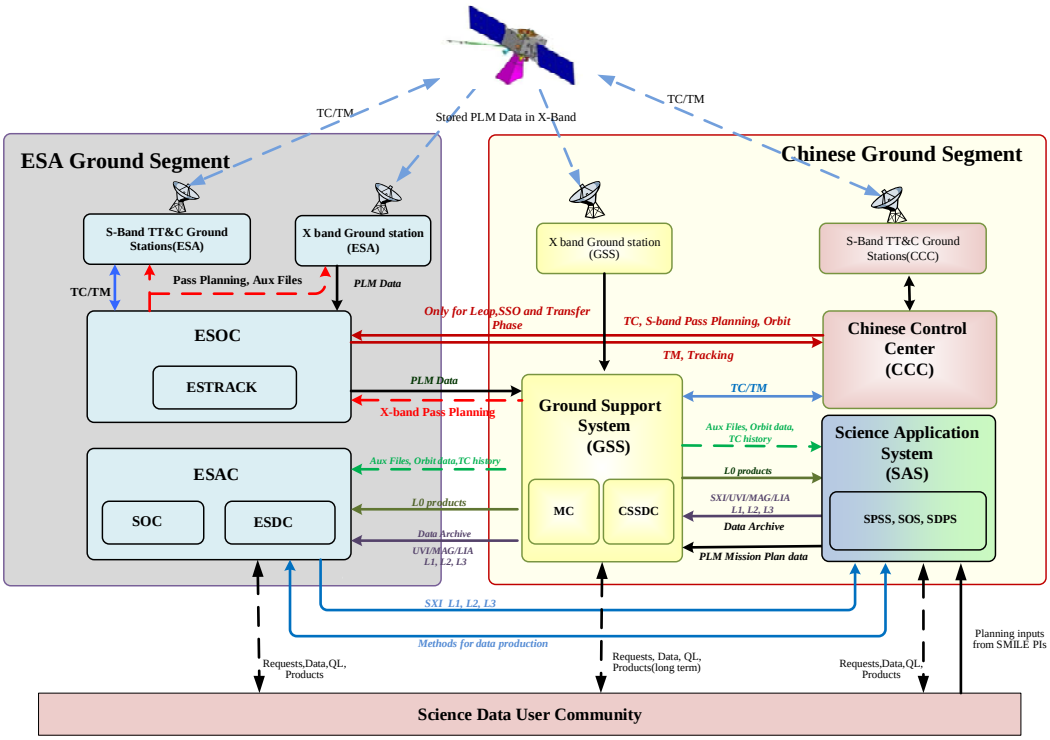

Fig.9 SMILE ground segment architecture

responsibilities and ground-to-space links. The ground segment responsibilities and operation principles for CAS are Science Operations (joint responsibility), Mission Operations, Telemetry, S-band Tracking and Command (TT&C) ground stations, X-band payload data communication station (Sanya as backup). The ground segment responsibilities and operation principles for ESA are Science Operations (joint responsibility), S-band TT&C ground stations (as support to Mission Operations), X-band payload data communication station(s) (DLR station as baseline).

3.4.1 Systems Advances

Since both CAS and ESA GS are used to support multiple satellite missions, the common infrastructure has been already established before SMILE mission. Besides the newly-built Science Application System (SAS), other parts of SMILE GS will be customized from the existing infrastructure, facilities and tools to meet the mission-specific requirements.

The joint GS CDR was completed in June 2022. Since then, efforts have been made in software development. Currently, most software solutions are in the status of coding or updating. The newly-built system SAS also has completed the hardware construction and entered software coding.

3.4.2 GS Activities

GS validation and verification activities define the interface activities between systems.

In Phase C, the interface compatibility tests included: S/C-CCC (Chinese Control Centre) S-Band compatibility test, S/C-ESOC (European Space Operations Center) X-Band compatibility test and S/C-GSS (Ground Support System) TC (Telecommand) test. In Phase D, up to now, the completed interface compatibility tests include S/C- GSS X-Band compatibility test, S/C-CCC S-Band RF compatibility test and S/C-ESOC X-Band RF compatibility test.

Other tests between systems, including GSS/SAS-ESOC interface compatibility test, CCC-GSS interface compatibility test, CCC-ESOC interface compatibility, GSS-ESOC interface compatibility test, S/C-GSS TC test, are scheduled to take place in 2024. After that, the System Operation Validation Test (SOVT) will be conducted during the Spacecraft AIT phase.

3.5 Launch Vehicle

SMILE will be launched by a Vega-C rocket provided by ArianeSpace. The fit check with the satellite and the Launch vehicle adapter has been conducted at the beginning of 2023 in ESTEC as shown in Figure 10. The mechanical interface with the satellite has been confirmed. In April 2023, ESA signed a launch agreement with ArianeSpace, with a launch window now expected between September 2025 and September 2026.

Fig.10 Vega-C fit check with satellite in 2023 in ESTEC (Credit to ESA)

Conclusions

Based on the status of the instruments, PLM and PF CDRs, the joint Mission CDR was completed successfully in June 2023 in Shanghai, which is the fourth joint review of the SMILE mission, marking the kick-off of Phase D activities. Currently, the SMILE mission is going through Phase-D, the final Flight Model (FM) assembly and testing phase. FMs of MAG, LIA, SXI and QM of UVI have been completed and will be integrated on the PLM. The FM of PF is under Assembly, Integration and Tests (AIT) and will be shipped to ESA for integration with the PLM in September 2024. The schedule remains challenging, but all work progresses smoothly. It is expected that the SMILE mission will be launched in the last quarter of 2025.

Acknowledgments

SMILE Mission is a joint project by CAS and ESA. Thanks for the great support of the CAS Strategic Priority Program and the ESA science program. Thanks also go to the study and engineering teams for their cooperation and hard work: National Space Science Center, Innovation Academy for microsatellites of CAS, China Satellite Launch and Tracking Control General, Shanghai Institute of Space Propulsion, National Center for Space Weather, Polar Research Institute of China and all involved parties from the Chinese side; University College London, University of Leicester, Bergen University, OEAW Space Research Institute, University of Liège, Institute National de Técnica Aerospacial, Imperial College, Rutherford Appleton Laboratory, Airbus Defence and Space, Arianespace and all involved parties from European side.

References

[1] WANG C, BRANDUARDI-RAYMONT G. Update on the ESA-CAS joint solar wind magnetosphere ionosphere link explorer (SMILE) mission[J]. *Chinese Journal of Space Science*, 2020, 40(5): 700-703. DOI: 10.11728/cjss2020.05.700

[2] WANG Chi, BRANDUARDI-RAYMONT Graziella, ESCOUBET C P. Recent Advance in the Solar Wind Magnetosphere Ionosphere Link Explorer (SMILE) Mission[J]. *Chinese Journal of Space Science*, 2022, 42(4). DOI:10.11728/cjss2022.04.yg05

[3] DUNGEY J W. Interplanetary magnetic field and the auroral zones[J]. *Phys. Rev. Lett*., 1961, 6:47-48

[4] DAI L, ZHU M, REN Y, *et al*. Global-scale magnetosphere convection driven by dayside magnetic reconnection[J]. *Nat. Commun.*, 2024, 15:639. DOI.org/10.1038/s41467-024-44992-y

[5] SUN T R, CONNOR H, SAMSONOV A. Preface to the Special Issue on Modeling and Data Analysis Methods for the SMILE mission[J]. *Earth Planet. Phys.*, 2024, 8(1):1-4 DOI.org/10.26464/epp2023089

[6] GUO J, SUN T R, LU S, *et al*. Global hybrid simulations of soft X-ray emissions in the Earth's magnetosheath. *Earth Planet. Phys*., 2024, 8(1): 47-58. DOI.org/10.26464/epp2023053

[7] YANG Z W, JARVINEN R K, GUO X C, *et al*. Deformations at Earth's dayside magnetopause during quasi-radial IMF conditions: global kinetic simulations and Soft X-ray Imaging [J]. *Earth Planet. Phys*., 2024, 8(1):59-69. https://doi.org/10.26464/epp2023059

[8] JORGENSEN A M, SUN T R, HUANG Y, *et al*. Tomographic reconstruction of the Earth's magnetosheath from multiple spacecraft: a theoretical study [J]. *Earth Planet. Phys*., 2024, 8(1):204-214. DOI.org/10.26464/epp2023088

[9] ZHANG Y J, SUN T R, CARTER J A, *et al*. , Two methods for separating the magnetospheric solar wind charge exchange soft X-ray emission from the diffuse X-ray background[J]. *Earth Planet. Phys*., 2024, 8(1):119-132. https://doi.org/10.26464/epp2023068

[10] WANG R C, WANG J Q, LI D L, *et al*. Using restored two-dimensional X-ray images to reconstruct the three-dimensional magnetopause[J]. *Earth Planet. Phys*., 2024, 8(1):133-154 https://doi.org/10.26464/epp2023064

[11] ZHANG J J, SUN T R, YU X Z, *et al*. Analysis of the joint detection capability of the SMILE satellite and EISCAT-3D radar[J]. *Earth Planet. Phys*., 2024, 8(1):299-306. DOI.org/10.26464/epp2023061

WANG Chi, SONG Tingting, LI Ming, CAO Song. Strategic Study on the Development of Space Science in China and Proposals for Future Missions. *Chinese Journal of Space Science*, 2024, **44**(4)

Strategic Study on the Development of Space Science in China and Proposals for Future Missions

WANG Chi, SONG Tingting, LI Ming, CAO Song

National Space Science Center, Chinese Academy of Sciences, Beijing 100190

Abstract

Since 2011, the Chinese Academy of Sciences (CAS) has implemented the Strategic Priority Program on Space Science (SPP). A series of scientific satellites have been developed and launched, such as Dark Matter Particle Explorer (DAMPE), Quantum Experiments at Space Scale (QUESS), Advanced Space-based Solar Observatory (ASO-S), Einstein Probe (EP), and significant scientific outcomes have been achieved. In order to plan the future space science missions in China, CAS has organized the Chinese space science community to conduct medium and long-term development strategy studies, and summarized the major scientific frontiers of space science as “One Black, Two Dark, Three Origins and Five Characterizations”. Five main scientific themes have been identified for China's future breakthroughs, including the Extreme Universe, Space-Time Ripples, the Panoramic View of the Sun and Earth, the Habitable Planets, and Biological & Physical Science in Space. Space science satellite missions to be implemented before 2030 are proposed accordingly.

Key words

Space science, Space missions, Space exploration

1 Introduction

In recent years, China's space science has entered the fast lane of innovation and development. With the implementation of a batch of space science missions, a series of original scientific results have been achieved. Chang’E-4 realized the world's first soft landing and roving on the far side of the moon, Chang’E-5 returned China's first sample from an extraterrestrial body, and Tianwen-1 left the imprint of a Chinese spacecraft on Mars for the first time. China Space Station has completed its in-orbit assembly and entered a new era of application and development, with the deployment of scientific experiment cabinets and extravehicular exposure platforms, as well as the Chinese Survey Space Telescope (CSST).

Since 2011, SPP, led by CAS, has been successfully implemented. The scientific achievements of the missions in the program, such as DAMPE, QUESS, Shi-Jian-10 (SJ-10) and Hard X-ray Modulation Telescope (HXMT), Taiji-1, the Gravitational wave high-energy Electromagnetic Counterpart All-sky Monitor (GECAM), ASO-S, EP, *etc*., have significantly improved our understanding of the Universe. The DAMPE spectral measurement of cosmic ray proton and Helium nuclei hints a hardening structure at about 150 TeV in space[1]. HXMT’s observations of a black hole x-ray binary indicate formation of a magnetically captured disk[2]. Observations with ASO-S at 360nm waveband show that about 25% of flares have enhanced emission

Received June 20, 2024

in the Balmer continuum, indicating white-light flares are not rare. This greatly benefits our understanding of energy deposit and transfer processes of the solar and stellar flares[3]. During the commissioning phase, EP has detected a number of transient sources, stellar flares, and a high-redshift (z=4.859) gamma-ray burst[4].

In recent years, China has exhibited breakthroughs in space science, However, the number of space science satellites in China is relatively small, and significant scientific achievements with great impact are few. In general, the development of China's space science is still in its early stage. To foster the high-quality development of space science, the Chinese space science community has conducted strategic research, resulting in a series of outcomes that lay a foundation for planning future missions.

2 China's Space Science Development Strategy

In recent years, the United States has released new versions of "Decadal Survey" in different areas of space science, such as the Pathways to Discovery in Astronomy and Astrophysics for the 2020s (Astro2020), Origins, Worlds, and Life: A Decadal Strategy for Planetary Science and Astrobiology 2023-2032, THRIVING IN SPACE: Ensuring the Future of Biological and Physical Sciences Research: A Decadal Survey for 2023-2032, *etc*. The European Space Agency (ESA) has released VOYAGE 2050: Long-Term Planning of the ESA Science Programme. Since 2022, CAS has organized scientists across the country to conduct a new round of study on the medium and long-term development planning for space science activities in China. It has sorted out the major scientific frontiers in space science and, and identified five major scientific themes for China to make breakthroughs in the future.

2.1 Major Space Science Frontiers

The major scientific frontiers in areas of space astronomy, heliophysics, lunar and planetary science, Earth science, microgravity physics and space life sciences can be summarized as "One Black, Two Dark, Three Origins and Five Characterizations".

2.1.1 One Black

The aim of "One Black" is to explore dense celestial bodies, as represented by black holes, and the physical laws under extreme conditions in the universe.

By means of multi-messenger, such as electromagnetic waves, gravitational waves, neutrinos, cosmic rays, *etc*., the aim is to reveal the internal structure of dense celestial bodies, the laws of matter movement in strong gravitational fields, and the nature of gravity and space & time.

2.1.2 Two Dark

"Two Dark" refers to dark matter and dark energy, the natures of which are poorly understood. The universe is filled with gamma rays and cosmic rays with very high energy, which may originate from dark matter particle annihilation or decay. Direct detection in space has significant advantages for gamma rays in the sub-TeV range and cosmic rays in the PeV range, which might prove the existence of dark matter particles indirectly.

Various hypotheses about dark energy are imperfect and fail to explain observations. There is an urgent need to detect and understand dark energy through photometric and spectroscopic surveys, utilizing a variety of means such as supernovae, baryon acoustic oscillations, gravitational lensing, and redshift spatial distortions of galaxies.

2.1.3 Three Origins

With approximately 13.8 billion years of evolutionary history since the Big Bang, the universe is still facing unanswered questions, such as how the universe began and how the early universe expanded.

The original matter of the solar system and its distribution on the protoplanetary disk determine the composition and evolutionary history of various types of planets. However, the intense impacts during the Late Heavy Bombardment made it difficult to preserve early information.

Life on Earth is the only confirmed existence of life by far, and the search for the most favorable environment for the emergence of life in Earth's early years and the earliest records of life in the solar system will shed some light on the question of "where did we come from". The pursuit of extraterrestrial life, the unraveling of the origins and evolution of life, and comprehending of biodiversity will address the fundamental question of the origin of life.

2.1.4 Five Characterizations

"Five Characterizations" explores the characteristics and working laws of the near-Earth system, Earth-Moon system, the solar system, and the extra-solar system, as well as the laws governing matter movement and life activity in the space environment.

The radiation and energy balance of the Earth system, the water cycle, the carbon cycle, the coupling of the Earth's layers, and the interaction between human activities and the natural environment are all intricately linked to global climate change, which directly impacts the sustainable development of humankind. There is an urgent need to address the complexities of the Earth system and understand the key processes within it.

The origin and evolution of the Earth-Moon system, the layers and structure of the Moon and terrestrial planets and their modification processes, as well as the surface topographical features, the causes and distribution of resources, and the Sun-Earth-Moon space environment are important frontiers.

Solar eruptions have an important impact on the Earth's space environment and the solar system. The magnetic fields and hydrospheres of solar system planets vary greatly, and there is an urgent need for further understanding of the internal composition, physical properties and structural characteristics of layers of the terrestrial planets, the giant planetary systems, the exoplanets, and the comets in the outer solar system.

Interstellar space beyond the heliopause is a "no man's land" rarely visited by human spacecraft. Space observations confirm the ubiquity of exoplanets, challenging the universality of our solar system. The discovery of potentially habitable worlds is desirable and promises to provide crucial evidence to answer the question "Are we alone in the universe?" Exoplanets also hold great scientific opportunities.

Conditions in space are characterized by variable gravity, strong radiation, weak magnetic fields *etc*., which are fundamentally different from those on the Earth, providing ideal laboratories to reveal the laws of matter and life activities, and to carry out space intelligent manufacturing, innovative energy and the terrestrial application of space medical science.

2.2 China's Main Scientific Themes

Facing the frontiers of space science and addressing the major needs of the country, we must also take China's reality into account, such as the disciplinary advantages, human resources, and the maturity level of the engineering and technology. Accordingly, China's space science will focus on five scientific themes, namely, "Extreme Universe", "Space-Time Ripples", "the Panoramic View of the Sun and the Earth", "Habitable Planets", and "Biological & Physical Science in Space".

The theme "Extreme Universe" explores the origin and evolution of the universe, and reveals the physical laws of the universe under extreme conditions. The main scientific questions to be addressed include the nature of dark matter particles, the sources of high-energy radiation in the universe, the nature of dark energy, the physical mechanisms of dynamic cosmic detections and transient sources, the dark age of the universe, and the history of reionization.

The theme "Space-Time Ripples" detects low and medium -frequency gravitational waves and primordial gravitational waves in order to reveal the nature of gravity and space-time. The scientific questions to be addressed include the formation of supermassive black holes and their co-evolution with host galaxies, as well as the testing of early cosmological models.

The theme "the Panoramic View of the Sun and the Earth" explores the Sun, Earth and the heliosphere, and reveals the physical processes and laws governing the complex system of the Sun-Earth and the Sun-Solar system connections. The main scientific questions to be addressed include the structure and coupling processes of the solid Earth's inner layers, the characteristics of the solar magnetic field and the mechanism of the origin of the solar magnetic cycle, and the processes and mechanisms of solar wind and interstellar medium interaction.

The theme "Habitable planets" explores the habitability of solar system planets and exoplanets, and searches for extraterrestrial life. The main scientific questions to be addressed include the mechanism of interaction between human activities and the natural environment, the composition of the Moon's deep matter and its layer structure, the origin and evolution of asteroids and comets, the evolution of habitable environments and potential life signals on Mars, and the habitability and life signatures of exoplanets.

The theme "Biological & Physical Science in Space" reveals the laws of matter movement and life activities under space conditions, and deepens the knowledge of fundamental physics such as quantum mechanics and general relativity. The scientific questions to be solved mainly include fire safety in manned spaceflight, preparation of high-performance materials and the behavior of materials in extreme space environments, quantum effects in the gravitational field, basic medical problems of medium- and long-term spaceflight and residence, and research on special biotechnology in space.

3 Proposals for China's near Future Space Science Missions

Based on the China's development strategy study for space science, a series of new space science satellite missions have been proposed for the near future, which will focus on major scientific issues in the category of "origins", such as the origins of the universe, the origins of space weather, the origins of life, *etc*. It is proposed that by 2030, in-orbit scientific exploration is expected to yield major discoveries and original results in the following directions, such as the dark age of the universe, the solar magnetic activity cycle and high-speed solar wind, Earth-like exoplanet, the physical laws of the universe under extreme conditions, and the nature of gravity and space-time.

Discovering the Sky at the Longest wavelength (DSL)[5]. With 1 mother satellite and 9 daughter satellites operating in a 300 km circular lunar orbit, DSL takes advantage of the highly clean electromagnetic environment on the far side of the Moon to conduct ultra-long-wave radio astronomy observations, which will provide key observational evidence to open a new window to image the dark age of the universe with MHz radio waves.

Solar Polar Orbit Observatory (SPO)[6]. With the implementation of the solar polar orbit observation system above the ecliptic plane, SPO aims to achieve the first-ever frontal imaging of the solar polar region, so as to make crucial breakthroughs in research on the origin of solar magnetic activity cycles and the origin of high-speed solar wind.

The Earth 2.0 (ET)[7]. A space observatory at the Earth-Sun L2 point conducts a long-term, large-scale survey of exoplanets, to explore habitable Earth-like planets outside our solar system, and target candidates for extraterrestrial life search.

Enhanced X-ray Timing and Polarimetry (eXTP)[8]. The mission will conduct research on the detection of dense celestial bodies, such as black holes and neutron stars, with high time resolution, high energy resolution and high-precision polarization, so as to explore the physical laws and principles under the extreme conditions in the universe, including extreme gravity, magnetism, and density.

Taiji-2[9]. A three-satellite constellation in a 60-million-kilometer heliocentric orbit, constituting a 3-million-kilometer ultra-long baseline space-based gravitational wave observation system, detects millihertz (0.1mHz～1.0Hz) gravitational waves in space.

In addition, with the successful implementation of the Chang'E-6 lunar sample-return mission, the future missions are also being developed, such as the Chang'E-7 Lunar Polar Regions Exploration, Tianwen-2 near-Earth asteroid sample return and main-belt comet exploration mission, the International Lunar Research Station (ILRS), and the China Space Station for Space Science and Applications.

4 International Cooperation

The peaceful use of outer space is a matter of concern for the well-being of all humankind. Since space exploration entails high investment and risk, a country cannot and should not be alone in its own endeavors. In the 21st century, international cooperation in space science has received increasing attention, and almost all flagship space science missions incorporate elements of international cooperation, which not only reduces a country's space investment and risks, but also multiplies scientific outputs, facilitates the country's scientific and technological diplomacy, and has become an important part of international foreign policy.

Missions such as the Solar wind Magnetosphere Ionosphere Link Explorer (SMILE) and the Einstein Probe (EP) involve in-depth international cooperation. Missions such as the planned DSL, ET, and eXTP will also involve specific international cooperation in scientific research. Chang'E-4, Chang'E-5, and Chang'E-6 missions of the Lunar and Planetary Exploration Project have carried onboard international payloads from other countries, and have produced influential scientific results. The China Space Station has also invited other countries to participate in international cooperation, and projects from Switzerland, Germany, Italy, and other countries have been selected.

In the future, China will actively initiate, propose and participate in international cooperation projects. Through mutual cooperation across missions, joint observations and scientific experiments, joint payload development, testing and calibration, or flying piggyback payloads on each other's platform, open access of scientific data, and joint scientific teams, China will engage in multi-level international cooperation to fully leverage the platforms such as China Space Station and ILRS, to

make significant contributions to answer fundamental scientific questions.

5 Summary

Space science in China is advancing from the initial stage into a new era of accelerated development. The release of the first national medium and long-term plan for space science is imminent, and a series of new space science satellite missions are about to be approved for implementation. China will cont inue to promote international scientific and technological cooperation to explore the vastness of the universe, and contribute more Chinese wisdom and solutions to the peaceful use of outer space.

References

[1] PRD Letter (2024), in press

[2] YOU Bei, ZHANG Shuangnan, *et al*. Observations of a black hole x-ray binary indicateformation of a magnetically arrested disk. *Science*, 2023, 381: 961-964

[3] JING Z, LI Y, FENG L, *et al*. A Statistical Study of Solar White-Light Flares Observed by the White-Light Solar Telescope of the Lyman-Alpha Solar Telescope on the Advanced Space-Based Solar Observatory (ASO-S/LST/WST) at 360 nm. *Sol. Phys.*, 2024, 299, 11

[4] Nature Astronomy, 2024, in review

[5] CHEN Xuelei *et al*. 2021 Discovering the sky at the longest wavelengths with a lunar orbit array. *Phil. Trans. R. Soc. A 379*: 20190566. DOI.org/10.1098/rsta.2019.0566

[6] DENG Yuanyong, ZHOU Guiping, DAI Shuwu, *et al*. Solar Polar-orbit Observatory. *Chinese Science Bulletin*, 2023, 68(4): 298-308

[7] GE J, ZHANG H, DENG H, *et al*. The ET mission to search for earth 2.0s. *The Innovation*, 2022, 3(4):100271

[8] ZHANG Shuangnan, *et al*. The enhanced X-ray Timing and Polarimetry mission—eXTP. *SCIENCE CHINA Physics, Mechanics & Astronomy*. February 2019, 62(2): 029502

[9] LUO Ziren, ZHANG Min, WU Yueliang. Recent Status of Taiji Program in China. Chinese Journal of Space Science, 2022, 42(4): 536-538

4 Ground-based Observation Project

WANG Chi, CHEN Zhiqing, XU Jiyao. Construction and Research Progress of the Chinese Meridian Project in 2022–2023. *Chinese Journal of Space Science*, 2024, **44**(4)

Construction and Research Progress of the Chinese Meridian Project in 2022–2023

WANG Chi, CHEN Zhiqing, XU Jiyao

National Space Science Center, Chinese Academy of Sciences, Beijing 100190

Abstract

The Chinese Meridian Project (CMP) is a major national science and technology infrastructure constructed in two steps. The first phase of the CMP has been operating for more than a solar cycle. From 2022 to 2023, utilizing the monitoring data collected by the CMP, scientists made major breakthroughs in fields of ionosphere, middle and upper atmosphere, and coupling between layers. The construction of the second phase of the CMP is nearly finished, and the project is expected to operate as a whole in 2025 after national acceptance of the second phase. The whole project was built in an architecture of so-called “One Chain, Three Networks and Four Focuses”. It is promising to make a three-dimensional observation of the whole solar-terrestrial space. The science community is looking forward to the great contribution of the CMP to space weather and space physics research.

Key words

Chinese Meridian Project (CMP), Space physics, Magnetosphere, Ionosphere, Middle and upper atmosphere

1 Introduction to the Chinese Meridian Project

Monitoring solar-terrestrial space and conducting related comprehensive research is crucial for humanity in the modern space age. In addition to satellite observation, ground-based detection is also an important and irreplaceable observation method. Ground-based space environmental monitoring has a long history, commencing with experiments such as geomagnetic surveys and auroral observations from ancient times. Due to its significant “5C” advantages (continuous, convenient, controllable, credible, and cost-effective), ground-based monitoring has been widely adopted nowadays. Presently, ground-based monitoring is developing toward a networking trend, with research groups worldwide establishing numerous ground monitoring networks, such as SuperDARN, MAGDAS, and INTERMAGNET.

To monitor the huge span of the solar-terrestrial space with regions of quite different physical characteristics, including the solar atmosphere, interplanetary space, magnetosphere, ionosphere, and middle and upper atmosphere, a highly comprehensive capability is desired. The Chinese scientists proposed to construct the Chinese Meridian Project (CMP). The overall scientific goals of the CMP can be summarized as follows. (1) Tracing the propagation and evolution of space weather events from the solar atmosphere to near-Earth space and their impact on the space environment. (2) Revealing regional characteristics of the space environment over different regions, and relationship between regions.

Received June 20, 2024

(3) Studying the coupling mechanism between different spatial layers and physical processes.

Construction of the CMP was divided into two stages, namely Phase I and Phase II. The CMP phase I was completed from 2008 to 2012 and entered the operational phase after 2012[1], and has accumulated data for more than a solar cycle. Significant research progress has been made utilizing the dataset[2]. The second phase, CMP phase II, with construction beginning at the end of 2019, is now waiting for final national acceptance. After the completion of CMP phase II, CMP can achieve a detection altitude range from near-Earth space to the solar atmosphere and has a rather full coverage of the territories of China's mainland and polar regions, providing a stereoscopic monitoring capability for the entire solar-terrestrial space.

This report aims to introduce the latest progress made between 2022 and 2023. Section 2 introduces the construction status of the CMP Phase II and outlines the facilities finally established. Section 3 will mainly introduce the research progress made using the facilities and data of the CMP Phase I, followed by some conclusions and future development prospects.

2 Construction Progresses of the CMP Phase II

2022-2023 is a critical two-year period for construction of the CMP Phase II. All the heavy works, such as laboratory experiments, on-site installation and debugging, were carried out during this period. After the construction was completed, each instrument was tested against design indicators under the witness of an expert group. On June 3, 2024, the project passed technique acceptance organized by Chinese Academy of Sciences and was put into overall trial operation. National acceptance is expected to be held by the end of 2024.

Each instrument started trial operation after completion of construction, so preliminary observation results have been accumulated, and related research is currently underway. Some preliminary open sharing and exchange activities are also carried out, such as the SuperDARN Beijing seminar held in June 2024.

According to the design, the CMP constructed three systems namely Space Environment Monitoring System, Data and Communication System and Scientific Application System. In the following paragraphs, a brief introduction of the constructed systems will be presented. For more detailed information, please refer to the "Chinese Meridian Project Special Collection"[3] published on the *Journal of Space Weather* or visit the website (http://www.meridianproject.ac.cn).

2.1 Space Environment Monitoring System

Space Environment Monitoring System is composed of nearly 300 instruments in 31 comprehensive stations that are strategically located approximately along longitude 120°E, longitude 100°E, latitude 30°N, and latitude 40°N, effectively covering the Chinese Mainland and the polar regions. To achieve comprehensive and three-dimensional detection of the entire solar-terrestrial space, the CMP adopted a well-designed architecture namely "One Chain, Three Networks, and Four Focuses" (Figure 1). The so-called "One Chain" is formed by optical, radio, Interplanetary Scintillation (IPS), and cosmic ray instruments, covering the entire space chain from the solar surface to interplanetary space, and further to the geospace. The "Three Networks" conduct grid-like monitoring for the ionosphere, middle and upper atmosphere, and geomagnetic field over the territory

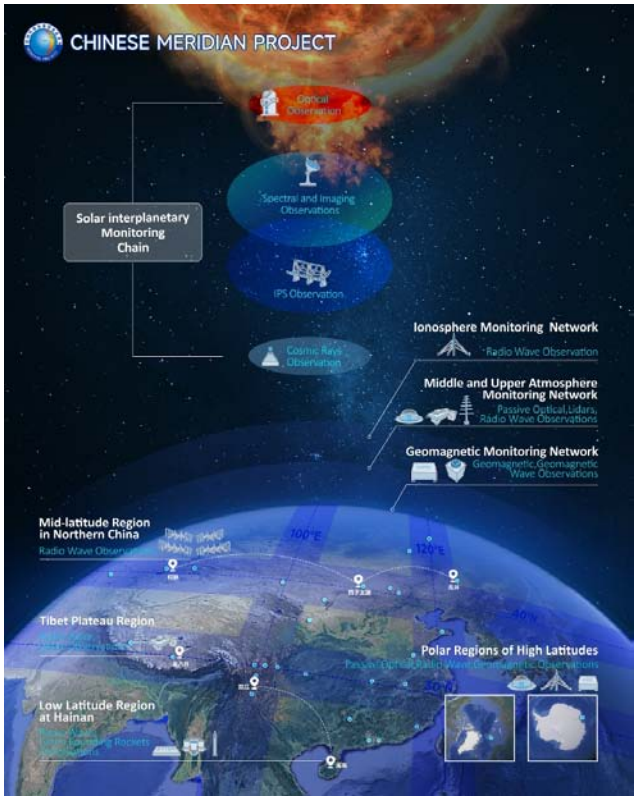

Fig.1 Schematic diagram of the CMP's space environment monitoring system (from Wang *et al*., 2024[3])

of China. Additionally, four key areas with special regional characteristics or serving as key nodes for the propagation of space weather disturbances have been identified, and large-scale instruments or powerful monitoring facilities have been established there to do more detailed observations. These key regions include the high-latitude polar regions, the mid-latitude regions in northern China, the low-latitude region at Hainan, and the Tibet Plateau region.

2.1.1 One Chain

The sun serves as the primary source of disturbances in the solar terrestrial space environment. Monitoring the solar atmosphere and interplanetary space is crucial for understanding the mechanisms of solar eruptions and the transmission laws of matter and energy, as well as improving space weather forecasting performance. One Chain, the solar interplanetary monitoring chain, was established to monitor from the solar surface to near-Earth space.

To account for significant differences existing in the frequency of electromagnetic radiation across various regions, the chain employs various detection methods, including optics, radio, InterPlanetary Scintillation (IPS), and cosmic rays. This comprehensive approach forms a full chain with tracking and monitoring capability for solar eruption activities from the solar surface to near-Earth space. The main monitoring instruments include Solar Magnetism and Activity Telescope, Solar Full-disk Multi-layer Magnetograph, Solar Disk Chromosphere Telescope, Spectral Imaging Corona Graph, Spectrometers and radio heliographs in multiple frequency bands (*e.g.*, Figure 2), IPS telescope (Figure 3), Moun telescope and neutron counter.

Fig.2 Circular Array Solar Radio Telescope (150MHz-450MHz)

Fig.3 IPS Telescope Array (the main station)

2.1.2 Three Networks

A comprehensive network of instruments was deployed to monitor the near-Earth space environment. These instruments are approximately located along the meridians (120°E and 100°E) and latitude lines (30°N and 40°N). This layout enables thorough monitoring of the rich longitude and latitude variations and regional characteristics of the near-Earth space environment over China.

The Geomagnetic Monitoring Network deployed more than 100 geomagnetic (and electrical) instruments to detect long-term changes, rapid changes, and fluctuations in the geomagnetic field and near-surface electric fields. Instruments include fluxgate magnetometers, fluxgate theodolites and the Overhauser magnetometers, magnetic field wave monitors, geoelectric field detectors, and so on.

The Middle and Upper Atmosphere Monitoring Network comprises various radio radars in Figure 4 (meteor radars, Mesosphere-Stratosphere-Troposphere radars), airglow monitoring instruments (airglow imagers, airglow interferometers), and LiDARs. These instruments collectively measure atmosphere density,

Fig.4 One of the MST radars (QinZhou Station)

wind, temperature, as well as ionospheric irregularities. The network can measure various parameters from an altitude of 0.3 km up to more than 110 km with a horizontal spacing of hundreds kilometers.

2.1.3 Four Focuses

In the four key regions, *i.e*., the high-latitude polar region, a mid-latitude region in northern China, the low-latitude region at Hainan Island, and the Tibet Plateau region, powerful monitoring facilities or large-scale instruments have been deployed there.

For the high-latitude polar region, the CMP utilizes existing scientific stations established by China in the polar regions or takes advantage of international cooperation, to deploy instruments monitoring the ionosphere, middle and upper atmosphere, auroras, and geomagnetic field waves. Stations include Zhongshan Station (76.4° E, 69.4° S) and Great Wall Station (59.0° E, 62.2° S) in Antarctica, and Longyearbyen Station (16.0° E, 78.2° N) in the Arctic.

For the mid-latitude region in northern China, a high-frequency radar array was built at three observation stations located in the northern region of China: Longjing (129.4° E, 42.8° N), Siziwang (111.6° E, 41.8° N), and Hejing (83.7° E, 42.9° N) (Figure 5). Each station is equipped with two high-frequency Radars, one facing northeast and the other facing northwest. The combination of the two radars forms a fan-shaped scanning region with an angle of approximately 158°. As a result, the combination of the detection region of the three stations is about 10000 km in the east-west direction and over 3500 km in the north-south direction. This huge coverage literally links domestic monitoring with polar region monitoring.

For the low-latitude region at Hainan Island, multiple large-scale radio wave and optical monitoring instruments were established to detect the fine spatial structure of the middle and upper atmosphere, ionosphere, and inner magnetosphere, spanning altitudes from 80 kilometers to thousands of kilometers. Among the instruments, Very High Frequency (VHF) radars in Danzhou, Hainan, and Shuangjiang, Yunnan, detect the distribution and movement of ionospheric irregularities. A low latitude high- frequency Radar built in DongFang, Hainan, explores the horizontal characteristics of magnetic field lines in the low latitude region by detecting ionospheric irregularities in the east and west directions. A parabolic mechanically steering incoherent scattering radar (ISR) was constructed in Qujing, Yunnan, during the first phase of the CMP, and a phased array incoherent scattering radar system (SYISR) was built in the second phase, with transmitters and receivers located in Sanya (Figure 6), Danzhou, and Wenchang, Hainan Island. An Array Type Large-Aperture LiDAR (Figure 7) built in Danzhou integrated multiple optical telescopes

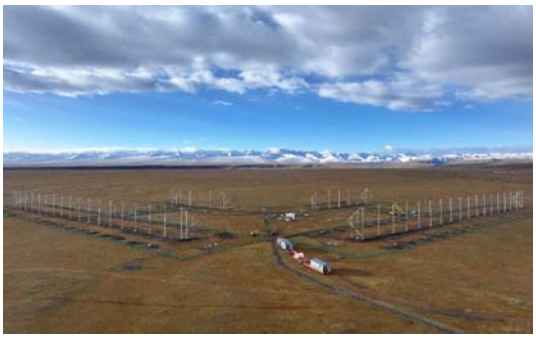

Fig.5 Mid-latitude high-frequency Radar (HeJing Station)

Fig.6 Multi-static incoherent scattering radar (the main station)

Fig.7 Array-type large aperture lidar

to detect metastable helium density in the altitude range of 200~1000 km and atmospheric density, temperature, and sodium atom density within an altitude range of about 30~105 km.

For the Tibet Plateau region, the Yangbajing Station (90.5°E, 30.1°N, 4290 m) was established to accommodate a multitude of instruments consisting of an MST radar, an Atmosphere Wind Temperature Lidar, and a Millimeter-Wave and Infrared Imager. These instruments monitor atmospheric temperature, wind field, density, metal layer, and other parameters in an altitude range from the surface up to the lower thermosphere.

2.2 Data and Communication System and Scientific Application System

The data and communication system includes the data network transmission subsystem, data processing and management subsystem, and data service subsystem, with core functions of data collection, processing, storage, and user services. To ensure security, the system has established a VPN network that connects all monitoring instruments to the data center. Most monitoring data can be transmitted to the data center and made publicly available within 15 minutes.

The Scientific Application System was constructed to efficiently manage monitoring instruments of the Space Environment Monitoring System, and promote scientific research using monitoring data. The system includes the Scientific Operation Subsystem, Research Support Subsystem, Forecast Support Subsystem, and Application Demonstration Subsystem.

Both the Data and Communication System and the Scientific Application System are built in the CMP Information and Operation Control Center Building in HuaiRou, Beijing (shown in Figure 8).

3 Research Progresses

3.1 Overview

For CMP Phase-II, although its construction has not been fully completed, preliminary observations have been obtained and published in journals. For example, Hou *et al*.[4] reported a type-II radio burst observed by the Rongcheng solar radio spectrometer, and Yue *et al*[5] presented an ionospheric pre-sunrise uplift event captured by the Sanya incoherent scatter radar. During the construction of CMP Phase-II, a series of equipment introduction articles and research papers were published, such as on Interplanetary scintillation observation and space weather modeling[6], active phased array[7], and Data Acquisition, Correction and Retrieval[8]. In particular, a special introduction collection on conventional instruments was published in the Chinese journal Review of Geophysics and Planetary Physics. Some introduction articles of large-scale monitoring equipment have been submitted to the special collection of Space Weather.

From 2022 to 2023, most research works were conducted using monitoring data from CMP Phase-I. These research works mainly involve near-Earth space regions, *i.e*. middle and upper atmosphere, ionosphere. For the sake of brevity, we will only introduce some of the highlights of our research works below.

3.2 Middle and Upper Atmosphere

The nonlinear interaction between waves in the atmosphere is an important topic for studying the physical mechanisms of the generation, evolution, and propagation of atmospheric waves. He *et al*.[9] reported a Rossby wave second harmonic generation event in meteor

Fig.8 (a) The Information and Operation Control Center Building, (b) The Operation Control Center hall, and (c) The Data and Computing Center Facility (from Wang *et al*., 2024[3])

radar wind observations. Bicoherence and biphase analyses demonstrate that the 16-day signature in wind data is a Rossby wave normal mode, and its second harmonic generation gives rise to an 8-day signature. For the first time, the study confirmed the theoretically anticipated Rossby wave nonlinearity.

The global middle and upper atmospheric wind field is a very important dynamic parameter that is difficult to be measured. Its characteristics of variation have always been an important scientific issue in the study of the middle and upper atmosphere. Using meteor radar observations and satellite TIMED/SABER temperatures, Liu *et al*.[10] derived a global balance wind dataset from 2002 to 2019 and studied the relationships between global zonal wind and several impactors. It was shown that the responses of zonal winds to QBO are approximately hemispheric symmetry and change from positive to negative with increasing height, and the responses of zonal winds to $F_{10.7}$ and ENSO are more prominent in the southern stratospheric polar jet region as compared to the northern counterpart. Using meteor radar measurements and the reanalysis data from 2011 to 2020, Gong *et al*.[11] for the first time investigated the characteristics of intraseasonal oscillations (ISOs) in the MLT region over Mohe (53.5°N, 122.3°E). They found a strong Intraseasonal Oscillation (ISO) with a period of 40~60 days in the mesosphere and lower thermosphere, and suggested that it is likely associated with the equatorial Madden-Julian Oscillations in the troposphere and strong El Niño and the positive Indian Ocean Dipole indices may also contribute.

Metal layers are important components of the atmosphere and good tracers for studying the dynamics and photochemistry in the mesosphere and lower thermosphere. In addition to metal Na, the Lidar at the Beijing station has been upgraded to detect other metal components in the mesopause and lower thermosphere region. Jiao *et al*.[12] reported a Ca^+ layer event up to a height of 300km, captured by the new Lidar. The thermosphere-ionosphere Ca^+ layer was likely formed by uplifting ions from sporadic Ca^+ at about 110 km, which was demonstrated by spread F occurred concurrently and strong sporadic E layers occurred before. Efforts were also made to improve metal layer models. Yu *et al*.[13] compared the WACCM-Na model against lidar observations and suggested that vertical transportation is underestimated in the model.

3.3 Ionosphere

The nighttime enhancement of electron density is a frequent phenomenon, but lacks a satisfactory and consistent explanation. Liu *et al*.[14] made case studies showing that the northern hemisphere GEO-TEC enhances in a limited latitudinal and longitudinal coverage usually with a hemispheric asymmetry at low latitudes. They suggested field-aligned transport and electric fields being possible regulator to the limited spatial scale of post-midnight enhancements in the low latitude ionosphere. The study also showed discrepancies between TEC and N_mF_2 as indicators for electron concentration.

Ionospheric plasma bubbles are a type of ionospheric irregularities that often occur in low latitude regions, referred to as Equatorial Plasma Bubbles (EPB) as well. Relative studies can help to understand ionospheric dynamics. Exploring measurements from an all-sky airglow imager and a Very High Frequency (VHF) radar and eight digisondes, Sun *et al*.[15] reported the evolution process of an EPB event that was supposed to be controlled by multiple factors. The EPB was seeded by gravity waves, and evolved into topside ionosphere via gradient drift instability and T-R instability. This equatorward wind-induced E × B gradient drift instability continuously forced topside depletions to extend poleward, resulting in 3.2 m irregularities around midnight.

Ionosphere modeling is not only crucial for prediction, but also helps to understand physical mechanisms. Yu *et al*.[16] constructed an Es layer (sporadic E layer) climatological model based on S4max data extracted from COSMIC satellite occultation measurements. This model can provide climatology of Es layer intensity as a function of altitude, latitude, longitude, universal time, and day of year.

3.4 Coupling between Layers

Some research was conducted on the coupling between solar wind, magnetosphere and ionosphere, using detection data of CMP. Liu *et al*.[17] found that the polar region ionosphere can be promptly affected by interplanetary shocks. Their study shows that the Ionosonde at Zhongshan station detected enhanced E region ionization and vertical plasma motion, and it is thought to be the result of sudden impulse (SI)-driven E-field drift-convergence and particle precipitation caused by an interplanetary shock. It was assumed the shock-triggered SI altered the dusk-to-dawn electric field that

drives a brief downward plasma motion at the dayside polar ionosphere.

Ionospheric response to storms was studied. Arslan *et al*.[18] presented the longitudinal dependence of ionospheric responses during two intense geomagnetic storms of May and September 2017. Two ionospheric enhancements were observed in TEC measurements during the storm of May 2017, both can be attributed to Prompt Penetration Electric Field (PPEF) while with the maximum TEC enhancements located in different regions. Negative storm time ionospheric responses were observed on 30 May, allegedly caused by a change of the thermospheric composition as O/N_2 depletion.

Lithosphere-atmosphere-ionosphere coupling plays a crucial role in the dynamics of the whole near-Earth space. Volcanos and typhoons are two major sources of upward propagating disturbances. Multiple studies have been conducted about the 2022 Tonga volcano eruption. Zhang *et al*.[19] showed enhanced ionospheric irregularities with highly variable velocities after the Tonga volcanic eruption, with the maximum amplitude of the line-of-sight velocity of the ionospheric oscillation approaching 150 m/s in the E layer. The study also showed magnetic field conjugation-related disturbances occurred much earlier than the arrival of surface air pressure waves. For typhoon-induced disturbance, Li *et al*.[20] presented an event in which a typhoon directly generated gravity waves in the mesopause region while the thermosphere was affected by the secondary waves generated by the dissipation processes in the mesopause region.

Stratosphere Sudden Warming (SSW) has been an important topic for studying coupling between different atmosphere layers and between the neutral atmosphere and ionosphere. From 2022 to 2023, many works using the CMP data were published on this topic. For example, Ma *et al*.[21] reported significant tide-like harmonics in the residuals of Total Electron Content (TEC) during SSWs. Their study shows that significant tide-like harmonics presented in the residuals of TEC were detected by five receivers at different latitudes during the 2018 SSW. After the SSW onset, the third harmonic enhanced and the fourth harmonic weakened for all receivers, while the second harmonic exhibited a response depending on latitude. Comparing TEC signals against mesospheric winds observed by four meteor radars showed good agreement, demonstrating the crucial role played by neutral winds in the formation of tide-like harmonics in the ionosphere.

4 Conclusion and Prospect

In this report, we reviewed the construction progress of CMP Phase II, including a brief introduction of established systems and instruments. The research progresses in the past two years using the monitoring data of the CMP Phase-I are also introduced. Recently, the second phase of the CMP has nearly finished construction and is expected to undergo national acceptance by the end of this year. The first phase of the project has been operating for more than a solar cycle. Utilizing the monitoring data, comprehensive research has made significant progress with topics varying from ionosphere, middle and upper atmosphere, and coupling between layers. On national acceptance of the second phase, the two phases of Chinese Meridian Project will operate as a whole to realize the scientific objectives of the project. It is very promising that the CMP will continue contributing to innovation in the field of space science at an even much higher level.

References

[1] WANG C, *et al* . New Chains of Space Weather Monitoring Stations in China. Space Weather, (2010)8, S08001. doi:10.1029/2010SW000603

[2] WANG C, XU J, LIU L, *et al*. Contribution of the Chinese Meridian Project to space environment research: Highlights and perspectives. Science China: Earth Sciences, 2023, 66, 1423–1438. DOI. org/10.1007/s11430-022-1043-3

[3] WANG Chi, XU Jiyao, CHEN Zhiqing, *et al*. China's Ground-based Space Environment Monitoring Network – Chinese Meridian Project (CMP). Space Weather. Accepted

[4] HOU Zhenyong, TIAN Hui, SU Wei, *et al*. A Type II Radio Burst Driven by a Blowout Jet on the Sun. The Astrophysical Journal, 2023, 953(2)

[5] YUE Xinan. Ionospheric pre-sunrise uplift: Comparison of Sanya Incoherent Scatter Radar observations and numerical simulations.; Journal of Geophysical Research: Space Physics. 2023

[6] XIONG Ming, FENG Xueshang, LI Bo, *et al*., Interplanetary scintillation observation and space weather modelling. Frontiers in Astron. & Space Sci., 2023, DOI:10.3389/fspas.2023.1159166

[7] YUE *et al*. An active phased array in China. Nature Astronomy, 2022

[8] XIA Y, CHENG X, WANG Z, *et al*. Design of a data acquisition, correction and retrieval of Na doppler lidar for diurnal measurement of temperature and wind in the mesosphere and lower thermosphere region. Remote Sens. 2023, 15, 5140. DOI.org/10.3390/rs15215140

[9] HE M, FORBES J M. Rossby wave second harmonic generation

observed in the middle atmosphere. Nat Commun 13, 7544 , 2022. DOI.org/10.1038/s41467-022-35142-3

[10] LIU X, XU J, YUE J, *et al*. Variations in global zonal wind from 18 to 100 km due to solar activity and the quasi-biennial oscillation and El Niño–Southern Oscillation during 2002–2019. Atmospheric Chemistry and Physics, 2023, 23(11), 6145–6167. DOI.org/10.5194/acp-23-6145-2023

[11] GONG Y, XUE J, MA Z, *et al*. Observations of a strong intraseasonal oscillation in the MLT region during the 2015/2016 winter over Mohe, China. Journal of Geophysical Research: Space Physics, 2022, 127, e2021JA030076. DOI.org/10.1029/2021JA030076

[12] JIAO J, CHU X, JIN H, *et al*. First Lidar Profiling of Meteoric Ca+ Ion Transport from 80 to 300 km in the Midlatitude Nighttime Ionosphere. Geophysical Research Letters, 2022, e2022GL100537

[13] YU B, XUE X, SCOTT C J, *et al*. An empirical model of the ionospheric sporadic E layer based on GNSS radio occultation data. Space Weather, 2022, 20(8), DOI.org/10.1029/2022SW003113

[14] LIU L, YANG Y, ZHANG R, *et al*. Structure of post-midnight enhancements in electron density at the low latitude F-layer ionosphere. Journal of Geophysical Research: Space Physics, 2023, 128, e2023JA031376. https://doi.org/10.1029/2023JA031376

[15] SUN L, XU J, ZHU Y, *et al*. Multi-source perturbations in the evolution of a low-latitudinal equatorial plasma bubble event occurred over China. Space Weather, 2023, 21, e2022SW003293. DOI.org/10.1029/2022SW003293

[16] YU B, XUE X, SCOTT C J. An empirical model of the ionospheric sporadic E layer based on GNSS radio occultation data. Space Weather, 2022, 20, e2022SW003113. DOI.org/10.1029/2022SW003113

[17] LIU J, CHAKRABORTY S, CHEN X, *et al*. Transient response of polar-cusp ionosphere to an interplanetary shock. Journal of Geophysical Research: Space Physics, 2023, 128, e2022JA030565. DOI. org/10.1029/2022JA030565

[18] TARIQ M Arslan, YANG Yuyan, MUNAWAR Shah, *et al* . Ionospheric-Thermospheric responses to the May and September 2017 geomagnetic storms over Asian regions. Advances in Space Research, 2022, 70: 3731-3744

[19] ZHANG J, XU J, WANG W, *et al*. Oscillations of the ionosphere caused by the 2022 Tonga volcanic eruption observed with SuperDARN radars. Geophysical Research Letters, 2022， 49, e2022GL100555. DOI. org/10.1029/2022GL100555

[20] LI Q, XU J, LIU H, *et al*. How do gravity waves triggered by a typhoon propagate from the troposphere to the upper atmosphere. Atmos. Chem. Phys., 22, 12077-12091, DOI.org/10.5194/acp-22-12077-2022, 2022

[21] MA H, HE M, LIU L, *et al*. Solar tide-like signatures in the ionospheric total electron content during the 2018 sudden stratospheric warming event. Space Weather. 2022. 20, e2022SW003042. DOI.org/10.1029/2022SW003042

5 Application Satellites

GUAN Min, WANG Jingsong, ZHAO Xiangang, QIN Danyu, FAN Cunqun, XIAN Di, LIU Chang. Progress and Achievements of Fengyun Meteorological Satellite Program since 2022. *Chinese Journal of Space Science*, 2024, **44**(4)

Progress and Achievements of Fengyun Meteorological Satellite Program since 2022

GUAN Min, WANG Jingsong, ZHAO Xiangang, QIN Danyu, FAN Cunqun, XIAN Di, LIU Chang

1 National Satellite Meteorological Center (National Centre for Space Weather), Innovation Center for Fengyun Meteorological Satellite (FYSIC),
2 Key Laboratory of Radiometric Calibration and Validation for Environmental Satellites/Key laboratory of Space Weather, China Meteorological Administration Beijing 100081

Abstract

Fengyun meteorological satellites have undergone a series of significant developments over the past 50 years. Two generations, four types, and 21 Fengyun satellites have been developed and launched, with 9 currently operational in orbit. The data obtained from Fengyun satellites is employed in a multitude of applications, including weather forecasting, meteorological disaster prevention and reduction, climate change, global environmental monitoring, and space weather. These data products and services are made available to the global community, resulting in tangible social and economic benefits. In 2023, two Fengyun meteorological satellites were successfully launched. This report presents an overview of the two recently launched Fengyun satellites and currently in orbit Fengyun satellites, including an evaluation of their remote sensing instruments since 2022. Additionally, it addresses the subject of Fengyun satellite data archiving, data services, application services, international cooperation, and supporting activities. Furthermore, the development prospectives have been outlined.

Key words

Fengyun meteorological satellites, Data services and application, International cooperation and support

1 Introduction

In April 2023, China marked a notable milestone for the successful launch of its first precipitation measurement satellite, the Fengyun-3G (FY-3G) meteorological satellite. Four months later, Fengyun-3F (FY-3F), a new member of the “mid-morning orbit” satellite series, was successfully launched. These accomplishments have positioned China as the sole nation in the world to operate civil meteorological satellites in four near-earth orbits: early-morning, mid-morning, afternoon, and inclined.

Currently, 9 Fengyun satellites are operational in space. Of these, five are in polar orbit, while the remaining four are in geostationary orbit[1,2]. Figure 1 illustrates the current Fengyun satellite that is operational in orbit. The FY-3G officially began operational services on 1st May 2024, while the FY-3F is anticipated to complete its commissioning by the end of June 2024, thereby enabling operation in July 2024.

Received June 20, 2024

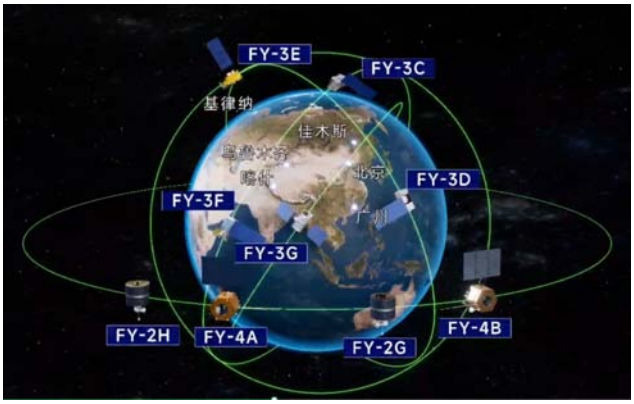

Fig.1 Operational Fengyun Satellites in Space

This report presents an update on the status of current polar orbiting, or Low Earth Observation (LEO), and Geostationary (GEO) meteorological satellites in Chapter 2 and Chapter 3. Chapter 4 introduces the data service, including the release of a user-friendly platform for FY satellite data utilization in 2023. As the Fengyun satellite system continues to evolve and develop, Chapter 5 discusses the growing international user community and highlights progress in international regional cooperation, with a particular focus on the Emergency Support Mechanism of Fengyun Satellite (FY_ESM) and its application in the Belt and Road countries. In Chapter 6, the future planning of the Fengyun satellites is presented.

2 Update on the Fengyun Satellite Program

2.1 FY-3G

FY-3G, the 6th flight of the FY-3 series, was launched on April 16, 2023. It is the third precipitation measurement satellite in the world, which is capable of proactive measurement. FY-3G is the first precipitation measurement satellite of Fengyun-3 batch 03, operating in an orbit inclined 50°. This marks the inaugural instance in China of a satellite-borne active-passive microwave joint measurement of a precipitation system, wherein measurement of three-dimensional structure is realized.

The FY-3G is equipped with four operational instruments, namely, a Ku/Ka-band dual-frequency Precipitation Measurement Radar (PMR), a micro-wave radiation imager (MWRI-RM), a medium-resolution spectral imager for rainfall mission (MERSI-RM), as well as a GNSS radio Occultation Sounder (GNOS). The primary payload of the satellite, a precipitation measurement radar, represents a significant technological advancement, as it is the first of its kind independently developed in China[3].

Table 1 Instruments on FY-3G

No.	Instruments	Statues
1	Precipitation Measurement Radar (PMR)	new
2	Micro-Wave Radiation imager (MWRI-RM)	improved
3	MERSI-RM	
4	GNOS-II	inherited

The primary objective of FY-3G is to detect precipitation in mid to low latitudes across the globe, while optimizing the detection capabilities of payloads. The products encompasse four categories: cloud radiation, land and sea surface, atmospheric parameters, and space weather, with 24 main parameters covering precipitation/snowfall within the range of 50 degrees north and south latitude. These products meet the main needs of the World Meteorological Organization Integrated Global Observing System (WIGOS). In response to the incorporation of active radar detection capabilities in FY-3G, a novel category of remote sensing products has been devised, comprising of three-dimensional raindrop spectral parameter profiles, three-dimensional phase states, and three-dimensional precipitation rate profiles. These are designed to detect the fine internal structure of precipitation.

2.2 FY-3F

FY-3F was launched on 3 August 2023. The FY-3F will replace the FY-3C, which has been in orbit for an extended period, and will continue to carry out optical and microwave imaging observations of the Earth's atmosphere system as well as vertical detection in the sun-synchronous morning orbit. On the basis of ensuring global meteorological imaging and atmospheric vertical detection services, it has strengthened the comprehensive observation capabilities of the Earth system, improved the detection capabilities of atmospheric components such as ozone and sulfur dioxide in the stratosphere and troposphere, as well as the energy balance of Earth radiation. FY-3F, along with FY-3D, FY-3E, and FY-3G in orbit, collectively constitute a low-orbit meteorological satellite observation network. It has further enhanced China's capabilities and levels in global numerical weather forecasting, global climate

change response, ecological environment monitoring, and comprehensive disaster prevention and metigation.

The designed operational lifespan of the FY-3F is 8 years. It is equipped with 10 remote sensing instruments, including MERSI (medium resolution spectral imager), HIRAS (hyper-spectral infrared atmospheric sounder), MWTS (Micro-Wave Temperature Sounder), MWHS (Micro-Wave Humidity Sounder), GNOS (GNSS Occultation Sounder), OMS-L (Ozone Monitoring Suite –Limb), OMS-N (Ozone Monitoring Suite –Nadir), ERM (Earth Radiation Measurement), and SIM (Solar Irradiance Monitor). FY-3F incorporates several new instruments, including the OMS-L and OMS-N. The MERSI, MWRI, and ERM have been improved, while the remaining 5 instruments are inherited.

Table 2 Instruments on FY-3F

No.	Instruments	Statues
1	Ozone Monitoring Suite –Limb (OMS-L)	new
2	Ozone Monitoring Suite –Nadir (OMS-N)	
3	MERSI-III	improved
4	MWRI-II	
5	ERM-II	
6	HIRAS-II	inherited
7	MWTS-III	
8	MWHS-II	
9	GNOS-II	
10	SIM-II	

Two new ultraviolet to visible hyper-spectral instruments, OMS-L and OMS-N, employ a combination of limb and nadir hyper-spectral detection to enhance the detection capabilities of atmospheric components, greenhouse gases, and aerosols. The performances of certain instruments have undergone a notable enhancement. The enhancement of the detection channels of MWRI and ERM, the improvement of the calibration device of MERSI, and the significant improvement of the signal-to-noise ratio have collectively led to an augmented detection capability for global atmospheric temperature, atmosphere system radiation budget, and weak ocean signals in the reflection band.

The products of FY-3F include 6 categories and 48 types, including images, cloud radiation, land and sea surface, atmospheric parameters, atmospheric composition, and space weather. These products address the primary requirements of the WIGOS.

3 Status of Current Fengyun Satellites

3.1 Status of Current LEO

At present, the operational Fengyun LEO satellites in orbit include FY-3C, FY-3D, FY-3E, and FY-3G, which were operational on 1 May 2024. In addition, FY-3F is currently undergoing commissioning and is scheduled to commence operational service in July 2024. FY-3 LEO meteorological satellites have successfully conducted observations in four distinct orbital regimes: early morning, morning, afternoon, and inclined orbits.

Table 3 Current Fengyun LEO satellites (as of 1 June 2024)

Orbit type (Local time of descending node/ascending node)	Satellites currently in orbit	Equatorial crossing time (designed)	Equatorial crossing time (present)	Launch date	Status	Main instruments
Morning orbit (07:00 LT–12:00 LT)/ (19:00 LT–24:00 LT)	FY-3C	10:00 LT	07:39 LT	23 Sept. 2013	Partially operational	VIRR(O); MERSI(S); IRAS(S); MWRI(S); MWTS-II(S); MWHS-II(O); TOU(O); SIM(S); ERM(O); GNOS(O); SEM(S)
Afternoon orbit (12:00 LT–17:00 LT)/ (00:00 LT–05:00 LT)	FY-3D	14:00 LT	13:45 LT	15 Nov. 2017	Operational	MERSI-II(O); HIRAS(O); MWTS-II(O); MWHS-II(O); MWRI(O); GAS(T); GNOS(O); WAI(O); IPM(O); SEM(O)
Early-morning orbit	FY-3E	5:30LT	5:30LT	5 Jul. 2021	Operational	MERSI-LL(O); HIRAS-II(O); MWTS-III(O); MWHS-II(O); GNOS-II(O); WindRAD(O); SSIM(O); SIM-II(O); X-EUVI(O); Tri-IPM(O); SEM(O)
Drifting	FY-3G			16 Apr. 2023	Operational	See Table 1
Morning orbit	FY-3F	10:00LT		3 Aug. 2023	Commissioning	See Table 2

Note: (O) indicates that the instrument is in a state of operational readiness, whereas, (S) denotes that the instrument is currently in a state of shutdown.

Information regarding the instruments carried on FY-3E/G/F is as follows[4].

MERSI-LL, comprises a total of 7 channels, including 1 low-light channel and 6 thermal infrared channels. Two infrared split window channels (10.8 and 12.0 microns) have a spatial resolution of 250 m, while the remaining channels have a spatial resolution of 1000 m.

HIRAS-II, an infrared sounding instrument with nadir spatial resolution of 16 km and a cross-track scanning model. It is primarily used for numerical weather prediction and atmospheric composition detection.

MWTS-III, the number of channels in the original 50~60GHz frequency band have been increased from 13 to 17. A 23.8 GHz water vapor column total measurement channel, a 31.4 GHz window channel, 53.246 ± 0.08 GHz and 53.948 ± 0.081 GHz channels for tropospheric temperature detection at 4km and 6km have been included.

MWHS-II (Micro-Wave Humidity Sounder), flying on FY-3E/F, 4-frequency/15-channel MW radiometer for nearly- all-weather humidity sounding, with a special resolution of 15 km and swath of 2700 km.

GNOS-II, receives signals from GPS and China Beidou satellites, with the capacity to observe over 1000 occultation events per day.

WindRad, is the first active microwave remote sensing instrument of the Fengyun series satellites. It is a dual-frequency, dual-polarization radar. It adopts a fan-beam conical scanning system with an observation width of over 1200km and a minimum detectable wind speed of 3 m/s. It adopts C and Ku dual bands, which are operated concurrently. Each band includes two polarization measurement methods, namely horizontal and vertical.

SSIM, measures the solar spectral irradiance through the ultraviolet, visible and infrared channels. This allows to obtain the solar spectral irradiance characteristics and capture the influence of solar activity on the spectral irradiance.

SIM-II, is a high-precision absolute radiometer with an automated Sun-tracking function that has been independently developed by China. Spectral range is 0.2~ 20 μm.

X-EUVI, is the first solar X-ray-extreme ultraviolet dual-band imager in the world, and the first domestic space solar telescope. It has two bands: X ray (0.6~8 nm) and EUV (19.5 nm)

Tri-IPM, UV spectrometry of the ionosphere performed under 3 different viewing angles.

SEM, monitors high energy proton, high energy electron, medium energy proton, medium energy electron, heavy ions, and geomagnetic field.

PMR, is a dual-frequency, single-polarization one-dimensional phased array radar. It provides a three-dimensional structure of precipitation. The information such as precipitation intensity and precipitation type will be retrieved.

MWRI-RM, 17 frequencies, 26 channels, in the range 10.65 to 183GHz. Conical: 53° zenith angle, Swath width 800 km.

MERSI-RM, is an 8-channel VIS/IR radiometer, comprising 5 solar reflection band channels and 3 thermal infrared channels, all with spatial resolution of 500 meters.

MERSI-III, flying on FY-3F, is a 25-channel radiometer (19 in VIS/NIR/SWIR + 6 TIR from 3.7.0~12.5 μm) designed for the measurement of ocean color and vegetation indices. The special resolution is 250 m for 4 VIS/NIR channels and 2 TIR channels, 1 km for other channels. Scan swath is 2800 km.

OMS-L, a new instrument used for detecting trace gases such as ozone on FY-3F, with a spectrum covering a continuous range of 290~500 nm and a total of 1000 channels.

OMS-N, is a new instrument on the FY-3F that is capable of providing provide high spectral resolution of Earth's reflected radiation in the ultraviolet to visible wavelength range. The instrument spectrum covers three bands: 250~300 nm, 300~320 nm, and 310~497 nm, with a spectral resolution of 0.5~1 nm and spatial resolution of 7 km x 7 km. It is capable of detecting the total amount of ozone, SO_2, NO_2, and vertical distribution information of ozone.

ERM-II, flying on FY-3F, comprises 3 broad-band channel radiometer for earth reflected solar flux and earth emitted thermal flux over total (0.2~100μm), long (5.0~50μm) waveband and short (0.2-5.0μm) waveband.

3.2 Status of Current GEO

The operational Fengyun GEO satellites in orbit include FY-2G, FY-2H, FY-4A and FY-4B[5]. FY-2F was decommissioned on 1 April 2022.

Information regarding the instruments on FY-2G/H is as follows.

VISSR (Visible and Infrared Spin Scan Radiometer): The improved version for FY-G/H, has five VIS/IR

Table 4 Current Fengyun GEO satellites in orbit (as of 1 April 2024)

Satellites	Location	Launch date	Status	Instruments
FY-2G	99.5°E	31 Dec. 2014	Operational	VISSR SEM
FY-2H	79°E	5 Jun. 2018	Operational	
FY-4A	86.5°E	11 Dec. 2016	Degraded operational	AGRI GIIRS LMI SEP
FY-4B	105°E	3 Jun. 2021	Operational	AGRI GIIRS GHI SEP

channels (0.55~0.75 μm, 3.5~4.0 μm, 6.3~7.6 μm, 10.3~11.3 μm, and 11.5~12.5 μm). The spatial resolution of VIS and IR channels is 1.25 km and 5.0 km, respectively. The image cycle is 30 min.

SEM (Space Environment Monitor): A space particle monitor and an X-ray monitor are mounted on FY-2 to detect the space environment in the proximity of the satellite, the solar activities, and relevant space phenomena. The SEM data is transmitted via telemetry to the ground system.

FY-4B has shifted its position from 133°E to 105°E, assuming the role of the FY-4A in providing operational observation services since March 5, 2024. FY-4A has undergone a shift from 104.7°E to 86.5°E for degrading operation. There are 4 instruments on the FY-4B. The principal observation capabilities are similar to those of FY-4A, exhibiting notable enhancements in performance.

AGRI, in comparison with FY-4A, 1 new water vapor channel is added, 4 channel band settings are optimized, and the resolution of short wave and medium wave is improved to 2 km[6].

GIIRS, the spatial resolution of the infrared channel has been enhanced from 16 km to 12 km. The resolution of the visible channel has been increased from 2 km to 1 km.

GHI (Geostationary High-speed Imager), a recently deployed instrument on FY-4B, is the first long-line array in geosynchronous orbit with the capability of uninterrupted, one-minute imaging and observation in a 2000km×2000km area with a resolution of 250 m. The visible and near-infrared spatial resolutions have been doubled in comparison to those of the ABI.

SEP, is a suite that contains a Magnetometer for 3D magnetic field intensity, an Energetic Particle Detector detecting high-energy electron storms and proton events, and Space Weather Effect Detectors for the impact of

Table 5 Detailed characteristics of AGRI on FY-4B

	Central wavelength/μm	Spectral interval/μm	SNR or NEΔT @ specified input	IFOV at s.s.p./ km
1	0.47	0.45~0.49	⩾90 @ 100% albedo	1
2	0.65	0.55~0.75	⩾150 @ 100% albedo	0.5
3	0.825	0.75~0.90	⩾200 @ 100% albedo or ⩾3 @ 1% albedo	1
4	1.378	1.371~1.386	⩾120 @ 100% albedo or ⩾2 @ 1% albedo	2
5	1.61	1.58~1.64	⩾200 @ 100% albedo or ⩾3 @ 1% albedo	2
6	2.25	2.10~2.35	⩾200 @ 100% albedo or ⩾2 @ 1% albedo	2
7	3.75 (high)	3.50~4.00	⩽ 0.7 K @ 315 K	2
8	3.75 (low)	3.50~4.00	0.2 K @ 300 K or 2.0 K @ 240 K	4
9	6.25	5.80~6.70	0.2 K @ 300 K or 0.9 K @ 240 K	4
10	6.95	6.75~7.15	0.25 K @ 300 K or 0.9 K @ 240 K	4
11	7.92	7.24~7.60	0.25 K @ 300 K or 0.9 K @ 240 K	4
12	8.55	8.30~8.80	0.2 K @ 300 K or 0.4 K @ 240 K	4
13	10.80	10.30~11.30	0.2 K @ 300 K or 0.4 K @ 240 K	4
14	12.00	11.50~12.50	0.2 K @ 300 K or 0.4 K @ 240 K	4
15	13.30	13.00~13.60	0.5 K @ 300 K or 0.9 K @ 240 K	4

Table 6 Detailed characteristics of FY-4B GIIRS

Spectral range/μm	Spectral range/cm^{-1}	Spectral resolution/cm^{-1}	NEΔR or SNR
14.7~8.85	680~1130	0.625	0.5 $mW \cdot m^{-2} \cdot sr^{-1} \cdot cm$
6.06~4.44	1650~2250	0.625	0.1 $mW \cdot m^{-2} \cdot sr^{-1} \cdot cm$
0.55~0.90	N/A	N/A	200 @ 100% albedo

Table 7 Detailed characteristics of FY-4B GHI

Central wavelength/μm	Spectral interval	SNR or NEΔT @ specified input	IFOV at s.s.p./ km
0.675	0.45~0.9	> 300 @ 100 % albedo	0.25
0.470	0.445~0.495	> 300 @ 100 % albedo	0.5
0.545	0.52~0.57	> 300 @ 100 % albedo	0.5
0.645	0.62~0.67	> 300 @ 100 % albedo	0.5
1.378	1.371~1.386	> 300 @ 100 % albedo	0.5
1.61	1.58~1.64	> 300 @ 100 % albedo	0.5
11.4	10.3~12.5	0.2 K @ 300 K	2.0

space weather on spacecraft.

4 Data service and Application

4.1 Data Archiving

National Satellite Meteorological Center (NSMC) Data Center enriches meteorological satellite data in various ways. As of June 2024, the amount of satellite data archived has reached nearly 44 PB, covering 55 satellites in 12 series both domestically and internationally, with over 1500 types of data products. The evolution of satellite data archiving from 1988 to 2024 is shown in Figure 2.

4.2 Data Service

NSMC Data Center has built an integrated meteorological satellite data service system that integrates space and terrestrial realms through the adoption of a unified design, progressive development, and batch expansion phylosophy for multiple batches of Fengyun meteorological satellite programs. Services have been developed to provide space-based data through satellite direct receiving stations and China Meteorological Administration's data broadcast system (CMACast). Through ground network data services such as the World Meteorological Organization Information System, Fengyun Satellite Data Service Network, and satellite data resource pool, access, exchange, management, and service of domestic and international satellite data have been achieved. The complete Fengyun meteorological satellite dataset, both real-time and historical data, will be accessible on the NSMC satellite data service website in English (http://data.nsmc.org.cn).

By the end of May 2024, the NSMC satellite data service website had registered in excess of 164000 users. The volume of data downloaded by users of Fengyun

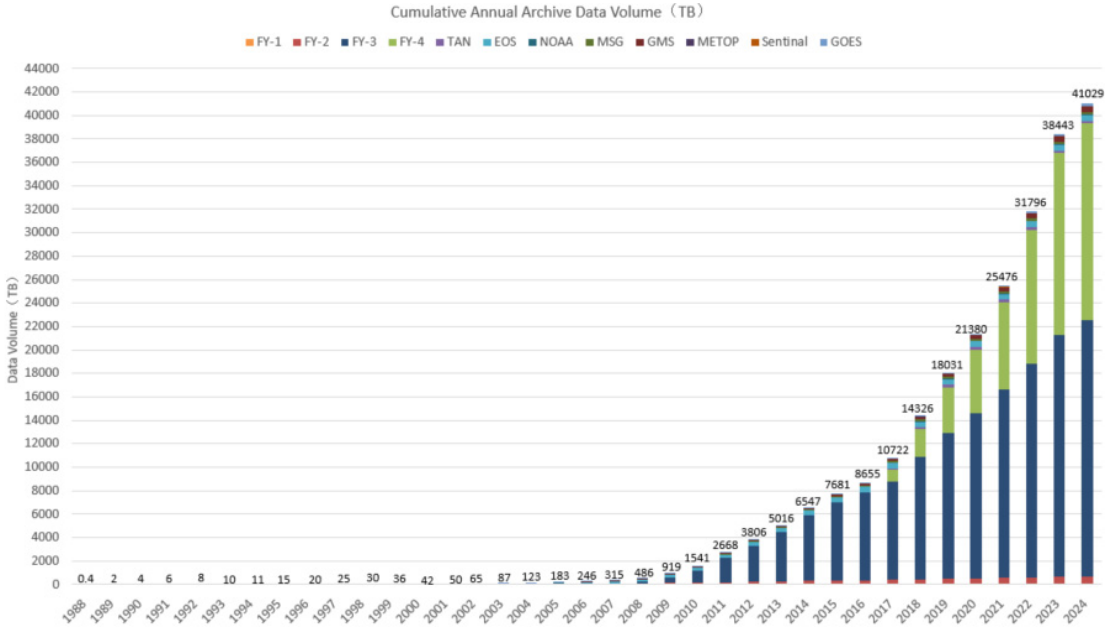

Fig.2 Cumulative annual archive data volume in NSMC

satellite data users has increased rapidly year on year, with a total cumulative service data of 39 PB since 2005, of which more than 13 PB was served in 2023 alone. In addition, NSMC actively explores the application of new technologies, including research on artificial intelligence applications and construction of a rapid service system for hot events.

4.3 Fengyun Earth

In 2022, a lightweight design and real-time satellite application service platform, designated "Fengyun Earth", was developed to enhance the pivotal role of Fengyun meteorological satellites in core meteorological operations and promote the integration of satellite data across national, provincial, municipal, and county-level platforms[7].

To meet the needs of forecasters, the Fengyun Earth utilizes big data, cloud computing, and artificial intelligence in order to efficiently manage a vast array of heterogeneous data sources and perform online real-time computations, providing users with a range of visualized remote sensing application products *via* a B/S architecture, including satellite cloud images, elements and events, severe weather, climate analysis, and model validation. The Fengyun Earth encompasses distinct 30 types with a total of 204 products under 5 categories, enabling rapid production of high-integrity, time-sensitive integrated products. The platform is based on a cloud-edge lightweight service model and is capable of supporting simultaneous access by tens of thousands of users. Furthermore, it is able to deliver satellite products directly to forecasters' desktops. The application of AI to product algorithms (*e.g.*, satellite precipitation estimation, convection initiation) results in enhanced quantification of products. It employs integrated intelligent observation and control technology, coupled with real-time scheduling and micro-services, to rapidly process and distribute multi-scale Fengyun satellite meteorological products. The times for accessing cloud image services are controlled within minutes. Furthermore, the integrated application of multi-source satellite inversion parameters enables detailed three-dimensional monitoring of critical weather systems.

Fengyun Earth was pilot-tested in May 2022, with the nationwide launch occurring in June of the same year. Fengyun Earth has provided a range of tiered services to professionals, industry users, and the general public, supporting a number of significant events, including the Universiade and Asian Games, critical weather processes like Typhoon *Doksuri*, and rural revitalization initiatives. To date, the platform has received in excess of three billion hits.

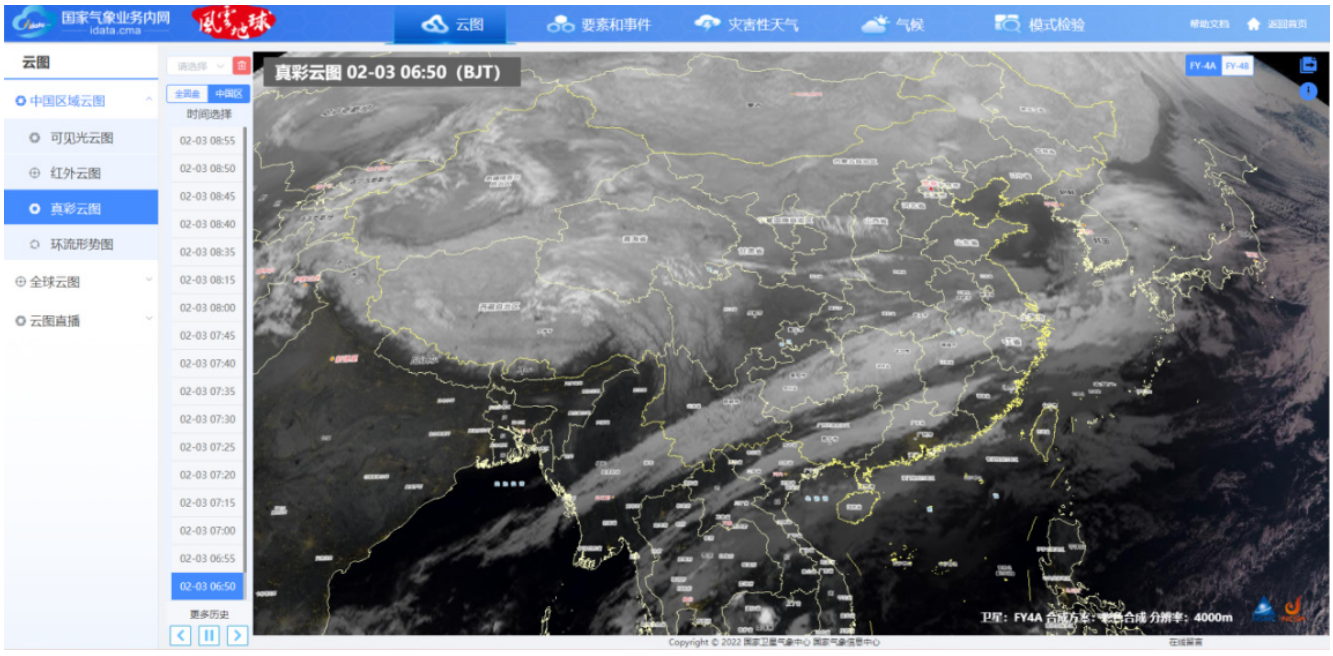

Fig.3 Interface of Fengyun Earth

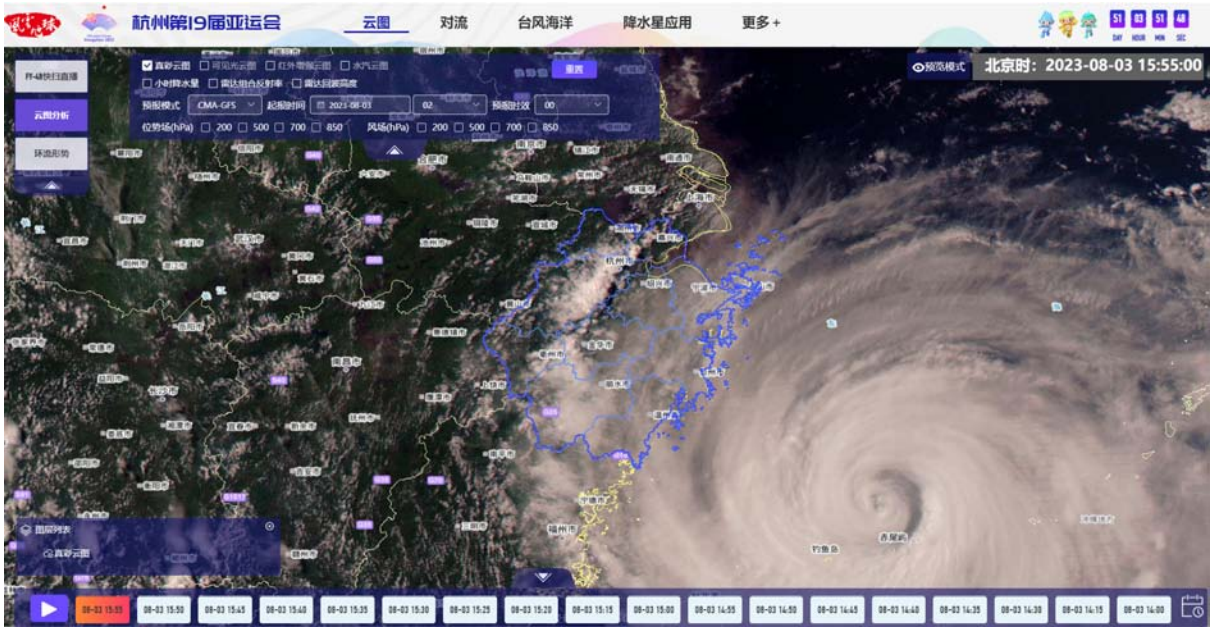

Fig.4 Fengyun Earth for 19th Asian Games

In order to provide support to international users engaged in satellite remote sensing applications and to enhance their capabilities, NSMC developed an international version of Fengyun Earth. This version enables the timely acquisition of meteorological satellite and numerical forecast data, the rapid production of quantified products and the provision of international services. It employs advanced AI technologies for the automated analysis, mining, and modelling of massive meteorological satellite data., enabling the intelligent identification of severe weather and extreme climate events, thereby enhancing user convenience and practicality. It offers five categories of quantified, multi-scale products including cloud images, elements, disaster events, climate, and model validation. These products are tailored to different business scenarios and customized to focus on specific meteorological elements, observational areas, and time frames for international users. The international version of Fengyun Earth was officially launched on 13 November 2023. As of the end of May 2024, it had been accessed by 47 countries with a total of 22000 visits.

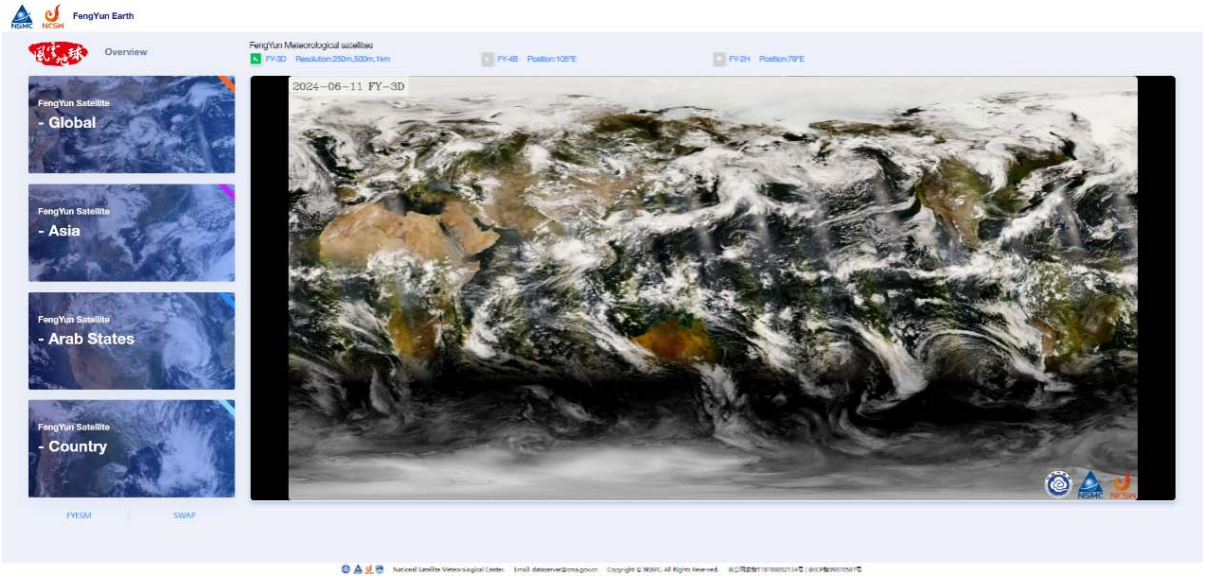

Fig.5 Interface of Fengyun Earth (International Version)

5 International Co-operation and Supporting

5.1 International Services

Fengyun meteorological satellites play a crucial role in the World Meteorological Organization's Space Programme. NSMC maintains close cooperation with WMO, CGMS, CEOS, GEO, APSCO, and other international organizations, as well as satellite operators such as EUMETSAT and NOAA, on matters pertaining to instrument development, remote sensing applications, data exchange, and applications. Furthermore, it plays an active role in international governance, providing support for the United Nations Sustainable Development Goals and the UN Early Warnings for All Initiative. It continues to facilitate bilateral cooperation, with CMA and EUMETSAT renewing their cooperation agreement on the application, exchange, and distribution of meteorological satellite data in 2024, to promote data sharing, ground segment operations, and remote sensing application services.

Till 2023, 34 countries registered with the FY_ESM. In that year, Fengyun satellite responded to 31 international emergency service requests, including 23 that were initiated under the CHARTER mechanism and 8 that were initiated through the FY_ESM. It provided global meteorological disaster emergency services to countries in Asia, Africa, South America, and Oceania for disasters such as earthquakes, tropical cyclones, floods, fires, and maritime search and rescue operations.

The integrated global data-sharing system of Fengyun satellites is being continuously improved. The Fengyun satellite data is disseminated internationally *via* a multitude of channels, including direct reception stations, CMACast, dedicated lines, the Fengyun Data Sharing Network, public clouds, FTP, and human services. As of June 2024, the data service website covers 132 countries and regions, including 96 along the "Belt and Road" Initiative, and the data services have increased by about 210TB since 2018.

Since its designation as a Global Space Weather Center of the International Civil Aviation Organization (ICAO) in 2021, the NSMC has established a full-process operational specification for ICAO space weather services and a robust application platform for ICAO space weather services. Additionally, it has conducted seven 14-day, 24-hour rotations[8].

The International Fengyun Meteorological Satellite Users Conference was successfully held in Xiamen, Fujian Province, on November 13-14, 2023. Participants from the WMO, the Food and Agriculture Organization, and more than 30 countries, including China, Yemen, Jordan, Thailand, Indonesia, the Maldives, and Tanzania, discussed the applications of Fengyun meteorological satellites in meteorological disaster mitigation and early warning. The conference comprised a training session, two roundtable meetings, and three sub-meetings, and four international service items were announced.

In 2023, a survey was conducted among 44 countries to ascertain the requirements and usage of Fengyun satellites. The survey was conducted both on-site and online, and the results indicated an overall international user satisfaction rate of 80%.

5.2 Belt and Road Services

Fengyun satellites provide services to global users, with a particular focus on those along the "Belt and Road". The map below shows the global distribution of Fengyun users.

Fig.6 Map of Fengyun users in the world

CMA has implemented a series of action plans with the objective of enhancing capability of countries along the "Belt and Road" to receive data from Fengyun meteorological satellites.

The construction or upgrading of Direct Broadcasting systems (DB), CMACast, cloud services, and other similar initiatives enables countries in the region to receive real-time Fengyun satellite data. By 2024, over 30 countries in the "Belt and Road" region have established a variety of satellite data receiving systems, including 15 CMACast stations, 8 FY-2 stations, 2 FY-3 stations, and 2 FY-4 stations. Furthermore, over 30 countries have also downloaded Fengyun data via the NSMC's

FTP server. Additionally, the FY-3 preprocessing software package has been made available for free download and installation in 30 countries.

Moreover, user capabilities in "Belt and Road" countries have been enhanced through new tools developed by the NSMC. Three application tools are provided to assist users in processing Fengyun satellite data. The international version of Fengyun Earth is designed to provide core meteorological services, integrating multi-source satellite data to offer timely, intelligent, detailed, and customizable remote sensing services. The Satellite Weather Application Platform 2.0 (SWAP 2.0) is tailored for weather analysis and forecasting, utilizing GEO Fengyun satellites. It is available in both web-based and standalone versions, displaying full-disk and regional images from FY-2H, FY-4A, and FY-4B, with support for multiple languages. The Satellite Monitoring and Remote Sensing Toolkit (SMART 2.0) harnesses data from FY-3, GAOFEN, NOAA, and other medium- and high-resolution Earth observation satellites. It focuses on monitoring environmental and biological changes across land surfaces, oceans, water bodies, and ice surfaces.

Additionally, ongoing endeavours are being made to facilitate scientific exchanges and enhance user training among "Belt and Road" countries. Initiatives include the organization of international users' conferences, the delivery of training courses, and the facilitation of scientific exchanges. At the 2023 International Fengyun Meteorological Satellite Users Conference, technical training sessions were conducted on the application of Fengyun satellite data.

6 Future Plan

In the future, Fengyun-3H and Fengyun-3 fourth batch of satellites in LEO orbit, along with Fengyun-4C and Fengyun-4 third batch of satellites in GEO orbit, will be launched. The operational status of the second-generation Fengyun meteorological satellites will be maintained, with the objective of ensuring continuous and stable in-orbit operation of the Fengyun satellites. The third-generation Fengyun meteorological satellites, including the Fengyun-5 series and Fengyun-6, have also been planned and are currently undergoing requirement demonstrations[9].

7 Summary

From 2022 to 2024, two Fengyun satellites were launched: FY-3G and FY-3F. Currently, 9 Fengyun satellites are in orbit. Fengyun LEO satellites have achieved network observation in four orbits, while Fengyun GEO satellites have formed an operational pattern of "network observation and in-orbit backup", providing data and product services to the world. They have been incorporated into the WMO global operational meteorological satellite sequence, becoming a pivotal force in the global earth observation network. Their deployment has led to significant economic, social, and international benefits.

Reference

[1] ZHANG Peng, CHEN Lin, XIAN Di, XU Zhe, GUAN Min. Update on Fengyun Meteorological Satellite Program and Development[J]. *Chin. J. Space Sci.*, 2020, 40(5): 884-897

[2] ZHANG Peng, YANG Jun, GUAN Min, *et al*. WMO Space Program and Internationalization of Fengyun Meteorological Satellites [J]. *Advances in Meteorological Science and Technology*, 2022, 12(5): 24-31

[3] ZHANG Peng, GU Songyan, SHANG Jian. Overview of the mission of China's first precipitation measurement satellite - Fengyun-3G[J]. *Space International*, 2023(6): 17-21. DOI:10.3969/j.issn.1009-2366.2023.06.005.

[4] National Satellite Meteorological Center. Fengyun3-03 User Requirement Specification [R]. Beijing: National Satellite Meteorological Center, 2015

[5] YANG Jun, ZHANG Zhiqing, WEI Caiying, et al. Introducing the new generation of Chinese geostationary weather satel-lites Fengyun-4 (FY-4)[J]. *Bull. Am. Meteor. Soc*., 2017, 98(8): 1636-1658

[6] National Satellite Meteorological Center. Fengyun4-02 Requirement Specification[R]. Beijing: National Satellite Meteorological Center, 2019

[7] https://www.cma.gov.cn/ztbd/2023zt/20230214/2023021403/202302/t20230203_5287712.html

[8] https://www.cma.gov.cn/ztbd/2023zt/20230524/2023052401/202311/t20231114_5885966.html

[9] WANG Jinsong, LU Naimeng, ZHAO Xiangang, XU Na, YAO Pengjuan, GUO Yang, SHANG Jian, LIAO Mi. Review and prospect on the meteorological small satellites[J]. *Advanced Small Satellite Technology*, 2024, 1(1): 23-39

ZOU Bin, LIU Yuxin. Networking Observation and Applications of Chinese Ocean Satellites. *Chinese Journal of Space Science*, 2024, **44**(4)

Networking Observation and Applications of Chinese Ocean Satellites

ZOU Bin, LIU Yuxin

1. National Satellite Ocean Application Service, Beijing 100081
2. Key Laboratory of Space Ocean Remote Sensing and Application, Ministry of Natural Resources, Beijing 100081

Abstract

This paper presents the networking observation capabilities of Chinese ocean satellites and their diverse applications in ocean disaster prevention, ecological monitoring, and resource development. Since the inaugural launch in 2002, China has achieved substantial advancements in ocean satellite technology, forming an observation system composed of the HY-1, HY-2, and HY-3 series satellites. These satellites are integral to global ocean environmental monitoring due to their high resolution, extensive coverage, and frequent observations. Looking forward, China aims to further enhance and expand its ocean satellite capabilities through ongoing projects to support global environmental protection and sustainable development.

Key words

Chinese ocean satellites, Networking observation, Ocean forecasting

1 Introduction

China’s extensive coastline and vast jurisdictional waters make the ocean crucial for its economy and ecological protection. Ocean satellites play an indispensable role in continuous, real-time, and large-scale monitoring of the ocean environment, contributing to scientific research, resource development, environmental protection, and disaster prevention.

Since the launch of China's first ocean satellite in 2002, there have been notable advancements, evolving from single satellite observations to coordinated networked observations[1]. As of now, China has successfully launched 13 ocean satellites, including the HY-1, HY-2, HY-3 series, and the China-France Oceanography Satellite (CFOSAT). Currently, 10 satellites are operational, forming a comprehensive ocean satellite observation system (see Table 1).

The launch of the new-generation ocean color satellite (HY-1E) in 2023 enhanced global monitoring capabilities for ocean color and Sea Surface Temperature (SST). The networking of HY-1E with HY-1C/D has formed a constellation for ocean color satellites. Similarly, HY-2D, launched in May 2021, forms a dynamic ocean environment satellite constellation with HY-2B/C and CFOSAT. The 1m C-SAR 02, launched in April 2022, forms an ocean surveillance satellite constellation with 1m C-SAR 01 and GF-3.

Networking observation by ocean satellites enables higher spatial and temporal resolution and coverage, providing precise and timely ocean environmental monitoring data. This improves the accuracy and timeliness of ocean disaster warnings, reduces the impact on coastal regions, supports rational ocean resource development, and provides robust support for global ocean environmental protection and sustainable development.

Received June 20, 2024

Table 1 Launch Details of Chinese Ocean Satellites

Satellite	Series	Launch Date	Operational Status
HY-1A		May 2002	Ceased March 2004
HY-1B		April 2007	Ceased February 2016
HY-1C	Ocean Color Satellite	September 2018	Operational
HY-1D		June 2020	Operational
HY-1E		November 2023	Testing
HY-2A		August 2011	Ceased February 2024
HY-2B		October 2018	Operational
HY-2C	Ocean Dynamic Satellite	September 2020	Operational
HY-2D		May 2021	Operational
CFOSAT		October 2018	Operational
GF-3		August 2016	Operational
1m C-SAR 01	Ocean Surveillance Satellite	November 2021	Operational
1m C-SAR 02		April 2022	Operational

2 Networking Observation Capabilities of Chinese Ocean Satellites

2.1 HY-1 Series Satellites and Their Networking Observation Capabilities

The HY-1 series are Chinese independently developed ocean color satellites, primarily used for monitoring SST, optical characteristics of seawater, chlorophyll concentration, and suspended sediments. These satellites provide valuable data for ocean resource management and scientific research.

On May 15, 2002, China successfully launched its first ocean satellite, HY-1A, equipped with a Chinese Ocean Color Temperature Scanner (COCTS) and a Coastal Zone Imager (CZI). On April 11, 2007, the HY-1B was launched, inheriting the main functions of HY-1A while further improving observation capabilities and accuracy. The HY-1C was successfully launched on September 7, 2018. Compared to its predecessors, it added ultraviolet observation bands and an onboard calibration system, expanded the CZI's coverage width, and improved spatial resolution. On June 11, 2020, the HY-1D was launched, achieving networked observations with the HY-1C in the morning and afternoon, significantly enhancing global coverage capability and data acquisition frequency for ocean color monitoring.

In 2023, HY-1E was successfully launched, further enhancing its observation performance[2]. The spatial resolution of the COCTS has been improved from 1.1 km to 500 m. The CZI's spatial resolution has been increased from 50 m to 20 m, and it has acquired the ability to detect panchromatic information of land cover with a spatial resolution of 5 m. Additionally, HY-1E includes a Programmable Medium-Resolution Imaging Spectrometer (PMRIS) with 100 m resolution.

The three-satellite network of the HY-1 series has established a more comprehensive ocean color satellite constellation, providing higher resolution and more frequent data (as detailed in Table 2). It can obtain medium-resolution images of 50 m or 100 m once per day, playing an important role in monitoring disasters such as sea ice, green tides, red tides, oil spills, and floods.

2.2 HY-2 Series Satellites and Their Networking Observation Capabilities

The HY-2 series satellites integrate active and passive microwave sensors to monitor ocean dynamic environment parameters in all weather conditions and at all times. These satellites primarily monitor elements such as Sea Surface Height (SSH), Sea Surface Wind (SSW), and SST, providing high-precision data support for ocean scientific research, resource management, and disaster warning.

On August 16, 2011, China successfully launched its first ocean dynamic environment monitoring satellite, HY-2A. This satellite was equipped with various remote sensors, including Radar Altimeter (RA), SCATterometer (SCAT), Scanning Microwave Radiometer (SMR), and Calibration Microwave Radiometer (CMR). On October 25, 2018, HY-2B was launched, inheriting the main

Table 2 Observation Capabilities of HY-1C/D/E[3]

Satellite	Payload	Spatial Resolution	Band Number	Swath Width	Monitoring Capability	Networking Coverage Capability
HY-1C/D, HY-1E	CZI	50 m (20 m+5m)	4 (8+1)	950 km (60 km, up to 1000 km side imaging)	Coastal zones, sea ice, red tide, Ulva Prolifera, suspended sediments, coral reefs, coastal wetlands, invasive species, mangroves, pollutants, large water bodies, vegetation, *etc*.	Once daily
	(PMRIS)	(Multi-spectral 100m/Hyperspectral 200m)	(Multi-spectral 19/ Hyperspectral 94)	(950 km)		
	COCTS	1 km (500 m)	10 (18)	2900 km (3000km)	Chlorophyll concentration, suspended sediments, dissolved organic matter, SST, polar sea ice, large water bodies, vegetation, soil moisture, *etc*.	Ocean color 3 times/day, SST 6 times/day

Note: The information in parentheses represents the HY-1E remote sensors.

functions of HY-2A while improving data quality and adding Data Collection System (DCS) and Automatic Identification System (AIS) payloads. In September 2020, HY-2C was launched, followed by HY-2D in May 2021. These satellites carried RA, SCAT, CMR, DCS, and AIS. Currently, the HY-2B/C/D satellites are conducting networked observations, forming a satellite constellation for monitoring the dynamic ocean environment. As detailed in Table 3, these three satellites equipped with SCATs can achieve 85% global ocean coverage every six hours.

Additionally, CFOSAT, launched in October 2018, carries SCAT and the Surface Waves Investigation and Monitoring instrument (SWIM). It achieved the first global continuous, large-scale, synchronous observation of wave direction spectra and SSW[5]. Working in conjunction with the HY-2 series satellites, CFOSAT enhances the capability to obtain data on the dynamic ocean environment.

Currently, the SSW and SSH products of the HY-2 series satellites have reached internationally advanced levels. According to evaluations by the China Meteorological Administration (CMA), this data significantly contributes to its global medium-range numerical weather prediction system.

In 2023, the National Satellite Ocean Application Service (NSOAS) released three types of fusion products based on the HY-2 series satellites: a global 1/4° resolution and regional 1/8° resolution SSH fusion product, a global 25 km resolution six-hourly SSW fusion product, and a 5 km resolution daily SST fusion product. These products will better serve climate change monitoring, ocean dynamics research, disaster warning, and ocean engineering support.

2.3 HY-3 Series Satellites and Their Networking Observation Capabilities

The HY-3 series satellites are independently developed ocean surveillance satellites, currently including GF-3 and the 1m C-SAR 01/02. These satellites are equipped with C-band multi-polarization Synthetic Aperture Radars (SAR), offering high-resolution, wide-coverage, multi-polarization, and multi-mode ocean and land observations. They provide high-resolution information on ocean dynamic environment parameters, natural disasters, maritime emergency events, land use, surface water monitoring, *etc*.

On August 10, 2016, the GF-3 was successfully launched, becoming China's first C-band multi- polarization SAR with a resolution of 1 m. It features 12 imaging modes, including two ocean observation modes (ocean mode and global observation mode), and is capable of acquiring single polarization, dual-polarization, and full polarization data.

Table 3 Observation Capabilities of HY-2B/C/D[4]

Satellite	Payload	Spatial Resolution	Working Frequency	Swath Width	Monitoring Capability	Networking Coverage Capability
HY-2 B/C/D	RA	7 km	13.585, 5.25GHz	7 km	SSH, significant wave height, and gravity field, *etc*.	About 14-day mesoscale coverage
	SMR (HY-2B only)	25~90 km	6.925, 10.7, 18.7, 23.8, 37.0 GHz	1600 km	SST, sea surface water vapor content, liquid water, and rain intensity, *etc*.	Daily coverage of over 80% of open ocean
	SCAT	25 km	13.256 GHz	1700 km	SSW, *etc*.	Global 85% coverage every six hours

Table 4 Observation Capabilities of GF-3, 1 m C-SAR 01/02

Satellite	Payload	Spatial Resolution	Band Number	Swath Width	Monitoring Capability	Networking Coverage Capability
GF-3, 1 m C-SAR 01/02	SAR	1~500 m	C-band, full polarization, 12 imaging modes	10~500 km	Global maritime targets, ocean structures, detailed ocean dynamic environment parameters, maritime emergency events, land use, surface water, *etc*.	Daily

In November 2021, the 1 m C-SAR 01 was successfully launched, followed by the 1 m C-SAR 02 in April 2022. These satellites are successors to GF-3, inheriting its mature technology with several improvements[6]. These enhancements include the addition of AIS to improve maritime vessel monitoring and the conversion of three traditional scanning imaging modes to TOPSAR mode. Additionally, they are equipped with onboard real-time processors, enabling real-time imaging processing, water body extraction, and oil spill detection functionalities.

The network of three satellites significantly enhances the spatio-temporal resolution and coverage of ocean monitoring, reducing the average revisit period to less than one day.

3 Applications of Chinese Ocean Satellites

3.1 Ocean Forecasting and Disaster Prevention

3.1.1 Typhoon Monitoring

SCAT and SAR are effective tools for SST monitoring, providing data on typhoon wind speed, direction, radius, center position, and intensity. These tools assist in tracking typhoon movement using multi-satellite observations. Figure 1 shows the observation of Typhoon Ewiniar by the HY-2B on May 30, 2024.

3.1.2 Sea Ice Monitoring

From late November to the end of March, sea ice in the Bohai Sea and northern Yellow Sea can severely impact maritime transport and offshore operations. By utilizing HY-1C/D/E for daily coverage and SAR during cloudy periods, the spatial distribution, area, boundary, and thickness of sea ice can be extracted. This provides critical information for sea ice forecasting and maritime disaster prevention. Figure 2 shows the HY-1D CZI image of the Bohai Sea area on January 22, 2024.

3.1.3 Sea Surface Height Monitoring

Currently, there are 10 satellites in orbit worldwide equipped with Radar Altimeters (RA), including

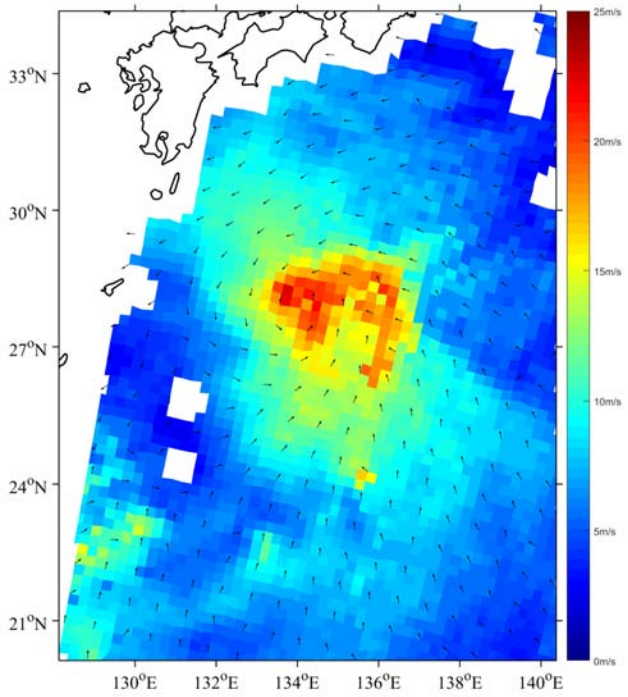

Fig.1 Observation of Typhoon Ewiniar by HY-2 B

China's HY-2B/C/D. These satellites can measure Sea Surface Height (SSH), significant wave height, and other related information. Additionally, by combining SSH with geoid data and using gravity inversion techniques, the ocean gravity field can be obtained. Through the modeling of gravity and topography, this allows further inference of seafloor topography. Figure 3 shows the regional 1/8° resolution sea level anomalies fusion product, primarily based on data from the HY-2 series satellites, released by NSOAS.

3.2 Ocean Ecological Monitoring

3.2.1 Monitoring of Ocean Ecological Disasters

Ulva prolifera green tides, Sargassum, and red tides pose significant threats to the ecological environment, economic development, and public health of coastal countries, necessitating effective monitoring and management measures.

The HY-1 series satellites are primarily used for ocean environmental monitoring and ocean resource

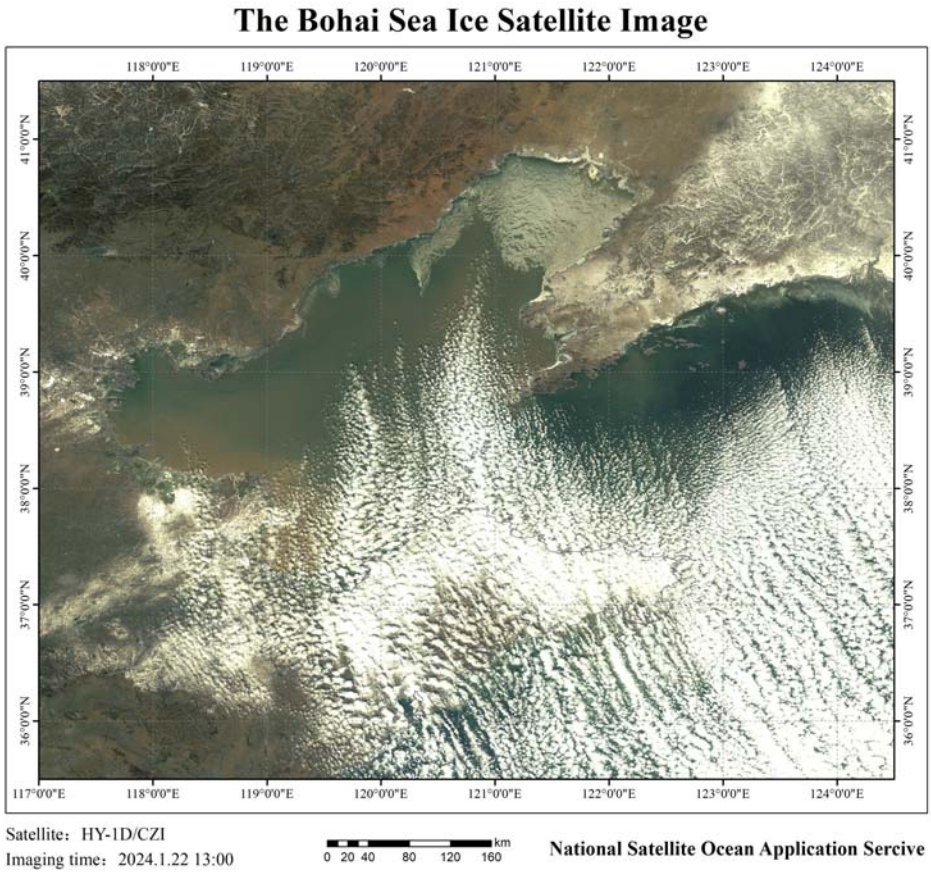

Fig.2 HY-1D CZI image of the sea ice in the Bohai Sea

investigation. Equipped with CZI and PMRIS with resolutions of 50 m and 100 m, these satellites can effectively identify and monitor large algae and abnormal ocean color distributions. By utilizing the coordinated monitoring capabilities of HY-1 and SAR, the dynamic changes of Ulva prolifera green tide and Sargassum can be promptly detected and tracked, providing robust technical support for ocean environmental protection and the management of ocean ecological disasters. Figure 4 and Figure 5 show the HY-1E CZI image of the Ulva prolifera green tide in the Yellow Sea on June 24, 2024, and the HY-1C CZI image of the red tide in the East China Sea on August 16, 2023, respectively.

Oil spill incidents not only pose serious threats to the ocean's ecological environment but also significantly impact fisheries, tourism, and the livelihoods of coastal residents. By comprehensively utilizing GF-3 and HY-1C/D, enhanced monitoring of affected areas can be conducted to obtain information on oil spills from offshore oil platforms and ships[7]. This provides crucial information support for safe production, ocean environmental assessment, and disaster response. Figure 6 shows the monitoring image of the oil spill incident in the Yellow Sea in China in 2023.

3.2.2 Monitoring of Ocean Ecological Elements

The COCTS on the HY-1 series satellites has a swath width greater than 2,900 km and a spatial resolution of up to 500 meters. It can cover the globe three times daily, enabling the acquisition of global ocean chlorophyll concentration and total suspended matter concentration.

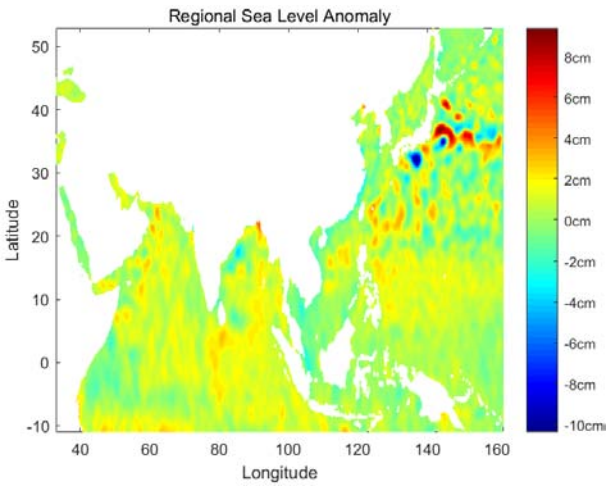

Fig.3 The regional 1/8° resolution sea level anomalies fusion product

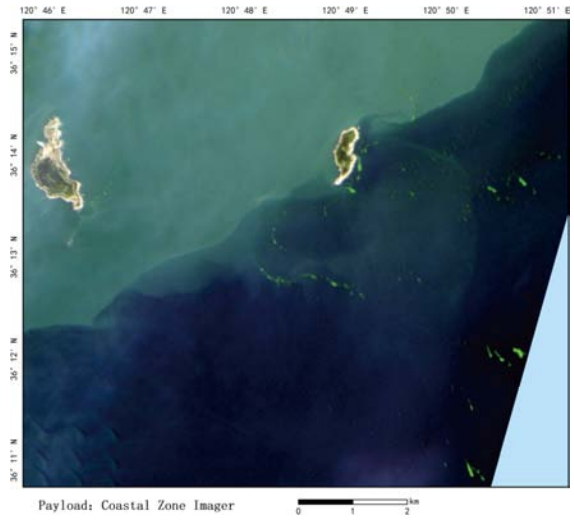

Fig.4 HY-1E CZI image of Ulva Prolifera green tide in the Yellow Sea

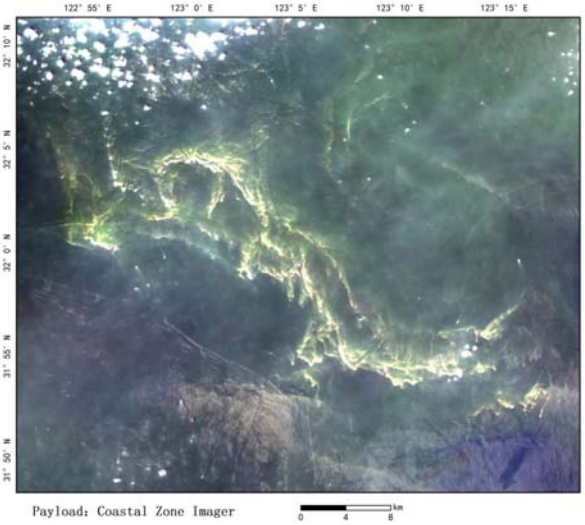

Fig.5 HY-1C CZI image of red tide in the East China Sea

This capability helps in assessing the health of the global ocean ecological environment. Figure 7 shows the monitoring product of chlorophyll-a concentration from HY-1C COCTS in the South China Sea.

3.3 Ocean Resource Development and Management

3.3.1 Offshore Wind Energy Monitoring

Offshore wind energy is an important source of clean energy. However, traditional monitoring methods struggle to achieve wide-area monitoring of the sea surface. The HY-2 series satellites can conduct wide-area SSW observations, but offshore wind farms are mainly distributed in nearshore areas within 50 m of water depth, where SCAT cannot effectively acquire data. SAR has the capability to observe high-resolution SSW. Using

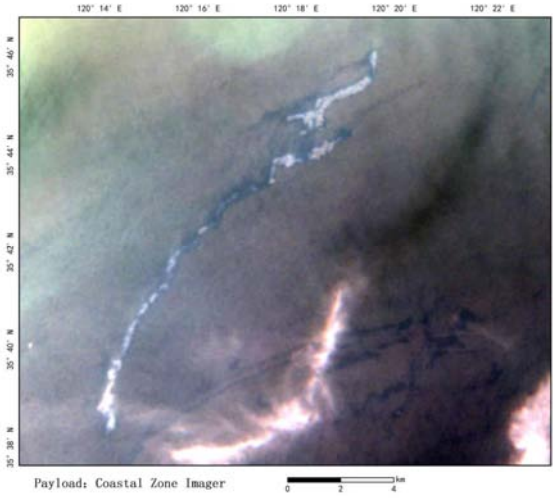

Fig.6 HY-1C CZI image of oil spill in the Yellow Sea

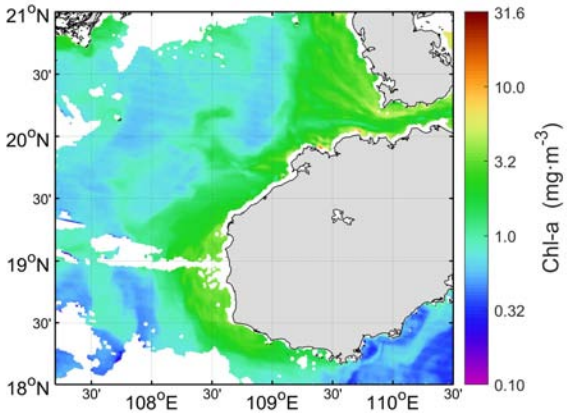

Fig.7 Chlorophyll-a concentration from HY-1C COCTS

high-resolution data from GF-3 and 1 m C-SAR 01/02, it is possible to perform wind vector inversion for offshore wind farms and evaluate wind resources. This provides operational services for wind power companies in the construction and operation of offshore wind farms. Figure 8 shows the wind energy assessment results of the Bohai Sea area in China using data from multiple SAR satellites.

3.3.2 Coastal Wetland Land Classification

Based on full-polarization SAR incoherent polarization decomposition technology, different types of land cover can be finely distinguished by analyzing the polarization information of radar echoes. By analyzing the remote sensing characteristics of coastal wetlands, a remote sensing information sample database and an information extraction index for coastal wetlands are established. Additionally, an information extraction model for coastal wetlands is constructed, enabling the extraction of coastal wetland information. Figure 9 illustrates the

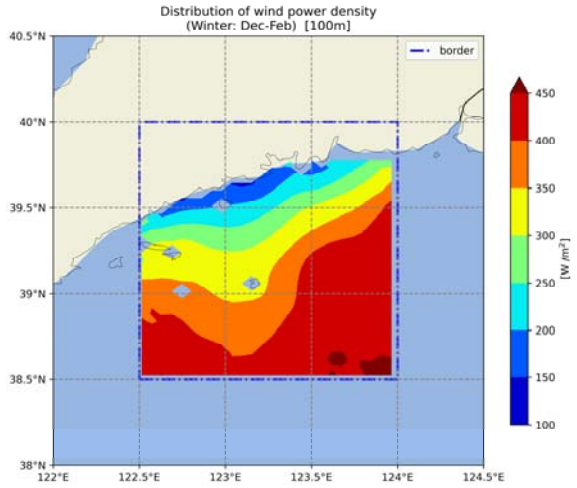

Fig.8 Wind energy average power density distribution assessment at 100 m height in the Zhuanghe sea area of the Bohai Sea, China

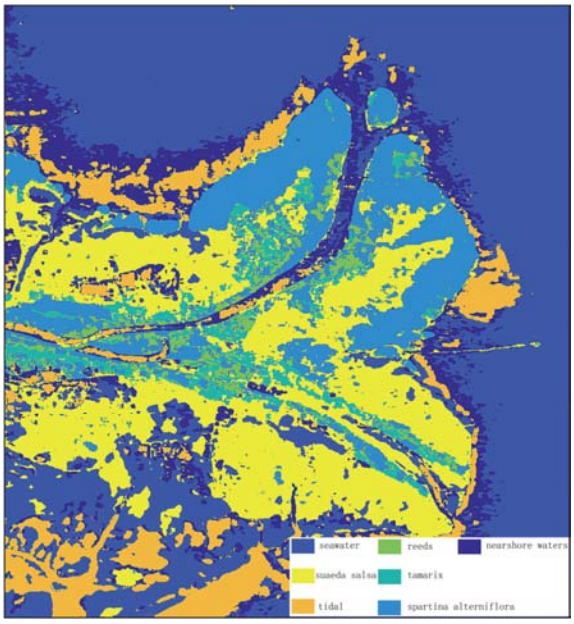

Fig.9 Wetland classification in the Yellow River Delta based on SAR polarization decomposition data

classification of wetlands in the Yellow River Delta, derived from SAR polarization decomposition data.

Furthermore, this technology has vast potential in the management of ocean and coastal natural resources. By enabling precise classification and monitoring of changes in land cover, it offers crucial information for overseeing offshore aquaculture areas, planning coastal land use, protecting ecosystems, and issuing disaster warnings.

3.4 Polar Monitoring

Using passive microwave brightness temperature data from the HY-2B, it is possible to generate daily sea ice concentration products, providing large-scale sea ice distribution information for the Arctic and Antarctic regions. These products are crucial for climate change monitoring and numerical model forecasting, and they also offer valuable reference information for navigation routes through ice zones, ensuring the safety of scientific expeditions and other vessels. Figure 10 displays the Antarctic sea ice concentration product derived from the HY-2B SMR.

In addition to large-scale sea ice concentration products, integrating multi-source remote sensing imagery from HY-1 series satellites, SAR, and other sources can provide detailed information on sea ice changes, land snow cover, glaciers, and ice shelf distribution, thereby enhancing polar monitoring.

3.5 Terrestrial Applications

3.5.1 Flood Monitoring

From July to August 2023, under the influence of Typhoon Doksuri, the Beijing-Tianjin-Hebei region and several areas in northeastern China experienced continuous heavy rainfall, resulting in widespread flooding. Utilizing the advantages of GF-3 and 1 m C-SAR, which are unaffected by clouds and rain, emergency observations of the flood-affected areas were conducted. By comparing pre- and post-disaster images, accurate information was provided for assessing the extent and severity of the damage. Figure 11 shows the GF-3 SAR image of the Songhua River basin on August 11, 2023.

Additionally, the high-frequency observations from HY-1C/D/E can monitor the occurrence and development of urban flooding, providing data support for urban flood prevention and drainage efforts.

3.5.2 Large Water Body Monitoring

Since July 2022, the middle and lower reaches of the Yangtze River have experienced prolonged high temperatures and low rainfall. This has led to increased evaporation and a continuous decline in the water surface area of bodies of water such as Poyang Lake and Dongting Lake due to multiple factors. Utilizing the advantages of HY-1C/D with their wide scanning swath, short revisit periods, and high-frequency observations, dynamic monitoring of the water bodies in these regions has been conducted. Figure 12 shows a comparison of the water surface area of Poyang Lake between August 22, 2022, and August 31, 2021, captured by the HY-1C CZI.

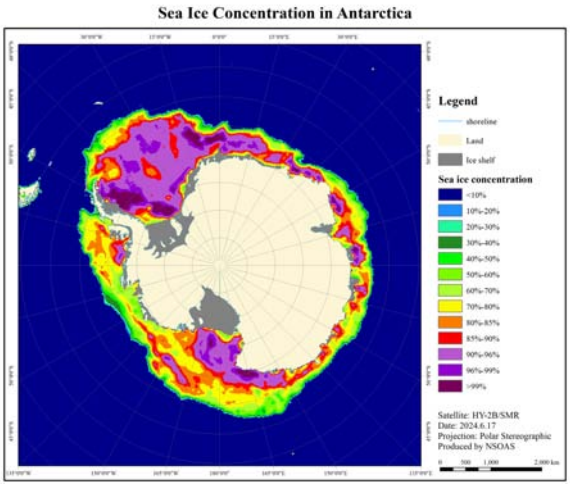

Fig.10 Antarctic sea ice concentration product of HY-2B

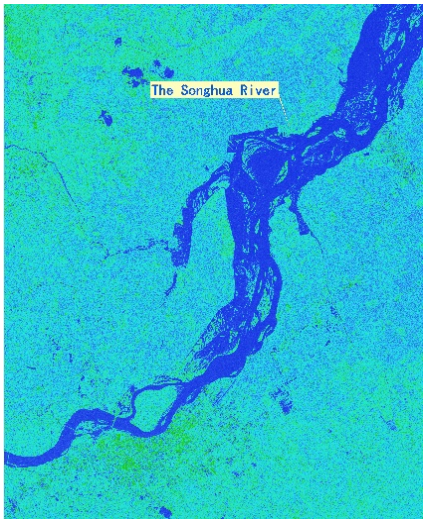

Fig.11 SAR image of the Songhua River basin

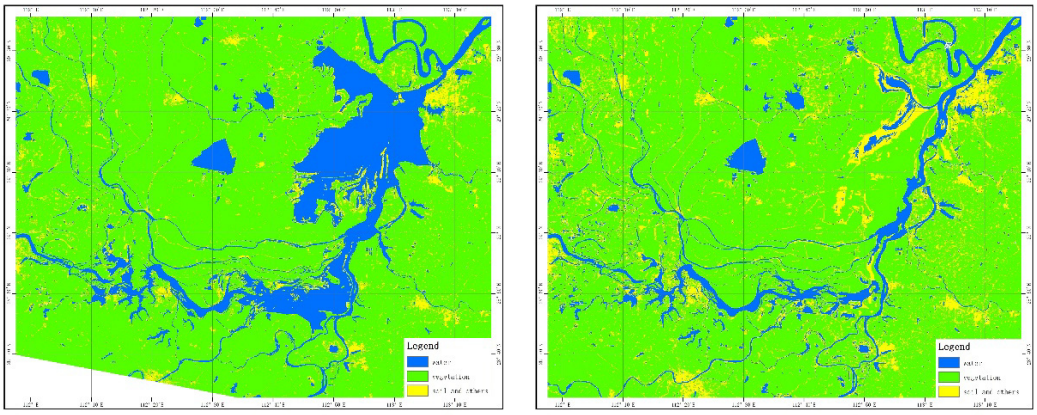

Fig.12 Comparison of the water surface area of Poyang Lake between August 22, 2022, and August 31, 2021

4 Summary

Currently, China has established an initial networked observation capability with the HY-1, HY-2, and HY-3 series satellites. These satellites play a significant role in ocean disaster prevention, ecological monitoring, and resource monitoring. Additionally, due to their wide coverage, high revisit frequency, and high quantitative accuracy, these ocean satellites also make valuable contributions to terrestrial and emergency monitoring.

The new satellites currently under development include the Ocean Salinity Satellite, HY-2E/F, and the Sea Wind and Wave Detection Satellite, with the Ocean Salinity Satellite scheduled for launch in 2024. Building on the long-term, continuous, and stable observation capabilities of the ocean color, ocean dynamics, and ocean surveillance and monitoring satellites, China will further expand observation elements, improve observation quality, develop high-orbit ocean satellites, and strive to achieve comprehensive detection of both surface and subsurface ocean information.

References

[1] JIANG X, ONGQ S. *8.10 - Ocean Satellite Programs in China*, in *Comprehensive Remote Sensing*, S. Liang, Editor. 2018, Elsevier: Oxford. p. 278-283
[2] NSOAS. *Successful Launch of the New Generation Ocean Color Observation Satellite*. 2023 [cited 2024 0705]; Available from: http://www.nsoas.org.cn/eng/item/266.html
[3] NSOAS. *HY-1 Series*. 2023 [cited 2024 0705]; Available from: http://www.nsoas.org.cn/eng/column/145.htm
[4] NSOAS. *HY-2 Series*. 2023 [cited 2024 0705]; Available from: http://www.nsoas.org.cn/eng/column/146.html
[5] WANG L, DING Z Y, ZHANG C. *CFOSAT-1 Realizes First Joint Observation of Sea Wind and Waves.* Aerospace China, 2019. **20**(1): p. 20-27.
[6] NSOAS. *On-orbit tests of 1-meter C-SAR 01 and 02 satellites were successfully completed*. 2023 [cited 2024 0705]; Available from: http://www.nsoas.org.cn/eng/item/264.html
[7] LIU J Q, *et al*. *Oil spills in China Seas revealed by the national ocean color satellites.* Chin Sci Bull, 2022. **67**(33): p. 3997-4008

ZENG Yong, HUANG Shusong, QI Wenping, XIA Tian, WANG Jingqiao, ZHANG Shuai. Recent Progress of Earth Observation Satellites in China. *Chinese Journal of Space Science*, 2024, **44**(4)

Recent Progress of Earth Observation Satellites in China

ZENG Yong, HUANG Shusong, QI Wenping, XIA Tian,
WANG Jingqiao, ZHANG Shuai

China Centre for Resources Satellite Data and Application, Beijing 100094

Abstract

Currently, China has 32 Earth observation satellites in orbit. The satellites can provide various data such as optical, multispectral, infrared, and radar. The spatial resolution of China Earth observation satellites ranging from low to medium to high. The satellites possess the capability to observe across multiple spectral bands, under all weather conditions, and at all times. The data of China Earth observation satellites has been widely used in fields such as natural resource detection, environmental monitoring and protection, disaster prevention and reduction, urban planning and mapping, agricultural and forestry surveys, land survey and geological prospecting, and ocean forecasting, achieving huge social benefits. This article introduces the recent progress of Earth observation satellites in China since 2022, especially the satellite operation, data archiving, data distribution and data coverage.

Key words

China Earth Observation Satellites, Satellite operation, Data archiving, Data distribution, Data coverage

1 Satellite Introduction

Earth observation satellites play a pivotal role in natural resource detection, environmental monitoring and protection, disaster prevention and reduction, urban planning and mapping, agricultural and forestry surveys, land survey and geological prospecting, and ocean forecasting. Their data and information are essential for a nation's economic development, social progress, and national security. Currently, there are 32 Earth observation satellites in orbit. Since 2022, China has launched 9 Earth observation satellites. The status of new China Earth observation satellites is shown in the Table1.

1.1 LT-1A and LT-1B

On 26 January 2022, the LT-1A satellite soared into space with a triumphant launch from the Jiuquan Satellite Launch Center. Following closely, on 27 February 2022, at the same time, the LT-1B satellite was flawlessly propelled into orbit by the Long March 4C carrier rocket, also originating from the Jiuquan Satellite Launch Center. The Land Exploration Satellite 1 project is an important component of the national medium- to long-term civilian space infrastructure development plan (2015-2025), and it is also the first scientific research satellite project approved by the plan. LT-1A and LT-1B satellites are developed by Shanghai Academy of Spaceflight Technology. The satellite has a design life of 8 years and has six imaging modes.

LT-1A and LT-1B operate on a sun-synchronous orbit at an altitude of 607 kilometers, equipped with advanced L-band multi-polarization multi-channel SAR payloads with a total antenna area exceeding 33 square

Received June 20, 2024

Table1 List of new Earth observation satellites in China

number	Satellite name	Code	Launch time	Design life/years
1	L-SAR 01A	LT-1A	Jan. 26, 2022	8
2	L-SAR 01B	LT-1B	Feb. 27, 2022	8
3	Gaofen-3 03	GF-3C	Apr. 7, 2022	8
4	Atmospheric environment monitoring satellite	DQ-1	Apr. 16, 2022	8
5	Terrestrial ecosystem carbon monitoring satellite	CM-1	Aug. 4, 2022	8
6	5m S-SAR 01	HJ-2E	Oct. 13, 2022	8
7	Gaofen-5 01A	GF-5 01A	Dec. 9, 2022	8
8	5 m S-SAR 02	HJ-2F	Aug. 9, 2023	8
9	Land Exploration Satellite 4-01	JZ-1	Aug. 13, 2023	8

meters, making them the largest-aperture SAR satellites currently in orbit in China. These satellites possess various imaging modes, with a maximum resolution of 3 meters and a maximum observation swath width of up to 400 kilometers. The L-band SAR payload, characterized by its long wavelength and strong ability to penetrate vegetation, can provide long-wave synthetic aperture radar data with extensive coverage, high measurement point density, and high repeat observation frequency, enabling early identification of disaster risks in areas with complex conditions and difficult ground access.

LT-1A and LT-1B satellites will operate in close proximity or as a network, utilizing differential deformation measurement and interferometric altimetry techniques to monitor ground deformation and conduct topographic mapping in specified regions. Featuring all-weather, all-time, multi-mode, and multi-polarization capabilities, they can be applied in geology, land use, Earthquake, disaster reduction, surveying and mapping, forestry, effectively enhancing China's capacity for independent satellite detection and prevention of geological disasters. The imaging mode of LT-1A and LT-1B is shown in Table 2.

1.2 GF-3C

The GF-3C satellite was successfully launched on 7 April 2022, from the Jiuquan Satellite Launch Center. Developed by the China Academy of Space Technology, which is part of the China Aerospace Science and Technology Corporation, it is designed to operate for eight years in orbit and features a suite of 12 conventional imaging modes.

Table 2 Imaging mode of LT-1A and LT-1B

Serial number	Imaging mode	Resolution (m)	Imaging width (km)	Polarization mode
1	Strip mode 1	3	50	Optional single polarization
2	Strip mode 2	12	100	Optional single polarization
3	Strip mode 3	3	50	Optional dual polarization
4	Strip mode 4	6	30	Total polarization
5	Strip mode 5	20~30	150~250	Optional single polarization
6	Scan mode	30	400	Optional single polarization

GF-3C satellite, one of the two operational satellites outlined in the national medium- to long-term civilian space infrastructure development plan (2015–2025), operates in a Sun-synchronous return orbit at an altitude of 755 kilometers. Its primary payload is a C-band synthetic aperture radar. This satellite fully inherits the technical solutions of the GF-3 satellite, a key scientific and technological project within the High-Resolution Earth Observation System. Once launched, it will integrate with the existing the GF-3 satellite to create a network, forming a constellation of land and sea radar satellites capable of 1-meter resolution and daily revisits. Additionally, it features enhancements such as a ship automatic identification signal receiving system and on-board real-time processing, enhancing capabilities for maritime vessel observation and monitoring of marine emergencies and the natural environment. With the formation of a three-satellite network, it will enhance capabilities for longer-term observation, greater clarity, faster imaging, and improved functionality, addressing a range of needs including maritime rights defense, disaster prevention and mitigation, environmental monitoring, disaster relief, territorial control, environmental protection, water conservancy, agriculture, and meteorology. This transition from demonstration to operational use of synthetic aperture radar satellite data will support China's strategy to become a leading maritime power. The imaging mode of GF-3C is shown in Table 3.

1.3 DQ-1

The atmospheric environment monitoring satellite, known as the DQ-1 satellite, was successfully launched on 16 April 2022, from the Taiyuan Satellite Launch

Table 3 The imaging mode of GF-3C

Number	Imaging mode[5]		Resolution/m			Imaging width/km		Total number of views[4]	Polarization mode
			Nominal	Azimuthal direction	Distance direction[1]	Nominal	Range		
1	Bunching[2]		1	1.0~1.5	0.9~2.5	10 × 10	10 × 10	1	Optional single polarization
2	Hyperfine stripe		3	3	2.5~5	30	30	1	Optional single polarization
3	Fine strip 1		5	5	4~6	50	50	1	Optional dual polarization
4	Fine stripe 2		10	10	8~12	100	95~110	2	Optional dual polarization
5	Standard strip		25	25	15~30	130	95~150	6	Optional dual polarization
6	Narrow range topsar		50	50~60	30~60	300	300	6	Optional dual polarization
7	Wide range topsar		100	100	50~110	500	500	8	Optional dual polarization
8	Fully polarized strip 1		8	8	6~9	30	20~35	1	Total polarization
9	Fully polarized strip 2		25	25	15~30	40	35~50	6	Total polarization
10	Wave imaging mode[3]		8	8	6~9	20 × 20	20 × 20	1	Total polarization
11	Global topsar model		500	500	350~700	650	650	12	Optional dual polarization
12	Extend incident angle	Low incident angle	25	25	15~30	130	120~150	6	Optional dual polarization
		High incident angle	25	25	20~30	80	70~90	6	Optional dual polarization
	Note 1		Ground distance						
	Note 2		The time interval between two consecutive observations is about 10 s, and the imaging range in azimuth and range is 10 km respectively						
	Note 3		The interval between two consecutive observations is about 100 km, which can be adjusted. The imaging range in azimuth and range is 20 km respectively						
	Note 4		Total viewing number is azimuth viewing number × distance viewing number						
	Note 5		With GMTI and high resolution and wide range test mode						

Center. This satellite serves as a cornerstone of scientific research within the national medium- to long-term civilian space infrastructure development plan (2015–2025). Developed by the Shanghai Aerospace Technology Research Institute, which is a subsidiary of the China Aerospace Science and Technology Corporation, the DQ-1 operates in a Sun-synchronous orbit and boasts a comprehensive array of payloads. These include atmospheric detection lidar, a high-precision polarization scanner, a multi-angle polarization imager, an ultraviolet hyperspectral atmospheric composition detector, and a wide-range imaging spectrometer.

Notably, this atmospheric environmental monitoring satellite is not just a research satellite in the nation's medium to long-term development plan for civil space infrastructure; it is also a world pioneer, being the first satellite capable of detecting carbon dioxide laser. Equipped with five advanced remote sensing instruments, it promises to significantly enhance global capabilities in carbon monitoring and atmospheric pollution detection. Once operational in orbit, it will usher in a leapfrogging improvement in quantitative remote sensing services across various fields, including the ecological environment, meteorology, and agriculture. This advancement will aid China in achieving national strategies such as carbon neutrality and carbon peaking, promoting ecological civilization construction, and bolstering the development of a strong aerospace nation. Additionally, during the "14th Five-Year Plan" period, China aims to launch a high-precision greenhouse gas comprehensive detection satellite to complement and enhance the network observation capabilities of the atmospheric environment monitoring satellite.

The satellite primarily serves as a tool for regional ambient air quality and ecological environment monitoring, offering crucial domestic data to further bolster China's comprehensive atmospheric environment monitoring, global climate change research, crop yield estimation, agricultural disaster monitoring, and other critical application capabilities. By doing so, it aims to advance remote sensing applications in China's ecological environment, meteorology, agriculture, and rural areas, thereby significantly enhancing the comprehensive utilization efficiency of satellite resources and promoting environmental protection efforts. The payloads of DQ-1 are shown in Table 4.

Table 4 The payloads of DQ-1

Atmospheric lidar	
Detection center wavelength/nm	532, 1064, 1572
Repetition frequency/Hz	20 (double pulse)
Laser pulse width/ns	15
Main telescope aperture/m	1
High precision scanning polarimeter	
Center wavelength/nm	380, 410, 443, 490, 670, 865, 1380, 1610, 2250; Each channel has polarization detection capability
Spatial resolution/km	Better than 10
Width/km	≥ 1800
Polarization measurement accuracy	Better than 0.5%
Directional polarization camera	
Spectral range/nm	433~453, 480~500 (P) 555~575, 660~680 (P) 758~768, 745~785 845~885 (P), 900~920
spatial resolution/km	Better than 3.5
Width/km	≥ 1800
Polarization measurement accuracy	Better than 2%
Ultraviolet hyperspectral atmospheric composition detector	
Spectral range/nm	240~315, 315~403, 403~550, 550~710
Width/km	≥ 2300
Spectral resolution/nm	Better than 0.3~0.5
Spatial resolution/km	Better than 24 (rail crossing direction) × 13 (along rail direction)
Wide imaging spectrometer	
Spectral range/μm	0.415, 0.443, 0.47, 0.49, 0.555, 0.659, 0.681, 0.753, 0.8 (Panchromatic channel), 0.865, 0.936, 0.94, 1.375, 1.64, 2.13, 3.8 (High gain), 3.8 (Low gain), 7.325, 8.55, 10.8, 12.0
spatial resolution/m	75 (Panchromatic channel), 150 (True color channel), 300 (Long wave infrared split window), Other channels: 600
Width/km	≥ 2300

1.4 CM-1

The Carbon Monitoring Satellite for Terrestrial Ecosystems (CM-1 Satellite) was successfully launched at 11:08 on 4 August 2022, from the Taiyuan Satellite Launch Center. As the world's first satellite to combine active and passive observation for forest carbon sink monitoring, its successful launch signifies China's entry into the era of remote sensing-based carbon sink monitoring.

The Carbon Monitoring Satellite for Terrestrial Ecosystems was developed by the China Academy of Space Technology, a subsidiary of the China Aerospace Science and Technology Corporation. It is equipped with four satellite payloads: a multi-beam lidar, a multi-angle multispectral camera, a hyperspectral detector, and a multi-angle polarization imager. By utilizing a remote sensing system that integrates point-to-surface and active-passive sensing, and employing comprehensive remote sensing techniques including "laser, multispectral, multi-angle, hyperspectral, and polarization", it captures multi-factor remote sensing information of forest carbon sinks, enhancing the accuracy of carbon sink inversion and significantly elevating China's quantitative capabilities in land remote sensing.

The satellite employs a combined active-passive measurement approach to detect the vegetation biomass of terrestrial ecosystems, addressing issues such as terrestrial ecosystem carbon monitoring, terrestrial ecology and resource survey monitoring, and monitoring and evaluation of major national ecological projects. It serves the national goal of achieving "carbon peak and carbon neutrality", providing operational support and research services for forestry, grassland, ecological environment, surveying and mapping, meteorology, agriculture, and emergency disaster relief. The payloads of CM-1 are shown in Table 5.

1.5 HJ-2E and HJ-2F

The HJ-2E and HJ-2F satellites, part of the Environmental Disaster Reduction II series, were triumphantly launched on 13 October 2022, and 9 August 2023, respectively, from the Taiyuan Satellite Launch Center. Developed by the Fifth Academy of China Aerospace Science and Technology Corporation, these satellites are designed to have an operational lifespan of 8 years and offer four distinct conventional imaging modes.

As outlined in the national medium- to long-term civilian space infrastructure development plan (2015–2025), the HJ-2E and HJ-2F satellites operate in a sun-synchronous orbit at an altitude of 499 kilometers. Their primary payload is an S-band synthetic aperture radar. Once in orbit, these twin satellites will form a network, marking the initial establishment of a constellation of satellites for emergency management and ecological environment monitoring, along with a comprehensive space-ground operational application system. This constellation will provide essential support for emergency management and ecological environment

operations, primarily aiming to localize SAR satellite remote sensing data for these purposes. Additionally, the satellites will serve industries such as natural resources, water conservancy, agriculture, forestry, grasslands, and Earthquake monitoring. The imaging mode of HJ-2E and HJ-2F is shown in Table 6.

Table 5 Payloads of CM-1

Multibeam lidar			
Laser beam	Vegetation detection 5 beam, aerosol detection 1 beam		
Laser wavelength/nm	1064/532		
Laser altimeter range/km	506 ± 20		
Aerosol polarization detection/nm	Horizontal and vertical polarization (532)		
Ranging accuracy (static)/m	≤ 0.3		
Vertical sampling interval for aerosol detection/m	≤ 30		
Multi angle multi spectral camera			
Angle	0° camera	± 19° camera	± 41° camera
Spectral segment/nm	B1 band: 450~520 B2 band: 520~590 B3 band: 630~690 B4 band: 770~890	B1 band: 450~520 B2 band: 520~590 B3 band: 630~690 B4 band: 770~890 P-band: 500~760	B1 band: 450~520 B2 band: 520~590 B3 band: 630~690 B4 band: 770~890 B5 band: 690~730
Ground pixel resolution (vertical rail direction)/m	Better than 2	Better than 4/8 (panchromatic/multispectral)	Better than 6/12 (red edge/multispectral)
Static MTF	≥ 0.2	P-band ≥ 0.18; Others ≥ 0.2	B5 band ≥ 0.15; Others ≥ 0.2
Width/km	≥ 20		
Quantization bits/bit	12		
Hyperspectral detector			
Spectral segment	670~780nm, ≥ 366 channels		
spectral resolution/nm	≤ 0.3		
Ground pixel resolution/km	≤ 2		
Width/km	≥ 30		
Quantization bits/bit	14		
Multi angle polarization imager			
Working spectrum segment/nm	There were 8 spectral bands: 433~453, 480~500 (P), 555~575, 660~680 (P), 758~768, 745~785, 845~885 (P), 900~920; 490, 670 and 865 spectral bands have polarization measurement capability		
Polarization analysis	Linear polarization, three polarization directions 0°, 60°, 120°		
Multi angle observation	Along the rail ≥ 9 angles		
Sub satellite point spatial resolution/km	≤ 3.5		
Width/km	≥ 800		

Table 6 Imaging mode of HJ-2E and HJ-2E

Serial number	Imaging mode	Resolution/m			Imaging width/km		Visual number $A \times E$[1]	Polarization mode
		nominal	Azimuthal direction	Distance direction	nominal	range		
1	Unipolar stripe	5	5	3.7~5	35	35~41	1×1	Selectable single polarization
2	Dual polarization strip	5	5	3.7~5	35	35~41	1×1	Optional dual polarization
3	Monopolar scanning	25	20-25	16.5~24.5	95	95~109	1×3[2] 1×4	Selectable single polarization
4	Dual polarization scanning	25	20-25	16.5~24.5	95	95~109	1×3[2] 1×4	Optional dual polarization
Note 1	$A \times E$ stands for azimuthal visibility × distance visibility							
Note 2	View number 1 × 3 is only used at the farthest wave position							

1.6 GF-5 01A

The GF-5 01A satellite was successfully launched from the Taiyuan Satellite Launch Center on 9 December 2022. As a successor to the Gaofen-5 satellite, GF-5 01A boasts three payloads: the Advanced Hyperspectral Imager for the Visible and Shortwave Infrared (AHSI), the Wideband Thermal Infrared Imager (WTI), and the Environmental Monitoring Instrument for Atmospheric Trace Gases (EMI). GF-5 01A possesses the world's foremost comprehensive capabilities in wide-band long-wave infrared detection with medium-to-high spatial resolution, offering unparalleled visible short-wave hyperspectral imaging and unprecedented spatial resolution for detecting atmospheric trace gases. Remarkably, it will mark the first time in orbit that a satellite performs three-axis maneuvering for lunar calibration.

The networking of GF-5 01A with GF-5 02 will significantly enhance China's hyperspectral observation capabilities in the atmospheric, aquatic, and terrestrial domains. This will cater to the urgent need for comprehensive environmental monitoring, providing domestic hyperspectral data support for critical environmental operations such as atmospheric and water environmental monitoring. The payloads of GF-5 01A are shown in Table 7.

Table 7 Payloads of GF-5 01A

Visible short wave infrared hyperspectral camera (AHSI)	
Spectral range	0.4~2.5 μm, 330 channels in total
Spatial resolution/m	30 ± 0.1
Width/km	60 ± 1
spectral resolution/nm	VNIR: ≤5; SWIR: ≤10
Quantization Bits/bit	12
Wide range thermal infrared imager (WTI)	
Spectral segment/μm	B1: 8.01 ± 0.08 ~8.39 ± 0.12; B2: 8.42 ± 0.12 ~8.83 ± 0.12; B3: 10.3 ± 0.15 ~11.3 ± 0.08; B4: 11.5 ± 0.08 ~12.5 ± 0.16;
Sub satellite ground pixel resolution/m	≤ 100 (star point) @705 km
Width/km	≥ 1500
Quantization Bits/bit	12
Atmospheric trace gas differential absorption spectrometer (EMI)	
Spectral range/nm	240~290, 290~380; 390~530, 550~710;
Spectral resolution/nm	0.3~0.6
Stray light	$< 6 \times 10^{-4}$
Total field of view/(°)	114 (rail crossing direction)
Spatial resolution/km	Better than 24 (perpendicular to the track) × 13 (along the track)
Quantization bits/bit	14

1.7 JZ-1

The JZ-1 satellite was successfully launched on 13 August 2023, from Xichang Satellite Launch Center. Developed by China Academy of Space Technology, a subsidiary of the China Aerospace Science and Technology Corporation, the satellite's ground system construction and operation are managed by the China Centre for Resources Satellite Data and Application and the Aerospace Information Innovation Research Institute, Chinese Academy of Sciences. With an on-orbit design life of 8 years, the satellite boasts four conventional imaging modes.

The JZ-1 is a remote sensing research satellite outlined in the national medium- to long-term civilian space infrastructure development plan (2015–2025). Operating in a near 36000-kilometer inclined geosynchronous orbit, satellites in this orbit resemble drawing an “8” in the sky, allowing for relatively consistent observation of vast areas with short revisit periods and wide imaging coverage.

As the world's first geosynchronous orbit SAR (Synthetic Aperture Radar) satellite, the JZ-1 is equipped with an L-band SAR as its primary payload. Upon successful launch, it will enable China to achieve all-weather, day-and-night, high-frequency revisit (hourly), and wide-coverage observation capabilities, covering both domestic and neighboring regions with 20-meter resolution. This significant achievement fills a gap in China’s high-orbit SAR field, primarily satisfying the needs of disaster prevention and mitigation applications while also catering to the requirements of industries such as land resources, water conservancy, meteorology, oceanography, forestry, and agriculture. The satellite is currently undergoing in orbit testing.

2 Satellite Operation

In daily situations, the imaging is arranged comprehensively based on user demands and satellite constraints. As of 31 May 2024, the GF-3C satellite has imaged a total of 8755 circles, the LT-1A satellite has imaged a total of 7076 circles, the LT-1B satellite has imaged a total of 6742 circles, the HJ-2E satellite has imaged a total of 4644 circles, the GF-5 01A satellite has imaged a total of 3595 circles in infrared and 2655 circles in hyperspectral. The satellite operation and control situation is detailed in Table 8.

Table 8 Statistics of satellite operation (cumulative, as of 31 May 2024)

Satellite	Number of imaging turns	Imaging time/h	Track adjustment/ times
GF-3C	8755	1090.22	21
LT-1A	7076	587.04	119
LT-1B	6742	562.37	127
HJ-2E	4644	373.44	6
GF-501a (infrared)	3595	1218.76	7
GF-501a (hyperspectral)	2655	203.95	7

3 Data Archiving

In general, data acquired by the satellites will be processed into Levels 0 and 1 for storage. As of 31 May 2024, the archiving of each satellite is shown in the table below.

Table 9 Statistical results of LT-1A satellite data archiving (as of 31 May 2024)

Satellite	Sensor	Level 0	Level 1
LT-1A	SAR	19335 scenes/ 292.69 TB	190213 scenes/ 317.63 TB

Table 10 Statistical results of LT-1B satellite data archiving (as of 31 May 2024)

Satellite	Sensor	Level 0	Level 1
LT-1B	SAR	18120 scenes/ 271.76 TB	182057 scenes/ 295.48 TB

Table 11 Statistical results of GF-3C satellite data archiving (as of 31 May 2024)

Satellite	Sensor	Level 0	Level 1
GF-3C	SAR	24109 scenes/ 260.44 TB	288748 scenes/ 649.24 TB

Table 12 Statistical results of HJ-2E satellite data archiving (as of 31 May 2024)

Satellite	Sensor	Level 0	Level 1
HJ-2E	SAR	13017 scenes/ 140.78 TB	205890 scenes/ 321.23 TB

Table 13 Statistical results of HJ-2F satellite data archiving (as of 31 May 2024)

Satellite	Sensor	Level 0	Level 1
HJ-2F	SAR	4864 scenes/ 52.46 TB	71121 scenes/ 109.49 TB

Table 14 Statistical results of GF-5A satellite data archiving (as of 31 May 2024)

Satellite	Sensor	Level 0	Level 1
GF-5A	ACPC	6314 scenes/35.17 GB	6255 scenes/130.94 GB
	AHSI	85679 scenes/236.43 TB	84887 scenes/127.17 TB
	EMI	8205 scenes/84.39 TB	8185 scenes/19.93 TB
Total		100198 scenes/320.85 TB	99327 scenes/147.22 TB

4 Data Distribution

The data of China Earth observation satellites are distributed to the research institutions, governments, commercial companies and individuals. By the end of May 2024, the distribution of each satellite is shown in the table below.

Table 15 Statistics of satellite data distribution (as of 31 May 2024)

Satellite (payload)	Distribution/scenes
LT-1A	197369
LT-1B	188308
GF-3C	247913
DQ-1 (WSI)	485734
Cm-1 (DMC)	657968
HJ-2E	354273
GF-5A	288289
HJ-2F	95319
total	2515173

5 Data Coverage

Since its launch, the satellite has demonstrated excellent global coverage capabilities. By the end of May 2024, the Level 1 data of LT-1A satellite had achieved an effective global coverage spanning 100.67 million square kilometers, while the LT-1B satellite covered 96.94 million square kilometers. The level-1 data of GF-3C satellite excelled, achieving an impressive 202.37 million square kilometers of effective global coverage. Similarly, the Level 1 data of DMC sensor on the CM-1 satellite delivered 55.61 million square kilometers of effective global coverage. The HJ-2E satellite covered 68.46 million square kilometers, and the HJ-2F satellite achieved 40.98 million square kilometers of effective global coverage. Lastly, the AHSI sensor on the GF-5 01A satellite achieved a remarkable 64.86 mil

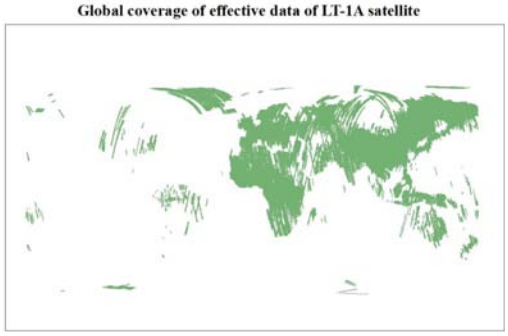

Fig. 1 Global coverage of effective data of LT-1A satellite (as of 31 May 2024)

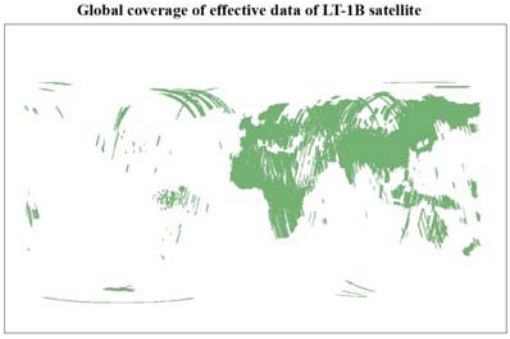

Fig. 2 Global coverage of effective data of LT-1B satellite (as of 31 May 2024)

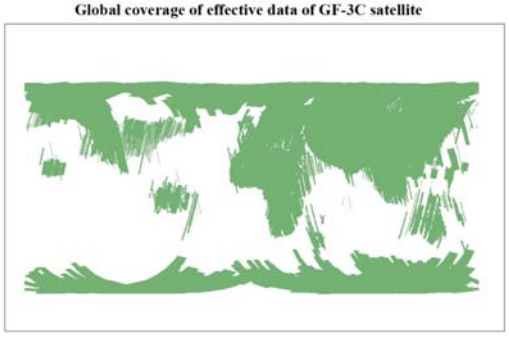

Fig. 3 Global coverage of effective data of GF-3C satellite (as of 31 May 2024)

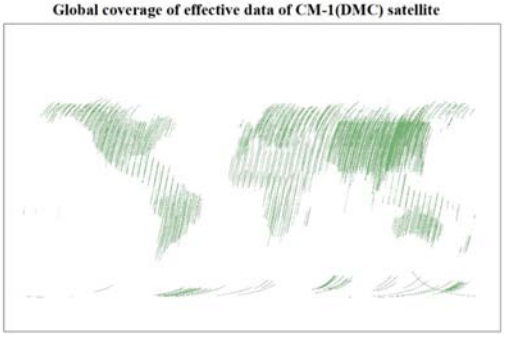

Fig. 4 Global coverage of effective data of CM-1(DMC) satellite (as of 31 May 2024)

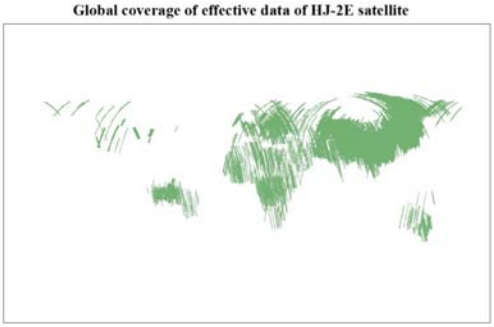

Fig. 5 Global coverage of effective data of HJ-2E satellite (as of 31 May 2024)

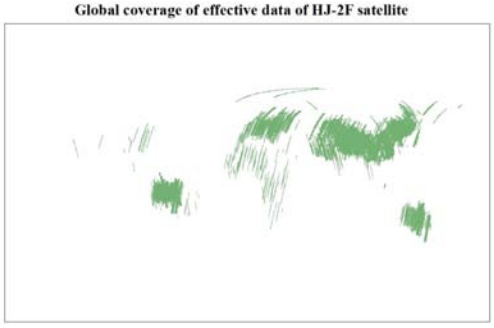

Fig. 6 Global coverage of effective data of HJ-2F satellite (as of 31 May 2024)

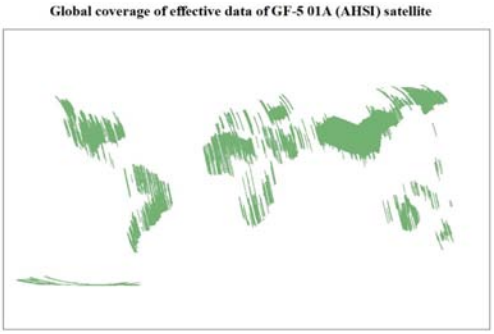

Fig. 7 Global coverage of effective data of GF-5 01A （AHSI）satellite (as of 31 May 2024)

lion square kilometers of effective global coverage. The respective satellite coverage maps are presented below for reference.

6 Conclusion

After more than 20 years of development, Earth observation satellites possess the capability to observe across multiple spectral bands, under all weather conditions, and at all times. The increasing number of civilian Earth observation satellites and diverse payload types have promoted the development of remote sensing technology applications. At the same time, the improvement of

remote sensing technology application level has put forward higher requirements for satellite payload indicators and image quality, promoting the development of civilian Earth observation satellites and ground processing systems.

By 2030, the number of Earth observation satellites in China will reach 40, and the payload and orbit types will become more diverse, further improving the high spatial, high temporal, high spectral, and high radiation resolution. Earth observation satellites will provide rich, stable, and sustainable scientific data for various fields of national economy and people's livelihood, promote the further improvement of remote sensing technology application level, and create greater social and economic benefits.

References

[1] State Administration of Science, Technology and Industry for National Defense, PRC. Notice on Issuing the national medium- to long-term civilian space infrastructure development plan(2015–2025) [EB/OL]. (2015-11-24)[2024-06-27]. https://www.sastind.gov.cn/n10086167/n10086216/c10404645/content.html

[2] SHI Jiancheng, LÜ Daren, WANG Yu, DU Yan, PANG Yong, YANG Dongxu, WANG Xin, DONG Xiaolong, YANG Xiaofeng. Recent progress of Earth science satellite missions in China[J]. *Chinese Journal of Space Science*, 2022, 42(4): 712-723. DOI:10.11728/cjss2022.04.yg21

[3] ZHOU Xiaoqing, PENG Mingyuan, HU Fen. Current status and prospects of land remote sensing satellite development in China [J]. *Satellite Application*, 2022(9):14-19

[4] China Geographic Information Industry Association. China Geospatial Industry and Science Report (2023) [M]. Beijing: Surveying and Mapping Press, 2023

[5] WANG Quan, YOU Shucheng. Land satellite remote sensing monitoring system and its application prospects[J]. *Acta Geodaetica et Cartographica Sinica*, 2022(004): 051. DOI:10.11947/j.AGCS.2022.20210714

6 International Cooperation

WANG Chi, BLANC Michel, ZHANG Shunrong, DENARDINI Clezio Marcos, LIU William, SHEN Xuhui, WU Jian, XU Jiyao, LI Hui, ZHANG Qinghe, REN Liwen, ZHU Yajun, LI Guozhu, DING Zonghua, LIU Zhengkuan, YANG Fang. Progress of International Meridian Circle Program. *Chinese Journal of Space Science*, 2024, **44**(4)

Progress of International Meridian Circle Program

WANG Chi[1], BLANC Michel[2], ZHANG Shunrong[3], De Nardini Clezio Marcos[4], LIU William[1], SHEN Xuhui[1], WU Jian[5], XU Jiyao[1], LI Hui[1], ZHANG Qinghe[1], REN Liwen[1], ZHU Yajun[1], LI Guozhu[6], DING Zonghua[5], LIU Zhengkuan[1], YANG Fang[1]

1. National Space Science Center, Chinese Academy of Sciences, Beijing 100190
2. IRAP (CNRS-University Toulouse III-CNES), Toulouse 31400
3. Haystack Observatory, Massachusetts Institute of Technology, MA 01886
4. Instituto Nacional de Pesquisas Espaciais, São José dos Campos (SP), Brazil -12227-010
5. China Research Institute of Radio wave Propagation, Qingdao 266000
6. Institute of Geology and Geophysics, Chinese Academy of Sciences, Beijing 100083

Abstract

In 2024, the Chinese Meridian Project (CMP) completed its construction, deploying 282 instruments across 31 stations. This achievement not only provides a robust foundation but also serves as a reference template for the International Meridian Circle Program (IMCP). The IMCP aims to integrate and establish a comprehensive network of ground-based monitoring stations designed to track the propagation of space weather events from the Sun to Earth. Additionally, it monitors various disturbances generated within the Earth system that impact geospace. Over the past two years, significant progress has been made on the IMCP. In particular, the second phase of construction for the China-Brazil Joint Laboratory for Space Weather has been completed, and the North Pole and Southeast Asia networks are under active construction. The 2024 IMCP joint observation campaign was successfully conducted. To facilitate these developments, the scientific program committee of IMCP was established, following the success of 2023 IMCP workshop and the space weather school, which was co-hosted with the Asia-Pacific Space Cooperation Organization (APSCO) and sponsored by SCOSTEP. Preparations are now underway for the 2024 workshop in collaboration with the National Institute for Space Research (INPE) in Brazil.

Key words

Chinese Meridian Project (CMP), International Meridian Circle Program (IMCP), China-Brazil Joint Laboratory for Space Weather, North Pole and Southeast Asia networks

1 Introduction

The International Meridian Circle Program is proposed to bring together over ten countries along the 120°E and 60°W meridians to create an integrated global monitoring network. Equipped with more than 1000 instruments, the IMCP aims to study Earth as a connected system encompassing space, atmosphere, and surface. Its goal is to understand how solar wind disturbances affect our mother planet and how disturbances originating from

Received June 20, 2024

the Earth's surface and atmosphere might also impact our space environment. This international effort addresses critical questions, such as how solar energy and matter outputs interact with Earth's magnetic field and atmosphere, and how space weather is in turn, impacted by global change and environmental hazards. The IMCP leverages a wide range of international collaborations to address these global scientific challenges through real-time monitoring, data sharing, and joint research activities.

Over the past two years, significant progress has been made on the IMCP. The Chinese Meridian Project completed its construction, the second phase of the China-Brazil Joint Laboratory for Space Weather (CBJLSW) was successfully concluded, and ongoing advancements are being made in the North Pole and Southeast Asia networks. The 2024 IMCP joint observation campaign was successfully conducted, making a significant milestone. The IMCP scientific committee was established, a successful workshop was held in 2023, and an IMCP space weather school was co-hosted with the APSCO. Preparations are currently underway for a 2024 workshop in collaboration with the INPE in Brazil.

2 Chinese Meridian Project

Construction of the second phase of the Chinese Meridian Project began in 2019 and successfully passed the engineering acceptance evaluation in June 2024. This expanded network has created a robust ground-based monitoring system that spans across China and the Earth polar regions. It comprises a range of conventional instruments such as optical, radio, and geomagnetic equipment, as well as several large and advanced devices including a radio heliograph, an interplanetary scintillation telescope, a Mesosphere-Stratosphere- Troposphere (MST) radar, a mid-latitude high- frequency radar, a new generation tristatic incoherent scatter radar with electronic beam steering, a low- latitude high-frequency radar, an array-type large-aperture helium lidar, and a large-aperture metal-layer lidar.

Once fully operational, the CMP will provide data from its diverse array of instruments to a wide spectrum of user communities. This will enhance our ability to monitor and understand the complex interactions between solar activities and terrestrial processes, contributing to the global scientific effort to mitigate the effects of space weather and understand Earth's dynamic system.

3 China-Brazil Joint Laboratory for Space Weather

The China-Brazil Joint Laboratory for Space Weather is set to complete its second phase of construction by the end of 2024. Sixteen sets of space environment monitoring equipment have been deployed across South America's low-latitude region, including geomagnetic, radio, and optical instruments. Headquartered in Brazil, CBJLSW aims to expand its network to encompass Peru and Chile.

Fig.1 Monitoring network of the CBJLSW

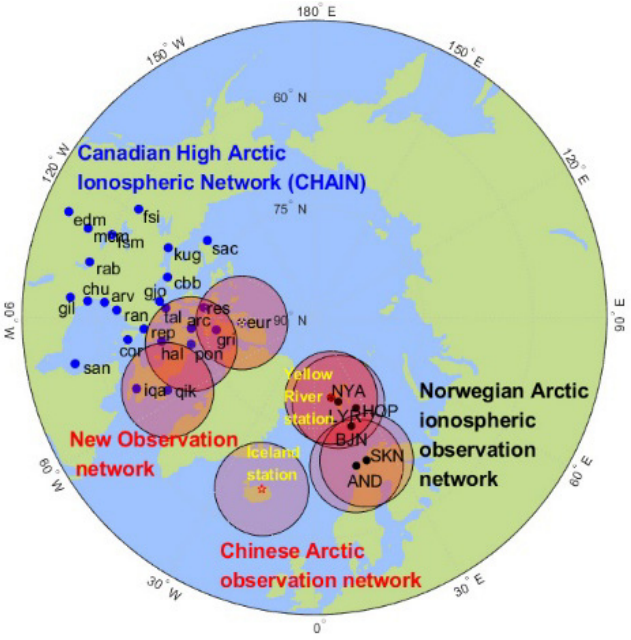

Fig.2 North polar ionospheric monitoring network

As a model project for the IMCP, the construction of the CBJLSW has systematically explored and continues to refine collaborative efforts in areas such as responsibility allocation, investment, personnel exchange and training, and data/result sharing. This focus maximizes return on investment and fosters sustainable development, ultimately establishing an efficient framework for joint observation and collaborative research.

4 North Polar Ionospheric Monitoring Network

Funded by a key international cooperation grant from the National Natural Science Foundation (NSFC), a collaborative effort is underway to establish the North Polar Ionospheric Monitoring Network. This joint project brings together researchers from the University of New Brunswick (Canada), the University of Oslo (Norway), NSSC and Shandong University of China.

The first phase involves to install GNSS TEC and Scintillation receivers and all-sky airglow imagers at three observation stations: Resolute Bay, Pond Inlet, and Iqaluit. This will facilitate comprehensive monitoring of the ionosphere in the North Polar region. Upon completion, real-time data sharing will be established with the Canadian High Arctic Ionospheric Network (CHAIN) and Norway monitoring network.

5 Ionospheric ISR Network in Northern Europe

China Research Institute of Radiowave Propagation (CRIRP) formally joined the European Incoherent Scattering Scientific Association (EISCAT) since 2006 approved by Ministry of Science and Technology of China (MOST). CRIRP has broadly contributed to the scientific production of EISCAT by performing a large number of experiments, observation,data analysis and model research activities on ionospheric irregularities, ionospheric radio propagation, space plasma and ionospheric incoherent scatter measurement methods. At present, the next generation European Incoherent Scatter radar system (EISCAT 3D) is being tested and will be put into operation in the end of 2024. EISCAT 3D consists of one core site in Skibotn, Norway and two reception sites in Kaiseniemi, Finland and Karesuvanto, Sweden.The key capabilities of EISCAT 3D include volumetric imaging, aperture synthesis imaging, multistatic imaging, and continuous monitoring, making it the leading radar equipment for the study of geospace environment. EISCAT thinks highly of the IMCP and signed the memorandum of understanding with CRIRP about the cooperation between IMCP and EISCAT 3D in 2018.

6 Southeast Asia Region Monitoring Network

Significant progress has been made on the southern extension of the East Asia/Southeast Asia Ionospheric Irregularity and Scintillation Observation Network (IONISE) and the China-Southeast Asia Upper Atmosphere Double-Layer Airglow Observation Network.

Agreements have been signed with the National Astronomical Research Institute of Thailand (NARIT), the Vientiane Meteorology and Hydrology Department in Laos, and Telkom University in Indonesia. In collaboration with these partners, new instruments have been deployed at stations in Songkhla and Chiang Mai (Thailand), Pontianak, West Sumatra, and Bandung (Indonesia), Vientiane, Pakse, and Attapeu (Laos). These instruments include all-sky airglow imagers, GNSS-TEC and scintillation monitors, PDI agile digital ionosondes, and wideband vector magnetometers.

7 IMCP Joint Observation Campaign

Leveraging capabilities from the CMP, the international Incoherent Scatter Radar network, CBJLSW, and other ground-based networks, we organize one to two IMCP Joint Observation Campaigns each year.

During the strong magnetic storm between November to December 2023, a call for joint observations was issued on 30 November, recognizing the potential impact. Observation participants responded swiftly, enabling the collection of highly valuable, synchronized multi-element observational data throughout the storm.

Ground-based facilities participating in these observations employed diverse detection methods, including radio waves, optical sensors and geomagnetic field measurements. This comprehensive approach, drawing on data from over 80 key stations, yielded a rich dataset encompassing the ionosphere and the middle-to-upper atmosphere. This data will be instrumental in providing researchers with a detailed picture of the space environment during such magnetic storm events. Scientific analysis of this campaign has resulted in presentations and publications.

8 IMCP Headquarters and Activities

Marking a significant milestone, the IMCP Headquarters Building was officially inaugurated and opened for the IMCP community in September 2023. This new facility now houses key organizations, including the Chinese office of the CBJLSW, the Sino-Russian Space Weather Joint Center, and the Regional Warning Center (China).

In 2023, IMCP successfully hosted its annual workshop from 14 to 17 September and co-hosted, with APSCO, a space weather school from 17 to 21 September. The workshop attrached the participation of 106 international scientific experts, and 41 students from 14 countries attended courses taught by 25 esteemed lecturers from five countries. In May 2024, the SuperDARN/IMCP school was successfully held at the Siziwang Observatory of Space Weather. These educational and training activities further demonstrate IMCP's commitment to knowledge sharing and capacity building within the space weather community.

Fig.4 2023 IMCP workshop in front of IMCP headquarters building

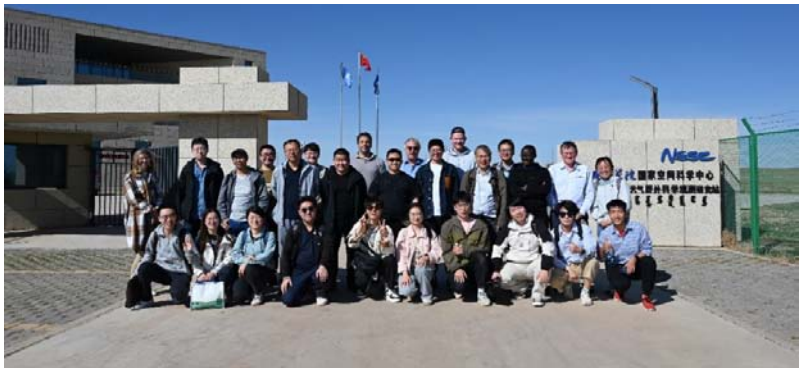

Fig.5 2024 SuperDARN and IMCP onsite group photo

In 23–27 September 2024, a new annual IMCP workshop will be organized under the theme "Monitoring Geospace Disturbances from the Ground: Scientific Challenges, Observational Networks, and International Collaboration". It will be held in São Paulo State, Brazil (https://workshop2024.imcp.ac.cn/), hosted by NSSC together with INPE, and sponsored by SCOSTEP, NSFC and other organizations.

9 Future Directions of IMCP

Space weather is a global phenomenon that requires international cooperation and participation. We have already collaborated with scientists from multiple countries to establish the IMCP framework. Moving forward, in addition to constructing and enhancing the 120°E–60°W Meridian circle, we also plan to expand the IMCP network along the 30°E–150°W Meridian circle in cooperation with the International Space Weather Initiative (ISWI). We envision a future where thousands of IMCP instruments observing together will form a three-dimensional information grid spanning five continents, providing real-time information about near Earth's space environment and contributing to safeguarding our planet against natural and anthropogenic hazards. We may also benefit from space weather monitoring systems commonly developed to shield our society.

References

[1] BLANC M, BOUNHIR A, DONOVAN E, *et al*. Science Objectives and Observation System for the International Meridian Circle [J]. *Taikong*, 2020, 19

[2] LIU W, WANG C, SHEN X, *et al*. b. International meridian circle program[J]. Chin J Space Sci., 2020, **40**(5):723-725

[3] WANG C. New chains of space weather monitoring stations in China[J]. *Space Weather*, 2010, **8**, S08001. Doi: 10.1029/2010SW000603

[4] SUN W, WU B, WU Z, *et al*. IONISE: An Ionospheric Observational Network for Irregularity and Scintillation in East and Southeast Asia[J]. *Journal of Geophysical Research: Space Physics*, 2020. DOI.org/10.1029/2020JA028055

[5] LIU W, BLANC M, WANG C, *et al*. Scientific challenges and instrumentation for the International Meridian Circle Program[J]. *Science China Earth Sciences*, 2001, **64**(12): 2090-2097. DOI.org/10.1007/s11430-021-9841-8

[6] LIU William, MICHEL Blanc, WANG Chi, *et al*. Progress of International Meridian Circle Program[J]. *Chinese Journal of Space Science*, 2022, **42**(4): 584-587. DOI:10.11728/cjss2022.04.yg10

[7] WANG C, XU J, LIU L, *et al*. Contribution of the Chinese Meridian Project to space environment research: highlights and perspectives[J]. *Sci. China Earth Sci*., 2023, **66**: 1423-1438. DOI.org/10.1007/s11430-022-1043-3

[8] SUN W, LI G, ZHANG S, *et al*. Regional ionospheric super bubble induced by significant upward plasma drift during the 1 December 2023 geomagnetic storm[J]. *Journal of Geophysical Research: Space Physics*, 2024, **129**(6). DOI.org/10.1029/2024ja032430

Progresses and Activities of the International Space Science Institute - Beijing (ISSI-BJ)

DONG Xiaolong

National Space Science Center, Chinese Academy of Sciences, Beijing 100190

1 Introduction

The International Space Science Institute in Beijing (ISSI-BJ) was jointly established by the National Space Science Center (NSSC) and the International Space Science Institute (ISSI) with the support of the International Cooperation Bureau and the Space Science Strategic Project of the Chinese Academy of Science (CAS). ISSI-BJ is a close cooperation partner of ISSI in Bern, Switzerland. Both institutes share the same Science Committee, the same study tools, and other information of mutual relevance and interest, however, both have independent operational methods and funding sources.

In the year 2022, despite the ongoing global pandemic, ISSI-BJ continued to advance under the leadship of the executive director, Professor Wing-Huen Ip, by organizing a multitude of online activities to sustain momentum and prepare research activities for the post-pandemic era. The institute conducted four series of online seminars, which enhanced its visibility in the international space science community.

The year 2023 marks a significant milestone for ISSI-BJ, as it commemorated the institute's 10th anniversary. This anniversary was of particular significance as it coincided with the resurgence of in-person exchanges and international collaborations following the global pandemic of COVID-19. Following 3-year of primarily virtual interactions, ISSI-BJ welcomed the opportunity to reconvene with the scientific community in person, reinvigorating its commitment to fostering global partnerships and scientific discourses.

2 International Teams

Since 2014, ISSI-BJ and ISSI have issued annual joint calls for International Teams in Space and Earth Sciences each year in January. This initiative is designed to encourage proposals for study projects from internationally collaborating teams of scientists from different institutions. The Call is open to scientists of any nationality actively involved in different fields of space and earth science: astrophysics and cosmology, solar and heliospheric physics, solar-terrestrial sciences, planetary science, fundamental physics and astrobiology in space, and earth sciences using space data.

In a similar vein to previous years, ISSI-BJ, in conjunction with ISSI, issued calls for international teams in space and earth sciences during the 2022-2023 period. Following a review by the Science Committee, eight ISSI/ISSI-BJ International Teams and one ISSI-BJ only International Team were approved for implementation in the following two years. These teams, comprising scientists from a range of institutions and different countries, addressed a diverse array of space science disciplines (Table 1).

As the Covid-19 pandemic abated, international travel to and from China resumed, ISSI-BJ in-person

Received June 20, 2024

Table 1 International Teams and Their Leaders

	International Team Subjects	Leader(s)
1	Magnetohydrostatic Modeling of the Solar Atmosphere with New Datasets	Xiaoshuai Zhu (NSSC, CAS, China)
2	Solar eruptions: preparing for the next generation multi-waveband coronagraphs	Alessandro Bemporad (INAF-Turin Astrophysical Observatory, Italy)
3	Strong Gravitational Lensing Studies with CSS-OS and EUCLID	Ran Li (NAOC, CAS, China)
4	Using Energetic Electron and Ion Observations to Investigate Solar Wind Structures and Infer Solar Wind Magnetic Field Configurations	Gang Li (University of Alabama in Huntsville, USA) & Linghua Wang (Peking Univ. China)
5	Understanding Electron-Scale Magnetic Structures in Space Plasmas	Elena Grigorenko (Space Research Institute of Russian Academy of Sciences) & Huishan Fu (Beihang Univ. China)
6	Magnetohydrodynamic Wavetrains as A Tool for Probing the Solar Corona	Bo Li (Shandong Univ. China)

events resumed in 2023, and international teams that had been approved but could not be held during the pandemic period were rescheduled and met in sequence. By the end of 2023, 6 teams had met in ISSI-BJ for one-week-long meetings, and as a result of their research, they have published 17 papers in peer-reviewed journals.

3 Forums

Forums are informal and free debates on open questions of scientific nature, science strategy matters among 20 to 30 high-level invited participants. Forums may lead to formal recommendations or decisions depending upon the topics or issues addressed during the activity. At ISSI-BJ, forums are also organized to discuss the science, technology, and international cooperation of future space science missions. The outcomes are white papers for future missions. The outputs of ISSI-BJ forums are published in the ISSI-BJ's TAIKONG magazine series, which reports on the contents of the Forums and reflects in a neutral way the Forum discussions and advice from all the participants. Forums organized by ISSI-BJ provided a platform for high-level discussions on critical scientific and policy matters. There are 1 forum conducted in 2023:

- **Detecting Missing Baryons in the Universe:** This forum discusses the problems of missing baryons on scales of galaxies and large-scale structures and makes plans for X-ray missions that are dedicated to solving these problems.

4 Workshops

The workshops are study projects on specific scientific themes, selected in consultation with the Science Committee. The typical duration of a workshop is one week. The organization of workshops is the responsibility of a group of conveners, who define the theme, set up the program, and list the group of participants. Participation is by invitation only. The number of participants in any given workshop is typically limited to 45 researchers, with a few young scientists included. The outcomes of the activity are disseminated in the form of peer-reviewed articles in the Space Science Reviews journal and in the Space Science Series of the International Space Science Institute (ISSI)/Beijing Institute of Space Astronomy (BJ) (SSSI).

Due to the global pandemic, the workshops recommended by the Scientific Committee (SC) and supposed to be held during the 2022-2023 period were suspended and did not resume until 2024.

5 Outreach Activities

- **Online Seminars:** The seminars included the "On Things to Come" series, which featured talks on space missions; "1001 Space Nights," which provided science education led by female scientists; "Topical Review," which included leading researchers from Chinese and French universities; and the "Space Science Bazaar," which focused on young scientists from the ISSI-BJ International Teams Program presenting their research. In the year 2022, ISSI-BJ held 12 On Things to Come webinars, 11 1001 Space Nights events, 9 Space Science Bazaar events, and 9 Topical Reviews. Since mid-2023, ISSI-BJ has resumed in-person activities, which has resulted in a reduction in online seminars. The sole remaining online series is "Infinite Horizon" which succeeds the "On Things to Come" series online seminars.
- **Space Science School:** In collaboration with the Asia-Pacific Space Cooperation Organization

(APSCO), ISSI-BJ held a biennial Space Science School on the topics of space sciences and space science missions. The school offered comprehensive training for international students. The students are provided with the requisite scientific background to enable them to produce a report. In 2023, the third joint space science school was held at the Geo-informatics and Space Technology Development Agency (GISTDA) in Si Racha, Chon Buri Province, Thailand. The focus of the school was on future collaboration in lunar or planetary sciences. A total of 25 Students from Bangladesh, China, Iran, Mongolia, Peru, Thailand, Turkey, Thailand and Germany attended this Space Science School.

- **The 3rd China-ESA Mars Advanced School** This event marked the first in-person activity since the pandemic. It took place in Huairou, Beijing in May 2023, jointly organized by ISSI-BJ and the European Space Agency (ESA), with the National Space Science Center, Chinese Academy of Sciences (NSSC, CAS) acting as a co-sponsor. The Mars School was inspired by the scientific investigations conducted by an ever-growing fleet of missions and provided a comprehensive overview of Martian science, from its interior and surface to its atmosphere and interactions with space. The lectures encompassed a theoretical background and modeling, observation techniques and datasets, as well as the search for the past or present life. A total of 63 Chinese students and 17 European students from institutes and universities, including individuals from Italy, Portugal, the Czech Republic, Switzerland, the United Kingdom, Poland, Spain, Germany and Hungary attended this Advanced School.
- **ISSI-BJ 10th Anniversary Symposium: Space Science in the Next Decade** This event was held as part of the celebrations marking the 10th anniversary of ISSI-BJ. This symposium brought together 6 ISSI-BJ's disciplinary scientists, and young leaders of the international team from 5 different countries to discuss the focus and importance of ISSI-BJ in the next decade. The presentations and discussions covered a range of topics, including solar physics, astrophysics, planetary science and ISSI-BJ's development strategy. This event was held in July 2023 in Beijing, China.

6 Publications

- **Taikong Magazine:** The Taikong magazine series reports on the content of the forums organized at ISSI-BJ, reflecting the discussions and advice from all participants in a neutral manner. Several issues have been published covering various topics discussed during the forums. In 2023, the 12th issue of Taikong magazine, entitled "Detecting Missing Baryons in the Universe," was published.
- **Space Sciences Series of ISSI (SSSI):** The SSSI published a topical volume first in Space Science Reviews and subsequently as part of the SSSI book series, focusing on significant findings and discussions from ISSI-BJ workshops.

Progress of Radiation Belt Exploration by a Constellation of Small Satellites TGCSS/SGRB, COSPAR

WU Ji, YANG Xiaochao, DAI Lei, DENG Li

National Space Science Center, Chinese Academy of Sciences, Beijing 100190

1. Introduction

In 2017, the Committee On SPAce Research (COSPAR) convened a diverse panel comprising researchers, managers, and policy makers to explore the potential applications of small satellites in advancing technology, scientific research, and space-based activities. The resulting two-year COSPAR study provided a comprehensive scientific roadmap aimed at offering specific direction on the utilization of small spacecraft.

"COSPAR should facilitate a process whereby international teams can come together to define science goals and rules for a modular, international small satellite constellation. The role of COSPAR is one of an honest broker, coordinating not funding. The results of an international effort to build small satellite constellations would be valuable for all participants and would be more valuable than the individual parts. COSPAR is in a position to help foster this international collaboration, creating a precedent for setting up community science in a very open way. "

To operationalize the recommendations outlined in the COSPAR Strategic Action Plan and the Scientific Roadmap on Small Satellites for Space Science, COSPAR established the Task Group on establishing a Constellation of Small Satellites (TGCSS) in late 2019, with Prof. Daniel Baker from Colorado University serving as chair. TGCSS highlights the importance of addressing various program components, including ionosphere/thermosphere studies, radiation belt exploration, solar energetic particle events, atmospheric remote sensing, and operational considerations such as ground station infrastructure, radio licensing, space access, and data management.

To address the specific challenges related to radiation belt measurements, TGCSS established a dedicated sub-group called the Sub-Group on Radiation Belt (SGRB), chaired by Prof. WU Ji from National Space Science Center (NSSC), Chinese Academy of Sciences (CAS), a TGCSS member. SGRB's primary focus is on implementing a Small/CubeSats constellation mission dedicated to radiation belt exploration. In pursuit of this mission, a proposal for a program named COnstellation of Radiation BElt Survey (CORBES) was presented by NSSC CAS during a TGCSS meeting in July 2021. Subsequently, SGRB has worded on demonstrating scientific objectives of CORBES, identifying potential international participants to this mission and organizing the related technical design.

2 CORBES mission

2.1 The Concept of CORBES

The CORBES mission aims to conduct an ultra-fast survey of the Earth's radiation belt using a constellation of multi-Small/CubeSats. The orbit of CORBES is de-

Received June 20, 2024

signed to closely align with the equatorial plane, with an apogee altitude of approximately 7 Earth radii, similar to that of Geostationary Transfer Orbits (GTO) (refer to Figure 1). By utilizing this multi-satellite constellation, the mission aims to differentiate between temporal and spatial variations in the radiation belts, thus significantly advancing our understanding of Earth's radiation belt dynamics. Each Small/CubeSat is expected to have a minimum operational lifetime of one year to manage costs effectively [Wu et al., 2022].

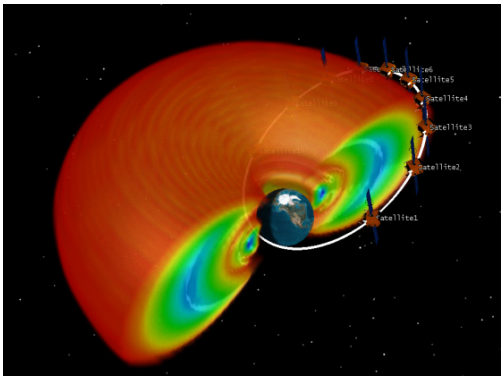

Fig.1 A constellation of multi-CubeSats to probe energetic particles of the radiation belt

CORBES is an international multilateral mission with potential participants from Asia, Europe, and America. Each entity is expected to contribute one or more satellites to form the constellation, equipped with baseline instruments to achieve CORBES's primary science goals, or provide related ground support system. A data-sharing policy will ensure open access to observations within the COSPAR mission, benefiting both contributors and the broader research community.

2.2 CORBES's Scientific Objectives

The CORBES mission aims to elucidate the physical mechanisms governing Earth's outer radiation belt dynamics, addressing key unresolved questions. Through a CubeSat constellation, CORBES will measure energetic electron flux, geomagnetic field variations, and plasma waves with unprecedented temporal and spatial resolution. This will enable detailed investigation of the outer radiation belt, potentially uncovering fundamental physical processes underlying its rapid dynamics. Below are primary targeted physical processes for quantitative or quasi-quantitative investigation (not exhaustive).

(1) Energy diffusion occurs due to local resonant interactions between electrons and Very Low Frequency (VLF) waves, including whistler-mode waves generated by unstable plasma distributions during storms [e.g, Thorne et al., 2013; Yang et al., 2017].

(2) Pitch angle scattering arises from local resonant interactions between electrons and magnetospheric plasma waves, including whistler hiss and electromagnetic ion cyclotron (EMIC) waves [e.g, Capannolo et al., 2019].

(3) Radial transport driven by the drift resonance between electrons and Ultra-Low-Frequency (ULF) magnetospheric waves [e.g, Dai et al., 2013, 2015a; Yang et al., 2014], alongside radial transport induced by sudden, intense electric fields resulting from large-scale magnetic field reconfiguration, including shock-induced injection, substorm depolarization injection [e.g, Dai et al., 2014,2015b; Xiong et al., 2022, 2024], and storm convection [e.g, Dai et al., 2024].

(4) Electron escape from the magnetosphere into the solar wind occurs via magnetopause shadowing and the combined effects of magnetopause shadowing and outward radial transport [e.g, Turner et al., 2010].

Analyzing these primary physical processes in detail will yield quantitative insights into electron transport, acceleration, and losses, elucidating their respective contributions to outer radiation belt dynamics. This comprehensive understanding will refine our knowledge of outer radiation behavior and improve prediction models for more accurate forecasts.

2.3 CORBES's Technical Design

The COnstellation of Radiation BElt Survey program (CORBES) is meant to launch small satellites into a highly elliptic orbit for multi-point exploration of the Earth's radiation belts. Its scientific purpose is to produce unprecedented high-time-resolution dynamics observations within the regions of Earth's outer radiation belts.

The CORBES program initiative contains satellites outfitted with three types of payloads: the Magnetometer (MAG), the Search Coil Wave Detector (SCWD), and the High Energy Electron Detector (HEED) [Wu et al., 2024].

In order to cover the outer radiation belts for the measurements, a highly eccentric and inclined orbit is suggested. The orbit apogee must permit adequate magnetic field exploration. An example of a standard science orbit is this: 280 km at the perigee, 7 R_e at the apogee, and approximately 11 degrees of inclination.

For such an orbit, the orbit period is then roughly 13.5 hours. The outer radiation band (3 R_e to 7 R_e) can be traveled through in around 10.5 hours. It is anticipated that every satellite will function in the same orbit, spinning at a speed of around eight revolutions per minute on a spin-stabilized axis that faces the sun. The mass of each satellite shouldn't be more than 30 kg. The program's lifespan cannot be shorter than a year.

For telecommand, either S-band or X-band will be utilized, while X-band is assigned for data downlink. The satellites are scheduled for launch by one or two rockets, with the fitted upper stage delivering them into the target orbit, and the connected dispenser releasing them individually according to the specified separation sequence.

Assembly Integration and Testing (AIT), radiation shielding, and cross-calibration are important components of the program. Cross-calibration of the payloads is optional before to launch. To calibrate the technical standards, the payloads will undergo testing in an identical setting. Cross-calibration in orbit after launch is required to preserve data consistency and comparability. With regard to HEED specifically, this entails choosing electrons in the same energy range during the magnetospheric quiet phase (Kp<3) and contrasting the outcomes of various HEED observations made under identical L, B conditions. When MAG and SCWD compare observations made during a chosen calm period, a similar methodology is used.

There are currently three small satellite contributions: the HIT satellite at the Harbin Institute of Technology (HIT), the IMACAS satellites at the Innovation Academy of Microsatellites (IMAC), and the Foresail satellites at the Finnish Centre of Excellence in Research of Sustainable Space (FORESAIL). IMAC is going to provide two satellites.

FGM has three contributions: MAG in the National Space Science Center, FGM at Beihang University (BHU), and FGM at the Space Research Institute Graz (IWF). The NSSC will contribute two sets of FGM. SCWD has two contributions: SCWD in the National Space Science Center and SCWD at Beihang University. The NSSC will contribute two sets of SCWD. HEED has four contributions: HEED at the National Space Science Center, HEED at Beihang University (BHU), HEED at the University of Turku (UTU), and HEED at the Paul Scherrer Institute. The NSSC will contribute two sets of HEED.

3 SGRB Science Activities on CORBES

Since its establishment, SGRB held more than forty on-line meetings to outline the profile of the CORBES mission, identify potential participants, discuss the science objectives, the instrument requirements and the technical design.

Dozens of reports from institutes, university, space agencies and commercial space companies, which are from China, America, Russia, Swiss, Finland, Japan, Brazil and Egypt, have been invited to be presented in the SGRB meetings. The potential participants contributing for the science payloads, CubeSats, deployer, launch and ground support system have been preliminarily identified. The CORBES scientist team has been set up. The CORBES's scientific objectives was discussed and defined, the scientific requirements of the payloads was preliminarily demonstrated, as well as the CORBES's technical design was organized.

Based on the discussion in the SGRB on-line meeting, NSSC wrote up three baseline technical documents of CORBES mission. Technical Document 1: Mission Description, which generally describes CORBES mission and presents an initial system design. Technical Document 2: Baseline Science Payloads and Reference Design Requirements, which describes three baseline science payloads of CORBES and the fundamental design requirements. Technical Document 3: Fundamental requirements of Small/CubeSat satellite platform, which describes fundamental requirements of Small/CubeSat platform for CORBES.

At the suggestion of SGRB chair, prof. WU Ji, to COSPAR headquarters, a TGCSS business meeting was arranged during the 5th COSPAR Symposium in Singapore. At this business meeting, the progress of the CORBES mission was presented. Two oral reports describing the CORBES mission, "Constellation of radiation belts survey (CORBES): a COSAR small satellite constellation survey program for Earth's radiation belt" and "System design for the constellation of radiation belt survey program", were presented at the 5th Symposium of COSPAR.

Two papers about the technical design and the scientific objectives of CORBES, "Multi-Satellite Survey Scheme for Addressing Open Questions on the Earth's Outer Radiation Belt Dynamics" and "CORBES: radiation

belt survey with international small satellite constellation", have been submitted to Advances in Space Research.

4 COSPAR HQs Coordinate Activities on CORBES

In November 2023, the COSPAR headquarters sent out a Call for Letters of Intent to several institutes, universities, and commercial space companies to accurately identify potential participants for the CORBES mission. Positive responses were received from some them.

To foster international cooperation for the CORBES mission, the COSPAR Secretariat facilitated two meetings between NASA and itself to discuss NASA's potential contribution to CORBES. The outcome of these meetings was generally positive. During these sessions, NASA representatives indicated that while they couldn't engage in bilateral space missions with China, they were open to participating in multilateral mission. They expressed enthusiasm for the CORBES program concept and their willingness to participate, on the condition that teams from at least one other country were involved. However, they highlighted a current challenge: the absence of budget allocation for such a program this year. Notably, GTOSat from LASP at the University of Colorado emerged as a feasible contribution from NASA, given that its construction has already been completed.

The COSPAR headquarters is currently in the process of establishing the COSPAR Small Satellite Constellation Project Office (SSC-PO), which will oversee the management of COSPAR small satellite science missions. SSC-PO will be tasked with managing the CORBES mission on behalf of COSPAR and coordinating related international cooperation efforts. The selection process for the SSC-PO manager is underway, with potential candidates being identified.

In April 2024, COSPAR headquarters sent a progress letter to all identified potential participants from various countries involved in CORBES. The purpose of this letter was to confirm the ongoing status of the mission and to initiate the mission kick-off process. Chinese institutions, universities, and commercial space companies involved in the mission have received this letter.

5 Summary

Following the COSPAR Scientific Roadmap on Small Satellites for Space Science, SGRB of TGCSS proposed the CORBES mission to address the Earth's radiation belt scientific survey program and has been propelling this mission over the past two years.

Over the past two years, SGRB has hosted more than forty online meetings to outline the CORBES mission profile, identify potential participants, establish the CORBES scientist team, and organize the mission's technical design. The CORBES scientist team discussed and defined the CORBES's scientific objectives and demonstrated the scientific requirements of the payloads. The general science goal for CORBES is to investigate two groups of physical processes related to the radiation belts: wave-particle interactions and radial transport. Two papers about the technical design and the scientific objectives of CORBES have been submitted to Advances in Space Research.

In propelling CORBES, COSPAR has played a key role in coordinating and managing the mission, as well as acting as a mediator between participating governments, universities, and research institutions.

The data set from CORBES will be shared among the contributors to the constellation and the broader research community. This data will be invaluable for comprehensively understanding the dynamics of magnetospheric energetic populations and developing a more standard model of the Earth's radiation belts. Additionally, from an application perspective, the ultra-fast survey of the radiation belt will serve as a crucial tool for monitoring Earth's space weather.

References

[1] Capannolo, L., Li, W., Ma, Q., Chen, L., Shen, X.-C., Spence, H. E., et al. (2019). Direct observation of subrelativistic electron precipitation potentially driven by EMIC waves. Geophysical Research Letters, 46. https://doi.org/10.1029/2019GL084202.

[2] Dai, L., K. Takahashi, R. Lysak, C. Wang, J. R. Wygant, C. Kletzing, J. Bonnell, C. A. Cattell, C. W. Smith, R. J. MacDowall, S. Thaller, A. Breneman, X. Tang, X. Tao, and L. Chen (2015a), Storm time occurrence and spatial distribution of Pc4 poloidal ULF waves in the inner magnetosphere: A Van Allen Probes statistical study. *J. Geophys. Res. Space Physics*, 120, 4748–4762. doi: 10.1002/2015JA021134.

[3] Dai, L., C. Wang, S. Duan, Z. He, J. R. Wygant, C. A. Cattell, X. Tao, Z. Su, C. Kletzing, D. N. Baker, et al. (2015b), Near-Earth injection of MeV electrons associated with intense dipolarization electric fields: Van Allen Probes observations, *Geophys. Res. Lett.*, 42, 6170–6179, doi:10.1002/2015GL064955.

[4] Dai, L., J. R. Wygant, C. A. Cattell, S. Thaller, K. Kersten, A. Breneman, X. Tang, R. H. Friedel, S. G. Claudepierre, and X. Tao (2014), Evidence for injection of relativistic electrons into the

Earth's outer radiation belt via intense substorm.

[5] Dai, L., Zhu, M., Ren, Y. *et al*. Global-scale magnetosphere convection driven by dayside magnetic reconnection. *Nat Commun* 15, 639 (2024). https://doi.org/10.1038/s41467-024-44992-y.

[6] Turner, D. L., Angelopoulos, V., Morley, S. K., et al. (2014). On the cause and extent of outer radiation belt losses during the 30 September 2012 dropout event. Journal of Geophysical Research: Space Physics, 119(3), 1530–1540. https://doi.org/10.1002/2013JA019446

[7] Wu, J., Yang X., & Dai L. (2022) Progress of Radiation Belt Exploration by a Constellation of Small Satellites TGCSS/SGRB, COSPAR. Chinese Journal of Space Science, 2022, 42(4): 836-840. https://doi.org/10.11728/cjss2022.04.yg18.

[8] Wu J., Deng L., J. Praks et al., (2024), CORBES: Radiation belt survey with international small satellite constellation, Advances in Space Research, https://doi.org/10.1016/j.asr.2024.04.051.

[9] Xiong, S., Dai, L., Wang, C., Yang, X., Wygant, J. R., & Baker, D. N. (2024). Rapid relativistic electron enhancements and associated particle injections: A multi-spacecraft statistical study. *Journal of Geophysical Research: Space Physics*, 129, e2023JA032095. https://doi.org/10.1029/2023JA032095

[10] Xiong, S.-L, Dai, L., Wang, C., Wygant, J., Cattell,C., Tao, X., Baker,D., Blake, J., (2022). Relativistic Electron Enhancements through Successive Dipolarizations during a CIR-driven Storm. *Journal of Geophysical Research: Space Physics*, 127,e2021JA030088. https://doi.org/10.1029/2021JA030088

[11] Yang, X. C., G. W. Zhu, X. X. Zhang, Y. Q. Sun, J. B. Liang, and X. H. Wei (2014), An unusual long-lived relativistic electron enhancement event excited by sequential CMEs, J. Geophys. Res. Space Physics, 119, doi:10.1002/2014JA019797.

[12] Yang, X., B. Ni, J. Yu, Y. Zhang, X. Zhang, and Y. Sun (2017), Unusual refilling of the slot region between the Van Allen radiation belts from November 2004 to January 2005, J. Geophys. Res. Space Physics, 122, 6255–6270, doi:10.1002/2016JA023204.

Secretariat Contact:

LI Xiaoyu, XU Yongjian

CNCOSPAR Secretariat

Nanertiao 1, Zhongguancun, Haidian District, Beijing 100190, China

Tel: 86-10-6258 6404

Fax: 86-10-6263 2257

E-mail: xuyongjian@nssc.ac.cn